Insights into the geochemical evolution and origin of Permian to Eocene (263-49 Ma) volcanism in Namibia

DISSERTATION

zur Erlangung des Doktorgrades

der Mathematisch-Naturwissenschaftlichen Fakultät

der Christian-Albrechts-Universität zu Kiel

Vorgelegt von

Hongpu Zhou

Kiel, 2021

Erster Gutachter: ..... Prof. Dr. Kaj Hoernle

Zweiter Gutachter: .....PD. Dr. Thor Hansteen

Tag der mündlichen Prüfung: 25.01.2021

.....

Der Dekan

Hiermit erkläre ich, dass die vorliegende Doktorarbeit selbständig, abgesehen von der Beratung durch den Betreuer und ohne Zuhilfnahme unerlaubter erstellt habe. Weder diese noch eine ähnliche Arbeit wurde an einer anderen Hochschule im Rahmen eines Prüfungsverfahrens vorgrlrgt, veröffentlicht oder zur Veröffentlichung vorgelegt. Auch wurde mir kein akademischer Grad entzogen. Ferner versichere ich, dass die Arbeit unter Einhaltung der Regeln guter wissenschaftlicher Praxis der Deutschen Forschungsgemeinschaft entstanden ist.

Kiel, den 15. Dez. 2020.....

Hongpu Zhou

Abstract

The South Atlantic and the adjacent voluminous Paraná-Etendeka igneous provinces in Brazil and Namibia, respectively, are considered a classic example of the succession of flood basalt volcanism, continental breakup and adjacent age-progressive hotspot track. Magmatism is commonly linked to the current Tristan-Gough hot spot, whose initial "plume head" stage created the Etendeka flood basalts and related magmatic complexes in western Namibia during the Mid-Cretaceous, followed by the "plume tail" stage forming Walvis Ridge and the Tristan-Gough seamount trail in the South Atlantic. Based on their Ti content, the Etendeka flood basalts are divided into high-Ti (and low-Ti (groups. The magmatic origin of both groups and their relationship to the Tristan-Gough plume (head) are still debated. The well-exposed Etendeka volcanism in western Namibia provide the opportunity to examine the classic plume head – plume tail concept, i.e. the geochemical relationship of the magmatism from both stages. The different rock-types associated with the Etendeka event (carbonatite, silica-undersaturated rocks and basalt) and their varying isotopic compositions and ages can be used to gain insights into the spatial and temporal evolution of the plume and, by inference, into the supposably deep plume source region in the lower mantle at the edge of the seismically imaged African large low-shear-velocity province (LLSVP). In my PhD thesis I present a comprehensive data set of major and trace element and C-O-Sr-Nd-Pb-Hf isotopic compositions, as well as geochronological data of the Etendeka flood basalts, silica-undersaturated and carbonatitic intrusions in Namibia and discuss the geochemical implications in context with the mantle plume model.

The obtained results confirm that the Tristan-Gough plume was responsible for creating the Etendeka flood basalts and those igneous complexes that were formed contemporaneously. The high-Ti basalts, mainly found in northern Etendeka, have the same isotopic “Gough-type” composition as the Walvis Ridge basement and the Gough seamount track lavas, indicating that the Gough-type component dominated the Tristan-Gough plume from the initial plume head stage (northern Etendeka) to the still persisting plume tail stage (Walvis Ridge, Gough seamount track, Gough island). The low-Ti basalts, exclusively occurring in southern Etendeka show a distinct isotopic composition which I term Doros-type (after a type locality). Considering published high $^{3}He/^{4}He$ ratios and high inferred potential temperatures for lavas belonging to the low-

Ti group, the Doros source should also have derived from the lower mantle and ascended within the Tristan-Gough plume head. Accordingly, the spatial division of the high-Ti/Gough and low-Ti/Doros groups in the Etendeka province point to a geochemical zonation within the plume head, a model that is here proposed for the first time.

Unfortunately, widespread crustal contamination of the siliceous plume magmas hampers the recognition of geochemical zonation in southern Etendeka. Carbonatites and silica-undersaturated rocks, however, are relatively insensitive to crustal contamination due to their natural enrichment in incompatible elements. They are therefore particular suitable for constraining their source composition and for revealing any spatial zonation. By combining published data with my new findings from analyzed carbonatitic and silica-undersaturated intrusions, the occurrence and distribution of the Doros-type (low-Ti) magmas could be further constrained: In southwestern Etendeka, Doros-type magma only created the eponymous Doros intrusion, Messum intrusion and the Tafelkop and Horingbaai formations. In contrast, the eastern/southeastern Etendeka intrusions (Okorusu, Paresis, Etaneno and Osongombo) show Gough-type composition, similar to the high-Ti basalts in northern Etendeka, Walvis Ridge and Gough seamount track lavas. Together with the northern Etendeka lavas, the Gough-type magmatism seems to form a horseshoe-shaped belt thatencloses the Doros-type (low-Ti) magmatism. I interpret this pattern to reflect a heterogeneous plume head with potentially denser, less buoyant material in the center (Doros) and less dense (more buoyant) in the periphery. Such distribution would be consistent with fluid-dynamic models, postulating that the denser (Doros) component can only be entrained and carried to the upper mantle within the voluminous plume head, which provides sufficient buoyancy. This model would explain why rocks with Doros composition were only produced during the 133 to 123 Ma lasting plume head stage but could not be found in any of the later (plume tail) eruption products (e.g. at Walvis Ridge or the seamount province) of the Tristan/Gough mantle plume/hotspot.

The detailed geochemical and geochronological investigations also revealed that several carbonatitic and silica-undersaturated intrusions were emplaced after the Etendeka event. In contrast to the Etendeka plume-associated Doros and Gough compositions, which both have an overall enriched mantle I (EM I) isotopic signature, these later magmatism shows an uniform HIMU-like (high time-integrated $^{238}U/^{204}Pb$

with radiogenic Pb and Nd but unradiogenic Sr isotope ratios) composition. Such temporal succession was recently also found at Walvis Ridge where low-voluminous, late-stage HIMU volcanism succeeded at any given site the massive EM I volcanism that formed the Walvis Ridge basement. My findings imply that the same process is also responsible for creating the younger, HIMU volcanism in Namibia. Accordingly, the existence of several age-progressive, but transient hotspot tracks of HIMU composition are proposed that extent from the SW border of the African continent into the SE Atlantic.

By combining the geochemical data with plate reconstructions and seismic tomographic mantle models, plumes of EM I-type composition (Tristan-Gough, Discovery and Shona) are proposed to ascend from the outer margin of the LLSVP, whereas subsequent (smaller) plumes of HIMU composition appear to detach from a steep topographic step on the inner surface of the LLSVP, recognizable at about 1000-1500 km east of the outer margin. In conclusion, my results support the hypothesis that the EM I and HIMU components are derived from distinct reservoirs within a compositionally layered LLSVP.

Zusammenfassung

Der südliche Atlantik mit den angrenzenden magmatischen Provinzen Paraná-Etendeka in Brasilien bzw. Namibia gelten als klassisches Beispiel für die Abfolge von Flutbasaltvulkanismus, Kontinentaufbruch und anschließender Hotspot-Spur. Der Ursprung des Magmatismus wird gemeinhin mit dem derzeitig noch aktiven Tristan-Gough-Hotspot verbunden, dessen initiales "Plumekopf"-Stadium in der mittleren Kreidezeit die Etendeka-Flutbasalte und assoziierte magmatische Komplexe erzeugte, gefolgt vom "Plumestamm"-Stadium, das für die Entstehung von Walvis-Rücken und schließlich der Tristan-Gough Seamount-Spur im Südatlantik verantwortlich ist. Die Laven der Etendeka-Flutbasalte können in Ti-reiche und Ti-arme Gruppen eingeteilt werden, wobei der Ursprung dieses Unterschiedes und dessen Beziehung zum Tristan-Gough Mantel Plume (-kopf) bisher nicht geklärt war. Die hervorragend aufgeschlossenen Gesteine des Etendeka-Magmatismus im westlichen Namibia ermöglichen die genauere Untersuchung des klassischen Plumekopf-Plumestamm Modells und insbesondere einen geochemischen Vergleich von beiden Stadien. Die unterschiedlichen Gesteinstypen (Carbonatite, Si-untersättigte Gesteine und Basalte), ihre unterschiedliche isotopische Zusammensetzung und verschiedenen Alter können genutzt werden um die zeitlich-räumliche Entwicklung des Plumes zu rekonstruieren und somit auch Rückschlüsse auf die tiefe Plumequelle am Rande der seismisch-definierten large low-shear-velocity province (LLSVP) im untersten Mantel zu ziehen. Dazu präsentiere ich in meiner Doktorarbeit einen umfassenden Datensatz von Haupt- und Spurenelement- und C-O-Sr-Nd-Pb-Hf- Isotopenzusammensetzungen sowie Altersbestimmungen von Etendeka-Flutbasaltlaven, und Si-untersättigten und carbonatitischen Intrusionen aus Namibia, die im Kontext das Mantel Plume-Modells diskutiert werden.

Die Untersuchungsergebnisse bestätigen das der Tristan-Gough Plume für die Entstehung der Etendeka-Flutbasalte und zeitgleich entstandener magmatischer Komplexe verantwortlich gemacht werden kann. Die Ti-reichen Basalte, die überwiegend im nördlichen Etendeka anstehen, haben eine „Gough-Type“-Isotopenzusammensetzung, identisch mit der Hauptphase des Walvis-Rückens und der Gough Seamount Spur, was darauf hindeutet dass die Gough-Komponente den Mantelplume von seinem initialen Plumekopf-Stadium (nördliches Etendeka) bis zum immer noch aktiven Plumestamm-Stadium (Walvis-Rücken, Gough Seamount Spur

und Gough Insel) dominiert hat. Die Ti-armen Basalte, die ausschließlich im südlichen Etendeka vorkommen, weisen eine andere Isotopenzusammsetzung auf, die ich nach einer Type-Lokalität „Doros-Type“ benannt habe. Da von Gesteinen des Doros-Types hohe $^{3}He/^{4}He$ Isotopenverhältnisse und Berechnungen hoher Aufschmelztemperaturen veröffentlicht wurden, kann auch für die Doros-Quelle von einem Ursprung im tiefen Erdmantel und somit einem Aufstieg im Tristan-Gough Plumekopf ausgegangen werden. Die räumliche Verteilung der Ti-reichen/Gough und Ti-armen/Doros Vulkanite in der Etendeka Provinz deutet daher auf eine laterale Zonierung innerhalb des Plumekopfes hin, ein Modell das hier zum ersten mal vorgeschlagen wird.

Leider haben nahezu alle silikatischen Magmen im südlichen Namibia beim Aufstieg krustales Nebengestein assimiliert, was die Erkennung von geochemischer Zonierung erschwert. Dagegen sind Carbonatite und Si-untersättigte Gesteine aufgrund ihrer natürlicherweise hohen Gehalte an inkompatiblen Spurenelementen relativ wenig von krustaler Kontamination betroffen und eignen sich daher besonders gut für die Bestimmung ihrer Magmenquellenzusammensetzung. Durch die Kombination von veröffentlichten Daten mit meinen neuen Analysen der Carbonatite und Si-untersättigten Gesteine konnte ich das Vorkommen des Doros-Type-Magmatismus in Namibia weiter präzisieren: Demnach finden sich Gesteine mit Doros-Signatur nur im südwestlichen Etendeka (die namensgebenden Doros Laven, die Intrusion von Messum sowie die Tafelkop und Horingbaai Formationen). Im Gegensatz haben die östlichen und südöstlichen Intrusionen (Okuruso, Paresis, Etaneno und Osongombo) eine Gough-Type-Signatur identisch mit den Ti-reichen Laven im nördlichen Etendeka sowie dem Walvis-Rücken und der Gough Seamount Spur. Der Gough-Type-Magmatismus scheint dabei die Vorkommen mit Doros-Zusammensetzung wie ein Hufeisen zu umschließen. Dieses Muster kann als Abbild einer großräumigen Zonierung innerhalb des Plumekopfes interpretiert werden, bei der dichteres Material (Doros) im Zentrum von Material mit höherem Auftrieb (Gough) umgeben ist. Fluid-dynamische Modelle zeigen das nur der verstärkte Auftrieb im voluminösen Plumekopf in der Lage ist eine schwere Lithologie in den oberen Mantel zu transportieren. Dies würde erklären warum die Doros-Komponente in der über 130 Millionen Jahre andauernden Geschichte des Tristan/Gough Mantle Plumes/Hotspots nur in Produkten des relativ kurzzeitigen Plumekopf-Stadiums gefunden werden kann und nicht in den nachfolgenden

Eruptionsprodukten des kleineren Plumestamms (z.B. Walvis-Rücken oder der Seamount Provinz).

Die detaillierten geochemischen und geochronologische Untersuchungen haben aber auch ergeben das verschiedene carbonatitische und Si-untersättigte Intrusionen erst deutlich nach dem Etendeka-Event entstanden sind. Im Gegensatz zu den auf den Etendeka-Plume zurückführbaren Doros- und Gough-Komponenten, die beide eine übergeordnete Enriched Mantle I (EM I)-Zusammensetzung aufweisen, zeigt dieser spätere Magmatismus eine einheitliche HIMU-Zusammensetzung (hohe, zeit-integrierte $^{238}U/^{204}Pb$ Quelle mit radiogenen Pb- und Nd- und unradiogenen Sr-Isotopenverhältnissen). Eine solche zeitliche Abfolge wurde kürzlich auch am Walvis-Rücken nachgewiesen, wo kleinräumiger HIMU-Vulkanismus stets auf den massiven EMI-Vulkanismus folgt, der den eigentlichen voluminösen Rücken aufgebaut hat. Meine Ergebnisse deuten darauf hin, dass der gleiche Prozess auch für die Entstehung des jüngeren HIMU-Vulkanismus in Namibia verantwortlich gemacht werden kann. Demnach können mehrere, überwiegend kurzlebige, altersprogressive Hotspot-Spuren mit HIMU-Zusammensetzung identifiziert werden, die sich vom südwestlichen Rand des afrikanischen Kontinents in den südöstlichen Atlantik erstrecken.

Die Kombination der neuen geochemischen Erkenntnisse mit plattentektonischen Rekonstruktionen und regionalen seismisch-tomographischen Mantelmodellen führt zu einem Modell bei dem regionale Mantelplumes mit EM I-Zusammensetzung (Tristan-Gough, Discovery und Shona) am äußeren Rand der LLSVP entstehen, während spätere (kleinere) Plumes mit HIMU-Zusammensetzung sich von einer tomographisch erkennbaren steilen Stufe an der Oberseite der LLSVP etwa 1000-1500 km weiter östlich abzulösen scheinen. Zusammenfassend unterstützen meine Ergebnisse die Hypothese, dass die EM I- und HIMU-Komponenten von unterschiedlichen Reservoiren einer in sich kompositionell geschichteten LLSVP abstammen.

Contents

Chapter 1.

General introduction

1.1. Mantle plume and large igneous province

The large igneous province (LIPs) are usually defined as sites of large volume of magmatism (>0.1 Mkm^3), composed mainly of mafic magma and associated silicates, carbonatites and kimberlites, emplaced in a short (<50 Ma) duration (Ernst, 2014). LIPs are important research objects for constraining mantle plume processes and composition. Mantle plumes are believed to originate from the core-mantle boundary and are considered as being nearly stationary (Wilson, 1963). Recently, improved plate reconstructions suggest that most plumes are generated at the boundaries of the two large low shear-wave velocity provinces (LLSVPs) beneath Africa and the Pacific Ocean, which are therefore also called "plume generation zones" (Burke et al., 2008; Torsvik et al., 2006; Torsvik et al., 2014). According to the classical model, a typical mantle plume is composed of a bulbous plume head followed by a narrow plume tail. When the plume head arrives at the base of the lithosphere, it flattens to a disk which can reach 2000-2500 km in diameter (Campbell, 2007), producing large volumes of magma by adiabatic decompression melting. Consequently, the overlying plate experiences intense volcanism within a relatively short geological period, leading to the formation of a LIP. Eventually, the fusible plume head material is exhausted and the "plume head stage" is followed by a long-lived "plume tail stage". Less voluminous but more focused magmatism is generated by the upwelling material of the narrow plume tail and plate motion leads to the formation of an age-progressive volcanic chain on the overriding plate. Thus, the plume head-tail model explains the close association of LIPs and hotspot tracks.

In recent years, spatial geochemical zonation have been discovered in volcanic areas produced by the plume tail stage, such as the Tristan-Gough (Hoernle et al., 2015; Rohde et al., 2013), Discovery seamounts (Schwindrofska et al., 2016), Hawaii (Loa and Kea lavas) and Samoa (Vai and Malu lavas) (Huang et al., 2011) hotspot chains. The origin of these heterogeneities is still debated. Besides directly reflecting spatial heterogeneity in the lower mantle (Hoernle et al., 2015; Homrighausen et al., 2019), an origin by shallow additions such as by assimilation of subcontinental lithosphere mantle

(SCLM) or continental crust is also widely suggested (Class and le Roex, 2011; Regelous et al., 2009).

In addition, the classical plume model (predicting the association of mantle plumes, LIPs and age-progressive hotspot tracks) is further challenged by observations such as: (1) seamount chains that are not long-lived, such as Ascension and Cape Verde (Courtillot et al., 2003), (2) LIPs without related plume tail stage, such as Siberian Trap (Ivanov, 2007), and (3) intraplate magmatic chains without age-progression, such as the Cameroon line (Guimarães et al., 2020). Besides utilizing the mantle plume model, LIP formation was therefore also explained by the shallow plate tectonic-related processes (e.g. plate deformation, thickness variations of lithosphere, fracture zones, back-arc settings; Ernst, 2014).

1.2. The characteristics and origin of carbonatite

Although occurring at relatively low volumes, carbonatite is a special rock-type in LIPs due to its distinctive trace element composition, unusual accessory mineral content, economic potential, and significance for the understanding of the mantle carbon cycle. Most carbonatites can be related to apparently deep-seated mantle plumes (Kogarko and Veselovskiy, 2019).Accordingly, they are believed to be formed by the low degree of melting of deep recycled carbonated oceanic crust (peridotite or eclogite; Dasgupta et al., 2007; Hammouda and Keshav, 2015; Hoernle et al., 2002) at 3-10 GPa (Dasgupta and Hirschmann, 2006; Dasgupta et al., 2004). The low degree of melting results in a strong enrichment of incompatible elements. Subsequently, the carbonatite melts will ascent through the upper mantle as buoyant diapirs (Litasov et al., 2013). Due to the fast and vertical upwelling and high enrichment of incompatible elements, carbonatites can provide reliable evidence of the plume's composition and distribution (Ernst, 2014). Alternatively, carbonatites could also form by low degree melting of metasomatized SCLM, as proposed for the “deformed alkaline rock and carbonatite (DARC)” in the orogenic belts (Burke et al., 2003; Cimen et al., 2019; Hou et al., 2015) or by plume metasomatized SCLM (Le Roex and Lanyon, 1998; Natali et al., 2018). The plume generation and metasomatized SCLM theory, however, can also be combined with the other models. The DARC might be derived from previously formed carbonatite/ alkaline rocks subducted to great depth and returned by young mantle plumes(Burke et

al., 2003). Accordingly, the plume-derived carbonatite melt diapirs can also metasomatize the ambient mantle (Hauri et al., 1993; Rudnick et al., 1993).

1.3. Studied area

For several decades, scientists have proposed that the Paraná-Etendeka flood basalts were formed by the plume head stage of the Tristan-Gough plume (Erlank et al., 1984; O'Connor and Duncan, 1990) during the break up of the Gondwana. Paraná locates on the South American and Etendeka on the African plate. All Etendeka basalts were divided by their trace elements (e.g Ti, Zr, Sr) into high-Ti and low-Ti groups. The high-Ti basalts locate on the continental extension of Walvis Ridge – Tristan-Gough hotspot tracks, but the isotope composition relationship between them is still unclear.

After the plume head stage, the Tristan-Gough plume interacted with the Mid-Atlantic Ridge, formed the Walvis Ridge. About 70 Ma, the plume left the Mid Ocean Ridge and split into 2-3 seamount chains with distinct geochemical compositions from each other (Hoernle et al., 2015; Sager et al., 2020). The Gough track and Walvis Ridge have a similar composition (Gough composition), which show higher $^{207}Pb/^{204}Pb$ at a given $^{206}Pb/^{204}Pb$ ratio and extend to lower $^{143}Nd/^{144}Nd$ and higher $^{87}Sr/^{86}Sr$ ratios than Tristan composition (Hoernle et al., 2015; Homrighausen et al., 2019; Rohde et al., 2013). Besides the spatial zonation, an independent hotspot track has been reported showing 30 Ma younger ages and unique HIMU-like composition (Homrighausen et al., 2018). The isotopic composition of these late-stage HIMU-like seamounts forms an array between St.Helena HIMU and an EM1 endmember and the EM1 endmember assumed to be a mixture of Gough composition and the mid-ocean ridge basalt (MORB). All of these heterogeneities in the plume tail stage are traced to the heterogenesis of the large low shear velocity province (LLSVP) (Homrighausen et al., 2019).

The HIMU-like composition was also discovered in many carbonatites intrusive complexes in Etendeka area. Based on their location and geochemical composition, carbonatites can be distinguished into two groups: (1) Post-Etendeka (< 120 Ma) carbonatites with more HIMU signatures. (2) pre- (> 140 Ma) and syn-Etendeka (120 to 140 Ma) carbonatites with more EM1 signatures. The Etendeka flood basalt is discussed in Chapter 2, the pre- and syn-Etendeka carbonatites in Chapter 3 and the post-Etendeka carbonatites in Chapter 4.

1.3.1. Etendeka flood basalts

The remnant of Etendeka flood basalts is about 0.8×10^5 km^2 in northwestern Namibia (Erlank et al., 1984). All rocks from Etendeka show a Bunsen-Daly gap of SiO_2 concentration (56 – 63 wt%), dividing samples into mafic and silicic suites. Silicic rocks are highly contaminated and are only used to constrain the composition of the crust beneath the Etendeka region to assess the extent of crustal contamination.

Etendeka mafic rocks were distinguished based on their geochemistry. The high-Ti magma type dominates the northern Etendeka and low-Ti magma type mainly locates in southern Etendeka (Erlank et al., 1984). The high-Ti basalt in Etendeka side is also named *Khumib* formation. It has been noticed that the high-Ti basalts are less contaminated than low-Ti basalts, resulting in highly restricted trace element composition. Thus, it has not been further divided into subgroups and its unique geochemical composition provides an excellent opportunity to study the magma source of high-Ti basalts. High-Ti magma is more enriched in incompatible elements than low-Ti magma, but the geochemical research on high-Ti magma is still poor and the relationship between high-Ti magma and Tristan-Gough plume is still problematic.

The low-Ti composition varies a lot and is divided into five units based on their trace element compositions, occurrences and locations. The *Tafelberg* type lava is the most widely distributed unit in Etendeka. It dominates the main remnant of low-Ti lava and is up to 800m thick (Duncan, 1987). Their most noticeable feature is the high $^{87}Sr/^{86}Sr$ and positive Pb anomaly. The *Horingbaai* dikes are unique in all Etendeka volcanism due to their relatively depleted incompatible elements. The *dolerite dikes* are comprised of *Albin, Huab* Sill and *Esmeralda* compositions (Marsh et al., 2001), Their compositions are in between an E-MORB and upper crust composition. Thus, low-Ti compositions was ascribed to shallow components, such as crustal contamination, SCLM and depleted upper mantle (Ewart et al., 2004; Thompson et al., 2001; Thompson et al., 2007). Furthermore, in many studies, the Tristan-Gough plume only plays a passive role in generating the Etendeka flood basalt (Duncan et al., 1989; Erlank et al., 1984; Peate and Hawkesworth, 1996). Although the involvement of Tristan-Gough plume can not be completely ignored in most low-Ti magma Ewart et al., 2004; Gibson et al., 2006), only *Doros* basalts (and associated *Tafelkop* basalts) show a recognizable plume signature, but their composition is still distinct from Gough and Tristan tracks (Owen-Smith et al., 2017).

The main pulse of lava emerged between 129 – 134 Ma and the whole volcanism lasted from 138 to 120 Ma (Peate, 1997). the absolute ages of high-Ti and low-Ti Etendeka samples largely overlap, as do their relative ages. The low-Ti Doros center intruded at 130±1 Ma (all errors reported as 2σ; Owen-Smith et al., 2017) and low-Ti Tafelkop-type lavas (that can be traced back to Doros igneous center) show a slightly older age at 132.9±0.6 (Jerram et al., 1999). The geochemically similar low-Ti Horingbaai dikes have ages of 125-132 Ma overlapping with the (1) Doros/Tafelkop rocks (130-133 Ma), (2) the Messum center rocks (129-132 Ma; Renne et al., 1996), and (3) the volumetrically greatest and most widely distributed low-Ti Tafelberg lavas (132.3±0.7 Ma; Renne et al., 1996). High-Ti Khumib lavas and low-Ti Tafelkop lavas are interbedded with low-Ti Tafelberg lavas (Ewart et al., 2004; Marsh et al., 2001). Low-Ti Tafelberg-type dikes usually intrude into high-Ti Khumib type, but Khumib-type dikes intruding into Tafelberg lavas have also been observed (Miller, 2008). Thus the high-Ti and low-Ti lavas/dikes have similar absolute age ranges and overlapping relative ages. There is no temporal change in composition from high-Ti to low-Ti or vice versa. To the contrary, these lava units represent regional features and indicate a spatial variation.

1.3.2. Pre-Etendeka alkaline and carbonatite intrusive volcanism

There are lots of alkalic intrusive volcanisms in the Etendeka area and southern Namibia during the late Cretaceous and Paleogene. Except for the highly involved phonolitic intrusive plugs, three carbonatite and basanite intrusive complexes (Agate Mountain, Dicker Willem and Swakopmund basanites) are sampled in this study.

The Agate Mountain is a satellite intrusion to a large offshore Phoenix Volcano, locating on the onshore extension of the Walvis Ridge. The whole Phoenix Volcano is assumed to be 100km in diameter. The Agate Mountain emplaced on the normal fault around phoenix Volcano, intruding into Skeleton Coast quartz latites in the west and Khumib basalts in the east of the normal fault. It is about 2.4km in diameter, which has been carefully illustrated by Miller (2000). The core of intruded sövite is about 1.1km in diameter and the outer part is fenitised quartz latite. About 31 carbonatite plugs have been recorded scattered in the outer part. Most plugs contain carbonatite fragments, indicating a younger age than the main carbonate core (Miller, 2008). Two phonolite plugs associated with the Agate Mountain yield ages of 82-83 Ma, which agree with

the late-stage HIMU-like hotspot track (Homrighausen et al., 2020), but whether the Agate Mountain also have HIMU composition is still unknown.

Dicker Willem is an inselberg with 2.8km diameter and 600m height in the Namib Desert plain. Five rock types are recognized, such as sövite, alvikite, beforsite, ferro-alvikite and tuffisite (Cooper, 1988). The main body of Dicker Willem is composed of sövite and alvikite, intruded into the gneiss country rock. The previous geochemical study show that the Dicker Willem carbonatites plot widespread between the HIMU endmember and local upper crust Namaqua gneiss composition (Cooper and Reid, 2000).

The alkaline plugs near Swakopmund have very low magma volume but unique composition from surrounding Etendeka dikes. There are four plugs between 50 and 100m in diameter. Ar-Ar whole-rock ages of two basanite samples were reported as 76.08 ± 0.86 and 74.86 ± 0.92 Ma (Whitehead et al., 2002). Abundant of mantle xenoliths are studied for the Damara belt SCLM and show a very depleted isotope composition similar to the Mid-Atlantic Ridge, distinct from the cratonic sub-continental lithospheric mantle and Tristan-Gough plume (Class and le Roex, 2006; le Roex and Class, 2014). The trace elements of basanites are more enriched than Etendeka dikes, similar to the late-stage HIMU-like hotspot tracks. The isotope compositions of the alkaline rocks, however, are still unknown.

1.3.3. Pre- and syn-Etendeka carbonatite intrusive complexes

The collision between Congo and Kalahari generated the Damara orogenic belt from about 580 Ma to 460 Ma (Miller, 2008). The pre- and syn-Etendeka carbonatites mainly formed a linear series in the Damara orogenic belt (also named Damara carbonatites), including Kalkfeld (242-153 Ma; Kramm et al., 2017; Ziegler, 1992), Okorusu (126 Ma; Milner et al., 1995), Okenyenya (129-123 Ma; Milner et al., 1993), Osongombo, Ondurakorume, Paresis (137 Ma; Milner et al., 1995) and Etaneno (134 Ma; Müller, 1996). According to the literature data, Damara carbonatites have intermediate Sr, Nd, Pb isotopes between HIMU and EM1, but are not merely the mixture of St.Helena HIMU and Gough-type EM1 (Le Roex and Lanyon, 1998).

We have sampled the Kalkfeld, a pre-Etendeka complex, and Okorusu, a syn-Etendeka complex. The Kalkfeld is a ring complex about 7km in diameter. Carbonatites dominate the center hill with high iron ore contents, which are assumed to undergo a

hydrothermal fluid alteration. The Okorusu is also a ring structure about 7km in diameter, but the center hill has lower volume and most carbonatites appeared at the outer part. Hydrothermal mineralization fluorites occurred in the outer ring and interacted with the carbonatites. Usually, the carbonatites are rarely exposed in Okorusu, but the commercial exploration of fluorite mine perfectly exposed our sampled site.

1.4. Main objectives

Based on the previous research, this thesis focuses on the geochemistry of Etendeka flood basalts and associated carbonatites to evaluate their origin and evolution. The main objectives are as follows:

(1) Are the Etendeka flood basalts formed by the plume head stage of the Tristan-Gough plume?
(2) What caused the distinct composition of high-Ti and low-Ti lavas: shallow lithospheric contamination or a heterogeneous plume source? What is their distribution in SW Africa?
(3) Is there any late-stage HIMU-like volcanism in the Etendeka area? Do the late-stage silica-undersaturated rocks and carbonatites fit into the late-stage hotspot track model?
(4) What are the geochemical fingerprints of Damara alkaline and carbonatitic intrusive complexes?
(5) Does the geochemical composition of the carbonatites in Namibia provide further insights into their origin?

To answer these scientific questions, I measured major and trace element and Sr-Nd-Pb-Hf isotope data of 149 samples from outcrops at: (1) Northern Etendeka flood basalts, (2) Southern Etendeka flood basalts, (3) Henties Bay – Outjo dikes swarm, (3) Horingbaai dike swarm, (4) intrusive complexes such as Agate Mountain, Dicker Willem, Swakopmund, Messum, Kalkfeld and Okorusu. The sample set comprises different rock types, occurrences, compositions, ages and tectonic settings, and thus provide unique perceptions of pre-, syn- and post- Etendeka event volcanism in Namibia.

References

Burke, K., Ashwal, L.D., Webb, S.J., 2003. New way to map old sutures using deformed alkaline rocks and carbonatites. Geology 31, 391-394.

Burke, K., Steinberger, B., Torsvik, T.H., Smethurst, M.A., 2008. Plume Generation Zones at the margins of Large Low Shear Velocity Provinces on the core–mantle boundary. Earth and Planetary Science Letters 265, 49-60.

Campbell, I.H., 2007. Testing the plume theory. Chemical Geology 241, 153-176.

Cimen, O., Kuebler, C., Simonetti, S.S., Corcoran, L., Mitchell, R., Simonetti, A., 2019. Combined boron, radiogenic (Nd, Pb, Sr), stable (C, O) isotopic and geochemical investigations of carbonatites from the Blue River Region, British Columbia (Canada): Implications for mantle sources and recycling of crustal carbon. Chemical Geology 529, 119240.

Class, C., le Roex, A., 2011. South Atlantic DUPAL anomaly — Dynamic and compositional evidence against a recent shallow origin. Earth and Planetary Science Letters 305, 92-102.

Class, C., le Roex, A.P., 2006. Continental material in the shallow oceanic mantle—How does it get there? Geology 34, 129.

Cooper, A., 1988. Geology of Dicker Willem, a subvolcanic carbonatite complex in south-west Africa. Comm. GeoI. Surv. SW Afr./Namibia 4, 3-12.

Cooper, A., Reid, D., 2000. The association of potassic trachytes and carbonatites at the Dicker Willem Complex, southwest Namibia: coexisting, immiscible, but not cogenetic magmas. Contributions to Mineralogy and Petrology 139, 570-583.

Courtillot, V., Davaille, A., Besse, J., Stock, J., 2003. Three distinct types of hotspots in the Earth's mantle. Earth and Planetary Science Letters 205, 295-308.

Dasgupta, R., Hirschmann, M.M., 2006. Melting in the Earth's deep upper mantle caused by carbon dioxide. Nature 440, 659-662.

Dasgupta, R., Hirschmann, M.M., Smith, N.D., 2007. Partial Melting Experiments of Peridotite + CO2 at 3 GPa and Genesis of Alkalic Ocean Island Basalts. Journal of Petrology 48, 2093-2124.

Dasgupta, R., Hirschmann, M.M., Withers, A.C., 2004. Deep global cycling of carbon constrained by the solidus of anhydrous, carbonated eclogite under upper mantle conditions. Earth and Planetary Science Letters 227, 73-85.

Duncan, A., Newton, S., Van den Berg, C., Reid, D., 1989. Geochemistry and petrology of dolerite sills in the Huab River valley, Damaraland, north western Namibia. Communications of the Geological Survey of Namibia 5, 5-17.

Duncan, A.R., 1987. The Karoo igneous province—a problem area for inferring tectonic setting from basalt geochemistry. Journal of Volcanology and Geothermal Research 32, 13-34.

Erlank, A., Marsh, J., Duncan, A., Miller, R.M., Hawkesworth, C., Betton, P., Rex, D., 1984. Geochemistry and petrogenesis of the Etendeka volcanic rocks from SWA/Namibia. Special Publication of Geological Society of South Africa 13, 195-245.

Ernst, R.E., 2014. Large igneous provinces. Cambridge University Press.

Ewart, A., Marsh, J.S., Milner, S.C., Duncan, A.R., Kamber, B.S., Armstrong, R.A., 2004. Petrology and geochemistry of early cretaceous bimodal continental flood volcanism of the NW Etendeka, Namibia. Part 1: Introduction, mafic lavas and re-evaluation of mantle source components. Journal of Petrology 45, 59-105.

Gibson, S.A., Thompson, R.N., Day, J.A., 2006. Timescales and mechanisms of plume–lithosphere interactions: 40Ar/39Ar geochronology and geochemistry of alkaline igneous rocks from the Paraná–Etendeka large igneous province. Earth and Planetary Science Letters 251, 1-17.

Guimarães, A.R., Fitton, J.G., Kirstein, L.A., Barfod, D.N., 2020. Contemporaneous intraplate magmatism on conjugate South Atlantic margins: A hotspot conundrum. Earth and Planetary Science Letters 536, 116147.

Hammouda, T., Keshav, S., 2015. Melting in the mantle in the presence of carbon: Review of experiments and discussion on the origin of carbonatites. Chemical Geology 418, 171-188.

Hauri, E.H., Shimizu, N., Dieu, J.J., Hart, S.R., 1993. Evidence for hotspot-related carbonatite metasomatism in the oceanic upper mantle. Nature 365, 221-227.

Hoernle, K., Rohde, J., Hauff, F., Garbe-Schonberg, D., Homrighausen, S., Werner, R., Morgan, J.P., 2015. How and when plume zonation appeared during the 132 Myr evolution of the Tristan Hotspot. Nature Communications 6, 7799.

Hoernle, K., Tilton, G., Le Bas, M.J., Duggen, S., Garbe-Schönberg, D., 2002. Geochemistry of oceanic carbonatites compared with continental carbonatites: mantle recycling of oceanic crustal carbonate. Contributions to Mineralogy and Petrology 142, 520-542.

Homrighausen, S., Hoernle, K., Geldmacher, J., Wartho, J.-A., Hauff, F., Portnyagin, M., Werner, R., van den Bogaard, P., Garbe-Schönberg, D., 2018. Unexpected HIMU-type late-stage volcanism on the Walvis Ridge. Earth and Planetary Science Letters 492, 251-263.

Homrighausen, S., Hoernle, K., Hauff, F., Wartho, J.-A., van den Bogaard, P., Garbe-Schönberg, D., 2019. New age and geochemical data from the Walvis Ridge: The temporal and spatial diversity of South Atlantic intraplate volcanism and its possible origin. Geochimica et Cosmochimica Acta 245, 16-34.

Homrighausen, S., Hoernle, K., Zhou, H., Geldmacher, J., Wartho, J.-A., Hauff, F., Werner, R., Jung, S., Morgan, J.P., 2020. Paired EMI-HIMU hotspots in the South Atlantic—Starting plume heads trigger compositionally distinct secondary plumes? Science Advances 6, eaba0282.

Hou, Z., Liu, Y., Tian, S., Yang, Z., Xie, Y., 2015. Formation of carbonatite-related giant rare-earth-element deposits by the recycling of marine sediments. Scientific reports 5, 10231.

Huang, S., Hall, P.S., Jackson, M.G., 2011. Geochemical zoning of volcanic chains associated with Pacific hotspots. Nature Geoscience 4, 874-878.

Ivanov, A.V., 2007. Evaluation of different models for the origin of the Siberian Traps. SPECIAL PAPERS-GEOLOGICAL SOCIETY OF AMERICA 430, 669.

Jerram, D., Mountney, N., Holzförster, F., Stollhofen, H., 1999. Internal stratigraphic relationships in the Etendeka Group in the Huab Basin, NW Namibia: understanding the onset of flood volcanism. Journal of Geodynamics 28, 393-418.

Kogarko, L.N., Veselovskiy, R.V., 2019. Geodynamic origin of carbonatites from the absolute paleotectonic reconstructions. Journal of Geodynamics 125, 13-21.

Kramm, U., Körner, T., Kittel, M., Baier, H., Sindern, S., 2017. Triassic emplacement age of the Kalkfeld complex, NW Namibia: implications for carbonatite magmatism and its relationship to the Tristan Plume. International Journal of Earth Sciences 106, 2797-2813.

le Roex, A., Class, C., 2014. Metasomatism of the Pan-African lithospheric mantle beneath the Damara Belt, Namibia, by the Tristan mantle plume: geochemical evidence from mantle xenoliths. Contributions to Mineralogy and Petrology 168.

Le Roex, A.P., Lanyon, R., 1998. Isotope and Trace Element Geochemistry of Cretaceous Damaraland Lamprophyres and Carbonatites, Northwestern Namibia: Evidence for Plume—Lithosphere Interactions. Journal of Petrology 39, 1117-1146.

Litasov, K.D., Shatskiy, A., Ohtani, E., 2013. Earth's Mantle Melting in the Presence of C–O–H–Bearing Fluid. Physics and Chemistry of the Deep Earth, 38-65.

Marsh, J., Ewart, A., Milner, S., Duncan, A., Miller, R.M., 2001. The Etendeka Igneous Province: magma types and their stratigraphic distribution with implications for the evolution of the Paraná-Etendeka flood basalt province. Bulletin of Volcanology 62, 464-486.

Miller, R.M., 2000. The Agate Mountain Carbonatite Complex, Cape Fria, NW Namibia. communs geol. Surv. Namibia 12, 369-382.

Miller, R.M., 2008. The geology of Namibia. Ministry of Mines and Energy, Geological Survey.

Milner, S., Le Roex, A., O'CONNOR, J., 1995. Age of Mesozoic igneous rocks in northwestern Namibia, and their relationship to continental breakup. Journal of the Geological Society 152, 97-104.

Milner, S.C., Le Roex, A.P., Watkins, R.T., 1993. Rb-Sr age determinations of rocks from the Okenyenya igneous complex, northwestern Namibia. Geological Magazine 130, 335-343.

Müller, B., 1996. Ring complexes of the Damaraland Alkaline Province, Namibia in the light of geochemistry and Rb-Sr, U-Pb, Pb-Pb isotopes. ETH Zurich.

Natali, C., Beccaluva, L., Bianchini, G., Siena, F., 2018. Coexistence of alkaline-carbonatite complexes and high-MgO CFB in the Paranà-Etendeka province: Insights on plume-lithosphere interactions in the Gondwana realm. Lithos 296-299, 54-66.

O'Connor, J.M., Duncan, R.A., 1990. Evolution of the Walvis Ridge Rio-Grande Rise Hot-Spot System - Implications for African and South-American Plate Motions over Plumes. Journal of Geophysical Research-Solid Earth and Planets 95, 17475-17502.

Owen-Smith, T., Ashwal, L., Sudo, M., Trumbull, R., 2017. Age and petrogenesis of the Doros Complex, Namibia, and implications for early plume-derived melts in the Paraná–Etendeka LIP. Journal of Petrology 58, 423-442.

Peate, D.W., 1997. The Paraná-Etendeka Province. Large igneous provinces: Continental, oceanic, and planetary flood volcanism, 217-245.

Peate, D.W., Hawkesworth, C.J., 1996. Lithospheric to asthenospheric transition in low-Ti flood basalts from southern Parana, Brazil. Chemical Geology 127, 1-24.

Regelous, M., Niu, Y., Abouchami, W., Castillo, P.R., 2009. Shallow origin for South Atlantic Dupal Anomaly from lower continental crust: Geochemical evidence from the Mid-Atlantic Ridge at 26°S. Lithos 112, 57-72.

Renne, P.R., Glen, J.M., Milner, S.C., Duncan, A.R., 1996. Age of Etendeka flood volcanism and associated intrusions in southwestern Africa. Geology 24, 659-662.

Rohde, J., Hoernle, K., Hauff, F., Werner, R., O'Connor, J., Class, C., Garbe-Schonberg, D., Jokat, W., 2013. 70 Ma chemical zonation of the Tristan-Gough hotspot track. Geology 41, 335-338.

Rudnick, R.L., McDonough, W.F., Chappell, B.W., 1993. Carbonatite metasomatism in the northern Tanzanian mantle: petrographic and geochemical characteristics. Earth and Planetary Science Letters 114, 463-475.

Sager, W., Hoernle, K., Petronotis, K., 2020. Expedition 391 Scientific Prospectus: Walvis Ridge Hotspot. . International Ocean Discovery Program.

Schwindrofska, A., Hoernle, K., Hauff, F., van den Bogaard, P., Werner, R., Garbe-Schönberg, D., 2016. Origin of enriched components in the South Atlantic: Evidence from 40 Ma geochemical zonation of the Discovery Seamounts. Earth and Planetary Science Letters 441, 167-177.

Thompson, R., Gibson, S., Dickin, A., Smith, P., 2001. Early Cretaceous basalt and picrite dykes of the southern Etendeka region, NW Namibia: windows into the role of the Tristan mantle plume in Paraná–Etendeka magmatism. Journal of Petrology 42, 2049-2081.

Thompson, R., Riches, A., Antoshechkina, P., Pearson, D., Nowell, G., Ottley, C., Dickin, A., Hards, V., Nguno, A.-K., Niku-Paavola, V., 2007. Origin of CFB magmatism: multi-tiered intracrustal picrite–rhyolite magmatic plumbing at Spitzkoppe, western Namibia, during early Cretaceous Etendeka magmatism. Journal of Petrology 48, 1119-1154.

Torsvik, T.H., Smethurst, M.A., Burke, K., Steinberger, B., 2006. Large igneous provinces generated from the margins of the large low-velocity provinces in the deep mantle. Geophysical Journal International 167, 1447-1460.

Torsvik, T.H., van der Voo, R., Doubrovine, P.V., Burke, K., Steinberger, B., Ashwal, L.D., Tronnes, R.G., Webb, S.J., Bull, A.L., 2014. Deep mantle structure as a reference frame for movements in and on the Earth. Proc Natl Acad Sci U S A 111, 8735-8740.

Whitehead, K., Le Roex, A., Class, C., Bell, D., 2002. Composition and Cretaceous thermal structure of the upper mantle beneath the Damara Mobile Belt: evidence from nephelinite-hosted peridotite xenoliths, Swakopmund, Namibia. Journal of the Geological Society 159, 307-321.

Wilson, J.T., 1963. Evidence from islands on the spreading of ocean floors. Nature 197, 536-538.

Ziegler, U.R.F., 1992. Preliminary results of geochemistry, Sm-Nd and Rb-Sr studies of post-Karoo carbonatite complexes in Southern Africa. Schweizerische Mineralogische und Petrographische Mitteilungen 72, 135-142.

Chapter 2.

Geochemistry of Etendeka magmatism: Spatial heterogeneity in the Tristan-Gough plume head

This Chapter was published in Earth and Planetary Science Letters in 2020 (DOI: 10.1016/j.epsl.2020.116123)

Authors: **H.Zhou**[a], K.Hoernle[a,b], J.Geldmacher[a], F.Hauff[a], S.Homrighausen[a], D.Garbe-Schönberg[b], S. Jung[c]

[a]GEOMAR Helmholtz Centre for Ocean Research Kiel, Wischhofstr. 1-3, 24148 Kiel, Germany

[b]Institute of Geosciences, Kiel University, Ludewig-Meyn-Str. 10, 24118 Kiel, Germany

[c]Institute of Mineralogy and Petrography, Universität Hamburg, Grindelallee 48, 20146 Hamburg, Germany

2.1. Abstract

The origin and distribution of geochemically distinct source components in continental flood volcanism (generally associated with the initial phase of a mantle plume head) are poorly understood. Here we present new geochemical (major and trace element and Sr-Nd-Pb-Hf isotope) data from the Etendeka flood basalts and associated dikes from northern and central Namibia that are believed to have been produced during the initial stage of the Tristan-Gough hotspot. Following earlier studies, the Etendeka lava flows and dikes are divided into high-Ti and low-Ti groups. The trace element and isotopic composition of the high-Ti tholeiitic basalts, exclusively outcropping in northern Etendeka (northwestern Namibia), are similar to the Gough-type enriched mantle I (EMI) composition found on the Walvis Ridge (the Atlantic type locality for the EMI end member). The low-Ti tholeiitic basalts, primarily outcropping in Southern Etendeka (central western Namibia), have higher $^{143}Nd/^{144}Nd$ and $^{207}Pb/^{204}Pb$ but lower $^{208}Pb/^{204}Pb$ ratios than the Gough composition. Combining our data with newly published $^{3}He/^{4}He$ data and estimates of the magma source's potential temperature from 1520-1680°C, we conclude that the source of the low-Ti basalts was also intrinsic to the Tristan-Gough plume, consistent with a spatially-zoned plume head. The low-Ti basalts were derived from a distinct EMI-type source component that has thus far only been detected in the initial Tristan-Gough plume head (~132 Ma), but not the later submarine hotspot track.

Keywords: Sr-Nd-Pb-Hf isotope ratios; Etendeka flood basalts; Large Igneous Province (LIP); Namibia; plume zonation; Gough

2.2. Introduction

The South Atlantic is considered a classic example of continental breakup associated with large-scale magmatism, resulting in conjugate large igneous provinces. The magmatism comprises the voluminous Paraná - Etendeka flood basalts in Brazil and Namibia, and the submarine Rio Grande Rise and Walvis Ridge oceanic plateaus in the South Atlantic (e.g. Renne et al., 1996; Rohde et al., 2013b; Hoernle et al., 2015; O'Connor and Jokat, 2015; Homrighausen et al., 2019). A chain of volcanic ridges and seamounts ("Guyot Province") further links the Walvis Ridge with the Gough and the (volcanically active) Tristan da Cunha Island groups (Figure 2-1). Accordingly, the

entire magmatism is commonly attributed to the Tristan-Gough hotspot, whose initial "plume head" stage is believed to have created the Paraná-Etendeka flood basalts contemporaneous with continental breakup between Africa and South America. The Rio Grande Rise and Walvis Ridge were subsequently formed largely through plume-ridge interaction while the plume was located close to the young Mid-Atlantic Ridge. After several ridge jumps split the Rio Grande from the Walvis Ridge, continuing volcanism above the presumed plume tail formed the Guyot Province on the African Plate. This classic example of the plume head / plume tail hotspot model is supported by a systematic age progression along the hotspot track (Homrighausen et al., 2019; O'Connor and Jokat, 2015; Rohde et al., 2013b) initiated with Paraná and Etendeka volcanism at 135-129 Ma (Renne et al., 1996).

Although the Tristan-Gough hotspot system represents one of the few examples that exhibits a clear spatial and temporal link between a presumed mantle plume head and tail, the evolution from initial LIP to hotspot track volcanism is poorly constrained and even the involvement of a mantle plume in the initial Etendeka flood basalt magmas is disputed. A number of studies have suggested a largely passive role for the plume i.e. merely facilitating melting of subcontinental lithospheric mantle (SCLM) by conductive heating (Erlank et al., 1984). In contrast, Ewart et al. (2004a) explained the geochemical composition of the Etendeka melts as a mixture of the modern Tristan da Cunha ocean island source, subducted material, and asthenosphere with a crustal contaminant. Hoernle et al. (2015) argued that the large range in chemical composition of both flood basalt provinces could largely be explained by plume melts with a Gough-type composition assimilating continental lithosphere (upper and lower crust and lithospheric mantle). Isotopically enriched lavas with elevated delta 7/4Pb but low delta 8/4Pb ratios have been recognized in southern Etendeka (Ewart et al., 1998; Gibson et al., 2000; Owen-Smith et al., 2017; Thompson et al., 2001), but their origin and relationship to the main phase of the plateau has remained unclear thus far.

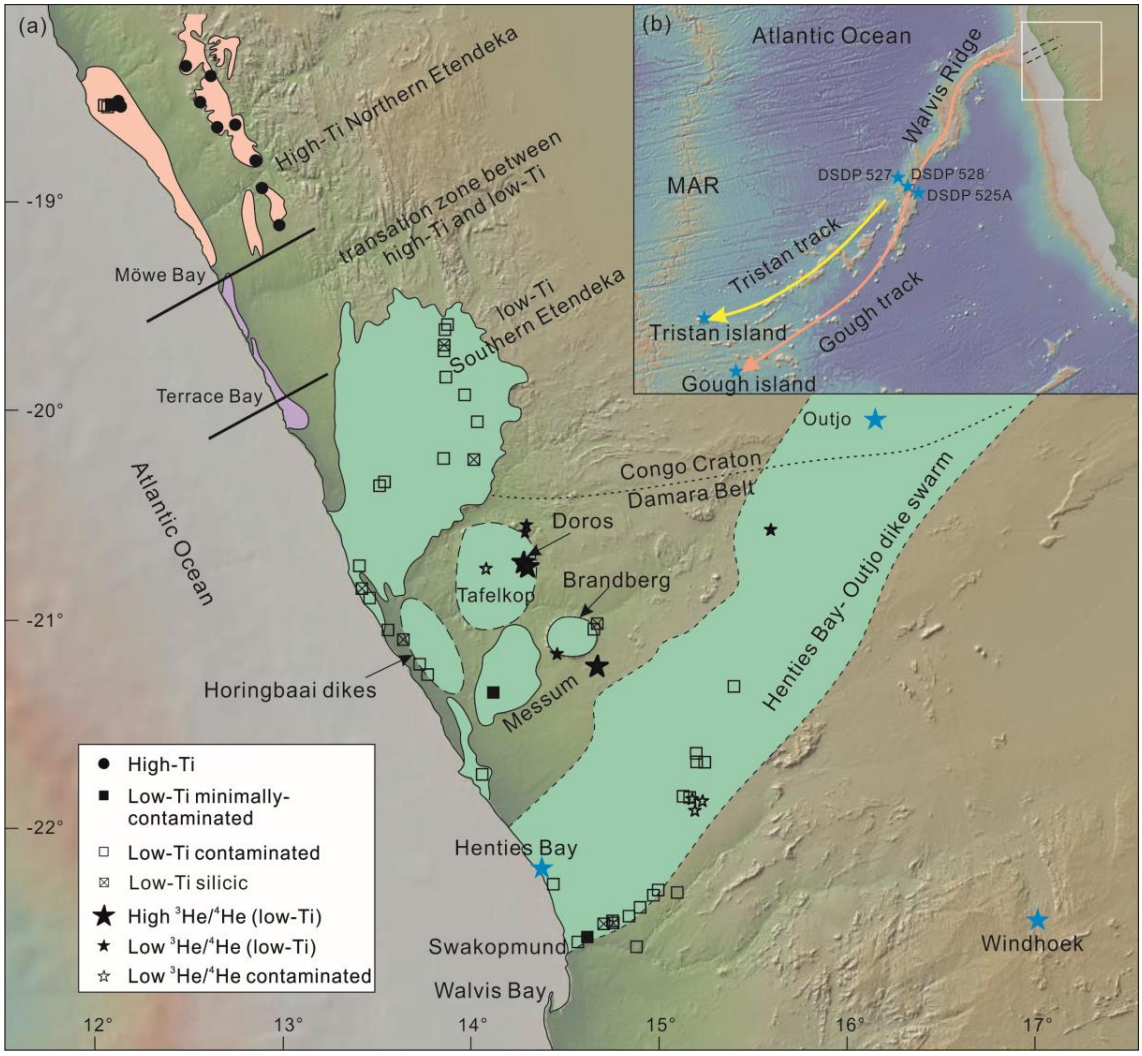

Figure 2-1: (a) Map of the Etendeka large igneous province outcrops in northwest Namibia, including sampling sites for this study. Transition zone lavas (purple) separate high-Ti lavas (pink) in northern Etendeka from low-Ti volcanism (green) in southern Etendeka after Marsh et al. (2001). The ranges of dikes are denoted with dashed lines. The range of Henties Bay – Outjo dike swarm and the boundary between Congo Craton and Damara Belt are based on Raab et al. (2002). Sample sites of high and low $^{3}He/^{4}He$ rocks taken from Stroncik et al. (2017). (b) Inset shows location of sampling area along the SW African (Namibian) coast and relationship to the submarine Walvis Ridge and Tristan and Gough hotspot sub-tracks in the South Atlantic. Maps generated by GeoMapApp (http:/www.geomapapp.org).

This study presents new major and trace element and Sr-Nd-Hf-Pb (double spike) isotope data from mafic Etendeka flood basalts and feeder dikes sampled at a variety of locations in northwestern Namibia to evaluate their compositional relationship to the marine parts of the Tristan-Gough hotspot track. Although Thompson et al., (2007) have published Hf isotope data for dikes near Spitzkoppe, this study is the first to present Hf isotope data for Etendeka lavas, as well as for dikes. We show that the contemporaneously-erupted low- and high-Ti basalts are derived from two spatially

distinct plume components derived from the lower mantle, suggesting that the initial (plume head) stage of the Tristan-Gough plume is likely to have been spatially zoned in geochemical composition.

2.3. Geological background and previous research

Although the heavily eroded Etendeka volcanic succession in NW Namibia only comprises ~6 % of the present-day combined Paraná-Etendeka large igneous province (Miller, 2008), the remaining lavas and intrusions are well-exposed and have been the subject of detailed studies (Erlank et al., 1984; Ewart et al., 1998; Ewart et al., 2004a; Gibson et al., 2000; Marsh et al., 2001; Milner et al., 1995; Owen-Smith et al., 2017; Stroncik et al., 2017; Thompson et al., 2001). Further south, where uplift and erosion has been more extensive, a dense network of feeder dikes is exposed (Figure 2-1), including the Henties Bay – Outjo dike swarm (Keiding et al., 2013), and the Horingbaai coastal dikes (Thompson et al., 2001). According to these studies, the Etendeka igneous rocks can be divided into high- and low-TiO_2 groups (Erlank et al., 1984). North of a transition zone between Möwe and Terrance Bay (Figure 2-1), where both types are present, the lavas are predominantly mafic and have high TiO_2 contents (> 2.2 wt.% TiO_2). South of the Möwe and Terrace Bay transition zone, all lavas, ranging from mafic to highly evolved compositions, have low-TiO_2 contents (< 2.2 wt.% TiO_2; Bellieni et al., 1984; Ewart et al., 2004b; Marsh et al., 2001). This division was further constrained using additional commonly-analyzed incompatible elements, such as Zr, Y and Sr (Marsh et al., 2001). Several previous studies have recognized variable extents of crustal contamination in the Etendeka magma suites, in particular in the low-Ti successions (Erlank et al., 1984; Ewart et al., 1998).

Based on their geochemistry, the mafic rocks of the Etendeka province were grouped by Marsh et al. (2001) into five extrusive basaltic and at least three intrusive units (e.g. doleritic dikes, sills and plugs). Equivalent units are regognized in the Paraná (Marsh et al., 2001). Only one high-Ti magma type (*Khumib)* has been defined in the Etendeka, which is exclusively confined to and dominates northern Etendeka (north of the transition zone). The low-Ti units of southern Etendeka can be largely distinguished by their different Zr/Y ratios. The low-Ti *Tafelberg* type, ranging from tholeiitic basalts to andesites, is the most common and voluminous and occurs throughout the southern Etendeka province. The low-Ti *Tafelkop basalt* type, characterized by low Ti and Zr

and high Ti/Zr, is believed to contain the highest proportion of plume-derived material in its magma source (Ewart et al., 2004a; Ewart et al., 1998). The Tafelkop basalts occur near the base of the volcanic succesion in central southern Etendeka and there is compelling geochemical evidence that they are related to the nearby Doros intrusive complex (Marsh et al., 2001; Owen-Smith et al., 2017). Magmas with Tafelberg, Khumib and other compositions also form dikes and intrusions. For some intrusive units, however, an assignment to erupted equivalents is unclear. This includes the *Horingbaai dolerites*, with only slightly enriched incompatible-element compositions similar to enriched mid-ocean-ridge basalt (E-MORB), which are therefore widely believed to reflect an asthenospheric contribution to the Etendeka magmatism (Erlank et al., 1984; Ewart et al., 2004a). Modeling of the parental liquid composition for some picritic Horingbaai dikes, however, yielded a komatiitic composition produced by a mantle with a potential temperature of 1520 - 1680°C (Jennings et al., 2019 and references therein). By comparing different modeling approaches, Thompson et al. (2001) concluded that the Horingbaai magmas were generated within a mantle plume bringing up hot mantle from depth.

In addition to the mafic units, several geochmicaly distinct latite and quartz latite units (which were used for correlations with rhyolite units in the Paraná; Milner et al., 1995) overlie the main basaltic lava sequences and contain minor amounts of interbedded basaltic lavas (Ewart et al., 2004b). Since both high- and low-Ti mafic and silicic units are intercalated in the north and the transition zone, and only low-Ti mafic and silicic units are present in southern Etendeka (Marsh et al., 2001), the spatial differences in composition suggest a fundamental petrogenetic or structural difference between both areas. The marked provinciality of the magma types appear to hamper a stratigraphic correlation of the igneous sequences in Etendeka (Marsh et al., 2001). Correlations between adjacent portions of Etendeka and Paraná, however, have been more successful than between north and south Etendeka (Erlank et al., 1984; Milner et al., 1995; Marsh et al., 2001; Ewart et al., 2004a, Ewart et al., 2004b). Whereas Tafelberg (mainly in southern Etendeka) and Khumib (exclusively in northern Etendeka) lava flows are intercalated in northern and transitional Etendeka, the Tafelkop and Horingbaai magma types are restricted to southern Etendeka. Radiometric age determinations of the different low-Ti mafic igneous (extrusive and intrusive) units presented in numerous studies yield largely overlapping ages between 135 and 125 million years (see

compilation in Appendix A). Although no radiometric ages are available from mafic high-Ti basaltic lavas, a quartz latite with clear high-Ti affinities from southern Angola (Ewart et al., 2004b) was dated at 132±0.4 Ma (Renne et al., 1996), providing a minimum age for the underlying intercalated low- and high-Ti basaltic lavas. The southern Etendeka igneous units were emplaced on/intruded into Neoproterozoic basement rocks, as well as metasedimentary and igneous rocks of Damara orogenic belt (Neoproterozoic; Miller, 2008). The northern Etendeka units were emplaced on a Paleoproterozoic basement as well as metasedimentary and igneous rocks of Kaoko orogenic Belt (Neoproterozoic; Miller, 2008 and references therein). In conclusion, high- and low-Ti basaltic (as well as silicic) igneous units appear to have formed contemporaneously, despite the spatial variations in geochemistry with high-Ti (Kumib) basalts restricted to northern and transitional Etendeka, whereas only low-Ti mafic igenous rocks (lavas, dikes and intrusions) outcrop in southern Etendeka.

After emplacement of the Etendeka flood basalts (135-129 Ma; Renne et al., 1996), the mantle plume interacted with the incipient Mid Atlantic Ridge, forming the aseismic Walvis Ridge on the African Plate and the Sao Paulo Plateau and Rio Grande Rise on the South American Plate between ~120 and 60 Ma (Homrighausen et al., 2019; O'Connor and Jokat, 2015; Rohde et al., 2013b). After the Rio Grande Rise was separated from Walvis Ridge by ridge jumps (O'Connor and Jokat, 2015), the hotspot was located beneath the African Plate and bifurcated to form a double chain of seamounts and ridges, Tristan subtrack and Gough subtrack (Hoernle et al., 2015; Rohde et al., 2013a). All lavas have Enriched Mantle (EM I) type composition, but compared to the Gough subtrack, the Tristan subtrack lavas are characterized by systematically lower $^{207}Pb/^{204}Pb$ at a given $^{206}Pb/^{204}Pb$ ratio. This isotopic zonation can be traced from the active islands to the old DSDP Sites 525, 527 and 528, located at the southwestern end of Walvis Ridge (Figure 2-1) with an age of ~70 Ma (Homrighausen et al., 2019; O'Connor and Jokat, 2015; Rohde et al., 2013b). North of these drill sites, lavas with almost exclusively Gough composition have been dredged from the Walvis Ridge plateau basement (Hoernle et al., 2015; Homrighausen et al., 2019), suggesting that Gough is the dominant composition in the Etendeka and Paraná flood basalts (Hoernle et al., 2015).

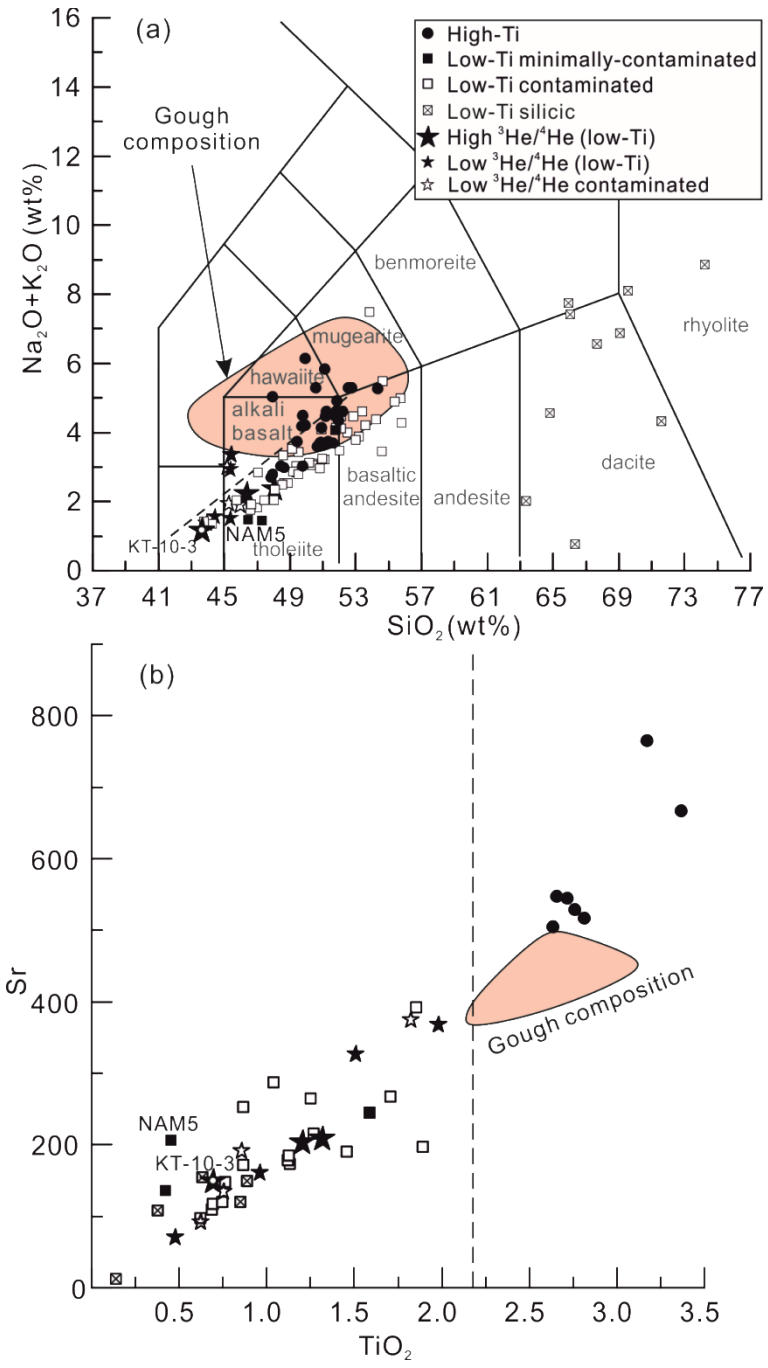

Figure 2-2: (a) Sampled mafic and silicic igneous rocks of the Etendeka LIP plotted on the total alkali vs. silica diagram (TAS) of Le Maitre et al. (1989). Dashed line dividing alkaline and subalkaline rocks after MacDonald and Katsura (1964). Open symbols denote samples with Th/Nb > 0.22 and Pb/Ce > 0.13, indicating significant crustal contamination of the magmas (see section 2.6.1 and Figure 2-4b). (b) Following the division of Marsh et al. (2001), the samples are grouped by their TiO2 content: low-Ti < 2.2 wt.% TiO2 and high-Ti > 2.2 wt.% TiO2. Low-Ti and high-Ti lavas can also be distinguished by their low (<450 ppm) high Sr concentrations (>450 ppm), respectively. The Gough composition is represented by DSDP site 525A lavas on the Walvis Ridge (Hoernle et al., 2015).

In recent years it has been shown that most hotspots that are believed to be associated with deep-seated mantle plumes are generated within or near seismically detected large

low-shear-velocity provinces (LLSVPs), such as Tristan-Gough, Discovery, Shona Segments at the western and Mozambique Ridge at the eastern margin of the Aftican LLSVP (Torsvik et al., 2006).

2.4. Samples and analytical methods

Samples for this study were collected from all major Etendeka lava fields in northern Namibia (having high-Ti contents) and southern Namibia (characterized by low-Ti contents) (Figure 2-1) to further extend the sample base for identifying potential plume components in the Etendeka magma province and their spatial distribution. Exact sample locations and assignment to the different units according to Marsh et al. (2001) are given in Table 2-1. All major and trace element data are reported in Table 2-1, and isotope data are reported in Table 2-2.

Most of our Northern Etendeka lavas have porphyritic textures with olivine, clinopyroxene and plagioclase as phenocrysts (0.5mm - 3.4mm). Both clinopyroxene and plagioclase generally show subhedral shape. The groundmass exhibits intergranular texture with plagioclase being larger than clinopyroxene.

The porphyritic Southern Etendeka (low-Ti) lavas have smaller clinopyroxene and plagioclase phenocrysts (0.1mm – 0.4mm) compared to those from Northern Etendeka. Olivine has not been observed as phenocrystic phase. A similar geographic variation of phenocrysts abundance and size was previously also reported by Ewart et al. (2004a). The mafic dikes usually display holocrystalline, ophitic textures (large crystals of augite pyroxene enclosing smaller laths of plagioclase) with up to 20% olivine phenocrysts which then classifies as picrites. Rare siliceous dikes contain quartz, feldspars and Fe-Ti oxides.

After removing weathered surfaces, samples were crushed in a jaw-crusher, cleaned in an ultrasonic bath with deionized water, sieved and carefully hand-picked under a binocular microscope to avoid the most altered portions of the samples. Selected whole rock chips (~10g) of each sample were ground to a fine powder and dried at 105°C overnight.

Table 2-1: Major and trace element concentrations

Sample	NAM14	NAM15	NAM17	NAM18	NAM19	NAM20	NAM21	NAM22	NAM23	NAM24	NAM25	NAM26	NAM27	NAM28
Location	Khumib	Khumib	Khumib	Khumib	Khumib	Khumib	Khumib	Khumib	Khumib	Khumib	Khumib	Khumib	Khumib	Khumib
Type	High-Ti	High-Ti	High-Ti	High-Ti	High-Ti	High-Ti	High-Ti	High-Ti	High-Ti	High-Ti	High-Ti	High-Ti	High-Ti	High-Ti
SiO_2	51.87	50.86	49.81	47.98	47.85	51.99	49.80	47.97	51.64	52.78	51.81	51.01	51.22	50.94
Al_2O_3	13.20	12.96	13.58	10.08	9.53	13.63	10.75	13.79	13.42	12.85	13.14	13.49	13.47	13.65
Fe_2O_3	12.71	13.14	12.05	12.64	12.87	12.50	12.05	12.54	11.97	12.26	12.06	12.17	12.12	12.29
MgO	3.99	4.51	5.04	12.70	13.35	4.93	10.29	5.80	4.63	4.15	4.82	4.94	4.82	4.88
MnO	0.15	0.16	0.14	0.16	0.16	0.16	0.16	0.15	0.15	0.15	0.15	0.15	0.15	0.16
CaO	7.27	8.64	8.67	8.48	8.35	8.09	9.32	8.07	8.77	6.92	8.18	8.73	8.76	8.38
Na_2O	2.58	2.34	2.30	1.74	1.66	2.47	1.86	3.24	2.55	2.80	2.41	2.26	2.47	2.39
K_2O	2.34	1.33	2.19	1.05	1.02	1.88	1.15	1.79	1.14	2.48	2.04	1.35	1.21	1.73
TiO_2	3.79	3.77	3.24	2.72	2.54	3.37	2.58	3.30	3.35	3.51	3.39	3.28	3.31	3.29
P_2O_5	0.54	0.51	0.40	0.34	0.32	0.48	0.31	0.44	0.47	0.52	0.45	0.45	0.46	0.46
SO_3		0.01						0.01						
Sum	99.64	99.47	99.58	99.70	99.38	100.51	100.28	99.54	99.64	99.50	99.57	99.80	99.46	99.65
L.O.I	1.20	1.24	2.17	1.81	1.73	1.01	2.01	2.44	1.56	1.08	1.13	1.98	1.48	1.49
Li				6.14	6.2		5.5							
Sc				28.1	25.6		27.6							
V				287	257		272							
Cr				704	725		941							
Co				66.7	65.9		52.5							
Ni				494	514		282							
Cu				127	121		126							
Zn				110	107		98.3							
Ga				19.7	18.5		19.4							
Rb				20	18.9		22.6							
Sr				517	505		547							
Y	40	38	36	27.8	27	38	28	37	37	38	36	36	37	37
Zr	352	325	283	227	214	315	226	294	323	343	311	304	313	307
Nb				20.7	19.5		21.5							
Cs				0.88	0.828		0.369							
Ba				397	366		413							
La				28.9	27.4		30.6							
Ce				62.4	59.2		65.8							

Pr	7.98	7.65	8.44
Nd	34.5	32.9	35.5
Sm	7.56	7.29	7.67
Eu	2.42	2.36	2.45
Gd	7.08	6.82	7.11
Tb	1.02	0.989	1.02
Dy	5.63	5.43	5.58
Ho	1.01	0.976	1.01
Er	2.49	2.41	2.54
Tm	0.332	0.32	0.337
Yb	2.01	1.96	2.07
Lu	0.288	0.276	0.3
Hf	5.14	4.94	5.22
Ta	1.16	1.1	1.2
Pb	3.88	3.72	4.64
Th	2.61	2.55	3.07
U	0.556	0.545	0.625

Table 2-1: (continued)

Sample	NAM29	NAM30	NAM31	NAM90	NAM91	NAM92	NAM93	NAM94	NAM95	NAM96	NAM97	NM3	NM4	NM6
Location	Khumib	Khumib	Khumib	Khumib	Khumib	Khumib	Khumib	Khumib	Khumib	Khumib	Khumib	Khumib	Khumib	Khumib
Type	High-Ti	High-Ti	High-Ti	High-Ti	High-Ti	High-Ti	High-Ti	High-Ti	High-Ti	High-Ti	High-Ti	High-Ti	High-Ti	High-Ti
SiO_2	51.87	51.13	49.93	54.37	51.18	52.26	51.25	50.89	50.70	49.94	49.74	48.66	48.46	49.48
Al_2O_3	13.32	13.62	13.53	13.48	13.71	13.32	13.49	13.71	13.67	13.21	13.30	10.09	10.10	12.80
Fe_2O_3	16.63	11.71	11.85	11.58	12.54	12.20	12.42	11.85	12.07	12.85	12.88	12.62	12.52	12.02
MgO	2.59	4.53	5.38	3.70	4.45	4.76	4.82	4.96	5.08	5.90	5.94	11.71	11.24	7.57
MnO	0.20	0.14	0.16	0.14	0.16	0.15	0.16	0.15	0.16	0.17	0.16	0.16	0.16	0.15
CaO	6.96	7.02	6.85	6.74	8.09	7.99	8.07	8.79	8.89	8.31	8.41	8.20	8.24	8.42
Na_2O	3.13	3.04	3.40	2.67	2.56	2.43	2.36	2.53	2.48	2.47	2.44	1.80	1.76	2.53
K_2O	1.49	2.80	2.74	2.60	1.89	2.17	2.25	1.17	1.10	1.74	1.74	1.05	1.11	1.06
TiO_2	2.40	3.32	3.31	3.46	3.71	3.44	4.06	3.82	3.82	3.40	3.37	2.61	2.63	3.06
P_2O_5	0.31	0.42	0.42	0.61	0.53	0.48	0.52	0.51	0.50	0.46	0.46	0.34	0.34	0.46
SO_3	0.11											0.05	0.06	0.02
Sum	100.02	99.82	99.73	100.39	100.73	100.30	101.15	100.30	99.34	100.72	99.34	99.45	98.89	98.91
L.O.I	1.01	2.10	2.16	1.04	1.91	1.10	1.75	1.92	0.87	2.27	0.90	2.55	2.67	1.34
Li												9.65	9.77	6.22
Sc												29.2	28	26.5
V												295	285	316
Cr												965	890	374
Co												68.7	65.5	50.7
Ni												340	318	254
Cu												120	125	127
Zn												117	113	119
Ga												19.4	19.3	24
Rb												19.6	19.9	23
Sr												544	529	765
Y	59	36	35	42	41	36	36	35	34	37	36	26.2	25.9	34.8
Zr	231	303	300	390	343	310	335	325	321	300	302	242	221	308
Nb												17.3	17.2	25.6
Cs												0.824	0.4	0.828
Ba												368	361	587
La												24.6	24.7	39
Ce												55.6	55.6	83.5

Pr	7.32	7.35	10.6
Nd	32.3	32.4	45.2
Sm	7.22	7.24	9.65
Eu	2.3	2.31	3.01
Gd	6.65	6.68	8.84
Tb	0.947	0.957	1.24
Dy	5.19	5.2	6.85
Ho	0.929	0.928	1.24
Er	2.31	2.31	3.11
Tm	0.307	0.308	0.416
Yb	1.88	1.87	2.57
Lu	0.269	0.27	0.371
Hf	5.31	4.99	6.72
Ta	1	0.998	1.45
Pb	4.28	4.25	6.6
Th	2.37	2.39	3.79
U	0.549	0.552	0.747

Table 2-1: (continued)

Sample	NM37	NAM1A	NAM1B	NAM4	NAM5	NAM6	NAM10A	NAM10B	NAM11	NAM12	NAM13	NAM14.1	NAM14.2	NAM16
Location	Khumib	HOD	HOD	HOD	Messum Crater	Messum Crater	Khumib	near Brandberg	near Brandberg	near Brandberg	near Tafelberg Mountain	near Tafelberg Mountain	HOD	HOD
Type	High-Ti	Low-Ti	Low-Ti	Low-Ti	Low-Ti	Low-Ti	Low-Ti	Low-Ti	Low-Ti	Low-Ti	Low-Ti	Low-Ti	Low-Ti	Low-Ti
SiO_2	50.58	49.41	49.39	49.20	47.32	46.50	48.68	48.90	69.61	54.28	52.03	47.01	46.64	52.51
Al_2O_3	13.75	15.43	13.28	13.43	16.42	19.03	14.94	14.90	12.43	13.79	14.38	11.72	11.12	13.23
Fe_2O_3	12.33	11.44	11.29	11.15	8.36	9.72	12.39	12.26	5.10	11.09	11.56	11.40	11.46	13.99
MgO	4.91	6.35	10.13	10.03	9.71	3.14	7.78	7.74	0.34	5.27	5.77	16.39	17.85	4.46
MnO	0.10	0.17	0.18	0.18	0.14	0.21	0.19	0.19	0.10	0.16	0.17	0.17	0.18	0.21
CaO	7.00	9.85	9.92	9.96	15.44	7.11	11.39	11.54	1.56	8.12	9.44	9.45	9.35	8.32
Na_2O	2.94	1.96	1.85	1.81	1.38	5.79	2.17	2.21	3.01	2.53	2.22	1.41	1.38	2.62
K_2O	2.15	1.05	0.99	1.04	0.07	3.21	0.35	0.32	5.09	1.84	1.26	0.40	0.37	1.38
TiO_2	3.24	1.15	1.10	1.09	0.45	1.45	1.23	1.27	0.62	1.21	1.17	0.67	0.61	1.68
P_2O_5	0.44	0.13	0.13	0.13	0.01	0.75	0.11	0.12	0.10	0.19	0.16	0.06	0.06	0.24
SO_3	0.02	0.09	0.02	0.01		0.11	0.03	0.03						0.02
Sum	99.67	99.81	99.46	98.90	99.64	98.83	99.40	99.74	99.19	99.71	100.46	99.15	99.48	99.30
L.O.I	2.67	3.00	1.18	0.87	0.34	1.81	0.14	0.26	1.24	1.24	2.31	0.47	0.46	0.64
Li	10.6		13.8	13.1	3.33	191	9.77		21.9			10.3	7.61	
Sc	29.8		31.7	31.9	47.5	9.07	36.8		8.06			35.8	32.7	
V	364		259	258	183	149	371		4.29			259	230	
Cr	94.9		608	616	391	11.4	160		3.87			1826	1941	
Co	42.8		50	50.6	45.1	22.9	48.5		2.32			75	72.9	
Ni	68.7		261	263	166	13.1	85.6		0.513			654	683	
Cu	155		82.4	81.7	27.3	38.1	73		3.11			89.2	84	
Zn	119		84.8	83.9	39.9	77.7	85.2		91.1			77.7	67.7	
Ga	24.7		17.3	17.8	14.7	15.8	19.9		23.7			13.4	12.4	
Rb	45.5		51.2	46.9	0.96	88	10.3		156			15.4	14.2	
Sr	666		172	178	206	1017	264		154			109	96.5	
Y	34.5	30	26.3	26.9	9.6	23.6	23.5	24	63.8	30	29	19.2	18	35
Zr	322	143	125	129	13.2	193	27.9	86	430	143	155	59.3	53.2	193
Nb	27.9		9.25	9.44	0.661	109	5.23		46.1			3.45	3.58	
Cs	0.601		3.69	6.77	0.042	1.36	0.581		2.13			1.07	0.738	
Ba	650		273	267	38.7	1113	110		972			98.9	87.3	

La	39.7	17	17.4	1.45	52.4	8.03	68.7	6.25	5.5
Ce	85.5	35.5	36.3	3.57	94.1	18.4	129	13.7	11.9
Pr	10.9	4.47	4.58	0.579	10	2.62	16.2	1.81	1.61
Nd	46.4	18.7	19.1	3.15	37.2	12.4	60.8	8.06	7.17
Sm	9.78	4.31	4.39	1.12	6.57	3.47	12.2	2.2	1.97
Eu	3.05	1.28	1.3	0.518	2.24	1.32	2.07	0.698	0.638
Gd	8.8	4.56	4.6	1.51	6	3.98	11.3	2.66	2.43
Tb	1.26	0.742	0.753	0.27	0.848	0.659	1.8	0.475	0.439
Dy	6.93	4.59	4.62	1.74	4.7	4.14	10.8	3.16	2.93
Ho	1.25	0.924	0.937	0.353	0.882	0.838	2.13	0.666	0.627
Er	3.15	2.53	2.56	0.932	2.34	2.27	5.91	1.9	1.78
Tm	0.423	0.372	0.373	0.134	0.332	0.33	0.884	0.286	0.27
Yb	2.62	2.41	2.42	0.833	2.1	2.13	5.81	1.88	1.79
Lu	0.377	0.364	0.368	0.124	0.318	0.317	0.867	0.291	0.277
Hf	7.04	3.01	3.04	0.502	3.22	0.841	10.6	1.49	1.34
Ta	1.55	0.52	0.526	0.044	6.23	0.287	2.48	0.218	0.232
Pb	6.51	5.67	5.91	0.347	6.06	2.34	27.8	2.78	1.96
Th	3.93	3.69	3.73	0.095	6.92	1.42	21.5	1.65	1.26
U	0.789	0.459	0.471	0.0292	1.69	0.242	6.06	0.466	0.373

Table 2-1: (continued)

Sample	NAM32	NAM33	NAM34	NAM35	NAM36	NAM37	NAM38A	NAM38B	NAM39	NAM41	NAM42	NAM43	NAM44	NAM45
Location	main Etendeka lava field	main Etendeka lava field	main Etendeka lava field	main Etendeka lava field	main Etendeka lava field	main Etendeka lava field	main Etendeka lava field	main Etendeka lava field	main Etendeka lava field	main Etendeka lava field	main Etendeka lava field	main Etendeka lava field	Coastal	Coastal
Type	Low-Ti	Low-Ti	Low-Ti	Low-Ti	Low-Ti	Low-Ti	Low-Ti	Low-Ti	Low-Ti	Low-Ti	Low-Ti	Low-Ti	Low-Ti	Low-Ti
SiO_2	54.61	55.74	69.10	55.80	55.43	53.23	53.63	52.16	67.72	53.45	53.04	52.88	51.13	50.95
Al_2O_3	13.41	12.92	12.16	12.50	12.55	13.58	13.28	13.35	12.45	13.65	14.28	14.08	14.45	14.05
Fe_2O_3	12.61	13.16	5.22	14.21	14.20	12.83	13.27	13.41	5.45	11.16	11.17	11.60	11.41	11.68
MgO	3.68	3.24	1.34	2.47	2.63	4.72	4.38	4.35	1.55	5.21	5.72	5.64	6.94	6.71
MnO	0.18	0.19	0.09	0.19	0.19	0.19	0.19	0.19	0.10	0.17	0.17	0.18	0.18	0.17
CaO	8.09	6.72	2.34	6.62	6.10	8.31	8.16	8.55	2.53	8.21	9.18	8.72	10.07	8.51
Na_2O	2.37	2.61	2.40	3.02	2.60	2.43	2.76	2.69	2.50	2.96	2.42	2.76	2.18	2.76
K_2O	1.08	2.38	4.47	1.26	2.28	1.45	1.45	1.41	4.07	1.63	1.35	1.70	1.04	1.33
TiO_2	1.42	1.62	0.83	1.81	1.83	1.43	1.56	1.56	0.85	1.22	1.24	1.24	0.99	1.00
P_2O_5	0.19	0.20	0.25	0.21	0.22	0.18	0.19	0.18	0.26	0.18	0.17	0.17	0.12	0.11
SO_3				0.04										
Sum	99.50	99.50	99.69	99.42	99.18	99.53	99.67	99.36	99.74	99.29	99.66	100.12	99.77	99.52
L.O.I	1.86	0.73	1.50	1.29	1.15	1.19	0.81	1.52	2.27	1.46	0.94	1.16	1.27	2.26
Li			27.1		18.5									
Sc			15.8		35.3									
V			49.6		473									
Cr			4.92		6.95									
Co			8.75		40.3									
Ni			2.96		10.2									
Cu			32.2		71									
Zn			93.9		121									
Ga			19.5		23.6									
Rb			182		89.6									
Sr			120		196									
Y	34	40	39.9	40	39.7	34	33	33	39	29	26	27	23	23
Zr	195	204	265	211	225	153	151	146	245	140	133	128	105	99
Nb			21.5		16									
Cs			7.46		2.41									
Ba			588		446									

La	42.2	31.7
Ce	85	66.4
Pr	10.3	8.19
Nd	39.8	33.2
Sm	8.21	7.29
Eu	1.6	1.87
Gd	7.56	7.24
Tb	1.18	1.14
Dy	6.91	6.89
Ho	1.35	1.37
Er	3.66	3.75
Tm	0.538	0.548
Yb	3.53	3.58
Lu	0.531	0.535
Hf	6.36	5.42
Ta	1.55	0.967
Pb	24.7	14.1
Th	14	8.67
U	4.99	2.1

Table 2-1: (continued)

Sample	NAM46	NAM47	NAM48	NAM49	NAM50	NAM51	NAM52	NAM53	NAM54	NAM55	NAM56	NAM57	NAM58	NAM59
Location	Coastal	Coastal	Coastal	Coastal	Coastal	Coastal	Coastal	Coastal	Coastal	Coastal	Albin Ridge	HOD	HOD	HOD
Type	Low-Ti	Low-Ti	Low-Ti	Low-Ti	Low-Ti	Low-Ti	Low-Ti	Low-Ti	Low-Ti	Low-Ti	Low-Ti	Low-Ti	Low-Ti	Low-Ti
SiO_2	66.07	50.55	48.58	71.62	63.40	66.38	64.84	47.09	49.25	51.00	48.67	50.42	49.55	46.48
Al_2O_3	12.65	14.36	16.14	11.70	9.88	10.28	13.94	15.46	13.20	14.50	13.07	16.15	13.09	13.79
Fe_2O_3	6.13	10.95	10.35	5.33	3.36	3.24	6.44	11.29	15.12	12.01	14.65	9.95	11.25	9.19
MgO	1.35	7.98	8.65	2.31	1.51	1.48	3.25	7.41	4.67	5.23	3.34	6.95	10.16	10.27
MnO	0.10	0.18	0.16	0.13	0.35	0.33	0.11	0.18	0.24	0.18	0.21	0.17	0.18	0.16
CaO	2.82	10.67	11.34	2.15	10.88	11.28	3.17	12.71	7.61	9.67	7.44	10.30	10.14	15.39
Na_2O	2.74	2.55	1.98	2.33	1.14	0.46	1.89	2.22	3.28	2.09	2.68	2.01	1.82	1.07
K_2O	4.68	0.54	0.49	2.00	0.86	0.30	2.67	0.62	1.45	1.15	1.94	1.04	0.97	0.40
TiO_2	0.95	0.85	1.02	0.92	0.81	0.79	0.86	1.26	2.18	1.54	2.18	0.84	1.10	0.41
P_2O_5	0.26	0.07	0.11	0.17	0.17	0.19	0.18	0.12	0.38	0.20	0.50	0.10	0.13	0.06
SO_3			0.02			0.12		0.04	0.24	0.03	0.33	0.05	0.01	0.02
Sum	98.88	99.89	99.38	99.65	99.74	99.03	98.23	99.82	99.61	99.96	99.32	99.16	99.59	99.04
L.O.I	1.14	1.20	0.54	1.00	7.39	4.18	0.89	1.42	1.99	2.36	4.31	1.18	1.19	1.80
Li		11.9	8.37	41.5			43.9	72.2		22.2			17.1	30.3
Sc		42.2	32.1	13.2			14.6	39.1		38.1			34.4	57.9
V		265	280	104			116	343		311			269	224
Cr		86	202	74.3			76.3	209		108			630	541
Co		49.1	45.9	12.7			16.2	43.7		41.5			51.4	47.2
Ni		64.5	161	24.6			36.7	103		44.6			261	192
Cu		102	86.9	43.6			4.53	131		95.3			82.7	91.7
Zn		68.5	74.8	77.2			117	73.5		110			92.6	53.7
Ga		16.8	17.9	15.4			20	17.3		18.9			17.6	11.2
Rb		19.5	13.8	83			128	27.2		36.9			42.1	21.8
Sr		252	287	128			148	299		262			185	135
Y	38	17.8	21.1	23.4	48	46	36.9	17.1	55	30.7	52	26	26.9	17.1
Zr	237	63.2	90.2	181	267	264	206	70.9	202	160	271	113	125	29.7
Nb		3.42	5.19	12.6			14.1	7.81		9.71			9.13	9.95
Cs		0.503	1.16	5.28			6.99	3.28		1.24			14.5	12.1
Ba		95.7	142	287			387	142		285			291	109
La		5.92	9.5	44.7			30.8	9.05		21.5			16.9	6.77

Ce	13.5	21.3	77.3	63	20.5	45.7	35.5	13.2
Pr	1.89	2.84	10.8	7.83	2.74	5.77	4.48	1.59
Nd	8.74	12.6	42.4	31.1	12.8	24.5	18.8	6.39
Sm	2.47	3.18	8.22	6.63	3.31	5.5	4.36	1.41
Eu	0.881	1.1	1.62	1.34	1.18	1.53	1.31	0.457
Gd	2.87	3.49	6.89	6.33	3.61	5.64	4.62	1.76
Tb	0.489	0.581	0.975	0.996	0.577	0.92	0.756	0.343
Dy	3.12	3.64	5.12	6.01	3.46	5.71	4.69	2.52
Ho	0.636	0.744	0.921	1.2	0.669	1.15	0.943	0.589
Er	1.73	2.05	2.38	3.35	1.76	3.18	2.58	1.78
Tm	0.254	0.303	0.344	0.495	0.251	0.473	0.379	0.279
Yb	1.64	1.98	2.23	3.26	1.56	3.05	2.47	1.93
Lu	0.25	0.301	0.35	0.493	0.234	0.473	0.371	0.305
Hf	1.6	2.18	4.86	5.08	1.95	4.03	3.03	0.781
Ta	0.205	0.269	0.932	0.974	0.413	0.536	0.515	0.597
Pb	1.87	2.69	19.4	15.8	0.892	6.77	5.59	0.991
Th	1.11	1.4	10.4	9.72	0.866	4.5	3.63	0.983
U	0.234	0.261	3.23	3.04	0.239	0.834	0.46	0.214

Table 2-1: (continued)

Sample	NAM60B	NAM60C	NAM66	NAM67	NAM68	NAM69	NAM70	NAM71	NAM72	NM5	NM13	NM14	NM28	NM52
Location	HOD	HOD	HOD	HOD	HOD	HOD	HOD	HOD	HOD	Khumib	Khumib	Khumib	Khumib	HOD
Type	Low-Ti	Low-Ti	Low-Ti	Low-Ti	Low-Ti	Low-Ti	Low-Ti	Low-Ti	Low-Ti	Low-Ti	Low-Ti	Low-Ti	Low-Ti	Low-Ti
SiO_2	65.97	53.87	74.25	48.59	51.85	47.49	50.84	48.05	48.10	51.78	50.19	52.16	49.54	44.91
Al_2O_3	12.84	15.59	12.43	15.45	15.20	12.56	15.57	12.35	16.29	13.72	13.23	13.22	13.55	11.44
Fe_2O_3	4.41	9.25	1.78	10.91	11.16	10.43	10.52	11.11	9.29	12.34	13.94	13.60	13.86	10.54
MgO	1.73	4.49	0.06	7.90	5.18	13.88	7.47	14.14	11.57	5.56	5.77	4.45	5.60	20.03
MnO	0.10	0.16		0.17	0.16	0.16	0.16	0.17	0.15	0.18	0.20	0.19	0.20	0.16
CaO	2.68	3.43	0.36	10.08	8.72	10.31	10.24	10.14	10.77	8.93	10.19	8.01	10.26	9.73
Na_2O	2.98	5.36	2.99	2.24	2.33	1.49	1.97	1.48	2.01	2.55	2.36	2.84	2.65	1.17
K_2O	4.77	2.12	5.86	1.09	1.81	0.53	0.99	0.56	0.32	1.38	0.67	1.46	0.64	0.18
TiO_2	0.36	0.82	0.14	1.23	1.46	0.67	0.97	0.73	0.75	1.19	1.54	1.65	1.41	0.39
P_2O_5	0.04	0.10	0.01	0.15	0.20	0.07	0.11	0.07	0.05	0.15	0.26	0.24	0.13	0.04
SO_3		0.04		0.01	0.05	0.01	0.06		0.04	0.06	0.06	0.02	0.05	
Sum	99.06	99.13	98.90	100.06	99.18	98.92	99.62	99.32	99.62	99.18	99.39	99.52	99.30	98.98
L.O.I	3.20	3.90	1.04	2.24	1.06	1.32	0.72	0.52	0.28	1.55	1.30	1.94	1.59	0.43
Li	31.4	127	15.7	19.6		15.9		9.72	6.62	6.03	10.1	18.9	27.2	6.68
Sc	8.31	25.9	0.686	28.6		33.7		36.2	31	44.3	43.5	39.9	49.3	32.2
V	56.6	192	0.263	259		240		257	174	367	407	443	450	186
Cr	31.7	105	3.91	369		1350		1238	488	54	54.2	32.8	81.5	2138
Co	9.63	34.1	0.106	44.7		59.6		61.2	51.8	46.9	50.5	46.1	50.8	81.2
Ni	22.3	72.7	0.262	205		492		487	273	55.7	60.6	41.6	63.2	881
Cu	20.6	29.3	2.68	109		84.7		97.3	60.2	144	175	168	201	57.8
Zn	101	771	39.2	84.2		65.5		67.7	65.5	99.7	113	123	109	61.6
Ga	27.9	24.7	29.9	20.1		14		13.9	14.6	19.8	21.7	23.1	20.9	9.93
Rb	408	393	530	42.8		24.6		23.6	12.3	35.2	19.2	44.8	25.4	7.47
Sr	108	172	11.5	216		117		119	147	223	244	267	190	67.7
Y	103	51.5	89.5	30.5	36	20.1	26	22.3	21.9	32	33	36.2	31.4	11.5
Zr	397	229	445	150	223	66.2	129	65.4	67.2	138	125	230	118	26.2
Nb	106	55.5	133	10.3		4.12		3.99	2.82	8.07	7.07	18.7	5.07	1.88
Cs	2.3	20.1	2.66	14.3		3.71		1.28	0.477	0.154	0.459	4.56	0.91	0.481
Ba	125	239	19.9	314		107		127	78.6	208	204	419	117	36.3
La	109	53.5	139	18.8		7.67		8.49	6.51	15.5	12.6	27.7	8.03	2.5
Ce	209	99.8	174	39.6		16.5		18	14.6	33.5	29	56.6	18.8	5.6

Pr	24.3	11.4	30	5.05	2.15	2.32	2.02	4.31	3.99	6.88	2.66	0.781
Nd	88.2	41	106	21.4	9.25	10	9.32	18.2	18.7	28	12.8	3.71
Sm	17	7.92	19.3	4.97	2.47	2.62	2.64	4.58	4.97	6.17	3.81	1.19
Eu	0.506	0.479	0.214	1.54	0.745	0.78	0.941	1.33	1.65	1.78	1.31	0.43
Gd	15.8	7.53	17	5.25	2.92	3.12	3.18	5.11	5.68	6.38	4.69	1.58
Tb	2.59	1.27	2.63	0.857	0.51	0.554	0.557	0.861	0.922	1.01	0.813	0.296
Dy	16.1	8.15	15.4	5.28	3.35	3.67	3.65	5.46	5.78	6.22	5.28	2.05
Ho	3.31	1.71	3.07	1.07	0.708	0.781	0.768	1.1	1.15	1.23	1.09	0.444
Er	9.55	5.01	8.56	2.9	1.99	2.2	2.15	3.03	3.07	3.38	2.97	1.25
Tm	1.47	0.771	1.27	0.42	0.297	0.328	0.322	0.446	0.438	0.492	0.438	0.197
Yb	9.89	5.22	8.26	2.73	1.97	2.2	2.12	2.92	2.81	3.23	2.87	1.27
Lu	1.47	0.791	1.18	0.407	0.302	0.334	0.325	0.442	0.42	0.489	0.436	0.2
Hf	11.1	5.8	14	3.52	1.69	1.69	1.7	3.29	2.95	4.69	2.57	0.789
Ta	7.24	3.51	3.8	0.571	0.26	0.24	0.179	0.521	0.415	1	0.315	0.149
Pb	26.9	63.5	10.3	6.11	2.91	3.43	2.55	6.95	3.12	8.47	2.87	1.08
Th	50.2	19	60.5	3.74	2.42	2.9	1.79	4.12	1.55	4.53	1.2	0.603
U	9.14	3.82	8.26	0.473	0.601	0.567	0.266	1.08	0.399	0.721	0.415	0.278

Table 2-1: (continued)

Sample	NM53	NM54	NM55	NM56	NM65
Location	HOD	HOD	HOD	HOD	HOD
Type	Low-Ti	Low-Ti	Low-Ti	Low-Ti	Low-Ti
SiO_2	44.46	46.42	47.03	54.67	49.80
Al_2O_3	12.77	12.65	13.69	17.79	16.24
Fe_2O_3	10.51	10.50	11.17	8.37	11.60
MgO	19.15	14.91	13.11	1.24	6.66
MnO	0.15	0.16	0.17	0.09	0.16
CaO	9.43	10.24	11.17	6.53	9.62
Na_2O	1.24	1.62	1.66	2.75	2.49
K_2O	0.20	0.43	0.32	2.47	1.13
TiO_2	0.41	0.75	0.75	1.77	1.10
P_2O_5	0.04	0.08	0.07	0.49	0.14
SO_3		0.02	0.01	0.12	0.07
Sum	99.02	99.01	99.36	98.94	99.74
L.O.I	0.70	1.33	0.29	3.26	0.94
Li	7.43	10.9	7.83	67.9	14.6
Sc	28.7	34.9	42.2	15.7	32.7
V	187	257	298	96.8	285
Cr	2141	1737	1701	10.1	163
Co	79.4	66.1	61.5	13.4	55.1
Ni	835	559	438	4.83	176
Cu	65	83.8	107	15.5	125
Zn	61.9	69.9	70.3	134	107
Ga	10.5	13	13.4	27.3	21.4
Rb	7.95	16.3	11	66.9	38.9
Sr	73	134	102	392	221
Y	12	17	22	55.3	31.9
Zr	29.2	59.7	51	350	146
Nb	2.15	3.56	3.98	39.1	8.09
Cs	0.56	2.21	0.463	2.06	1.38
Ba	43.3	96.1	82.8	877	290
La	2.83	6.5	5.18	54.3	17.7
Ce	6.2	14.7	11.5	111	37.3

Pr	0.843	2	1.54	13.9	4.73
Nd	3.95	9.14	7.2	58.1	20
Sm	1.28	2.5	2.25	12.5	4.79
Eu	0.465	0.794	0.793	3.34	1.33
Gd	1.7	2.89	3.04	11.9	5.19
Tb	0.315	0.504	0.568	1.79	0.861
Dy	2.17	3.21	3.92	10.2	5.43
Ho	0.467	0.666	0.847	1.89	1.09
Er	1.32	1.86	2.42	4.84	3.02
Tm	0.206	0.279	0.37	0.665	0.446
Yb	1.33	1.81	2.43	4.08	2.91
Lu	0.207	0.277	0.376	0.581	0.438
Hf	0.863	1.72	1.5	7.84	3.44
Ta	0.164	0.249	0.269	1.81	0.464
Pb	1.26	2.49	2.1	15.1	7.34
Th	0.702	1.61	1.17	4.74	3.83
U	0.305	0.498	0.46	0.856	1.08

Major element oxides (by XRF) in wt% and trace elements (by ICP-MS) in μg/g

L.O.I. = loss on ignition

HOD = Henties Bay - Outjo dikes swam

Table 2-2: Sr-Nd-Pb-Hf isotope data from the Etendeka flood basalts

Sample name	$^{143}Nd/^{144}Nd$	$^{143}Nd/^{144}Ndi$	$^{87}Sr/^{86}Sr$	$^{87}Sr/^{86}Sri$	$^{206}Pb/^{204}Pb$	$^{207}Pb/^{204}Pb$	$^{208}Pb/^{204}Pb$	$^{206}Pb/^{204}Pb_i$	$^{207}Pb/^{204}Pb_i$	$^{208}Pb/^{204}Pb_i$	$^{176}Hf/^{177}Hf$	$^{176}Hf/^{177}Hfi$
NAM18	0.512369	0.512255	0.705139	0.7049	17.4275	15.4848	37.9796	17.24	15.4759	37.70		
NAM19	0.512375	0.512260	0.705124	0.7049	17.4159	15.4842	37.9569	17.23	15.4751	37.67	0.282639	0.282618
NAM21	0.512299	0.512187	0.705634	0.7054	17.2853	15.4948	37.9332	17.11	15.4863	37.66	0.282564	0.282543
NM3	0.512365	0.512249	0.705591	0.7054	17.7157	15.5453	38.2120	17.55	15.54	37.98	0.282625	0.282606
NM4	0.512366	0.512250	0.705622	0.7054	17.7204	15.5447	38.2111	17.55	15.54	37.97		
NM6	0.512265	0.512154	0.705822	0.7057	17.3540	15.5170	38.0854	17.21	15.51	37.84		
NM37	0.512267	0.512158	0.706023	0.7057	17.3058	15.5158	38.1398	17.15	15.51	37.89		
NAM4	0.512137	0.51202	0.716883	0.7155	18.8190	15.7271	39.4884	18.71	15.72	39.21	0.282502	0.282458
NAM5	0.512833	0.51265	0.704553	0.7045	18.6677	15.6539	38.4135	18.56	15.65	38.30	0.283016	0.282926
NAM10A	0.512728	0.51258	0.708426	0.7082	18.7603	15.6632	38.9315	18.62	15.66	38.67		
NAM11	0.512313	0.51221	0.719144	0.7136	19.8432	15.7480	39.6206	19.55	15.73	39.28	0.282600	0.282571
NAM14.1	0.512423	0.51228	0.709904	0.7091	19.2095	15.7097	39.0658	18.98	15.70	38.81		
NAM14.2	0.512433	0.51229	0.710000	0.7092	19.2485	15.7070	39.0593	18.99	15.69	38.78	0.282758	0.282682
NAM34	0.512149	0.51204	0.729914	0.7216	19.2176	15.7255	38.9291	18.95	15.71	38.68	0.282471	0.282440
NAM36	0.512235	0.512121	0.715886	0.713407	18.8453	15.6943	38.9618	18.65	15.68	38.69		
NAM47	0.512540	0.512393	0.710245	0.709824	18.4944	15.6458	38.7827	18.33	15.64	38.53		
NAM48	0.512621	0.51249	0.707321	0.7071	18.6467	15.6523	38.6676	18.52	15.65	38.44	0.282852	0.282802
NAM52	0.512197	0.51209	0.733218	0.7285	18.9786	15.6878	38.4261	18.72	15.68	38.16	0.282500	0.282465
NAM58	0.512145	0.51202	0.716954	0.7157	18.8056	15.7246	39.4630	18.70	15.72	39.18	0.282502	0.282457
NAM59	0.512618	0.51250	0.710586	0.7097	19.1311	15.6943	39.2747	18.84	15.68	38.84	0.282822	0.282679
NAM60B	0.512270	0.51217	0.751093	0.7305	19.3144	15.7310	39.9017	18.85	15.71	39.07		

NAM60C	0.512303	0.51220	0.737162	0.7247	18.9333	15.7139	39.2391	18.85	15.71	39.11		
NAM66	0.512258	0.51216	1.018998	0.7609	20.1472	15.7726	41.1756	19.02	15.72	38.48	0.282573	0.282542
NAM67	0.512262	0.512141	0.712418	0.711339	18.5957	15.6901	39.0824	18.49	15.69	38.82		
NAM69	0.512325	0.51219	0.712093	0.7110	19.3469	15.7289	39.5332	19.07	15.72	39.17		
NAM71	0.512278	0.51214	0.711939	0.7109	19.1000	15.7187	39.6386	18.88	15.71	39.27	0.282732	0.282659
NAM72	0.512410	0.51226	0.708742	0.7083	18.1742	15.6567	39.7023	18.04	15.65	39.40		
NM5	0.512356	0.51223	0.708752	0.7079	18.8497	15.6892	38.9265	18.64	15.68	38.67		
NM13	0.512493	0.51235	0.705740	0.7053	18.2052	15.6106	38.3496	18.04	15.60	38.14	0.282781	0.282729
NM14	0.512263	0.512148	0.709106	0.708195	18.3691	15.6419	38.7912	18.26	15.64	38.56		
NM28	0.512641	0.51249	0.706176	0.7054	18.7176	15.6644	38.7135	18.53	15.66	38.53	0.282887	0.282825
NM52	0.512633	0.51247	0.708035	0.7074	19.7143	15.7288	38.9525	19.37	15.71	38.71	0.28294	0.282847
NM54	0.512499	0.51236	0.709104	0.7084	19.3253	15.7205	39.2163	19.06	15.71	38.93	0.282803	0.282744
NM56	0.512355	0.51224	0.712050	0.7111	18.9027	15.6908	38.8755	18.83	15.69	38.74		

Major elements and selected trace elements were measured at the Institute of Mineralogy and Petrography at the University of Hamburg on a Magix Pro PW 2540 X-ray fluorescence spectrometer (XRF). International rock standards JGB-1, JB-3, JB-2, JA-3, JG-3, JG-2 were analyzed together with the samples. The difference between measured and accepted literature values (Govindaraju, 1994) is less than 4%, except for MnO (because of the low concentration of Mn in these rocks) (see Table A2 in Appendix A).

Trace elements were determined with an AGILENT 7500cs inductively coupled plasma mass spectrometer (ICP-MS) at the Institute of Geosciences at Kiel University. Powder (~100 mg) was dissolved by pressure digestion and analyzed following the methods of Garbe-Schönberg (1993). Five more evolved (silicic) samples were dissolved using 2ml HNO_3 + 4ml HF in bombs at 180°C to ensure complete dissolution of possible zircon crystals (Garbe-Schönberg, 1993). The international rock standards BIR-1, BHVO-2 and BCR-2 were measured with samples. The accuracy of most measured element abundances is within 4% of the accepted reference values (http://georem.mpch-mainz.gwdg.de), except for Cr, Ni, Er, Tm, Hf, Ta and Zr. The relative standard deviation (RSD) is better than 2% (Table A3 in Appendix A).

The Sr-Nd-Pb isotope ratios were measured at the GEOMAR Helmholtz Centre for Ocean Research Kiel by thermal ionization mass spectrometry (TIMS) using a Thermo-Scientific TRITON *Plus*. About 100-250 mg of the 1-2mm chip fraction were leached in 2N HCl at 70°C for 1-2 hours, then triple rinsed in 18MΩ H_2O, before digestion in a mix of concentrated HF and HNO_3 (5:1) at 140°C for 2 days. Ion chromatography followed standard procedures described in Hoernle et al. (2008). The Sr and Nd isotopic ratios were mass-bias corrected to $^{86}Sr/^{88}Sr = 0.1194$ and $^{146}Nd/^{144}Nd = 0.7219$ during the measurement and normalized off-line to NBS987 and La Jolla standards measured along with the samples. Since installation of the instrument in 2014 normalized NBS987 values are $^{87}Sr/^{86}Sr = 0.710250 \pm 0.000009$ (n=536; 2 standard deviation (SD)) and La Jolla yields $^{143}Nd/^{144}Nd = 0.511850 \pm 0.000007$ (n=347; 2SD). Pb isotopes were measured using the double-spike (Pb-DS) technique (Hoernle et al., 2011). The DS corrected NBS981 values since 2014 are $^{206}Pb/^{204}Pb = 16.9407 \pm 0.0018$, $^{207}Pb/^{204}Pb = 15.4976 \pm 0.0018$, $^{208}Pb/^{204}Pb = 36.7200 \pm 0.0046$ (n=116; 2SD). Hf isotope ratios were also measured at GEOMAR on a NU MC-ICP-MS and samples data obtained in

standard bracketing mode. Unleached powders (200-300 mg) were prepared following the established method of Blichert-Toft et al. (1997). The in-house standard SPEX Hf ICP solution (lot#9) yielded $^{176}Hf/^{177}Hf$ = 0.282170 ± 0.000009 (n=19; 2SD) corresponding to a JMC457 value = 0.282163 (Blichert-Toft et al., 1997). Procedural blanks were <30pg for Pb and <100pg for Sr-Nd-Hf.

2.5. Results

2.5.1. Major and trace elements

Major and trace element data are given in Table 2-1. Overall the rocks are well-preserved with loss on ignition (LOI) values of 0.14-2.78 wt.% for all but four samples with LOI of 3.9-7.4 wt.% (NAM50, NAM51, NAM56 and NAM60C), which are thus excluded from further consideration. Accordingly, most samples show reasonably good correlations between mobile and immobile element enrichment, such as K vs. Th (r = 0.86), K vs. Hf (r = 0.90) and K vs. Zr (r = 0.85).

The analyzed rocks show a wide compositional range on the total alkali-silica (TAS) diagram (Figure 2-2a). The SiO_2 content ranges from 43 to 76 wt.% with a gap between 56 and 63 wt.% (Bunsen-Daly gap), dividing the samples into mafic (MgO = 1.3-20.8 wt.%) and silicic (MgO = 0.06-3.36 wt.%) suites (Milner et al., 1995).

As noted by Marsh et al. (2001) and Ewart et al. (2004b), relatively high Ti, Zr and Sr are found in mafic and silicic Etendeka igneous rocks north of Terrace Bay (Figure 2-1), whereas comparatively low Ti, Zr and Sr contents dominate the Etendeka rocks south of the bay. This geographic division is confirmed by our new data. Accordingly, samples with TiO_2 >2.2wt% and Sr >450ppm are henceforth labeled as “high-Ti” rocks and samples with lower Ti and Sr contents as “low-Ti” rocks (Figure 2-2b; Marsh et al., 2001). The high-Ti rocks have MgO ranging from 2.7-13.8 wt% and the low-Ti rocks from 0.3-20.8 wt%. Using the nomenclature of Marsh et al. (2001), all our high-Ti rocks from northern Etendeka would classify as “Khumib-type” (Table 2-1).

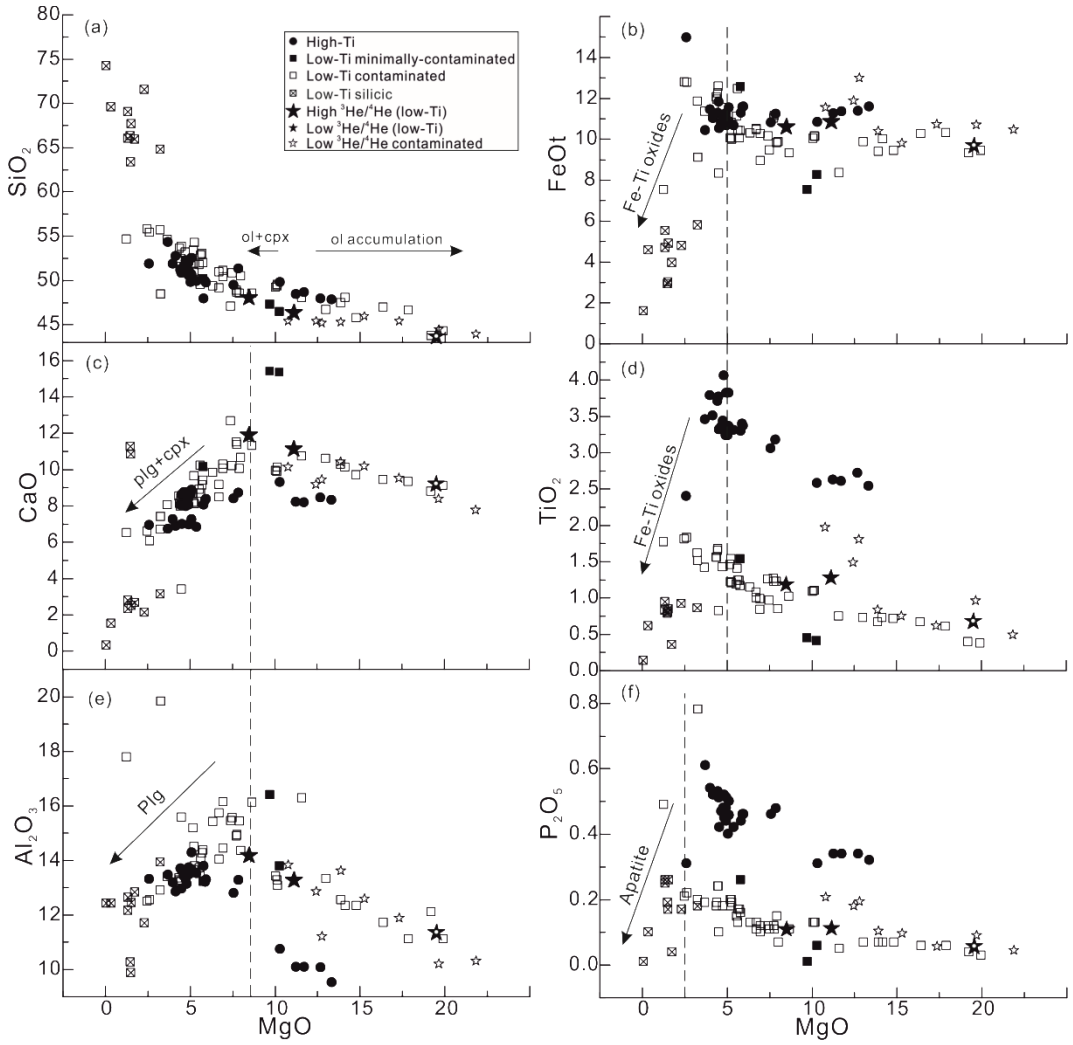

Figure 2-3: MgO content versus major oxides (in wt.%). Olivine (ol) accumulation is apparent for lavas with >10wt.% MgO. The low-Ti lavas crystalized clinopyroxene (cpx) and plagioclase (plg) at MgO < 8wt%, Fe-Ti oxides at MgO < 5wt% and apatite at MgO < 2.2 wt%. High-Ti samples show similar trends to low-Ti samples, but the mafic (MgO > 7wt.%) high-Ti samples contain less CaO (c) and Al2O3 (e), but generally higher FeOt (b) and significantly higher TiO2 (d), and P2O5 (f) than low-Ti lavas. The high-Ti lavas show fractionation of olivine ± clinopyroxene (MgO > 8wt%), clinopyroxene and plagioclase (MgO < 8wt%), but no evidence for significant Fe-Ti oxide or apatite fractionation. Two low-Ti samples with high P2O5 have accumulated apatite.

Plots of MgO versus other major oxides are shown in Figure 2-3. MgO vs. SiO_2 shows an inverse hyperbolic (concave-up) array. Rocks with MgO >10-12wt% have apparently accumulated olivine consistent with petrographic examinations. For the low-Ti lavas, CaO, Al_2O_3, FeOt and TiO_2 initially increase with decreasing MgO and then decrease, reflecting fractionation of plagioclase (in samples with MgO<8wt%), Fe-Ti oxides (MgO<5wt%) and apatite (MgO<2.5wt%). The high-Ti lavas form parallel trends to the low-Ti rocks on the MgO vs TiO_2 and P_2O_5 diagrams but are shifted to

higher values (Figure 2-3). The high-Ti samples with MgO>10wt% have significantly lower Al_2O_3 and slightly lower CaO and slightly higher SiO_2 and FeO. The overall constant CaO values with decreasing MgO, but marked increase in Al_2O_3, Sr and Eu (not shown) of the high-Ti lavas point to primarily clinopyroxene rather than plagioclase fractionation, in contrast to the low-Ti rocks for which the data indicate both plagioclase and clinopyroxene fractionation. With the exception of the sample with the lowest MgO, there is no evidence for significant Fe-Ti oxide or apatite fractionation in the high-Ti samples. According to the division scheme of Marsh et al. (2001), most of our low-Ti samples from southern Etendeka would classify as Tafelberg-type except for samples with distinct lower Zr/Y ratios consistent with a Horingbaai composition (See the Table 2-1 for overview).

On the Nb/Yb vs. Th/Yb diagram (Figure 2-4a), our samples plot both within or above the mid-ocean-ridge basalt – ocean-island basalt (MORB-OIB) array. In addition, the data form a crude positive correlation on a diagram of Pb/Ce vs. Th/Nb (Figure 2-4b), indicating variable extents of continental crustal contamination. We have therefore divided the samples into a minimally ($Pb/Ce \leq 0.13$, $Th/Nb < 0.22$; filled symbols) and a more strongly crustally-contaminated group (open symbols; Figure 2-4), based on the range of these ratios observed in the lavas from the submarine hotspot track, which did not pass through continental crust.

The high-Ti samples show uniform patterns on incompatible multi-element diagrams with moderate depletions of U, Nb, Ta and Pb compared to the neighboring elements of similar incompatibility (Figure 2-5a). The high-Ti samples also have high ratios of large ion lithophile elements (LILE) and light rare earth element (LREE) versus high field strength elements (HFSE) (e.g. high Ba/Nb, K/Nb, La/Nb) and high Ba/Th and Ba/La, as is typical for incompatible-element patterns of EM I-type lavas (Willbold and Stracke, 2006), such as those from the Gough track. Moreover, the multi-element patterns of the high-Ti group samples are nearly identical to and plot within the relatively narrow range of the Gough Track lavas. Like the Gough-Track lavas, the high-Ti group samples possess enrichment of the more incompatible over less incompatible elements but display steeper HREE patterns. Compared to the high-Ti rocks, the low-Ti rocks show less depletion of the HFSE Nb and Ta and relative enrichment of Pb (Figure 2-5b). In addition, the low-Ti lavas are characterized by

relatively flat heavy rare earth element patterns, similar to enriched mid-ocean-ridge basalt (E-MORB) (Figure 2-5). These low-Ti group samples, considered to be strongly contaminated by continental crust (see section 2.6.1), have generally higher concentrations of all incompatible elements and more pronounced negative Nb and Ta and positive Pb anomalies (Figure 2-5c).

2.5.2. Isotopes

The high-Ti group rocks display relatively unradiogenic initial Sr, Nd Hf and $^{206}Pb/^{204}Pb$ isotope ratios and plot consistently within the Gough compositional field of the marine hotspot track in all isotope systems (Figure 2-6, Figure 2-7, Figure 2-8). The low-Ti samples reveal more complex chemistry: Those low-Ti samples, considered to be less affected by crustal contamination, have more radiogenic initial $^{143}Nd/^{144}Nd$, $^{176}Hf/^{177}Hf$, and $^{207}Pb/^{204}Pb$ ratios (15.55-15.68) but less radiogenic $^{208}Pb/^{204}Pb$ ratios at a given $^{206}Pb/^{204}Pb$ (Figure 2-6, Figure 2-7, Figure 2-8) than the high-Ti group samples. The composition of our low-Ti samples largely overlaps with the isotope ratios for the Horingbaai dikes (and the Doros intrusion). Low-Ti lavas that show evidence for crustal contamination, however, yield variable to very radiogenic $^{87}Sr/^{86}Sr$, radiogenic $^{206}Pb/^{204}Pb$, $^{207}Pb/^{204}Pb$ and $^{208}Pb/^{204}Pb$, and unradiogenic $^{143}Nd/^{144}Nd$ and $^{176}Hf/^{177}Hf$ ratios.

2.6. Discussion

2.6.1. Crustal Contamination

In contrast to magmas that traverse young (<200 Ma), depleted, mafic oceanic crust or have enriched incompatible-element compositions, magmas passing through old (Proterozoic), thick, felsic and incompatible-element-enriched continental lithosphere, especially those with relatively depleted initial compositions, are highly sensitive to crustal contamination during their ascent. The lithospheric mantle beneath continents is in many cases additionally enriched, due to the past passage of melts and fluids through it. In general, continental crust is highly enriched in Th and Pb relative to Nb and Ta. The respective enrichment/depletion of these elements in some of our samples indicate variable contamination by local crustal lithologies. On the Nb/Yb vs. Th/Yb discrimination diagram (Figure 2-4) after Pearce (2008), only a few of our samples plot within the MORB-OIB array. Most samples plot well above the array, near the average

composition of the Nosib and Swakop metasedimentary groups (McDermott and Hawkesworth, 1990), a major constituent of the (upper crustal) orogenic Damara and Kaoko belts, underlying most of the Etendeka igneous units (Miller, 2008). Although they vary widely in composition, most Damara granites have less radiogenic Pb (average $^{206}Pb/^{204}Pb = 18.03$, $^{207}Pb/^{204}Pb = 15.63$ and $^{208}Pb/^{204}Pb = 37.84$, age-corrected to 132Ma; Jung et al., 2015; Paul et al., 2014; Stammeier et al., 2015) than our contaminated samples. Therefore, we use the average composition of Nosib and Swakop group metasedimentary rocks to evaluate (and quantify) potential crustal contamination.

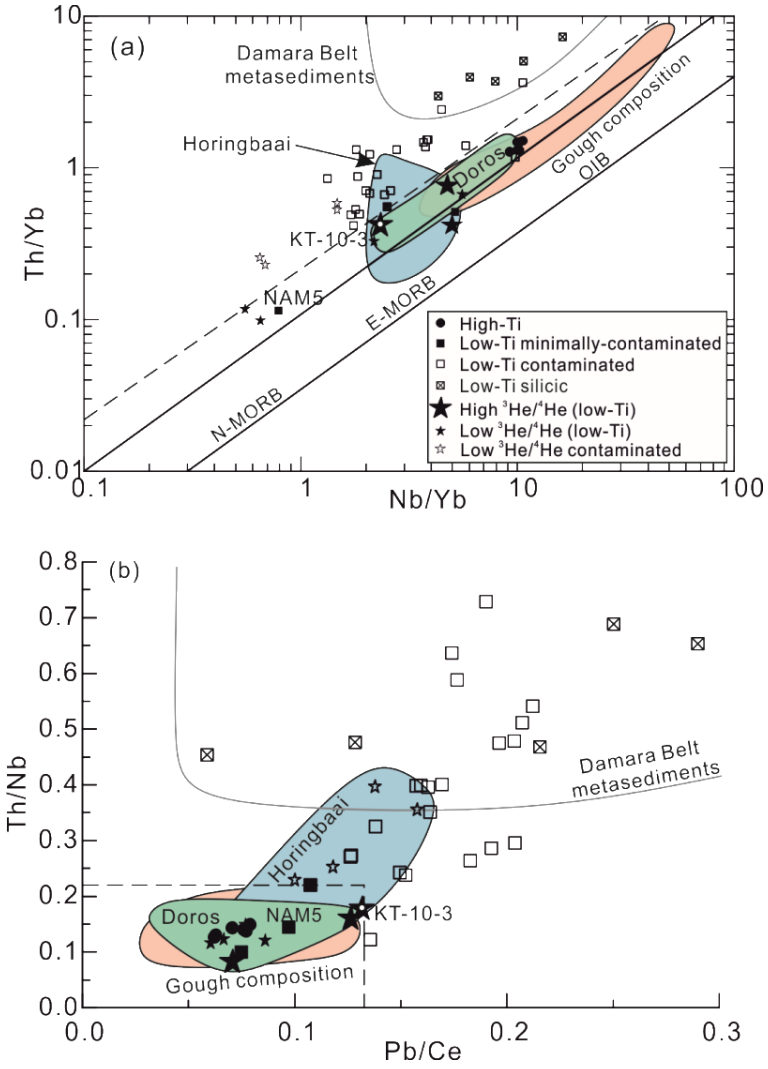

Figure 2-4: (a) Nb/Yb vs Th/Yb (Pearce, 2008). The "mantle" array comprises data from normal mid ocean ridge basalts (N-MORB), enriched MORB (E-MORB) and oceanic island basalts (OIB). Melts formed in subduction zones and those that have been contaminated by continental crust generally have higher Th/Yb contents at a given Nb/Yb and plot above the mantle array. (b) Pb/Ce vs Th/Nb. The dashed line shows the highest Th/Nb ratio for Gough-type samples.

Samples with Th/Nb < 0.22 and Pb/Ce <0.13 are considered to reflect only minimal continental crustal contamination, because Gough-type samples, erupted on oceanic crust, extend to these values. Samples with higher values are likely to have experienced some continental crustal contamination (see section 2.6.1). Gough compositional field comprises samples from the present Gough Island, Gough seamount subtrack, as well as the Walvis Ridge (Rohde et al., 2013a; Hoernle et al., 2015; Homrighausen et al., 2019). The Nosib and Swakop metasedimentary groups and their average composition (McDermott and Hawkesworth, 1990) are shown to assess upper crustal contamination. Doros (Owen-Smith et al., 2017; Stroncik et al., 2017) and Horingbaai (Thompson et al., 2001) composition are also shown.

Ratios of elements with similar partition coefficients to Nb, Ta and Pb, for example, (Th, La)/(Nb,Ta) and (Pb, Nd)/Ce, which are distinct between intraplate volcanism and continental crust, can also be used to evaluate the extent of crustal contamination. Lavas that have ratios of these elements within the range of Gough-type lavas from the submarine hotspot track (Th/Nb<0.22 and Pb/Ce≤0.13; Figure 2-4) are considered to be not or only minimally affected by crustal contamination and are shown with filled symbols in all diagrams. Consistent with this interpretation, contaminated lavas show isotopic ratios (e.g. high $^{87}Sr/^{86}Sr$ and $^{207}Pb/^{204}Pb$) that trend toward local upper crustal lithologies, like the Nosib and Swakop group metasedimentary rocks (Figure 2-6, Figure 2-7, Figure 2-8). Simple (bulk) mixing model calculations indicate that the isotopic composition of contaminated lavas can be explained by the addition of ~10% of these metasedimentary rocks to an initial Gough or Doros-type magma composition, respectively (Figure 2-6, Figure 2-7, Figure 2-8). Other studies have also identified upper crustal lithologies as apparent contaminants for Etendeka lavas. For example, a positive correlation of Pb/Ce and $^{206}Pb/^{204}Pb$ in Tafelberg and Horingbaai basalts was interpreted to indicate their contamination by the upper crust rather than lower crust or SCLM, which possess relatively low $^{206}Pb/^{204}Pb$ ratios of < 18 (Thompson et al., 2001; Ewart et al., 2004a). The low-Ti samples, especially the picrites, have very low concentrations of incompatible elements due to dilution of incompatible elements through olivine accumulation, making their Sr, Nd, Pb and Hf isotope ratios especially sensitive to even very small amounts of crustal contamination. Since assimilation of continental crust can drastically change the geochemical composition of mantle-derived magmas, the contaminated low-Ti group samples (with open symbols in all diagrams) are not considered in the discussion of potential mantle source compositions below.

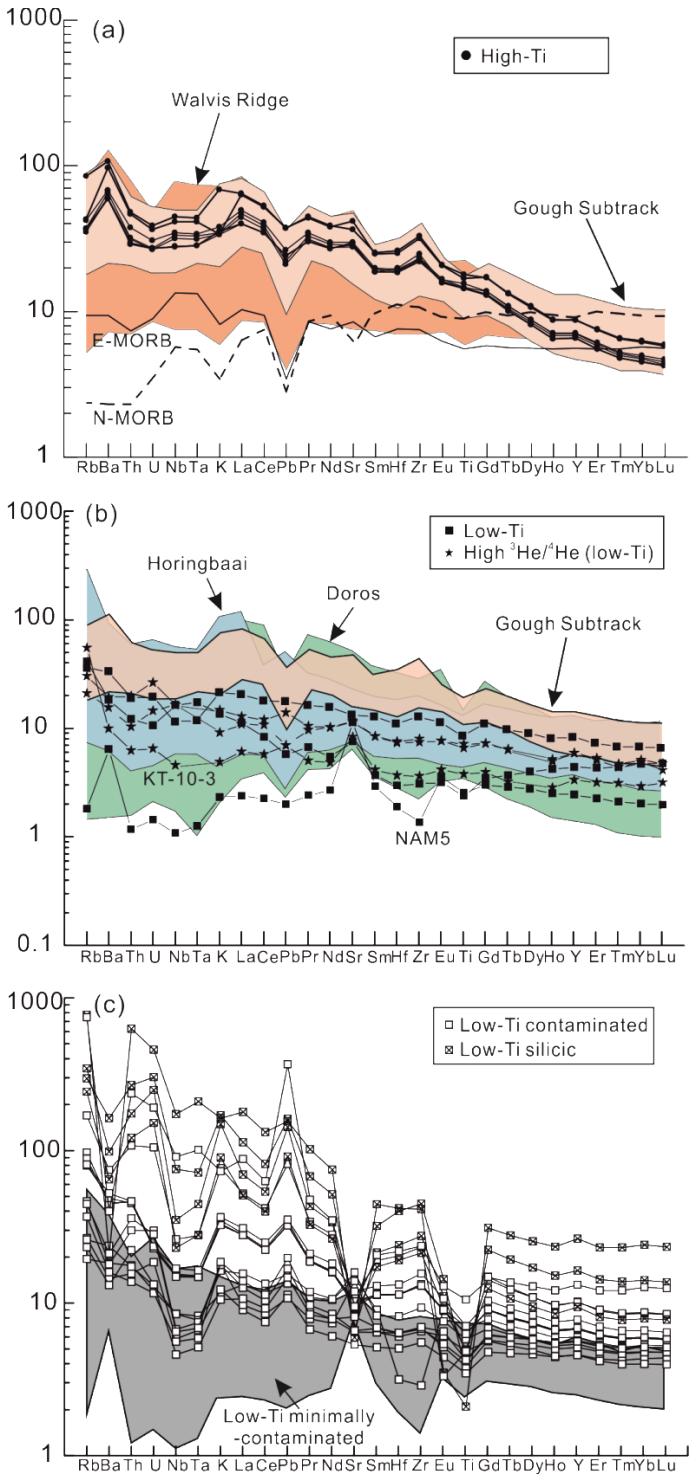

Figure 2-5: Primitive mantle normalized multi-element diagrams for: (a) high-Ti lavas compared to Gough composition from the submarine Walvis Ridge and Gough hotspot subtrack (Rohde et al., 2013a; Hoernle et al., 2015; Homrighausen et al., 2019), N-MORB and E-MORB (Sun and McDonough, 1989); (b) minimally-contaminated low-Ti lavas from this study and low-Ti lavas with high 3He/4He ratio from Stroncik et al. (2017) compared with low-Ti Doros intrusion samples (Owen-Smith et al., 2017) and Horingbaai dikes (Thompson et al., 2001), and (c) comparison of clearly crustally-contaminated with minimally-contaminated low-Ti lavas.

2.6.2. Source composition of the low-Ti basalts

Only three of our low-Ti lavas plot within/near the mantle array in Figure 2-4a and are therefore considered to be minimally contaminated by continental crustal. These samples have N-MORB and E-MORB-type trace element compositions, similar to the Doros and Horingbaai magma-types (Owen-Smith et al., 2017; Thompson et al., 2001; Figure 2-5). A slight effect of continental contamination, however, cannot be ruled out for NAM59 (elevated $^{87}Sr/^{86}Sr$ and low $^{143}Nd/^{144}Nd$), but is considered to be insignificant compared to all other low-Ti samples. In comparison with the Gough composition, the minimally-contaminated low-Ti lavas have slightly higher $^{143}Nd/^{144}Nd$ and lower $^{208}Pb/^{204}Pb$ for a given $^{206}Pb/^{204}Pb$, but similar to higher $^{207}Pb/^{204}Pb$ and $^{206}Pb/^{204}Pb$. The low-Ti lavas in Paraná have similar composition (Peate et al., 1999), but the $^{208}Pb/^{204}Pb$ is not as low as in our Etendeka low-Ti lavas.

Previously, the isotopic composition of the low-Ti Etendeka lavas was explained to represent a mixture of 1) Tristan plume component with MORB mantle and upper crust (Ewart et al., 1998) or 2) depleted mantle peridotite, lower crust and upper crust (Thompson et al., 2001; Thompson et al., 2007). No mixtures of Gough- or Tristan-type plume mantle, however, with depleted upper (MORB-source) mantle and/or local continental crust (e.g. metasediments, felsic granite (Stammeier et al., 2015) and mafic basement (Jung et al., 2015)) can produce the combined uranogenic and thorogenic Pb isotopic systematics of the Horingbaai dikes and low-Ti samples (Figure 2-7). If the Gough endmember mixed with depleted MORB-source mantle, then the $^{207}Pb/^{204}Pb$ isotope ratios of the resulting magma would also have to be lower than the Gough composition - not just the $^{208}Pb/^{204}Pb$ isotope ratios (Hoernle et al., 2015). Mixing of a (hypothetically already present) Tristan plume component with depleted upper mantle ± crust also cannot explain the composition of the minimally contaminated low-Ti samples. Therefore, a different magma source having low $^{87}Sr/^{86}Sr$, intermediate to high $^{143}Nd/^{144}Nd$ and high $^{207}Pb/^{204}Pb$ but low $^{208}Pb/^{204}Pb$ relative to $^{206}Pb^{204}Pb$ is required to explain the composition of the low-Ti lavas and dikes. The high $^{207}Pb/^{204}Pb$ yet low $^{208}Pb/^{204}Pb$ relative to $^{206}Pb^{204}Pb$ precludes the low-Ti basalts from being derived from an upper mantle Atlantic (or Indian) MORB-type source.

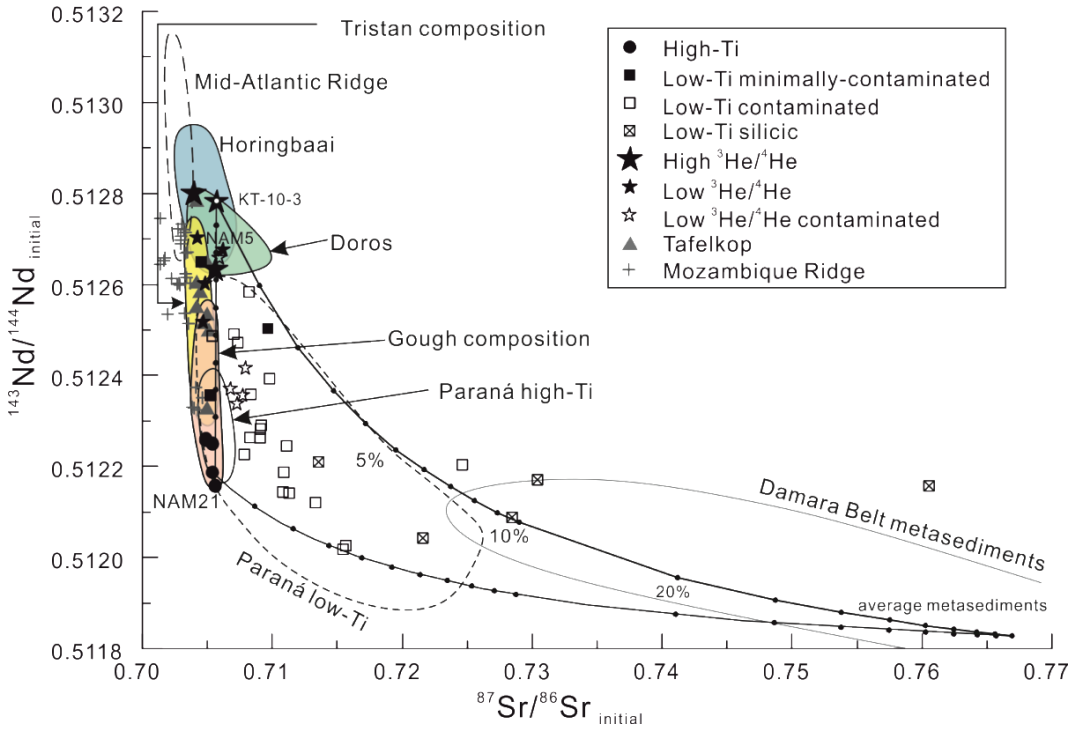

Figure 2-6: Initial (at 132 Ma) Sr and Nd isotopic compositions Etendeka samples from Namibia. The Etendeka and Paraná high-Ti samples plot within the lower part of the Gough field, whereas most of the minimally-contaminated Etendeka low-Ti samples overlap with the Doros and Horingbaai fields or extend toward Damara Belt metasediments. Mixing lines are calculated for mixing endmember compositions represented by 1) enriched high-Ti Gough-type sample NAM21, 2) a depleted low-Ti sample with the highest 3He/4He and the lowest 18O olivine (18O=5.3‰), which lies within the mantle-range (KT-10-3, large black star with white dot at the center; Stroncik et al., 2017), and 3) an upper continental crustal component (average composition of the Nosib and Swakop metasedimentary group samples; McDermott and Hawkesworth, 1990). The extension of the Horingbaai dike field towards more radiogenic Nd isotope compositions could indicate the involvement of a fourth upper mantle (MORB-type) component or that the plume contains depleted material similar to N-MORB. All samples were age-corrected to 132 Ma, the average age of Etendeka volcanism. The parent/daughter ratios of Etendeka samples and the upper crustal component are derived from their trace element data. Gough-type data were first age-corrected to their initial ratios at time of eruption and then extrapolated to 132 Ma by using the following assumed parent/daughter ratios of their source: U/Pb=0.137, Th/Pb=0.6758, Rb/Sr=0.0204, Sm/Nd=0.3378 (Stracke et al., 2003; Willbold and Stracke, 2006). To project the MORB source to 132 Ma, we used the following parent/daughter ratios: U/Pb=0.1667, Th/Pb=0.4444, Rb/Sr=0.0065, Sm/Nd=0.4114 (Workman and Hart, 2005). References: Gough-type EMI (Rohde et al., 2013a; Hoernle et al., 2015; Homrighausen et al., 2019), Doros intrusion (Owen-Smith et al., 2017; Stroncik et al., 2017), Tafelkop lavas with Th/Nb < 0.22 and Pb/Ce <0.13 (Ewart et al., 1998; Gibson et al., 2000), Horingbaai dikes (Thompson et al., 2001), Mozambique Ridge (Jacques et al., 2019), Paraná flood basalt (Peate and Hawkesworth, 1996; Peate et al., 1999; Rocha-Júnior et al., 2013; Turner et al., 1999), Damara belt metasediments (McDermott and Hawkesworth, 1990), and Mid-Atlantic Ridge (compilation of Class and Lehnert (2012).

Such a low-Ti end member is found in the Doros intrusion (130Ma; Owen-Smith et al., 2017) and related Tafelkop lava flows (Ewart et al., 1998; Gibson et al., 2000), which

are believed to originate from the Doros igneous center (Marsh et al., 2001), and the Horingbaai dikes (131-132Ma; Thompson et al., 2001). The isotopic composition of the Horingbaai dikes could be derived through two component mixing of a depleted normal (N)-MORB type component (with $^{206}Pb/^{204}Pb$ ~ 17.7, $^{207}Pb/^{204}Pb$ ~ 15.43, $^{208}Pb/^{204}Pb$ ~ 37.5, $^{143}Nd/^{144}Nd$ ~ 0.5130 and $^{87}Sr/^{86}Sr$ ~ 0.7040 at 132 Ma) and an upper continental crustal (Damara belt meta-sediment) component. Such two-component mixing, however, does not work for a combination of the Doros and Tafelkopf rocks, which require mixing of at least 3 components. Modeling of the parental liquid composition for picritic Horingbaai dikes, however, yielded a potential temperature of 1520-1680°C (Jennings et al., 2019 and references therein), confirming that the Horingbaai magmas were generated within a hot mantle plume from the lower mantle (Thompson et al., 2001).

For Doros/Tafelkop rocks, a predominantly plume derivation was already proposed (Ewart et al., 1998; Gibson et al., 2000; Milner and le Roex, 1996; Owen-Smith et al., 2017). Ewart et al. (2004a) calculated a plume contribution between 25 and 75% for these magmas (although still using the Tristan component, which does not work in all isotope systems and did not exist then, instead of the Gough composition as a mixing endmember). Further support for a lower mantle origin of the low-Ti source comes from high $^{3}He/^{4}He$ isotope ratios reported from low-Ti dikes (Stroncik et al., 2017). The isotopic composition of 11 southern Etendeka low-Ti rocks for which He isotopes were generated are shown in Figure 2-6 to Figure 2-8 as stars. As can be seen on the Pb/Ce vs. Th/Nb diagram (Figure 2-4b), seven of these samples (filled stars) plot within the field that indicates minimal crustal assimilation. Of these seven samples, three (one associated with Brandberg and two associated with the Doros intrusive complex) have $^{3}He/^{4}He$ ratios higher than 12 R_A (normalized to atmospheric helium; filled large stars in Figure 2-6, Figure 2-7, Figure 2-8), indicating a deep, lower-mantle source. These rocks plot consistently within the Doros/Horingbaai compositional fields in all isotope systems. The $\delta^{18}O$ values of olivine phenocrysts from these three high $^{3}He/^{4}He$ samples range from 5.30-5.71‰, overlapping with or extending to slightly higher values than olivines from mantle peridotites (5.0-5.4‰, Eiler et al., 1997), indicating a small amount of assimilation (<5% to raise $\delta^{18}O$ from 5.2 to 5.7‰) of the adjacent Neoproterozoic Damara Supergroup schist (mean $\delta^{18}O$ = 14.75‰, n=12, SD = 0.48;

Jung et al., 2001). The three samples with highest $^{3}He/^{4}He$ plot within the field for Atlantic MORB on the thorogenic Pb isotope diagram but above the MORB field on the uranogenic Pb isotope diagram, and thus clearly are not derived from depleted upper mantle. We conclude that the Doros/Horingbaai end member, as characterized by sample KT-10-3 (Stroncik et al., 2017) with low $^{206}Pb/^{204}Pb$ (~17.74), $^{208}Pb/^{204}Pb$ (~37.50) and $^{87}Sr/^{86}Sr$ (~0.704), high $^{207}Pb/^{204}Pb$ (~15.58), $^{143}Nd/^{144}Nd$ (~0.5127) and $^{3}He/^{4}He$ (~20.3 R_A), and mantle-like $\delta^{18}O$ olivine (5.3‰), stems from the lowermost mantle and was transported to the base of the lithosphere by a mantle plume. Accordingly, we use this endmember for our mixing calculations shown in Figure 2-6, Figure 2-7, Figure 2-8.

The isotopic characteristics of Tafelkop lavas (having transitional composition between low- and high-Ti) and low-Ti lavas in Paraná require both the Gough and Doros end members, as well as various amounts of crustal contamination (Figure 2-7b). Accordingly, all low-Ti samples (including the contaminated samples) lie within triangular mixing fields that are spanned by the Doros end member, the Gough composition and the (local) Damara upper crust.

In summary, the geochemical composition of the (minimally contaminated) low-Ti rocks in southern Etendeka can be best explained by derivation from plume material derived from the lower mantle (high $^{3}He/^{4}He$ and high temperatures) with an isotopic composition similar to the Doros/Horingbaai rocks. Picritic magmas from this relatively incompatible-element depleted source, in part due to dilution as a result of olivine accumulation, experienced various extents of contamination while passing through the continental lithosphere in southern Namibia (Thompson et al., 2007). The isotopic composition of all of our (contaminated) low-Ti samples is variably offset towards crustal compositions hampering identification of their original isotopic composition. Stroncik et al. (2017) also report low-Ti dikes with low $^{3}He/^{4}He$ composition that have $\delta^{18}O$ values of 5.74-6.70‰, showing clear evidence of crustal contamination despite their low Pb/Ce and Th/Nb. Applying a simple mixing model, ~15% of adjacent Neoproterozoic Damara Supergroup schist (Jung et al., 2001) is needed to increase the $\delta^{18}O$ from 5.2‰ to 6.7‰ (Stroncik et al., 2017), consistent with our calculation of crustal contamination based on Sr, Nd and Pb isotope ratios (Figure 2-6, Figure 2-7, Figure 2-8). In conclusion, the composition of the low-Ti samples can

be explained by mixing of a Doros-type end member, possibly with some minor Gough-type end member contribution (source of high-Ti basalts) (Figure 2-8), plus variable amounts of subsequent continental crustal contamination.

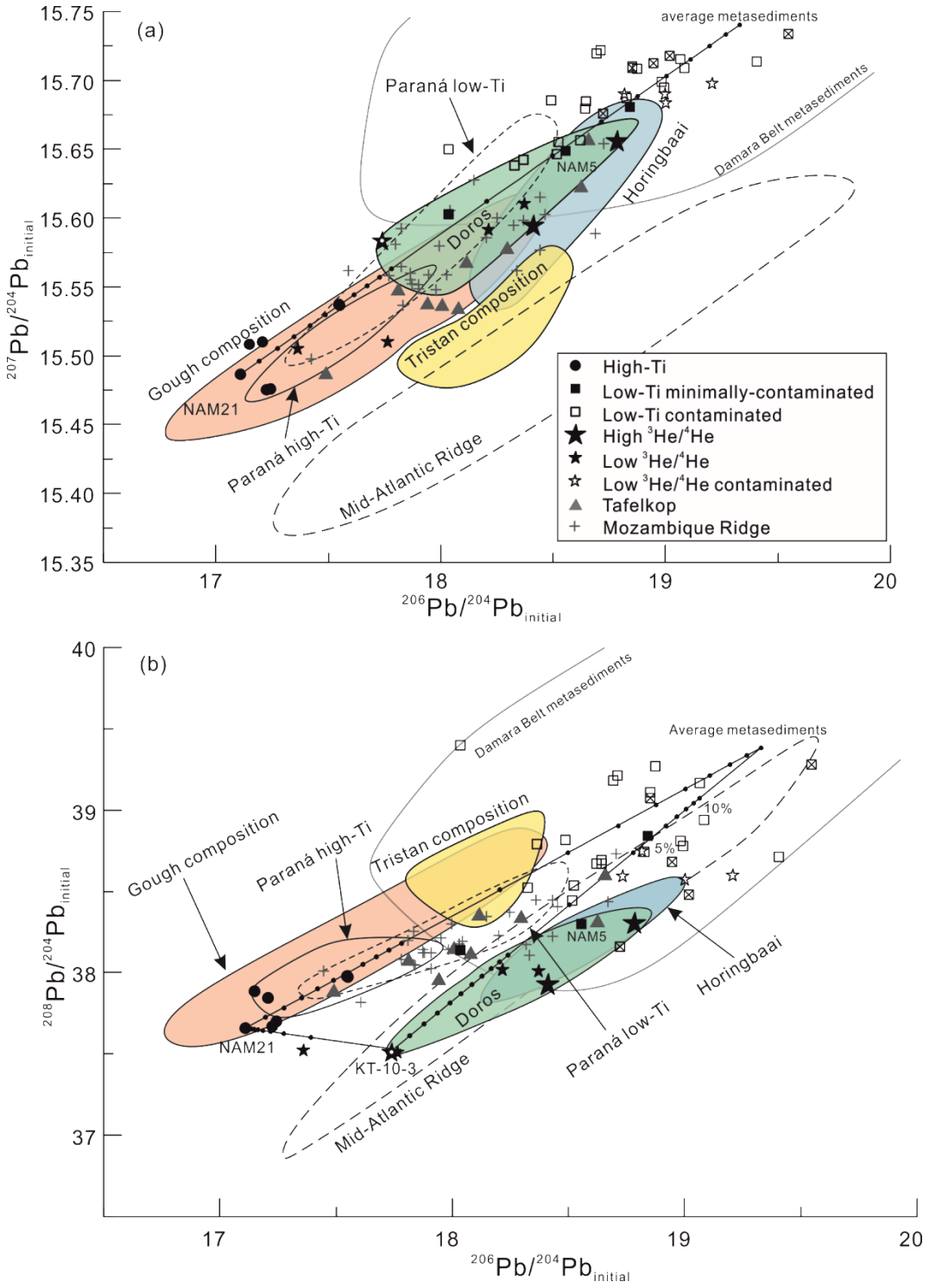

Figure 2-7: Initial (at 132 Ma) (a) 206Pb/204Pb vs 207Pb/204Pb and (b) 206Pb/204Pb vs 208Pb/204Pb for Etendeka lavas. The composition of the contaminated low-Ti samples can be explained by mixing of Doros-type end member (source of low-Ti basalts) with a possible

minor contribution of the Gough-type end member (source of high-Ti basalts) similar to NAM 21 and an upper crustal component at 132 Ma. Data sources and endmember compositions used for calculating mixing lines in (b) are the same as in Figure 2-6.

2.6.3. Source composition of the high-Ti basalts

High-Ti basalts are exclusively found in Northern Etendeka (e.g. Marsh et. al. 2001; this study). Since the high-Ti basalts have high concentrations of incompatible elements, they are less vulnerable to crustal contamination and we see no evidence of significant contamination. Instead the rocks show very similar trace element and isotopic compositions to the Gough-type lavas erupted on oceanic crust (Figure 2-5 - Figure 2-8).

Before it was known that the Tristan composition didn't appear until ~70 Ma ago, resulting in a zoned hotspot track, it was proposed that the high-Ti basalts represent a mixture of a Tristan-type composition, MORB and recycled subducted sediment (Ewart et al., 2004a). The high-Ti lavas, however, display higher $^{207}Pb/^{204}Pb$, yet lower $^{208}Pb/^{204}Pb$ than the Tristan composition, and thus it is not possible to explain the high-Ti magma source composition by mixing of the Tristan component with a depleted MORB-source component and sediments (Figure 2-7). Instead, the high-Ti samples have very restricted trace element compositions (Figure 2-5), overlapping the narrow field for the marine Gough lavas on multi-element and on Sr-Nd-Pb-Hf isotope diagrams (Figure 2-6, Figure 2-7, Figure 2-8). Therefore, we believe that the high-Ti lavas reflect the composition of their mantle plume source having a Gough-type composition. A predominant derivation of the high-Ti Etendeka magmas by the Tristan-Gough plume was already recognized by Ewart et al. (2004a), but these authors still assumed a Tristan-type endmember for their mixing calculations. Our new data confirm Hoernle et al. (2015), who found no evidence for compositional Tristan-type lavas erupted in either the Etendeka or Paraná large igneous provinces.

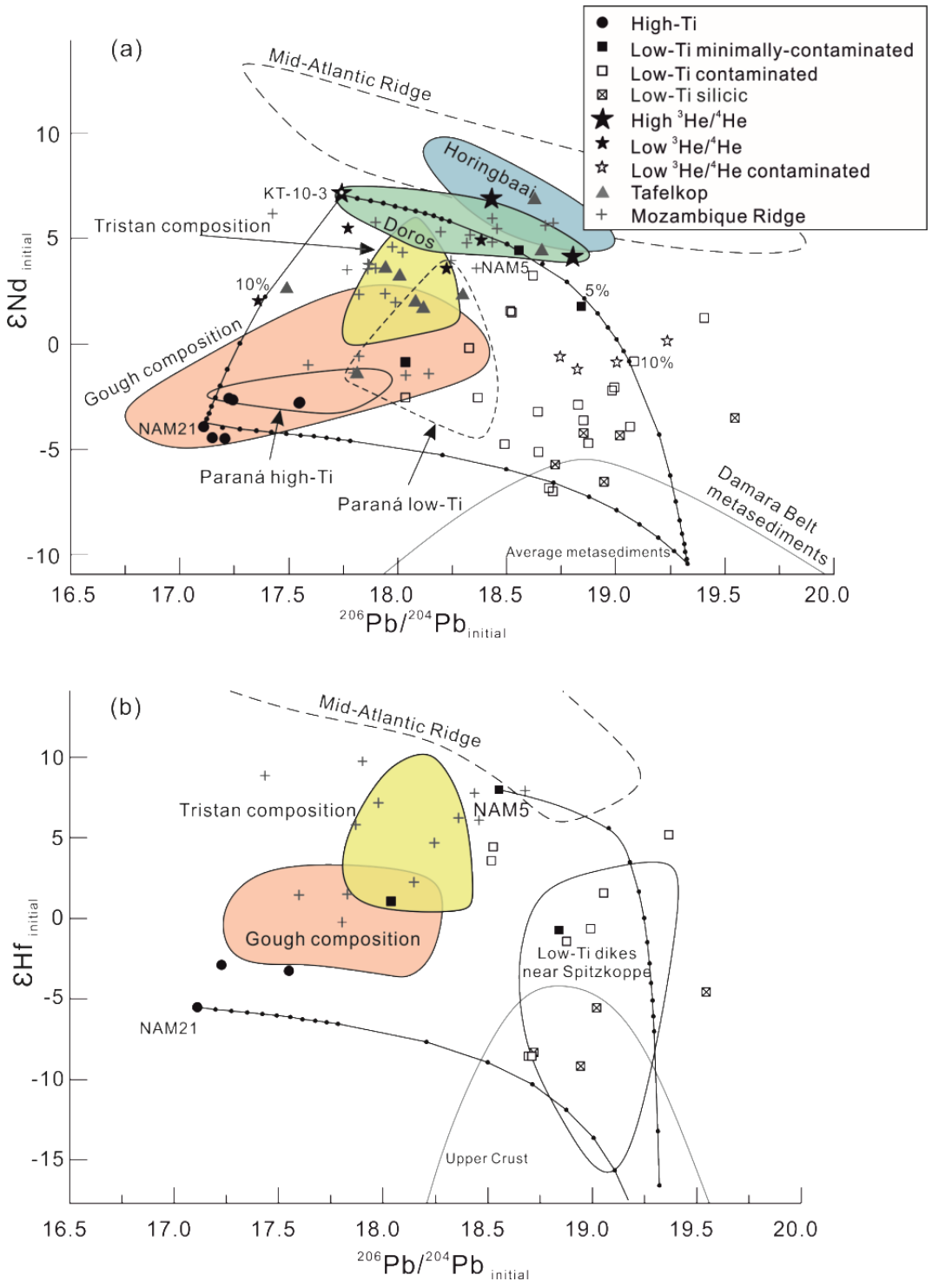

Figure 2-8: Initial (at 132 Ma) (a) 206Pb/204Pb vs εNd and (b) εHf. The composition of the low-Ti rocks can be explained by mixing of 1) an enriched high-Ti Gough-type composition such as sample NAM21, 2) a depleted low-Ti component represented by sample KT-10-3 (from Stroncik et al., 2017) with high 3He/4He and the lowest 18O olivine (5.3‰), which lies within the mantle-range , and 3) an upper continental crustal component (average composition of the Nosib and Swakop metasedimentary group samples at 132 Ma; McDermott and Hawkesworth, 1990). The extension of the Horingbaai dike field towards more radiogenic Nd isotope compositions could indicate the involvement of a fourth upper mantle (MORB-type)

component or that the plume contains depleted material similar to N-MORB. Data sources and endmember compositions used for mixing calculations are the same as in Figure 2-6. The mixing lines for 206Pb/204Pb vs εHf relationships were calculated with Gough-type end member (NAM21), Doros-type composition (NAM5) and the Damara metamorphic rocks at 132 Ma.

Compared to the trace element pattern of the marine part of the hotspot track, the high-Ti lavas show slightly steeper primitive-mantle normalized HREE patterns (Figure 2-5a), indicative of a greater role of residual garnet in the magma source (which fractionates the HREE) and thus deep melting starting at ≥70-80 km. This is consistent with melting of plume material beneath thick continental lithosphere in contrast to the Walvis Ridge, which formed through plume-ridge interaction, and the Guyot province magmas that formed beneath young and comparably much thinner oceanic lithosphere. Plume melting beneath Walvis and the Guyot province could thus continue to much shallower depths with increasing dilution of the garnet signal by mixing with melts that formed at the upper end of the melting column (spinel stability zone). Finally, the nearly flat HREE patterns of the low-Ti, compared to steep slope of the high-Ti, basalts points to shallower melting (under thinner NeoProterozoic Damara Belt lithosphere compared to Paleoproterozoic lithosphere beneath NW Namibia) to form the low-Ti basalts.

In summary, we propose that the high-Ti basalts in Northern Etendeka were derived from the same (Gough) plume component as found in the Walvis Ridge and Gough subtrack lavas. The absence of any evidence for a Tristan composition implies that this component was not present in the early plume (head) stage. The Gough component has also been shown to be the dominant component of the northern Discovery hotspot track (Schwindrofska et al., 2016) and the Shona hotspot (Hoernle et al., 2016) in the South Atlantic. At both of these hotspots, the Gough-type composition is associated with high $^{3}He/^{4}He$ at the southern Mid-Atlantic Ridge segments that interact with these hotspots, pointing to a lower mantle origin of this source material (Sarda et al., 2000).

2.6.4. A possible model for the Etendeka flood basalt lavas

As shown above, our study confirms that the Gough-type EMI component of the Tristan-Gough hotspot track was already present in the initial Etendeka plume head stage, sampled by the high-Ti lavas of northern Namibia. The high-Ti lavas with Gough-like incompatible element and isotopic composition are located exclusively in northern Etendeka (NW Namibia) adjacent to the intersection with the offshore hotspot

track (Walvis Ridge). Additional high-Ti lava compositions occur at the Bero volcanic complex (SW Angola) (Marsh and Swart, 2016) and in the Urubici magma type (Paraná, South America) (Peate et al., 1999), which were spatially connected before the break-up of Gondwana. Thus, the Gough component appears to have been widespread in the plume head and apparently dominated the entire northern portion of the plume head (Figure 2-9a).

In contrast, the low-Ti lavas are primarily located in southern Etendeka (western central Namibia) and were derived from a different (Doros-type) source. This component was primarily present in the southern part of the early plume (head) stage and is not found in the marine (plume tail) part of the hotspot. In addition, effusive Doros-type lavas (Tafelkop type) have only been found at the base of the (southern) Etendeka lava succession so far (Gibson et al., 2000; Miller, 2008), although they seem to have once covered a far greater area than their present extension (Owen-Smith et al., 2017). It is not clear why the low-Ti (Doros) source material was only present in the initial plume-head stage and not thereafter but three options are possible: 1) This component may have been completely exhausted in the plume source during formation of the Etendeka flood basalts; 2) the base of the plume stem (in the lower mantle) may have migrated to a different location where different material was entrained (Hoernle et al., 2015); or 3) only plume heads may be able to carry dense deep mantle material (carrying the Doros signal?) to the surface whereas the plume tail does not (Jones et al., 2019). In any case, we note that plume zonation can vary with time as is evident by the sudden appearance of the Tristan plume component on the northern side of the plume and hotspot track at ~70 Ma. Since entrainment of ambient mantle material into a plume head is improbable based on fluid dynamic considerations (Lohmann et al., 2009), it is unlikely that the plume head entrained this material during ascent through the lower or mid mantle. Instead, the low-Ti source material might represent another (intrinsic) lithology of the African LLSVP. An isotopically similar composition was recently found in the submarine Mozambique Ridge lavas (Figure 2-7, Figure 2-8), a north-south trending oceanic plateau located south of Africa up to 2500 km away from southern Etendeka (Jacques et al., 2019). However, the Mozambique Ridge was emplaced at the same time (ca. 135-125 Ma) (Jacques, 2019 and references therein) and is believed to

have also formed by a deep mantle plume rooted at the (southern) edge of the African LLSVP (Jacques et al., 2019).

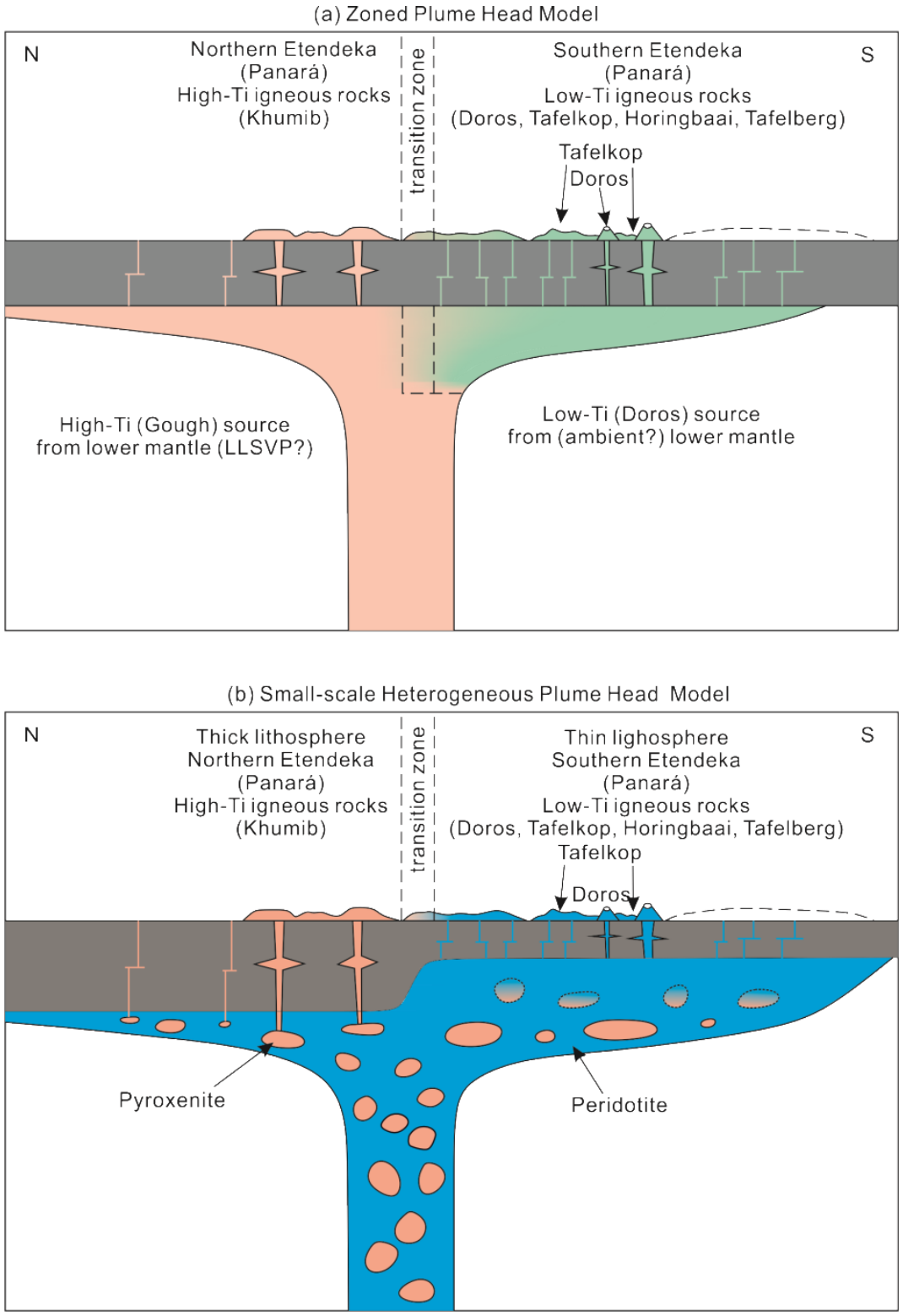

Figure 2-9: Schematic models of Etendeka volcanism at ~132 Ma illustrating the proposed origin of the high-Ti northern Etendeka lavas from Gough-type plume material and the low-Ti

southern Etendeka lavas, dikes and intrusives from a Doros/Horingbaai type plume material. (a) Zoned plume head model: The plume head contains two distinct compositional domains. A high-Ti (Gough-type) domain beneath northern Etendeka and a low-Ti (Doros-type) domain beneath southern Etendeka. The plume stem, which subsequently formed the Walvis Ridge (submarine hotspot track), only contains Gough-type material. (b) Small-scale heterogeneous plume head model: Beneath thick lithosphere, a fertile (Gough-type) component, for example, pyroxenite, melts at greater depth to form high-Ti magmas. Beneath thin lighosphere, a less-fertile lithology (Doros-type), for example peridotite, melts at shallower depth and dilutes the early stage fertile melts. Dashed line in the southernmost part of southern Etendeka indicates inferred distribution of low-Ti lava flows before erosion. At present, only dikes outcrop in this area. Minor low-Ti lava flows also extend into northern Etendeka but are not shown here for clarity.

Considering hotspot volcanism around the southern tip of Africa and along the southern margin of the African LLSVP, four distinct enriched mantle components have been identified thus far. These components are all characterized by low $^{206}Pb/^{204}Pb$, but are variably enriched in $^{207}Pb/^{204}Pb$ and/or $^{208}Pb/^{204}Pb$ ratios, as well as more radiogenic Sr and less radiogenic Nd and Hf isotope ratios than MORB. They include: 1) the Gough (high-Ti) component, the dominant component in the northern Etendeka and Paraná LIPs, and in the Tristan-Gough, northern Discovery and Shona hotspot tracks, 2) the Tristan component, that is only found along the northern subtrack of Tristan-Gough hotspot trail since ~70 Ma, 3) the southern Discovery component (identified in lavas of the zoned Discovery hotspot track located south of the Tristan-Gough hotspot track, Schwindrofska et al., 2016), and 4) the Doros/Horingbaai or Mozambique (low-Ti) component found in southern Etendeka and the Mozambique Ridge. High $^{3}He/^{4}He$ ratios were reported from lavas from the Gough (northern Discovery and Shona; Sarda et al., 2000) and the Doros (Stroncik et al., 2017) components, pointing to a lower mantle origin for at least these two components. Considering the common geochemical characteristics of these four spatially and temporally related enriched components, they could very well represent different derivatives of a once genetically related source (for example, ancient subducted lithospheric material with different ages or parent/daughter fractionation at different times subsequent to their formation/subduction; Geldmacher et al., 2008).

From a global perspective, geochemically enriched (e.g. high-Ti) and relatively depleted (e.g. low-Ti) source components have been described in several oceanic LIPs, such as the Karoo LIP (Cox et al., 1965), the Manihiki Plateau (Golowin et al., 2018; Golowin et al., 2017), the Caribbean LIP (Dürkefälden et al., 2019a; Dürkefälden et al.,

2019b) and the Shatsky Rise (Sano et al., 2012). Although different sources may be sampled at different times in the evolution of a LIP, as is the case with the Ontong Java Plateau and the Caribbean LIPs, the enriched (high-Ti) and depleted (low-Ti) lavas appear to have been at least in part erupted contemporaneously during the Etendeka, Manihiki and Shatsky LIP events.

When erupted contemporaneously, spatial compositional differences could reflect either 1) spatially separated source material (zonation) in the plume head (Figure 2-9a), or 2) heterogeneity on a relatively small scale in the plume head and differences in the melting properties of the different components/lithologies (Figure 2-9b). In a heterogeneous upwelling column of mantle containing different lithologies, fertile components (e.g. garnet pyroxenite) will begin melting first, controlling the melt composition formed at greater depths (Dasgupta et al., 2007). Thus, on thick lithosphere (e.g. Paleo-Proterozoic lithosphere beneath northern Etendeka), erupted melts will have primarily enriched high-Ti Gough-type composition, whereas beneath thinner lithosphere (e.g. Damara mobile belt, which probably represented a region of thinned and weakened lithosphere; Ritter et al., 2003), less-fertile lithologies (e.g. Doros/Horingbaai garnet peridotitic matrix) will mainly melt at shallow depth, thereby diluting the early melts from fertile Gough-type material. The lower HREE fractionation (less steep HREE patterns on a multi-element diagram) of the Doros/Horingbaai magmas, compared to the high-Ti Gough magmas (Figure 2-5), is consistent with higher degrees of melting at shallower depth to form the low-Ti melts. It is, however, difficult to reconstruct the thickness of the lithosphere at the time of the Etendeka event, because it is difficult to assess the effects of thermal erosion of the lithospheric mantle by the Tristan-Gough plume head. We note that, consistent with this model, the Mozambique Ridge formed on or directly adjacent to the southwest Indian spreading center and thus melting was able to continue to very shallow depths, certainly shallower than anywhere in the Etendeka volcanic province. Nevertheless, if the plume head had been heterogeneous on a small scale and Gough melts dominated beneath thick lithosphere and Doros/Horingbaai melts beneath thinner lithosphere, why have only high-Ti Gough-like and no low-Ti Doros-like lavas been found on the Walvis Ridge thus far, since the Walvis Ridge also formed by plume-ridge interaction and thus under similarly thin lithosphere as the Mozambique Ridge? This can be explained more

easily, if the plume head was spatially zoned and tapped two distinct source reservoirs at the time of Etendeka/Paraná volcanism (Figure 2-9a).

2.7. Conclusions

The high-Ti samples, which only occur in Northern Etendeka, display enriched incompatible-element and isotopic compositions, similar to the Gough composition of the marine Tristan-Gough hotspot track. The low-Ti samples, primarily found in southern Etendeka, have lower abundances of incompatible elements and were thus more easily contaminated during passage through enriched felsic continental crust. Minimally contaminated low-Ti samples have an isotopic composition which cannot be explained by mixing of a Gough component with depleted MORB source asthenosphere or SCLM composition. They therefore point to the presence of an additional plume component in the early plume head stage.

We propose that the high-Ti lavas in Northern Etendeka, which formed directly adjacent to the Walvis Ridge and have a similar Gough-type composition, and the lavas of the adjacent Angola and Paraná regions were derived from the northern portion of the starting plume head. The low-Ti lava source represents a composition not found thus far in the marine hotspot track. The recognition of high $^{3}He/^{4}He$ in some low-Ti dikes (Stroncik et al., 2017) indicates that this component was also derived from the lower mantle and primarily constituted the southern portion of the plume head. This is the first time that clear spatial geochemical zonation has been found in a continuous flood basalt sequence, suggesting a zoned plume head.

References:

Bellieni, G., Comin-Chiaramonti, P., Marques, L., Melfi, A., Piccirillo, E., Nardy, A., Roisenberg, A., 1984. High-and low-TiO2 flood basalts from the Paraná plateau (Brazil): petrology and geochemical aspects bearing on their mantle origin. Neues Jahrbuch für Mineralogie Abhandlungen 150, 273-306.

Blichert-Toft, J., Chauvel, C., Albarède, F., 1997. Separation of Hf and Lu for high-precision isotope analysis of rock samples by magnetic sector-multiple collector ICP-MS. Contributions to Mineralogy and Petrology 127, 248-260.

Class, C., Lehnert, K., 2012. PetDB Expert MORB (Mid-Ocean Ridge Basalt) Compila-tion, Version1.0. Interdisciplinary Earth Data Alliance (IEDA). https://doi .org /10 .1594 /IEDA /100060.

Cox, K.G., Johnson, R., Stillman, C., Vail, J., Wood, D., 1965. The geology of the Nuanesti Igneous Province. Philosophical Transactions of the Royal Society of London. Series A, Mathematical and Physical Sciences 257, 71-218.

Dasgupta, R., Hirschmann, M.M., Smith, N.D., 2007. Partial melting experiments of peridotite+ CO2 at 3 GPa and genesis of alkalic ocean island basalts. Journal of Petrology 48, 2093-2124.

Dürkefälden, A., Hoernle, K., Hauff, F., Wartho, J.-A., van den Bogaard, P., Werner, R., 2019a. Age and geochemistry of the Beata Ridge: Primary formation during the main phase (~ 89 Ma) of the Caribbean Large Igneous Province. Lithos 328, 69-87.

Dürkefälden, A., Hoernle, K., Hauff, F., Werner, R., Garbe-Schönberg, D., 2019b. Second-stage Caribbean Large igneous Province volcanism: The depleted Icing on the enriched Cake. Chemical Geology.

Eiler, J.M., Farley, K.A., Valley, J.W., Hauri, E., Craig, H., Hart, S.R., Stolper, E.M., 1997. Oxygen isotope variations in ocean island basalt phenocrysts. Geochimica et Cosmochimica Acta 61, 2281-2293.

Erlank, A., Marsh, J., Duncan, A., Miller, R.M., Hawkesworth, C., Betton, P., Rex, D., 1984. Geochemistry and petrogenesis of the Etendeka volcanic rocks from SWA/Namibia. Special Publication of Geological Society of South Africa 13, 195-245.

Ewart, A., Marsh, J.S., Milner, S.C., Duncan, A.R., Kamber, B.S., Armstrong, R.A., 2004a. Petrology and geochemistry of early cretaceous bimodal continental flood volcanism of the NW Etendeka, Namibia. Part 1: Introduction, mafic lavas and re-evaluation of mantle source components. Journal of Petrology 45, 59-105.

Ewart, A., Marsh, J.S., Milner, S.C., Duncan, A.R., Kamber, B.S., Armstrong, R.A., 2004b. Petrology and geochemistry of early cretaceous bimodal continental flood volcanism of the NW Etendeka, Namibia. Part 2: Characteristics and petrogenesis of the high-Ti latite and high-Ti and low-Ti voluminous quartz latite eruptives. Journal of Petrology 45, 107-138.

Ewart, A., Milner, S., Armstrong, R., Duncan, A., 1998. Etendeka volcanism of the Goboboseb Mountains and Messum Igneous Complex, Namibia. Part II: Voluminous quartz latite volcanism of the Awahab magma system. Journal of Petrology 39, 227-253.

Garbe-Schönberg, C.D., 1993. Simultaneous determination of thirty-seven trace elements in twenty-eight international rock standards by ICP-MS. Geostandards and Geoanalytical Research 17, 81-97.

Geldmacher, J., Hoernle, K., Kluegel, A., van den Bogaard, P., Bindeman, I., 2008. Geochemistry of a new enriched mantle type locality in the northern hemisphere: Implications for the origin of the EM-I source. Earth and Planetary Science Letters 265, 167-182.

Gibson, S., Thompson, R., Dickin, A., 2000. Ferropicrites: geochemical evidence for Fe-rich streaks in upwelling mantle plumes. Earth and Planetary Science Letters 174, 355-374.

Golowin, R., Portnyagin, M., Hoernle, K., Sobolev, A., Kuzmin, D., Werner, R., 2017. The role and conditions of second-stage mantle melting in the generation of low-Ti tholeiites and boninites: the case of the Manihiki Plateau and the Troodos ophiolite. Contributions to Mineralogy and Petrology 172, 104.

Golowin, R., Portnyagin, M., Hoernle, K., Hauff, F., Werner, R., Garbe-Schönberg, D., 2018. Geochemistry of deep Manihiki Plateau crust: Implications for compositional diversity of large igneous provinces in the Western Pacific and their genetic link. Chemical Geology 493, 553-566.

Govindaraju, K., 1994. compilation of working values and sample description for 383 geostandards. Geostandards and Geoanalytical Research 18, 1-158.

Hoernle, K., Abt, D.L., Fischer, K.M., Nichols, H., Hauff, F., Abers, G.A., Van Den Bogaard, P., Heydolph, K., Alvarado, G., Protti, M., 2008. Arc-parallel flow in the mantle wedge beneath Costa Rica and Nicaragua. Nature 451, 1094.

Hoernle, K., Hauff, F., Kokfelt, T.F., Haase, K., Garbe-Schönberg, D., Werner, R., 2011. On- and off-axis chemical heterogeneities along the South Atlantic Mid-Ocean-Ridge (5–11°S): Shallow or deep recycling of ocean crust and/or intraplate volcanism? Earth and Planetary Science Letters 306, 86-97.

Hoernle, K., Rohde, J., Hauff, F., Garbe-Schonberg, D., Homrighausen, S., Werner, R., Morgan, J.P., 2015. How and when plume zonation appeared during the 132 Myr evolution of the Tristan Hotspot. Nature communications 6, 7799.

Hoernle, K., Schwindrofska, A., Werner, R., van den Bogaard, P., Hauff, F., Uenzelmann-Neben, G., Garbe-Schönberg, D., 2016. Tectonic dissection and displacement of parts of Shona hotspot volcano 3500 km along the Agulhas-Falkland Fracture Zone. Geology 44, 263-266.

Homrighausen, S., Hoernle, K., Geldmacher, J., Wartho, J.-A., Hauff, F., Portnyagin, M., Werner, R., van den Bogaard, P., Garbe-Schönberg, D., 2018. Unexpected HIMU-type late-stage volcanism on the Walvis Ridge. Earth and Planetary Science Letters 492, 251-263.

Homrighausen, S., Hoernle, K., Hauff, F., Wartho, J.-A., van den Bogaard, P., Garbe-Schönberg, D., 2019. New age and geochemical data from the Walvis Ridge: The temporal and spatial diversity of South Atlantic intraplate volcanism and its possible origin. Geochimica et Cosmochimica Acta 245, 16-34.

Jacques, G., Hauff, F., Hoernle, K., Werner, R., Uenzelmann-Neben, G., Garbe-Schönberg, D., Fischer, M., 2019. Nature and origin of the Mozambique Ridge, SW Indian Ocean. Chemical Geology 507, 9-22.

Jennings, E.S., Gibson, S.A., Maclennan, J., 2019. Hot primary melts and mantle source for the Paraná-Etendeka flood basalt province: New constraints from Al-in-olivine thermometry. Chemical Geology 529, 119287.

Jones, T., Davies, D., Sossi, P., 2019. Tungsten isotopes in mantle plumes: Heads it's positive, tails it's negative. Earth and Planetary Science Letters 506, 255-267.

Jung, S., Kröner, A., Hauff, F., Masberg, P., 2015. Petrogenesis of synorogenic diorite–granodiorite–granite complexes in the Damara Belt, Namibia: Constraints from

U–Pb zircon ages and Sr–Nd–Pb isotopes. Journal of African Earth Sciences 101, 253-265.

Jung, S., Mezger, K., Hoernes, S., 2001. Trace element and isotopic (Sr, Nd, Pb, O) arguments for a mid-crustal origin of Pan-African garnet-bearing S-type granites from the Damara orogen (Namibia). Precambrian Research 110, 325-355.

Keiding, J.K., Frei, O., Renno, A.D., Veksler, I.V., Trumbull, R.B., 2013. Conditions of magma crystallization in the Henties Bay-Outjo dyke swarm, Namibia: Implications for the feeder system of continental flood basalts. Lithos 179, 16-27.

Le Maitre, R., Bateman, P., Dudek, A., Keller, J., Lameyre, J., Le Bas, M., Sabine, P., Schmid, R., Sorensen, H., Streckeisen, A., 1989. A classification of igneous rocks and glossary of terms. Recommendations of the IUGS Subcommission on the Systematics of Igneous rocks. London: Blackwell Scientific Publications.

Lohmann, F.C., Hort, M., Phipps Morgan, J., 2009. Flood basalts and ocean island basalts: A deep source or shallow entrainment? Earth and Planetary Science Letters 284, 553-563.

MacDonald, G.A., Katsura, T., 1964. Chemical composition of Hawaiian lavas. Journal of petrology 5, 82-133.

Marsh, J., Ewart, A., Milner, S., Duncan, A., Miller, R.M., 2001. The Etendeka Igneous Province: magma types and their stratigraphic distribution with implications for the evolution of the Paraná-Etendeka flood basalt province. Bulletin of Volcanology 62, 464-486.

Marsh, J.S., Swart, R., 2016. The Bero Volcanic Complex: Extension of the Paraná-Etendeka Igneous Province into SW Angola. Journal of Volcanology and Geothermal Research.

McDermott, F., Hawkesworth, C., 1990. Intracrustal recycling and upper-crustal evolution: a case study from the Pan-African Damara mobile belt, central Namibia. Chemical Geology 83, 263-280.

Miller, R.M., 2008. The geology of Namibia. Ministry of Mines and Energy, Geological Survey.

Milner, S., Duncan, A., Whittingham, A., Ewart, A., 1995. Trans-Atlantic correlation of eruptive sequences and individual silicic volcanic units within the Parana-Etendeka igneous province. Journal of Volcanology and Geothermal Research 69, 137-157.

Milner, S.C., le Roex, A.P., 1996. Isotope characteristics of the Okenyenya igneous complex, northwestern Namibia: constraints on the composition of the early Tristan plume and the origin of the EM 1 mantle component. Earth and Planetary Science Letters 141, 277-291.

O'Connor, J.M., Jokat, W., 2015. Age distribution of Ocean Drill sites across the Central Walvis Ridge indicates plate boundary control of plume volcanism in the South Atlantic. Earth and Planetary Science Letters 424, 179-190.

Owen-Smith, T., Ashwal, L., Sudo, M., Trumbull, R., 2017. Age and petrogenesis of the Doros Complex, Namibia, and implications for early plume-derived melts in the Paraná–Etendeka LIP. Journal of Petrology 58, 423-442.

Paul, A., Jung, S., Romer, R., Stracke, A., Hauff, F., 2014. Petrogenesis of synorogenic high-temperature leucogranites (Damara orogen, Namibia): Constraints from U–Pb monazite ages and Nd, Sr and Pb isotopes. Gondwana Research 25, 1614-1626.

Pearce, J.A., 2008. Geochemical fingerprinting of oceanic basalts with applications to ophiolite classification and the search for Archean oceanic crust. Lithos 100, 14-48.

Peate, D.W., Hawkesworth, C.J., 1996. Lithospheric to asthenospheric transition in low-Ti flood basalts from southern Parana, Brazil. Chemical Geology 127, 1-24.

Peate, D.W., Hawkesworth, C.J., Mantovani, M.M., Rogers, N.W., Turner, S.P., 1999. Petrogenesis and stratigraphy of the high-Ti/Y Urubici magma type in the Paraná flood basalt province and implications for the nature of 'Dupal'-type mantle in the South Atlantic region. Journal of Petrology 40, 451-473.

Raab, M.J., Brown, R.W., Gallagher, K., Carter, A., Weber, K., 2002. Late Cretaceous reactivation of major crustal shear zones in northern Namibia: constraints from apatite fission track analysis. Tectonophysics 349, 75-92.

Renne, P.R., Glen, J.M., Milner, S.C., Duncan, A.R., 1996. Age of Etendeka flood volcanism and associated intrusions in southwestern Africa. Geology 24, 659-662.

Ritter, O., Weckmann, U., Vietor, T., Haak, V., 2003. A magnetotelluric study of the Damara Belt in Namibia: 1. Regional scale conductivity anomalies. Physics of the Earth and Planetary Interiors 138, 71-90.

Rocha-Júnior, E.R., Marques, L.S., Babinski, M., Nardy, A.J., Figueiredo, A.M., Machado, F.B., 2013. Sr–Nd–Pb isotopic constraints on the nature of the mantle sources involved in the genesis of the high-Ti tholeiites from northern Paraná Continental Flood Basalts (Brazil). Journal of South American Earth Sciences 46, 9-25.

Rohde, J., Hoernle, K., Hauff, F., Werner, R., O'Connor, J., Class, C., Garbe-Schonberg, D., Jokat, W., 2013a. 70 Ma chemical zonation of the Tristan-Gough hotspot track. Geology 41, 335-338.

Rohde, J.K., van den Bogaard, P., Hoernle, K., Hauff, F., Werner, R., 2013b. Evidence for an age progression along the Tristan-Gough volcanic track from new 40Ar/39Ar ages on phenocryst phases. Tectonophysics 604, 60-71.

Sano, T., Shimizu, K., Ishikawa, A., Senda, R., Chang, Q., Kimura, J.I., Widdowson, M., Sager, W.W., 2012. Variety and origin of magmas on Shatsky Rise, northwest Pacific Ocean. Geochemistry, Geophysics, Geosystems 13.

Sarda, P., Moreira, M., Staudacher, T., Schilling, J.G., Allègre, C.J., 2000. Rare gas systematics on the southernmost Mid-Atlantic Ridge: Constraints on the lower mantle and the Dupal source. Journal of Geophysical Research: Solid Earth 105, 5973-5996.

Schwindrofska, A., Hoernle, K., Hauff, F., van den Bogaard, P., Werner, R., Garbe-Schönberg, D., 2016. Origin of enriched components in the South Atlantic: Evidence from 40 Ma geochemical zonation of the Discovery Seamounts. Earth and Planetary Science Letters 441, 167-177.

Stammeier, J., Jung, S., Romer, R., Berndt, J., Garbe-Schönberg, D., 2015. Petrology of ferroan alkali-calcic granites: Synorogenic high-temperature melting of undepleted felsic lower crust (Damara orogen, Namibia). Lithos 224, 114-125.

Stracke, A., Bizimis, M., Salters, V.J., 2003. Recycling oceanic crust: Quantitative constraints. Geochemistry, Geophysics, Geosystems 4.

Stroncik, N.A., Trumbull, R.B., Krienitz, M.-S., Niedermann, S., Romer, R.L., Harris, C., Day, J., 2017. Helium isotope evidence for a deep-seated mantle plume involved in South Atlantic breakup. Geology 45, 827-830.

Sun, S.-S., McDonough, W.F., 1989. Chemical and isotopic systematics of oceanic basalts: implications for mantle composition and processes. Geological Society, London, Special Publications 42, 313-345.

Thompson, R., Gibson, S., Dickin, A., Smith, P., 2001. Early Cretaceous basalt and picrite dykes of the southern Etendeka region, NW Namibia: windows into the role of the Tristan mantle plume in Paraná–Etendeka magmatism. Journal of Petrology 42, 2049-2081.

Thompson, R., Riches, A., Antoshechkina, P., Pearson, D., Nowell, G., Ottley, C., Dickin, A., Hards, V., Nguno, A.-K., Niku-Paavola, V., 2007. Origin of CFB magmatism: multi-tiered intracrustal picrite–rhyolite magmatic plumbing at Spitzkoppe, western Namibia, during early Cretaceous Etendeka magmatism. Journal of Petrology 48, 1119-1154.

Torsvik, T.H., Smethurst, M.A., Burke, K., Steinberger, B., 2006. Large igneous provinces generated from the margins of the large low-velocity provinces in the deep mantle. Geophysical Journal International 167, 1447-1460.

Turner, S., Kirstein, L., Hawkesworth, C., Peate, D., Hallinan, S., Mantovani, M., 1999. Petrogenesis of an 800 m lava sequence in eastern Uruguay: insights into magma chamber processes beneath the Paraná flood basalt province. Journal of Geodynamics 28, 471-487.

Willbold, M., Stracke, A., 2006. Trace element composition of mantle end-members: Implications for recycling of oceanic and upper and lower continental crust. Geochemistry, Geophysics, Geosystems 7.

Workman, R.K., Hart, S.R., 2005. Major and trace element composition of the depleted MORB mantle (DMM). Earth and Planetary Science Letters 231, 53-72.

Chapter 3.

Etendeka-related and Earlier Carbonatitic Volcanism in Namibia: Evidence for a concentrically-zoned Etendeka plume head

This chapter is ready for submission

Authors: **H.Zhou**[a], K.Hoernle[a, b], J.Geldmacher[a], F.Hauff[a], J-A.Wartho[a], D.Garbe-Schönberg[b], S.Jung[c], I. Bindemann[d]

[a]GEOMAR Helmholtz Centre for Ocean Research Kiel, Wischhofstr. 1-3, 24148 Kiel, Germany

[b]Institute of Geosciences, Kiel University, Ludewig-Meyn-Str. 10, 24118 Kiel, Germany

[c]Institute of Mineralogy and Petrography, Universität Hamburg, Grindelallee 48, 20146 Hamburg, Germany

[d]Department of Earth Sciences, University of Oregon, Eugene, OR, USA.

3.1. Abstract

The Etendeka large igneous province in central Namibia is proposed to be caused by widespread melting of the arriving of Tristan/Gough mantle plume head at 137-123 Ma. To explain the observed compositional variations of the Etendeka eruption products, including several carbonatitic and silica-undersaturated igneous complexes and intrusions, a laterally zoned plume head is assumed. Here we present new geochemical (major and trace element and Sr-Nd-Pb-O-C isotopes) and ^{40}Ar-^{39}Ar age data from the Kalkfeld, Okorusu and Messum carbonatites and silica-undersaturated rocks. The Kalkfeld carbonatites show a distinct isotopic composition from all other Etendeka-related magma. Considering its distinct composition and significant older (Triassic) age, Kalkfeld carbonatites cannot be derived from the Tristan-Gough plume and are thus not related to the Etendeka magmatism. Okorusu carbonatites, located at the far eastern end of the Etendeka province, show a specifically enriched mantle one (EM1) composition (Gough-type), consistent with derivation from a common magma source with the northern Etendeka flood basalts. Messum basanite, also related with the Etendeka event, indicate a different EM1 flavor (more radiogenic Nd, less radiogenic Sr and thorogenic Pb), similar to the Doros-type basalts emplaced at Doros intrusion and Tafelkop, Horingbaai formations. Combining our new findings with published data from carbonatites and silicate rocks, we propose a refined zonation model for the presumed plume head, reflected by a horseshoe pattern of distinctly isotopically enriched magmatism throughout the Etendeka igneous province.

3.2. Introduction

Carbonatite is a unique igneous rock type containing more than 50% carbonate ((Le Maitre et al., 2005)), and is relatively rare compared with the occurrence of siliceous igneous rocks. The origin of carbonatite magma is still debated. There are mainly two hypotheses: (1) The plume hypothesis assumes that carbon-rich material was subducted to the lower mantle and recycled by ascending mantle plumes ((Ernst and Bell, 2010; Hoernle and Tilton, 1991; Hoernle et al., 2002; Kogarko and Veselovskiy, 2019)). For instance, the only three known oceanic carbonatite occurrences are all found on volcanic islands associated with hotspots/plume volcanism (Cape Verde, Canary and

Kerguelen Islands) ((Ernst and Bell, 2010; Hoernle et al., 2002)). In addition, most carbonatites on the continents can be associated with deep mantle plume processes ((Bell, 2001)). (2) The metasomatized lithosphere hypothesis postulates that the shallow lithospheric mantle was metasomatized either by ancient subduction of carbonate-bearing sediments at collisional margins or by upwelling mantle plume material ((Green and Wallace, 1988; Hou et al., 2015; Le Roex and Lanyon, 1998; Song et al., 2016)). Interestingly deformed alkaline rock and carbonatite rock suites on the African and North American cratons are concentrated along known or inferred ancient suture zones ((Burke et al., 2003; Cimen et al., 2019; Hou et al., 2015)). Alternatively, carbonatite and related silicate rocks could represent mantle-derived magmas that have undergone extensive fractionation or silicate-carbonate liquid immiscibility of carbonated silicate melts at lower pressures (e.g. (Le Roex and Lanyon, 1998)). Additional complexities involve hydrothermal alteration by associated fluids shortly after emplacement and low-temperature alteration after emplacement.

The Etendeka large igneous province (LIP) in Namibia (**错误!未找到引用源。**)), originally connected with the Parana LIP in South America, provides one of the best opportunities to study the evolution of a presumed starting mantle plume head leading to widespread plateau volcanism, continental breakup and eventually the formation of an age-progressive hotspot track (e.g. (Erlank et al., 1984; O'Connor and Duncan, 1990)). At the same time, the region hosts a number of pre-, syn-, and post-Etendeka carbonatitic or silica-undersaturated igneous complexes ((Homrighausen et al., 2020; Miller, 2008; Milner et al., 1995; Trumbull et al., 2000)). Also, considering the excellent exposure of the extrusive and intrusive igneous rocks in NW Namibia, this makes the Etendeka volcanism a primary site for studying the genetic relationship of plume processes, lithosphere metasomatism and carbonatite magmatism.

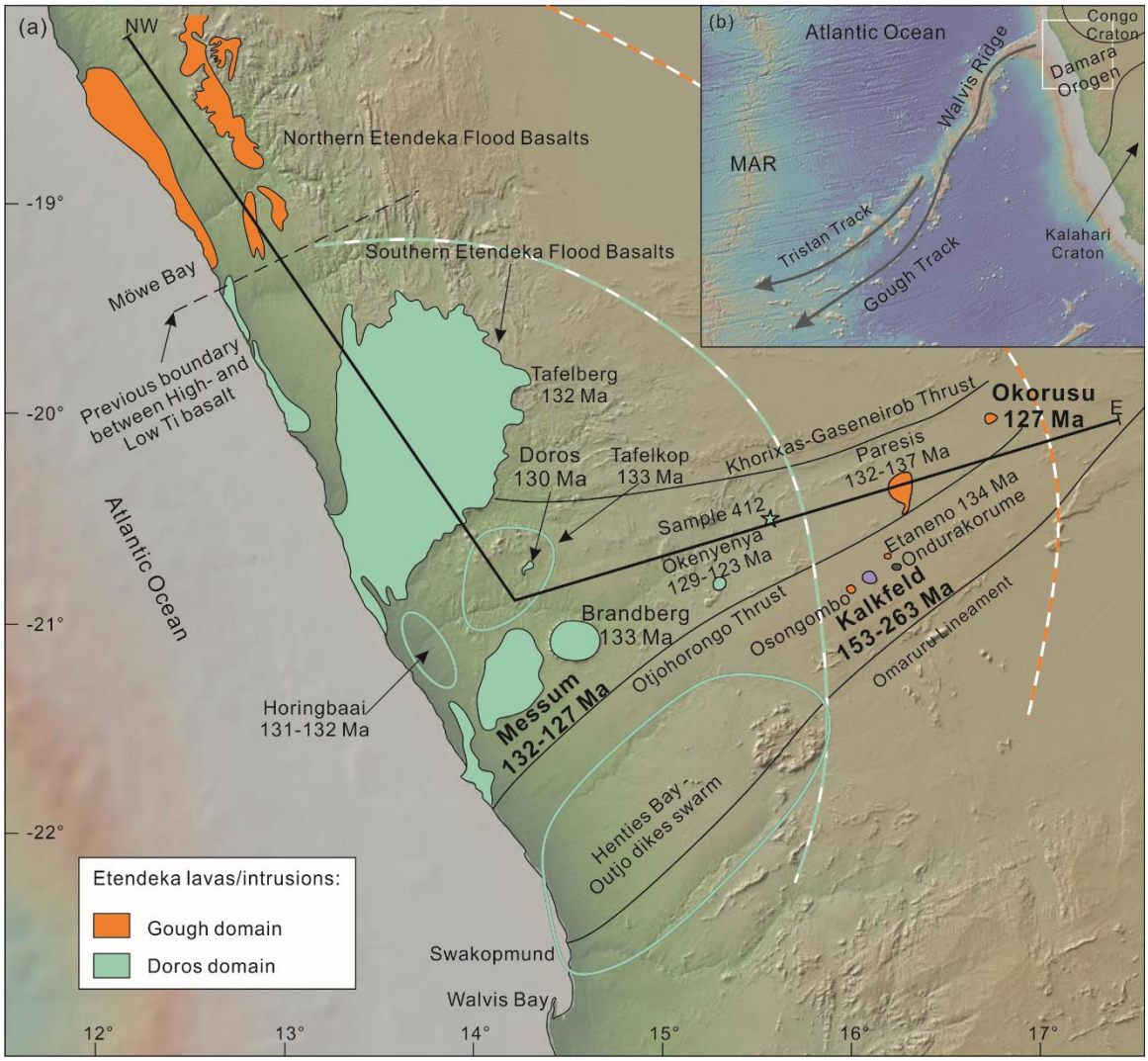

Figure 3-1: (a) Map of the Etendeka large igneous province in northwest Namibia showing exposed plateau lavas and alkaline-carbonatite intrusive complexes. Based on their isotopic composition, igneous units from the Etendeka event can be divided according to their possible derivation from Gough or Doros plume components, respectively ((Zhou et al., 2020)). Site of sample 412 (from (Stroncik et al., 2017)), the easternmost uncontaminated sample showing Doros-type composition, is marked by a green star. Stippled green and orange lines mark approximate extent of Gough/Doros source domains within the postulated Etendeka plume head when projected to the surface (see Section 3.6.4). Major tectonic structures taken from (Miller, 2008)). Age data from: Doros ((Owen-Smith et al., 2017)), Tafelkop ((Jerram et al., 1999)), Horingbaai ((Thompson et al., 2001)), Tafelberg ((Renne et al., 1996)), Messum ((Milner et al., 1995; Renne et al., 1996)), Okenyenya ((Milner et al., 1993)), Paresis ((Milner et al., 1995; Pirajno et al., 2000)), Okorusu ((Milner et al., 1995)), Etaneno ((Müller, 1996)), Kalkfeld ((Kramm et al., 2017; Ziegler, 1992); this study). The black line from EW to E indicates approximate strike of cross section in Figure 3-12. (b) Inset shows the studied location in relation to the Gough plume hotspot track in the South Atlantic. Maps generated by GeoMapApp (http://www.geomapapp .org).

The plume-related magmatism in southwestern Africa and the associated hotspot tracks in the southeast Atlantic can be roughly divided into two phases: The first phase, or

main igneous event, comprises the presumed arrival of the Tristan-Gough mantle plume head that formed the Etendeka-Parana (~137-130 Ma) flood basalts (LIP) and subsequent hotspot volcanism. Igneous rocks of this phase are characterized by their enriched mantle 1 (EM1) isotope signature. This phase is followed by low-volume but widespread occurrence of magmatism with HIMU (high-time integrated $^{238}U/^{204}Pb$ = high μ) isotopic composition. ((Homrighausen et al., 2018a; Homrighausen et al., 2020)). In a companion paper, we have shown that the post-Etendeka carbonatitic and silica-undersaturated complexes in southwestern Africa (<120 Ma) can be assigned to the second HIMU stage (Zhou et al., under review). This study focusses therefore on the pre- and syn- Etentdeka carbonatites and silica-undersaturated rocks, whose origin is still a matter of debate. Proposed models range from a direct derivation from the Etendeka plume head event ((Trumbull, 2003)) to generation by melting of metasomatized sub-continental lithosphere mantle (SCLM) ((Le Roex and Lanyon, 1998)). This study presents major and trace element and Sr-Nd-Pb-O-C isotope data of carbonatites and silica-undersaturated rocks from the Kalkfeld, Okorusu and Messum igneuos complexes of Damara Orogenic Belt in central Namibia and U/Pb age data for Kalkfeld carbonatites to constrain their origin and to discuss the current models for the widespread Damara carbonatite magmatism.

3.3. Geological background and previous work

3.3.1. General geological setting

Central Namibia is comprised by the late Proterozoic to early Cambrian Damara Orogenic Belt (Figure 3-1b), which formed as an orogenic fold belt between the Congo and Kalahari cratons during the amalgamation of southern Gondwana ((Kasch, 1983; Miller, 2008)). This convergence caused the closure of an ocean basin (Khomas Sea) that existed from >720–560 Ma ago between both cratons and which contained abundant biogenic carbonate sediments ((Miller, 2008)). Northward subduction beneath the Congo Craton eventually led to continental collision and orogeny in the Neoproterozoic (~580 Ma) which lasted to about ~460 Ma ((Miller, 1983)). The collision created/reactivated prominent thrust faults, such as the Omaruru Lineament and Otjohorongo Thrust (Figure 3-1), which now separate zones of different stratigraphic and structural evolution ((Goscombe et al., 2003)). Mesozoic reactivation of the Omaruru Lineament is documented by local unconformities, Triassic sediments

filling half graben structures, and reverse faults cutting the Triassic sediments ((Clemson et al., 1997; Hegenberger, 1988; Raab et al., 2002)). The alkaline and carbonatitic intrusive complexes within the Damara Belt also seem to be oriented along/near these thrust faults forming a broad linear chain that extends from Okenyenya in the SW to Okorusu in the NW (Figure 3-1). No spatial age-progression was detected, but their ages range from 137-132 Ma at Paresis ((Milner et al., 1995; Pirajno et al., 2000)) to 134 Ma at Etaneno ((Müller, 1996)) to 127 at Okorusu ((Milner et al., 1995)), to 129-123 at Okenyenya ((Milner et al., 1995)), therefore overlapping with the Etendeka plateau volcanism (138–120 Ma; (Peate, 1997))(Figure 3-1). Although dikes are rarely observed cutting the intrusive complexes, the "hour-glass" fault patterns near the Paresis complex indicate small age difference between Etendeka plateau volcanism and the alkaline intrusions ((Trumbull et al., 2004; van Wyk de Vries and Merle, 1996)). An exception to this is the Kalkfeld complex, which yields a distinctly older, Triassic age of 242±13 Ma (2σ error) based on a mineral Rb-Sr isochron of silicic rocks surrounding the carbonatites ((Kramm et al., 2017)). The carbonatites, however, have not yet been directly dated.

The widespread Etendeka plateau basalt volcanism is generally believed to be related to a mantle plume head, associated with the break-up of the South Atlantic ((Erlank et al., 1984; O'Connor and Duncan, 1990)). An age-progressive chain of volcanic ridges (Walvis Ridge) and seamounts ("Guyot Province") links the continental flood basalts with the volcanically active Tristan da Cunha and Gough island groups in the South Atlantic interpreted as a classical hotspot track (Figure 3-1b). The <70 Ma portion of the hotspot track is spatially zoned and bifurcated into a Tristan subtrack and a Gough subtrack ((Hoernle et al., 2015; Rohde et al., 2013)). All lavas have Enriched Mantle (EM 1) isotopic composition, but lavas of the Tristan subtrack are characterized by systematically lower $^{207}Pb/^{204}Pb$ at a given $^{206}Pb/^{204}Pb$. The older parts of the hotspot track (including most of the Walvis Ridge) have almost exclusively Gough composition, suggesting that the Gough component represents the dominant, long-lived composition of the Tristan-Gough plume ((Hoernle et al., 2015; Homrighausen et al., 2019)).

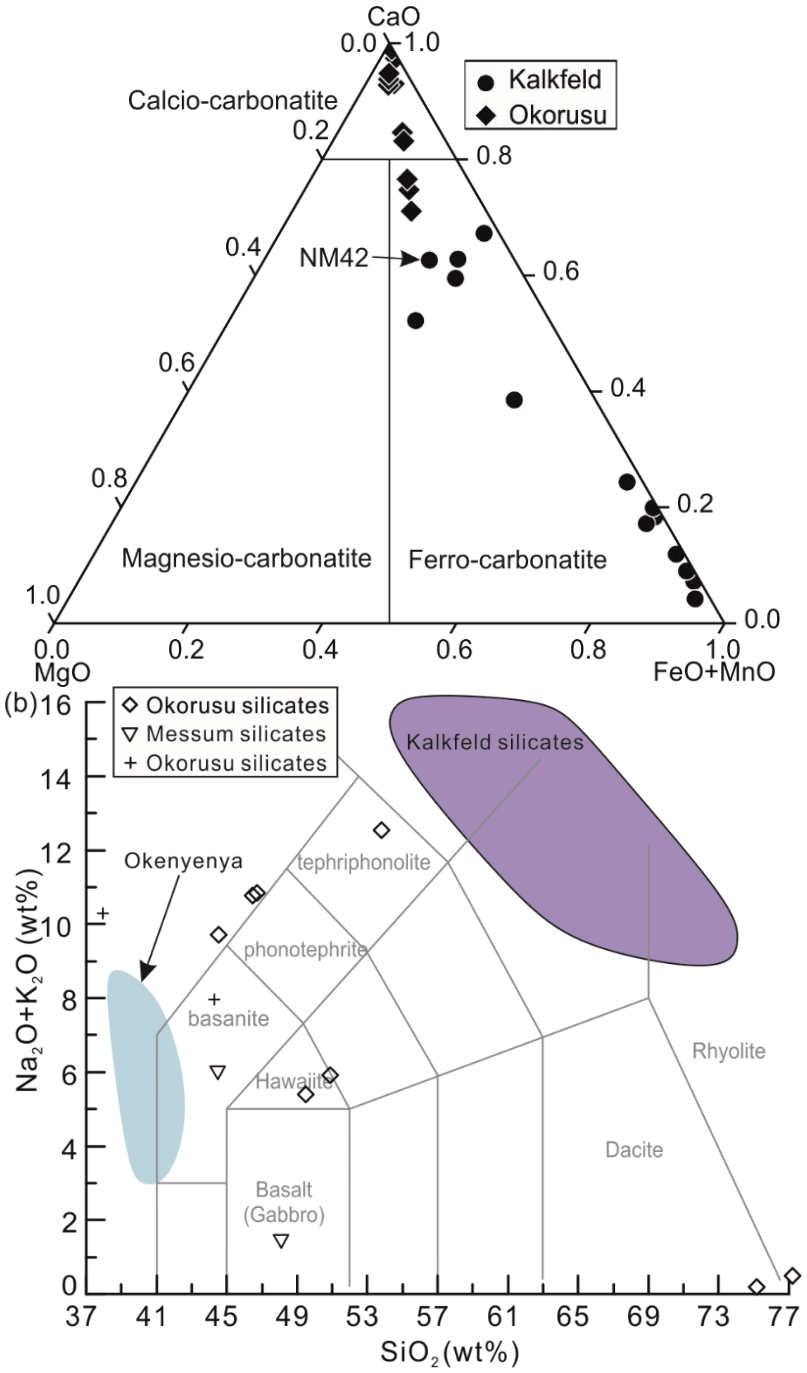

Figure 3-2: Carbonatite classification diagram after Le Maitre et al. (1989). Carbonatites from Okorusu are mainly calcio-carbonatites. Only three Okorusu carbonatites possess higher whole rock FeO. All carbonatites from Kalkfeld classify as ferro-carbonatites.

Intriguingly, our recent study of the plateau lava geochemistry also found a spatial zonation in the plateau basalt (plume head) stage for Etendeka: High-Ti basalts, exclusively occurring in northern Etendeka, possess Gough-type EM 1 composition,

whereas low-Ti basalts, primarily outcropping in southern Etendeka, were derived from a distinct EM1-type source component ((Trumbull, 2003; Trumbull et al., 2007)), termed “Doros” (after the Doros intrusion, (Zhou et al., 2020)) (Figure 3-1). The Doros component has yet not been detected in the submarine hotspot track, but because it has high $^{3}He/^{4}He$ of up to 26 R_A ((Stroncik et al., 2017)) is considered as being intrinsic to the initial mantle plume ((Zhou et al., 2020)). This component has also been observed in the Mozambique Ridge ((Jacques et al., 2019)). Therefore geochemically distinct components can appear at different times in plume history leading to temporarily zonation as also observed for the Hawaiian plume (e.g. (Harrison et al., 2017)). The geographic distribution and temporal occurrence of rocks with Doros composition is still not fully resolved. In particular in central western Etendeka, feeder dikes and intrusive rocks are primarily preserved instead of extrusive rocks. Also, tholeiitic rocks with ages of <130 Ma and/or outcropping east of Brandberg, Doros and Tafelberg (east of longitude 14.5° E) are extremely rare or absent. Furthermore, most low-Ti tholeiitic lavas and dikes in central western Etendeka were subject to enhanced crustal contamination, due to their depleted incompatible-element compositions. The carbonatitic and highly alkaline intrusions in the Damara Belt (Figure 3-1) are far less effected by shallow level crustal contamination and are thus are well-suited for revealing their magma source and are therefore the subject of this composition.

Adding further complexity, Homrighausen et al. (2020) showed that the Etendeka-Tristan-Gough EM1 hotspot track superimposed on the Tristan-Gough-Walvis track, volcanism was followed 30 Ma later (at any given site) by a second, age-progressive hotspot track producing lavas with exclusively HIMU composition. This relationship attests to the close spatial proximity of both distinct global isotopic mantle endmembers EM1 and HIMU in the deep root region of the plumes, which is believed to be the southwestern edge of the African Large Low Shear Velocity Province (LLSVP) in the lower mantle. It was proposed that removal of a large amount of EMI type material from the outer LLSVP margin by the Tristan-Gough plume head triggered instabilities with HIMU-type composition along a steep step in the inner part of the LLSVP. Such a step is observed in seismic tomographic mantle models and runs sub-parallel and in ~900–1200 km distance from the outer margin of the LLSVP. (Homrighausen et al. 2018a; Zhou et al., under review). Secondary, transient plumes or upwelling blobs,

generated along this step, and formed a belt of HIMU volcanism along the continent-ocean margin and adjacent oceanic crust in southwestern Africa. Beneath the thick continental lithospheric lid, upwelling mantle could only melt to lower degrees producing carbonatites, kimberlites and other low-degree silica-undersaturated rocks ((Braunger et al., 2020; Hammouda and Keshav, 2015); Zhou et al., under review). In contrast, mantle could upwell to shallower depths beneath the thinner oceanic lithospheric lid, resulting in greater degrees of decompression melting and the generation of alkali basaltic and basanitic seamounts from the same HIMU plume source.

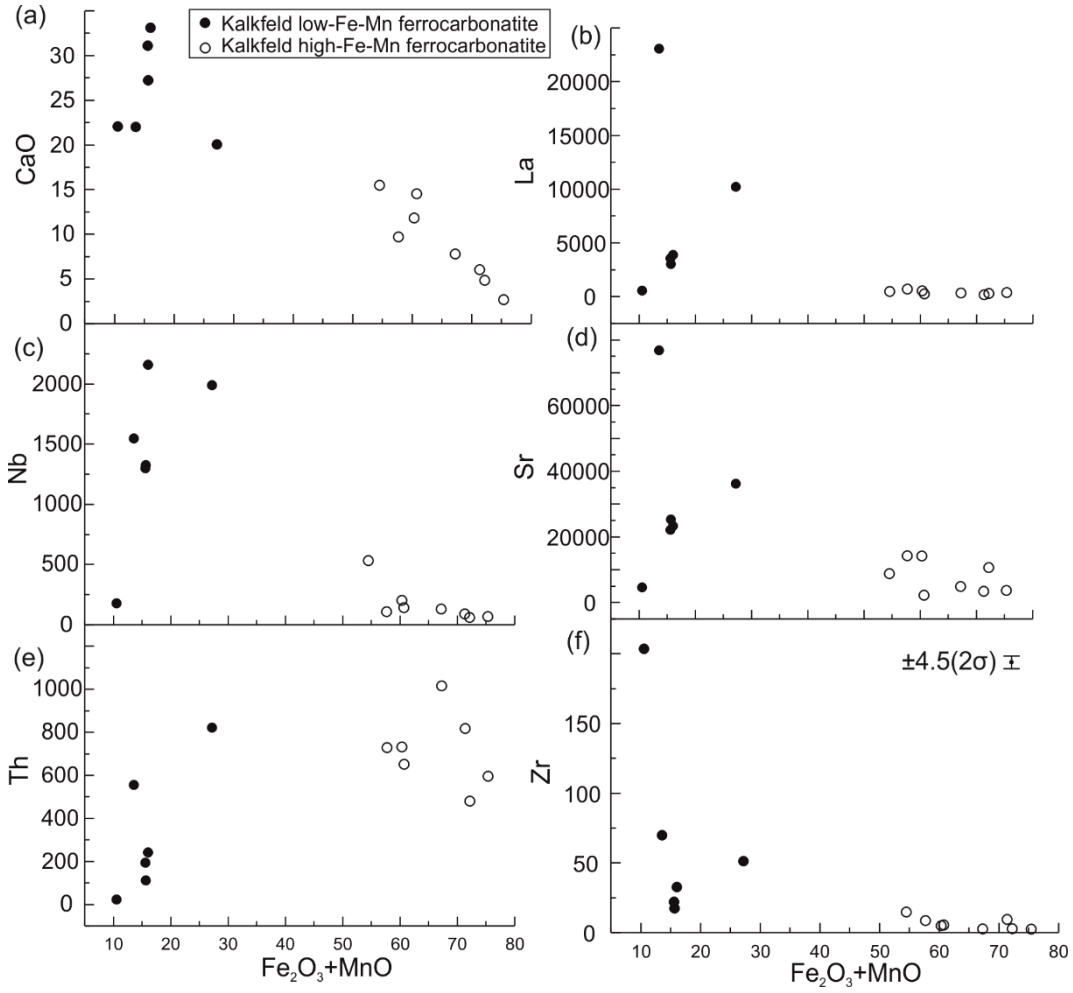

Figure 3-3: Fe_2O_3+MnO vs (a) CaO, (b) La, (c) Nb, (d) Sr, (e) Th, (f) Zr of Kalkfeld ferrocarbonatites. Kalkfeld samples are divided into two groups: high-Fe-Mn ferrocarbonatites and low-Fe-Mn ferrocarbonatites. The high-Fe-Mn ferro-carbonatites have lower CaO, La, Nb, Sr, Zr but higher Th concentrations than the low-Fe-Mn group. All trace element concentrations are reported by ppm. The 2 standard deviation (σ) of

most samples are smaller than the symbols, except Zr which is presented as an error bar in (f).

3.3.2. Alkaline-carbonatitic complexes sampled for this study

Kalkfeld is an intrusive ring complex in the Damara Belt (Figure 3-1) with a diameter of ~7 km, comprised of an iron-rich carbonatitic central hill, called Eisenberg, and an outer ring of syenite and fenitized country rock. A specific iron ore, enriched in Th, Cu and Pb, is present in the center of the Eisenberg carbonatites ((Van Zijl, 1962)), which is interpreted to reflect a hydrothermal replacement of sövite ((Miller, 2008)). The latest volcanism is represented by several lamprophyric and syenitic dikes, which were intruded into the iron ore ((Van Zijl, 1962)). In addition, several NE-striking dolerite dikes cut both carbonatites and iron ore and extend beyond the intrusion boundary of Kalkfeld, probably belonging to the Henties Bay–Outjo dike swarm of the Etendeka group ((Trumbull et al., 2004)). Therefore, the Kalkfeld intrusion clearly predates at least part of the Cretaceous Etendeka flood basalt event. Chloritized biotite phenocrysts of carbonatites from Eisenberg yield questionable Jurassic (153 – 172 Ma) ages by K-Ar dating ((Ziegler, 1992)), while more modern combined whole-rock (syenite and tinguaite) and mineral (biotite, clinopyroxene, feldspar and nepheline) Rb-Sr isochron dating of the outer ring syenites produced a well-defined middle Triassic age (242 ± 13 Ma; all reported errors in this manuscript are at the 95% confidence limit; (Kramm et al., 2017)).

Okorusu is the most northeasterly in the chain of Damara intrusions, and is ~7km in diameter. Rb-Sr isochron dating of whole-rock (nepheline-syenite) and Ar-Ar step-heating of mineral (feldspar, pyroxene and amphibole) separates yield overlapping ages of 126.6 ± 7.3 Ma and 126.8 ± 0.6 Ma, respectively ((Milner et al., 1995)), contemporaneous with Etendeka plateau volcanism. The centeral hill has a much lower volume than the outer ring and is mainly composed of syenite. Presently, only the southern sector of the ring is exposed which is comprised of carbonatite, ijolite and fenitized country rock ((Hagni, 2007)). The excellent exposure is due to the commercial exploration of this structure, which was considered one of the World's largest fluorite mining sites (130,000 tons/a of fluorite concentrate) until 2011 ((Hagni, 2012)).

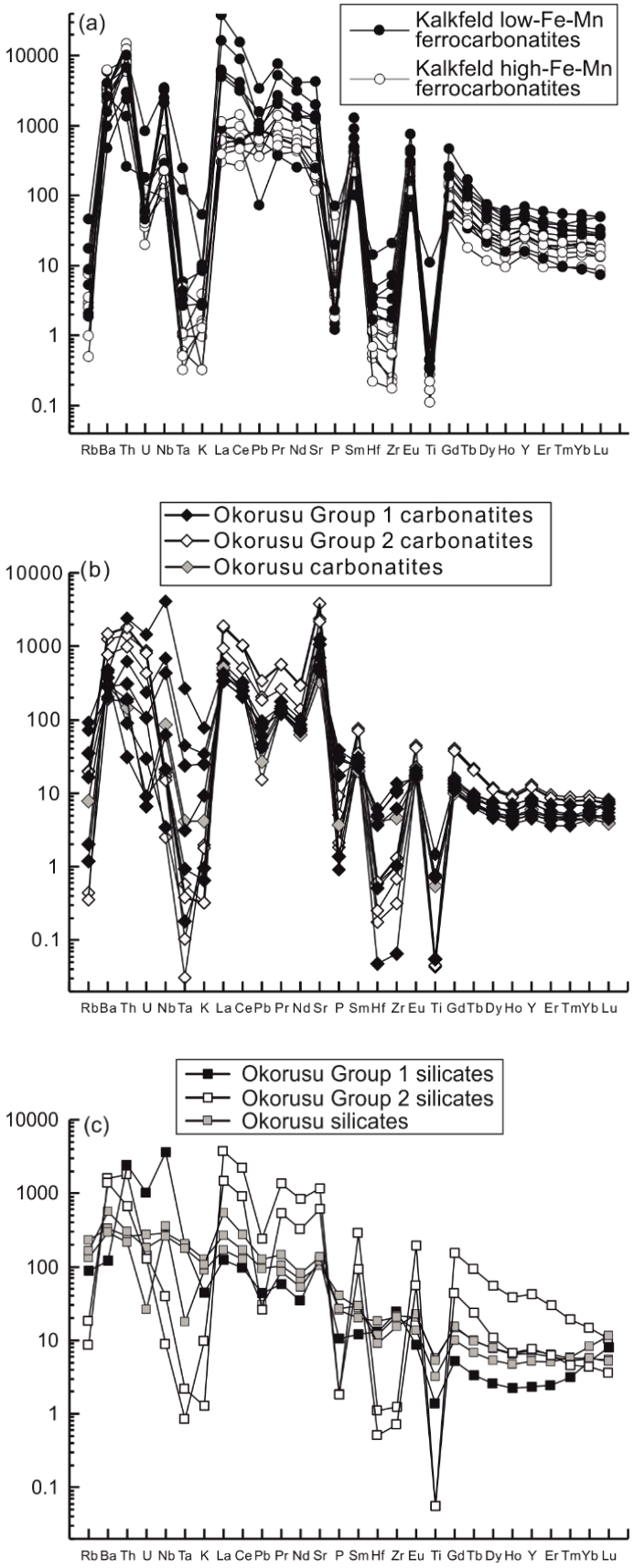

Figure 3-4: Primitive mantle ((Hofmann, 1988)) normalized trace element pattern for (a) Kalkfeld carbonatites, (b) Okorusu carbonatites and (c) Okorusu silicate rocks.

Messum intrusive complex is composed of a syn-Etendeka outer ring (~132 Ma; (Renne et al., 1996)) about 18km in diameter and a slightly younger nepheline syenite core (127-129 Ma; (Milner et al., 1995; Renne et al., 1996)) about 6km in diameter. The complex intruded into the Etendeka flood basalts and quartz latites, indicating that early phase of Messum formed immediately after the Etendeka flood basalts and the alkaline core 3–5 Ma later. The Messum basalts were proposed to be derived from the Doros-domain of Tristan-Gough plume ((Ewart et al., 1998b; Zhou et al., 2020)), and in this study, a basanite from Messum was measured and compared with other alkaline and carbonatitic rocks in Damara Belt.

3.4. Sample description and analytical methods

3.4.1. Petrography

Carbonatite samples from Kalkfeld were collected from the Eisenberg central hill and are ferro-carbonatites. Most carbonatites contain abundant Fe-oxides due to their close vicinity and genetic relationship with the iron ore. Fresh carbonates contain subhedral to anhedral calcite/siderite crystals of 0.1–1mm size. Parts that were effected by hydrothermal fluids (e.g. up to 50% carbonate in NM48, which is highly fractured) are indicated by turbid crystals. Miller (2008) assume that these altered minerals are probably strontianites ($SrCO_3$) or ankerites ($Ca(Fe,Mg,Mn)(CO_3)_2$). In our samples, the altered minerals show saddle-shaped outlines, consistent with being ankerites ((Sibley, 1978)). Accessory phases, are mainly subhedral to octahedral pyrochlore (~0.1 mm), anhedral Fe-oxides, garnet and biotite. Rare malachite is identified as a druse in NM48. Sample NM42 was taken from a 5m thick dike in the iron ore body, which contains the most silicate minerals (~40 volume %) of all Kalkfeld samples, and features abundant calcite (~0.2 mm; 50%), altered amphibole and biotite (~0.2 mm), anhedral quartz (< 0.1 mm), feldspar (~0.1 mm) and subhedral opaque Fe-oxides (~0.05 mm).

Samples from the Okorusu complex were collected from the southern sector of the outer ring structure at the “D-pit” outcrop of the fluorite mine ((Cangelosi et al., 2019)). Carbonatites have more than 50% anhedral coarse-grained calcite. Besides calcite, most carbonatites contain silicic accessories, such as pyroxene, amphibole, apatite, biotite, feldspar and nepheline. Amphiboles are euhedral and ~0.4mm in size and show obvious

zonation. Nepheline shows anhedral to subhedral habitus less than 0.1 mm. Small amounts of biotite (~2 mm) and pyrite (~0.05 mm) can also be observed. Samples taken near the interface between carbonatite and the fluorite deposits contain up to 60% euhedral fluorite crystals (~ 1.5 mm). About 40% of subhedral calcites and rare anhedral quartz fill the intergranular spaces between the fluorite crystals. In addition to the carbonatites, rocks dominated by siliceous minerals that occur in association with the carbonatites were also sampled for comparison. These silicates are rich in pyroxenite or nepheline. The pyroxenites (Hawaiite in TAS diagram) are featured by the accumulation of subhedral pyroxene, with anhedral calcite, euhedral amphibole (fine grain to 0.2mm) and a fine grain silicate mineral matrix. The nepheline syenites (phonotephrite and tephriphonolite in TAS diagram) have abundant nepheline (up to 75% of the matrix), elongated feldspar, altered mica, fine grain euhedral apatite and Fe-oxides. Miller (2008) refer to these silicates as syenite intrusive plug and dikes and tinguaite dikes, which both pre-date (are cut by) and post-date (cut) the carbonatite dikes and intrusives.

3.4.2. Analytical Methods

Rock samples were crushed in a jaw-crusher, cleaned in an ultrasonic bath with deionized water, sieved and carefully hand-picked under a binocular microscope to avoid secondary fillings of cavities and fractures. Selected whole-rock chips (~10g) of each sample were milled to fine powders and dried at 105°C overnight.

Major elements of all silicate samples were measured at the Institute of Mineralogy and Petrography at the University of Hamburg on a Magix Pro PW 2540 X-ray fluorescence spectrometer (XRF). International rock standards JGB-1, JB-3, JB-2, JA-3, JG-3, JG-2 were analyzed together with the samples. The difference between measured and accepted literature values ((Govindaraju, 1994)) is less than 6%, except for the very low contents of MnO_2 and P_2O_5 in the JG2 standard (Appendix A). Since carbonatites possess extremely high concentrations of Sr and Ba (beyond the silicate XRF calibration curve and therefore yielding high analytical errors), major elements of the respective samples were measured by inductively coupled plasma optical emission spectrometry (ICP-OES) on a SPECTRO CIROS SOP at the Institute of Geosciences at Kiel University (see table 3-1 and table caption for analytical details). The reference standards MACS-3 ((Jochum et al., 2019)) and COQ-1 ((Ray et al., 2013)) were

measured together with the samples. The difference between measured and literature values are less than 6%, except for elements which are lower than 1 wt%. The precision of ICP-OES measurements based on duplicate measurements is less than 5% except for the extremely low P concentration in samples NM48 and NM75.

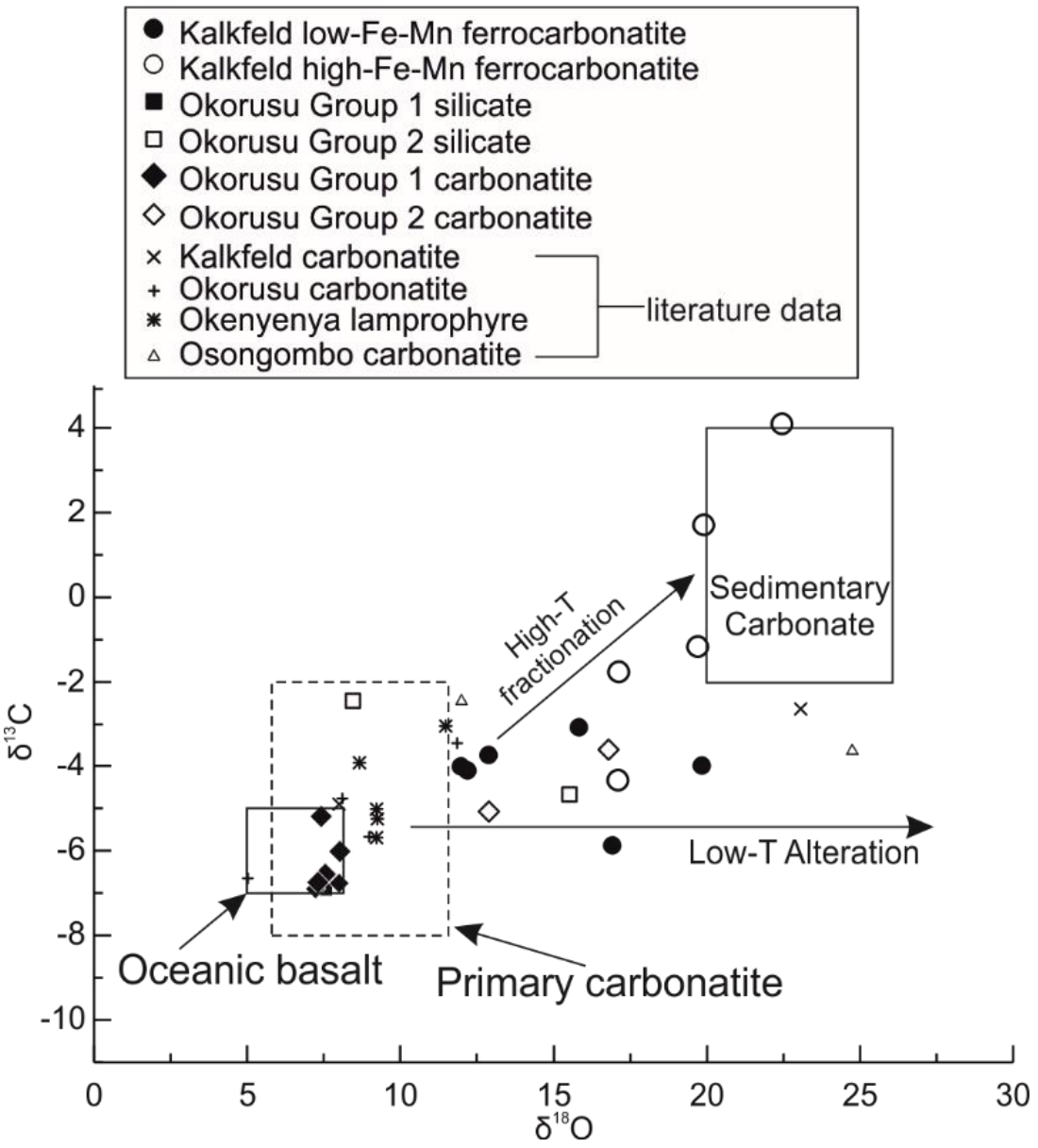

Figure 3-5: Oxygen and carbon isotopes of the investigated rocks from Kalkfeld and Okorusu. The composition of primary carbonatite from Deines (1989). Oceanic basalts are from Keller and Hoefs (1995). The sedimentary carbonate from Valley et al. (2018). Literature data from Le Roex and Lanyon (1998). Kalkfeld low-Fe-Mn samples have mantle-like $\delta^{13}C$ but elevated $\delta^{18}O$ except for sample K2 from Le Roex and Lanyon (1998) with mantle-like $\delta^{18}O$; high-Fe-Mn samples have high $\delta^{18}O$ and $\delta^{13}C$. Okorusu Group 1 samples fall within the box for primary carbonatites and oceanic rocks, whereas Group 2 samples extend to higher $\delta^{18}O$ and $\delta^{13}C$ than in primary carbonatites.

Trace elements were determined with an AGILENT 7500cs inductively coupled plasma mass spectrometer (ICP-MS) also at the Institute of Geosciences at Kiel University. Carbonatites were decarbonized by diluted hydrochloic acid before all treatments. All rock powders (~100 mg) were then treated with Hf-HClO4-aqua regia following the standard decomposition procedure of ((Garbe-Schönberg, 1993)). Some carbonatitic powders, however, could not be fully dissolved by this method, due to the presence of accessory phases. Therefore, these samples were milled to nano-particulate powders and measured by laser ablation inductively coupled plasma mass spectrometer (LA-ICP-MS). About 2g powders for every sample was milled with 8 ml deionized water for 3 min in a planetary mill at 700-800 rpm. All samples were then carefully rinsed into polycarbonate beakers and freeze-dried. After 5 minutes of re-homogenization, about 300 mg powder was pressed into tablets under 0.74×10^6 kPa ((Garbe-Schönberg and Müller, 2014)). The tablets were measured by Agilent 7900 ICP-MS coupled with a GeoLas HD (Coherent) 193 nm ArF excimer laser ablation system at Kiel University. We measure each tablet three times and report the average value. A carbonatite standard, MACS-3 NP, was measured together with the nano-powders. The difference between measured and literature data ((Jochum et al., 2019)) is less than 8.3%, except Zr and elements which are lower than 0.1 ppm.

The Sr-Nd-Pb isotope ratios were measured at the GEOMAR Helmholtz Centre for Ocean Research Kiel by thermal ionization mass spectrometry (TIMS) using a Thermo-Scientific TRITON *Plus*. About 20-30 mg powders were dissolved in concentrated HF and HNO3 (5:1) at 140 °C for 2 days. Ion chromatography followed Hoernle et al. (2008). The Sr and Nd isotopic ratios were normalized within-run to $^{86}Sr/^{88}Sr = 0.1194$ and $^{146}Nd/^{144}Nd = 0.7219$ and fractionation-corrected to NBS987 and La Jolla standards that were measured along with the samples. Since installation of the instrument in 2014, NBS987 values yield $^{87}Sr/^{86}Sr = 0.710250 \pm 0.000009$ (n=743; 2 standard deviation (SD)) and La Jolla averages $^{143}Nd/^{144}Nd = 0.511850 \pm 0.000007$ (n=505; 2σ). Pb isotopes were measured using the double-spike (Pb-DS) technique ((Hoernle et al., 2011)). The DS corrected NBS981 values since 2014 are $^{206}Pb/^{204}Pb = 16.9408 \pm 0.0018$, $^{207}Pb/^{204}Pb = 15.4975 \pm 0.0018$, $^{208}Pb/^{204}Pb = 36.7207 \pm 0.0047$ (n=178; 2σ). Procedural blanks were <30pg for Pb and <100pg for Sr, Nd.

Measured isotope data has been corrected for radiogenic ingrowth using an average age of 132 Ma for most Damara carbonatites and the Etendeka flood basalts. To allow comparison, we have projected the ratios to the initial ages using the measured parent/daughter ratios of rocks, then to 132 Ma using the assumed mantle source parent/daughter ratios: EM1 source (including Kalkfeld): U/Pb =0.137, Th/Pb =0.6758, Rb/Sr =0.0204, Sm/Nd =0.3378 ((Stracke et al., 2003; Willbold and Stracke, 2006)); HIMU source: U/Pb = 0.3043, Th/Pb = 0.9565, Rb/Sr = 0.0071, Sm/Nd = 0.3590 ((Stracke et al., 2003; Willbold and Stracke, 2006)); MORB source: U/Pb =0.1667, Th/Pb =0.4444, Rb/Sr =0.0065, Sm/Nd =0.4114 ((Workman and Hart, 2005)).

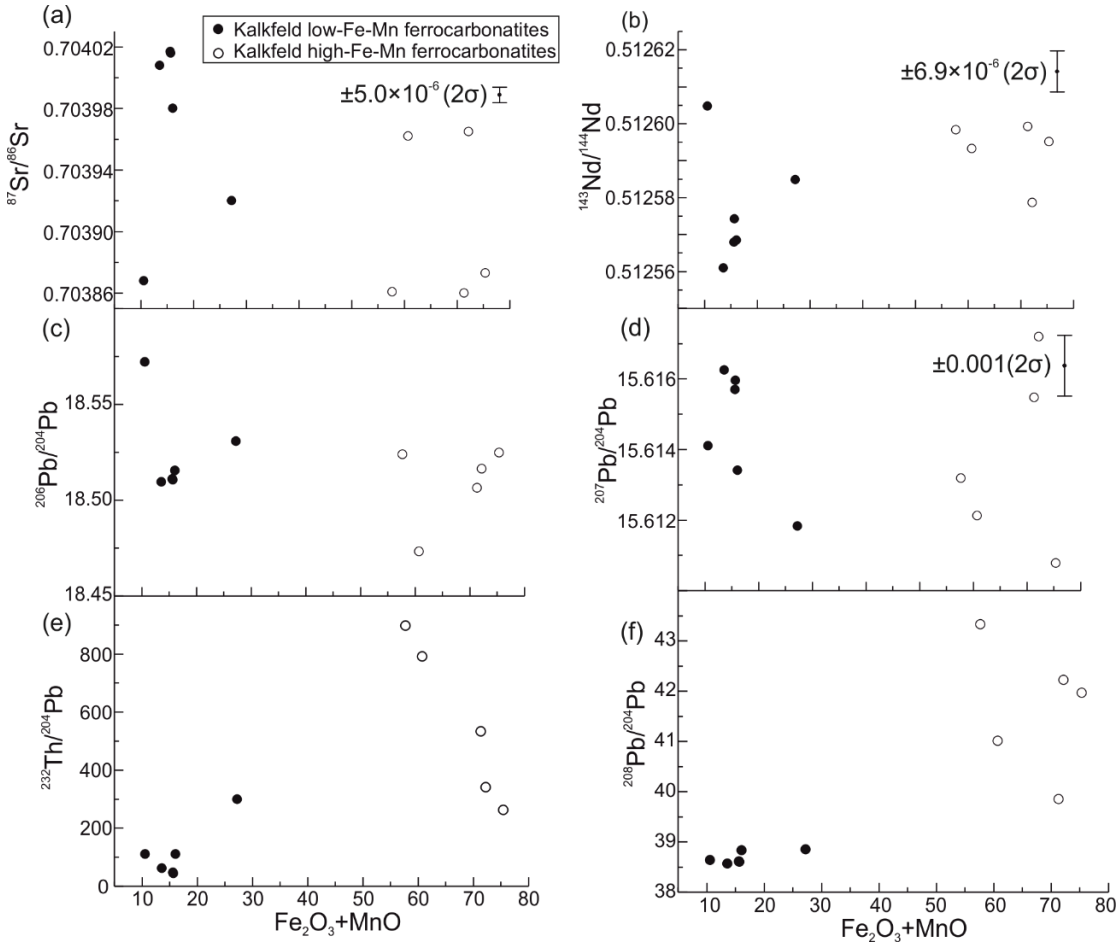

Figure 3-6: Fe_2O_3+MnO vs (a) $\delta^{13}C$, (b) initial $^{143}Nd/^{144}Nd$, (c) initial $^{206}Pb/^{204}Pb$, (d) initial $^{207}Pb/^{204}Pb$, (e) $^{232}Th/^{204}Pb$, (f) initial $^{208}Pb/^{204}Pb$ of Kalkfeld ferrocarbonatites. High-Fe-Mn ferrocarbonatites show higher $^{232}Th/^{204}Pb$ and $^{208}Pb/^{204}Pb$, but largely overlapping 87Sr/86Sr, $^{143}Nd/^{144}Nd$, $^{206}Pb/^{204}Pb$ and $^{207}Pb/^{204}Pb$ to low-Fe-Mn ferrocarbonatites. The 2 standard deviation (2σ) of most samples are smaller than the symbols, except when marked by error bars.

Carbon and oxygen isotopes were measured at the University of Oregon using a Gasbench continuous flow line coupled with Thermo-Finnigan MAT253 gas isotope

ratio mass spectrometer. First 0.4 mg of the freshest carbonate minerals were ground and put into 10 ml exetainers, which were flushed with He, then acidified with phosphoric acid inside of a thermal block held at 70°C. After equilibration for 2 h, they were run sequentially, and an analysis run included NBS19 standard and in-house carbonatite standard MCA. Carbon isotope values are reported relative to the PDB standard. NBS19 standard was measured during the measurement and yield $\delta^{13}C$ =2.09±0.032‰ PDB (2σ). Oxygen isotope values are reported relative to the international Vienna Standard Mean Ocean Water (VSMOW) standard. The measured $\delta^{18}O$ values of NBS19 are 28.03±0.057 (2σ). The analytical values were adjusted by the difference between our measured and recommended values of standard (0.14 for $\delta^{13}C$ and -0.61 for $\delta^{18}O$).

3.5. Results

Major and trace element contents and isotope ratios are provided in Table 3-1.

3.5.1. Kalkfeld

All samples from Kalkfeld have high contents of Fe_2O_3 (8.4–67.4 wt and classify as ferro-carbonatites in the carbonatite classification diagram ((Le Maitre et al., 1989)), including dike sample NM42 (Figure 3-2a). CaO contents (2.7–33.1 wt%) decrease and MnO increase with increasing of Fe_2O_3 (Figure 3-3a). Kalkfeld carbonatites have low SiO_2 (4.0–12.7 wt%), Na_2O, K_2O and TiO_2 contents, except for sample NM42, which comes from a dike, cutting the massive ferro-carbonatite intrusive. The dike has higher SiO_2 (27.2 wt%) and lower Fe_2O_3 (10.0 wt%) and MnO_2. Due to the large range of Fe_2O_3+MnO content and the obvious gap between 30–54 wt%, We divide Kalkfeld ferro-carbonatites into two groups. The low-Fe-Mn ferro-carbonatites contain less than 30 wt% Fe_2O_3+MnO but systematically higher concentrations of LREE (Figure 3-3b, Figure 3-4a), most high field strengths elements (HFSE; e.g. Nb, Ta, Zr, Hf, Ti;Figure 3-3c, f and Figure 3-4a) and Large Ion Lithophile Elements (LILE; e.g. Rb, Sr, K; Figure 3-3d and Figure 3-4a), but overall lower concentrations of Th (Figure 3-3e). The low-Fe-Mn samples have higher $\delta^{18}O$ (12.0–19.8‰) than the primary carbonatite range ($\delta^{18}O$ = 6–12‰; (Deines, 1989)), whereas $\delta^{13}C$ (-5.9 to -3.1‰) largely overlaps the range for primary mantle-derived carbonatites ($\delta^{13}C$ = -8 to -2‰; (Deines, 1989)) (Figure 3-5). In contrast, the high-Fe-Mn ferro-carbonatites extend to higher $\delta^{18}O$

(17.1–22.5‰) and $\delta^{13}C$ (-4.3 to 4.1‰). The low-Fe-Mn Kalkfeld carbonatites show a fairly to very restricted range in initial $^{87}Sr/^{86}Sr$ (0.70387–0.70402), $^{143}Nd/^{144}Nd$ (0.512561–0.512605), $^{206}Pb/^{204}Pb$ (18.51–18.57), $^{207}Pb/^{204}Pb$ ratios (15.613–15.617) and $^{208}Pb/^{204}Pb$ (38.57-38.85) ratios. The high-Fe-Mn ferro-carbonatites show very nearly identical $^{87}Sr/^{86}Sr$ (0.70386-0.70397), $^{143}Nd/^{144}Nd$ (0.512579-0.512599), $^{206}Pb/^{204}Pb$ (18.48-18.53) and $^{207}Pb/^{204}Pb$ (15.612-15.618) ratios but significantly higher $^{232}Th/^{204}Pb$ (263–898 compared to 45-299 for low-Fe-Mn samples) and $^{208}Pb/^{204}Pb$ ratios (39.85–43.33) (Figure 3-6). Additionally, the $^{238}U/^{204}Pb$ versus $^{206}Pb/^{204}Pb$ of Kalkfeld low-Fe-Mn ferro-carbonatites form a positive correlation (errorchron) with an age of 263.0±2.9 Ma (Figure 3-7; 95% confidence, 2σ).

3.5.2. Okorusu

In the total alkali-silica diagram, Okorusu silicate samples include evolved nephelinitic, basanitic, tephriphonolitic and hawaiitic compositions. Two samples plot in the dacite and rhyolite fields but contain almost no alkalis (Figure 3-2b). Most Okorusu carbonatities are calcio-carbonatites (also commonly referred to as sövites) but three samples plot in the ferro-carbonatite field (Figure 3-2a). In contrast to Kalkfeld, Okorusu carbonatites have notably higher contents of CaO (31.5–54.2 wt%) and lower Fe_2O_3 contents (0.3–8.1 wt%). Fe_2O_3 correlates inversely with CaO and positively with MgO and MnO. Seven samples (six carbonatites and one hawaiite) have $\delta^{13}C$ and $\delta^{18}O$ values within the primary carbonatite field and also fall within the more restricted field for oceanic basalts with $\delta^{18}O$ (7.2 to 8.0‰) and $\delta^{13}C$ (-6.9 to -5.2‰) (Figure 3-7). Two of these carbonatites and the hawaiite also contain fluorite. Four fluorite-bearing carbonatite/silicate samples have higher $\delta^{18}O$ (8.5-16.8‰) and higher $\delta^{13}C$ (-5.1 to -2.5‰) with $\delta^{18}O$ and $\delta^{13}C$ (for two samples) being higher than typical mantle values.

Accordingly, Okorusu samples with mantle-like O and C isotopes are classified as Okorusu Group 1 carbonatite and silicate rocks, whereas samples with heavier O and C isotopes are classified as Okorusu Group 2 carbonatite and silicate rocks. According to the isotope composition, one silicate rock without O and C isotope data is added into Group 1 and two silicate rocks into Group 2. The Group 2 carbonatite and silicate rocks have significantly higher Sr (1904–68572 ppm vs. 2289–22781 ppm for Group 1), Ba (1150–9751 ppm vs. 730–2885 ppm) and light rare earth elements, e.g. La (165–2257 ppm vs. 75–354 ppm) concentrations and higher initial $^{87}Sr/^{86}Sr$ (0.7044–0.7047 vs.

0.7043–0.7044), but lower Zr, Hf, Nb, Ta and Pb isotope ratios (Figure 3-8). The fluorite-bearing samples largely overlap in composition with the non-fluorite-bearing samples, but $^{238}U/^{204}Pb$ and $^{232}Th/^{204}Pb$ are higher in the fluorite-bearing samples (up to 40 and 845, respectively, in the non-fluorite-bearing samples are <10 and <221, respectively, in the fluorite-bearing samples) (Figure 3-9).

3.5.3. Messum

The fairly fine-grained Messum olivine gabbro sample (NAM8) has a basanitic composition. It has high incompatible element abundances (Sr=837 ppm, Ba=954 ppm, La=39.7 ppm) but lower HREE compared to carbonatite-related silicates at Okorusu. It also has more radiogenic initial $^{143}Nd/^{144}Nd$ (0.51258) and less radiogenic Pb isotope ratios ($^{206}Pb/^{204}Pb$=17.95, $^{207}Pb/^{204}Pb$=15.56, $^{208}Pb/^{204}Pb$=37.72) than all Kalkfeld and Okorusu carbonatites and associated silicate rocks.

Table 3-1: Major and trace element concentrations from Cretaceous intrusive complexes

Sample name	NAM8	NM38	NM39	NM40	NM41A	NM41B	NM41C	NM42	NM43	NM44	NM46	NM47	NM48	NM49
Location	Messum	Kalkfeld	Kalkfeld	Kalkfeld	Kalkfeld	Kalkfeld	Kalkfeld	Kalkfeld	Kalkfeld	Kalkfeld	Kalkfeld	Kalkfeld	Kalkfeld	Kalkfeld
Rock type	basanite	ferro-carbonatite	iron-rich carbonatite	ferro-carbonatite	iron-rich carbonatite	iron-rich carbonatite	iron-rich carbonatite	silicocarbonatite	carbonatite	iron-rich carbonatite	carbonatite	iron-rich carbonatite	carbonatite	ferro-carbonatite
SiO2 [a]	43.36	5.65	6.58	4.79	4.54	4.73	5.66	27.02	11.04	5.21	12.65	4.40	12.45	4.00
Al2O3	15.08	0.50	0.31	0.23	0.55	0.80	0.32	6.64	0.34	0.43	0.54	0.65	0.31	0.35
Fe2O3	10.6	54.24	65.80	48.45	59.23	65.13	67.42	9.97	10.81	47.54	11.11	54.33	11.15	20.80
MgO	8.36	0.83	0.64	1.50	0.79	0.75	1.42	4.47	4.13	1.72	1.10	0.49	4.74	6.29
MnO	0.19	6.09	6.38	6.07	8.02	6.19	7.93	0.61	4.83	10.11	4.99	6.36	4.53	6.40
CaO	13.05	11.84	4.86	15.49	7.82	6.04	2.68	22.04	31.06	9.72	33.09	14.48	27.18	20.04
Na2O	4.00	-	-	-	-	-	-	0.38	-	-	-	-	-	-
K2O	2.00	0.07	0.05	0.05	0.08	0.15	0.05	1.79	0.09	0.09	0.26	0.06	0.08	0.29
TiO2	1.52	0.05	0.02	0.03	0.06	0.08	0.06	1.17	0.14	0.03	0.08	0.05	0.08	0.06
P2O5	0.38	1.04	0.05	0.08	0.16	0.19	0.09	0.70	0.03	0.06	0.03	0.03	0.05	0.43
SO3	0.03	0.55	0.56	0.47	0.26	0.13	0.24	0.12	4.31	0.24		0.05	3.35	0.35
L.O.I	0.98	16.49	12.25	20.09	15.91	13.13	11.97	20.66	34.59	19.19	32.74	17.97	34.66	35.98
SrO		1.67	1.24	1.02	0.57	0.40	0.43	0.54	2.61	1.68	2.76	0.25	2.99	4.28
BaO		1.53	1.81	2.20	2.27	2.40	1.97	4.03	0.33	4.21	0.65	0.93	1.77	1.07
Sum	99.55	100.00	100.00	100.00	100.00	100.00	100.00	100.00	100.00	100.00	100.00	100.00	100.00	100.00
Li	7.90	1.17	0.41	0.468	1.44	3.5	0.504	18.2	1.28	1.98	1.89	0.87	0.995	10.9
Sc	34.1	12.5	3.85	13	5.15	1.96	1.83	10.5	7.62	4.71	8.75	2.49	6.29	33.6
V	294						33.9		31.6		29.2		28	80.5
Cr	298						2.38		1.95		3.1		1.7	8.04
Co	46.6						14.2		5.84		4.79		4.38	17.3
Ni	160						0.729		0.57		0.827		0.272	0.676
Cu	119	0.953	0.765	0.76	0.814	0.714	0.196	23.9	1.71	0.652	1.74	1.27	0.437	10.1
Zn	76.6	1254	899	884	1230	1162	1651	134	2486	858	1610	762	2084	3243
Ga	17.1						15.3		87.6		110		87.3	155
Rb	48.7	4.48	1.59	1.35	1.89	9.37	0.265	24.4	0.986	4	2.82	0.533	1.1	9.47
Sr	837	14112	10476	8656	4854	3347	3600	4534	22110	14242	23308	2133	25296	36186
Y	24.9	208	68.3	110	138	96.7	57.1	61.8	135	102	216	126	188	269
Zr	153	5.12	2.43	14.6	2.1	9.38	1.69	203	21.8	8.6	32.6	5.31	17.3	51.1
Nb	84.0	201	59.3	530	130	89.7	65.4	177	1297	108	2158	141	1323	1986

Mo	2.13	506	159	13.5	222	45.9		4.38		125		149		
Cs	0.57	0.549	0.414	0.518	0.53	1.02	0.00639	1.53	0.0372	1.01	0.0212	0.217	0.0156	0.054
Ba	954	13664	16240	19745	20343	21517	17659	36131	2910	37728	5851	8310	15877	9606
La	39.70	558	293	445	323	185	382	557	3557	695	3857	241	3011	10194
Ce	74.20	1566	844	1002	1058	429	920	896	5472	2261	6685	740	5048	14257
Pr	8.31	333	230	164	173	93.4	152	89.6	513	340	660	126	492	1262
Nd	32.10	1308	935	611	745	513	667	301	1603	1284	2137	560	1610	3704
Sm	5.99	173	116	99.4	165	131	99.4	39.4	194	157	257	83.5	188	352
Eu	1.99	39.9	23.5	23.4	37.7	28.1	16.1	10	44.6	32.8	59	17	42.6	66.8
Gd	5.58	92.1	50.9	50.6	70.8	49.7	24.3	27.4	98.5	76.6	134	35.2	97.2	126
Tb	0.80	8.95	3.98	4.61	5.99	4.14	1.7	3.18	7.93	6.78	12	3.57	9.04	10.1
Dy	4.55	34.4	11.9	17.4	22.5	15.1	7.38	13.8	30.4	21.3	48.2	17.8	38.5	46.3
Ho	0.86	5.65	1.89	2.91	3.73	2.55	1.34	2.25	4.71	3.08	7.41	3.86	6.29	8.57
Er	2.26	15.5	5.91	8.08	10.1	7.38	3.98	5.18	12.2	8.31	18.2	10.8	15.7	24.9
Tm	0.32	2.14	0.808	1.21	1.42	1.13	0.606	0.629	1.74	0.985	2.45	1.37	2.05	3.55
Yb	2.00	13.5	5.83	8.67	9.42	7.73	3.92	3.6	11.5	6.32	14.8	7.42	12.4	22.4
Lu	0.30	1.81	0.863	1.27	1.28	1.08	0.549	0.475	1.7	0.836	2.09	0.868	1.72	3.18
Hf	3.00	0.292	0.125	0.547	0.146	0.36	0.0592	3.84	0.721	0.319	0.96	0.185	0.455	0.93
Ta	4.27	0.0344	0.021	0.115	0.0381	0.0374	0.0113	4.29	0.0942	0.0179	0.208	0.173	0.15	8.74
W	0.58	0.996	0.406	1.87	0.894	2.1	0.505	1.04	0.464	0.35	0.552	0.632	0.392	5.31
Tl	0.05	0.746	0.0992	0.0755	0.234	0.287		0.186		0.121		0.0927		
Pb	3.85	115	102	154	155	111	162	12.7	274	64.4	145	62.8	162	189
Th	4.64	733	481	1215	1015	816	597	20.9	193	729	240	652	110	820
U	1.10	2.48	2.46	1.47	0.401	0.725	0.824	3.68	1.23	1.22	1.14	1.07	0.923	17.1

Table 3-1: (continued)

Sample name	NM50	NM69	NM70	NM71	NM72	NM73	NM74	NM75	NM76	NM77C	NM78	NM79	NM80	NM81
Location	Kalkfeld	Okorusu	Okorusu	Okorusu	Okorusu	Okorusu	Okorusu	Okorusu	Okorusu	Okorusu	Okorusu	Okorusu	Okorusu	Okorusu
Rock type	carbonatite	phonotephrite	phonotephrite	hawaiite	tephriphonolite	carbonatite	carbonatite	fluorite-rich carbonatite	carbonatite	fluorite-rich carbonatite	carbonatite	carbonatite	carbonatite	carbonatite
SiO2 a	6.23	43.14	43.62	47.53	50.70	1.37	2.31	62.76	4.40	6.95	31.51	28.34	26.33	27.63
Al2O3	0.37	16.31	16.73	7.40	12.51	0.03	-	0.30	0.01	0.12	1.91	1.48	1.64	1.68
Fe2O3	8.39	8.91	8.74	9.91	5.79	0.42	0.43	1.39	0.90	0.51	1.73	8.12	4.46	7.34
MgO	8.41	4.30	4.33	5.53	4.44	0.07	0.07	0.68	0.13	0.20	1.32	4.96	2.70	4.48
MnO	5.21	0.24	0.21	0.75	0.30	0.19	0.25	0.51	0.19	0.47	0.43	0.56	0.51	0.58
CaO	21.99	8.76	8.51	16.59	8.12	51.31	50.97	17.68	48.51	50.45	44.17	31.50	39.76	34.53
Na2O	0.13	6.39	6.28	2.76	4.94	0.01	-	-	-	-	0.93	1.85	0.93	1.54
K2O	0.32	3.67	3.92	2.81	6.96	0.03	0.02	0.10	0.01	0.06	0.13	0.77	0.69	0.29
TiO2	0.06	1.05	1.03	0.58	0.78	0.01	0.01	0.02	-	0.01	0.10	0.13	0.10	0.13
P2O5	0.12	0.90	0.89	0.56	0.25	0.03	0.03	0.05	0.07	0.20	0.08	0.83	0.22	0.67
SO3	0.98	0.24	0.23	-	0.02	0.28	0.26	0.68	0.65	0.22	-	0.45	-	-
L.O.I	36.99	2.94	3.26	4.62	2.33	42.31	41.64	12.9	35.47	35.83	17.22	20.17	22.18	20.33
SrO	9.08							2.53		5.07				
BaO	2.70							1.09		0.13				
Sum	100.00	96.61	97.52	99.04	97.12	95.78	95.73	100.00	89.69	100.00	99.53	98.71	99.52	99.20
Li	1.92		10.4	40.1		1.13		52.9		1.84	4.69	44		21.5
Sc	17.2		12.3	11.3		0.671		1.74		0.766	3.12	7.72		4.09
V	43.8		154	328		2.27				4.08	18.2	274		157
Cr	5.95		96.7	74.1		2.61				2.2	10.1	29.6		10.2
Co	8.43		27.1	13.3		0.178				0.186	3.37	12.4		8.87
Ni	0.699		53.4	22.7		0.375				0.348	3.79	10.9		5.59
Cu	1.87		58.9	0.604		0.455		2.97		0.447	0.436	7.35		0.769
Zn	2935		90.5	252		8.72		60.1		4.9	77.6	194		233
Ga	342		17.1	12.5		5.65				4.39	6.4	7.47		6.81
Rb	4.66		123	71.5		1.09		4.63		0.237	4.23	18.9		8.91
Sr	76790		1904	2184		22781		21429		42886	6099	8431		8191
Y	201		26	20.2		33.1		169		20.1	23.5	21.4		20
Zr	69.7		207	198		9.94		12.2		3.09	45.1	106		60.1

Nb	1545	178	218	2.12	24.4	1.56	52.7	264	38.4
Mo					24.7				
Cs	0.0384	2.35	1.18	0.0852	0.266	0.00882	1.4	1.05	0.541
Ba	24219	2028	1776	2885	9751	1150	1795	1690	1812
La	23073	165	104	354	2257	248	316	201	209
Ce	25034	269	204	515	3492	386	393	336	324
Pr	1871	25.3	20.5	43	326	32.3	29.7	30.6	28.8
Nd	4924	80.1	62.9	121	982	90.9	74.3	90.7	83.3
Sm	497	10.6	7.83	11.7	110	8.87	7.72	9.76	8.85
Eu	111	3.02	1.97	3.01	28.6	2.37	2.34	2.5	2.45
Gd	236	7.45	5.06	7.72	78.3	5.6	5.09	6.2	5.66
Tb	15.7	0.926	0.634	0.908	8.73	0.663	0.626	0.693	0.63
Dy	47.6	4.93	3.4	4.87	34.9	3.42	3.48	3.48	3.22
Ho	6.52	0.92	0.669	0.98	5.52	0.63	0.686	0.68	0.605
Er	16.3	2.5	2.1	2.9	12.2	1.81	1.97	1.96	1.78
Tm	2.45	0.346	0.38	0.45	1.23	0.274	0.291	0.312	0.285
Yb	18.4	2.3	3.44	2.79	6	1.83	1.85	2.43	2.26
Lu	3.17	0.346	0.73	0.387	0.664	0.255	0.249	0.486	0.449
Hf	1.28	3.15	4.86	0.135	0.294	0.0466	1.08	1.3	0.991
Ta	0.118	7.19	0.632	0.00636	0.0759	0.0011	0.148	0.832	0.108
W	0.898	5.06	1.73	2.56	1.17	0.357	20	1.41	0.746
Tl					0.0659				
Pb	598	16.3	5.24	10.7	42.4	2.65	4.74	13.6	15
Th	555	21.1	17.3	7.34	146	14.4	11.8	24.8	15.4
U	1.19	5.49	0.534	0.595	2.85	2.17	0.182	2.14	0.133

Table 3-1: (continued)

Sample name	NM82A	NM82B	NM82C	NM83	NM84A	NM84B	NM85	NM86	NM87	NM88
Location	Okorusu	Okorusu	Okorusu	Okorusu	Okorusu	Okorusu	Okorusu	Okorusu	Okorusu	Okorusu
Rock type	fluorite-rich carbonatite	fluorite-rich carbonatite	fluorite-rich carbonatite	phonotephrite	fluorite-rich carbonatite	fluorite-rich hawaiite	fluorite-rich carbonatite	fluorite-rich carbonatite	carbonatite	carbonatite
SiO2 a	24.03	24.81	28.01	41.73	19.14	45.45	23.38	68.56	0.04	0.52
Al2O3	0.11	0.10	0.08	14.04	2.72	5.78	4.24	0.44	-	-
Fe2O3	1.69	1.50	1.27	8.83	4.40	11.95	6.21	0.56	0.27	0.34
MgO	2.03	1.77	1.52	7.93	2.57	7.18	3.77	0.07	0.06	0.07
MnO	0.22	0.19	0.15	0.26	0.35	0.66	0.41	0.12	0.18	0.16
CaO	50.35	51.78	54.19	10.99	33.87	16.53	31.93	18.43	50.61	51.35
Na2O	-	-	-	5.93	0.78	3.61	1.54	-	-	-
K2O	0.07	0.07	0.06	3.29	2.43	1.38	1.06	0.35	0.02	0.03
TiO2	0.01	0.01	0.01	0.97	0.27	0.25	0.14	0.02	0.01	0.01
P2O5	0.14	0.05	0.05	0.59	0.02	0.23	0.62	0.05	0.38	0.21
SO3	0.52	0.53	0.31	0.23	0.56	-	0.24	0.43	0.19	0.16
L.O.I	12.39	10.73	9.4	3.35	28.29	5.97	24.89	9.16	42.44	41.46
SrO	8.11	8.02	4.75					1.31		
BaO	0.84	1.00	0.52					0.93		
Sum	100.00	100.00	100.00	97.91	94.84	98.99	98.19	100.00	94.01	94.15
Li	4.33	4.33	1.35	21.4	27.6	122	71.8	65.5	0.347	
Sc	0.795	0.598	0.458	18.4	7.25	18.9	10.4	0.667	0.19	
V			7.36	176	171	539	193		1.97	
Cr			0.747	386	39.7	78.8	41.7		3.31	
Co			0.795	36	7.87	14.6	9.36		0.119	
Ni			1.7	171	6.37	12	12.7		0.311	
Cu	0.953	1.02	0.618	73.1	6.52	2.67	10.5	1.29	0.397	
Zn	25.8	24.3	17.5	111	112	270	148	9.76	2.91	
Ga			7.87	17.8	9.72	11.1	9.71		4.65	
Rb	10.8	10.5	0.189	87	49.5	47.3	38.3	9.68	0.636	
Sr	68572	67784	40128	2479	12782	2289	9456	11050	19332	
Y	51.5	47.1	30	28.9	32.5	9.19	17.6	29.8	27.7	
Zr	9.91	12.7	6.55	151	99.3	236	133	6.92	0.63	

Nb	11.7	10.5	9.27	161	2529	2247	419	5.5	12.9
Mo	69.9	43.6						18.4	
Cs	0.211	0.241	0.00381	1.6	0.511	3.41	2.62	0.211	0.0114
Ba	7560	8937	4660	3393	2671	730	1222	8339	2235
La	1108	1156	575	329	290	75	202	902	260
Ce	1595	1634	794	441	453	156	337	1444	400
Pr	137	137	63.2	35.6	36.7	14.2	30.4	131	34.5
Nd	360	353	164	96.9	102	40.5	88.3	382	101
Sm	29.1	27.4	13.6	11.3	10.8	4.66	9	35.4	10.4
Eu	6.51	6.07	3.29	3.28	2.77	1.26	2.32	8.06	2.61
Gd	20.5	19.4	8.19	7.82	7.12	2.66	5.43	22.3	6.76
Tb	2.04	1.94	0.843	0.921	0.864	0.317	0.588	2.21	0.782
Dy	7.57	7.11	4.13	5.02	4.85	1.64	2.91	6.78	4.13
Ho	1.36	1.25	0.779	0.946	0.999	0.315	0.538	0.971	0.82
Er	3.92	3.62	2.23	2.68	2.94	1.02	1.49	2.6	2.37
Tm	0.562	0.502	0.32	0.368	0.438	0.203	0.234	0.294	0.336
Yb	3.79	3.36	2.11	2.34	2.84	2.17	1.81	1.82	1.99
Lu	0.526	0.46	0.309	0.332	0.405	0.511	0.348	0.23	0.286
Hf	0.157	0.167	0.0671	2.42	1.36	3.47	1.65	0.135	0.0128
Ta	0.0203	0.0133	0.00365	6.14	9.31	6.68	1.56	0.0295	0.0324
W	0.47	0.55	0.288	6.19	3.8	1.43	2.42	0.117	0.156
Tl	0.0856	0.0756						0.11	
Pb	36.1	59.7	32.5	21.8	16.8	7.69	7.25	4.55	8.15
Th	114	145	79.5	24.5	195	197	50.3	54.2	2.53
U	17.6	16.6	8.71	3.64	29.1	20.4	4.76	2.64	0.186

- Lower than the limit of detection

[a] SiO2 contents of samples which are measured by ICP-OES are calculated by 100 minus all major elements including SrO and BaO.

Table 3-2: Sr-Nd-Pb-Hf isotope data from the Cretaceous intrusive complexes

Sample name	$^{143}Nd/^{144}Nd$	$^{143}Nd/^{144}Ndi$	$^{87}Sr/^{86}Sr$	$^{87}Sr/^{86}Sri$	$^{206}Pb/^{204}Pb$	$^{207}Pb/^{204}Pb$	$^{208}Pb/^{204}Pb$	$^{206}Pb/^{204}Pb_i$	$^{207}Pb/^{204}Pb_i$	$^{208}Pb/^{204}Pb_i$	$\delta^{18}O$	$\delta^{13}C$
NAM8	0.512679	0.512582	0.70466	0.7043	18.3243	15.5731	38.2331	17.952	15.555	37.717		
NM39	0.512550	0.512579	0.703874	0.7040	18.4269	15.6137	46.0788	18.516	15.617	42.225	17.13	-1.77
NM41B	0.512697	0.512599	0.703796	0.7039	18.3746	15.6098	46.0367	18.506	15.615	39.847	19.89	1.68
NM41C	0.512591	0.512595	0.703782	0.7039	18.3846	15.6047	44.8780	18.525	15.611	41.964	22.47	4.07
NM42	0.512583	0.512605	0.703829	0.7039	19.1478	15.6445	39.7330	18.572	15.614	38.639	16.92	-5.88
NM43	0.512537	0.512568	0.703926	0.7040	18.3752	15.6098	38.9300	18.511	15.616	38.610	15.85	-3.10
NM44	0.512569	0.512598	0.703771	0.7039	18.4234	15.6092	53.8970	18.524	15.613	43.331	19.71	-1.19
NM46	0.512537	0.512568	0.703889	0.7040	18.3875	15.6079	39.9275	18.515	15.613	38.835	19.84	-4.00
NM47	0.512589	0.512593	0.703872	0.7040	18.3697	15.6079	50.2914	18.473	15.612	41.007	17.11	-4.34
NM48	0.512539	0.512574	0.703924	0.7040	18.3777	15.6102	38.9038	18.511	15.616	38.606	11.98	-4.01
NM49	0.512529	0.512585	0.703831	0.7039	18.6143	15.6171	42.2141	18.531	15.612	38.848	12.20	-4.10
NM50	0.512511	0.512561	0.703917	0.7040	18.3676	15.6100	39.0618	18.509	15.616	38.564	12.88	-3.74
NM70	0.512498	0.512425	0.705008	0.7047	18.4652	15.5830	38.8603	18.032	15.562	38.313		
NM71	0.512537	0.512468	0.704560	0.7044	18.6802	15.6214	39.8644	18.542	15.615	38.458		
NM73	0.512553	0.512498	0.704390	0.7044	18.5822	15.6158	38.8580	18.504	15.612	38.560	7.41	-5.18
NM75	0.512542	0.512479	0.704514	0.7045	18.4181	15.5990	40.0599	18.324	15.594	38.592	8.45	-2.46
NM77C	0.512547	0.512492	0.704672	0.7047	19.2412	15.6423	40.3832	18.162	15.590	38.040	12.88	-5.08
NM79	0.512553	0.512492	0.704328	0.7043	18.7615	15.6246	39.4361	18.553	15.614	38.661	7.54	-6.56
NM81	0.512543	0.512483	0.704358	0.7043	18.5336	15.6138	39.0787	18.515	15.613	38.637	8.02	-6.01
NM82A	0.512554	0.512507	0.704574	0.7046	18.8834	15.6255	39.7256	18.245	15.594	38.377	16.78	-3.61
NM83	0.512504	0.512439	0.704631	0.7044	18.5084	15.5959	39.0350	18.289	15.585	38.555		

NM84A	0.512543	0.512483	0.704358	0.7043	21.5282	15.7578	45.4132	19.021	15.636	39.921	7.99	-6.77
NM84B	0.512557	0.512493	0.704455	0.7043	23.5752	15.8598	55.7359	19.178	15.646	41.875	7.49	-6.89
NM85	0.512552	0.512495	0.704308	0.7043	19.6287	15.6673	42.4314	18.733	15.624	39.345	7.23	-6.89
NM86	0.512524	0.512471	0.704606	0.7046	18.8777	15.6136	43.8130	18.080	15.575	38.477	15.51	-4.66
NM87	0.512557	0.512499	0.704304	0.7043	18.5722	15.6156	38.7042	18.536	15.614	38.564	7.31	-6.75

3.6. Discussion

3.6.1. Secondary processes

As described above, Kalkfeld carbonatites have very high iron contents. Although the exact process of ore genesis at Kalkfeld is still unclear, it is most likely caused by circulation of carbonatitic fluids or fluid-rich melts at the final stage of the intrusion ((Bühn and Rankin, 1999)). The low-Fe-Mn ferrocarbonatites show mantle-like $\delta^{13}C_{PDB}$ (-5.9 to -3.1‰ with four of six samples in the mantle range) but elevated $\delta^{18}O_{SMOW}$ (12.0–19.9‰), indicating low-temperature alteration/recrystallization of the carbonate. The heavy $\delta^{18}O_{SMOW}$ (17.1–22.5‰) and $\delta^{13}C_{PDB}$ (-4.3 to 4.1‰) values of the Kalkfeld high-Fe-Mn ferrocarbonatites and the positive correlation between them (Figure 3-5) could indicate either high-temperature alteration and/or the assimilation of sedimentary carbonate. Both processes could also have caused the dilution of trace elements, such as LREE, Sr, Zr, Hf, Nb, Ta, Pb and U. The initial $^{87}Sr/^{86}Sr$, $^{143}Nd/^{144}Nd$, $^{206}Pb/^{204}Pb$ and $^{207}Pb/^{204}Pb$ isotope ratios of high-Fe-Mn ferrocarbonatites (0.70386–0.70397, 0.51258–0.51260, 18.476–18.527, 15.612–15.618, respectively), however, are very similar or identical to those of the low-Fe-Mn ferrocarbonatites (0.70387–0.70402, 0.51256–0.51261, 18.512–18.575, 15.613–15.617). If sedimentary carbonates were involved, they do not appear to have affected the radiogenic isotopic composition of the Kalkfeld carbonatites, which is unlikely since the high-Fe-Mn Kalkfeld ferro-carbonatites have lower concentrations of Sr, Nd and Pb than the low-Fe-Mn ferro-carbonatites. Therefore, the high-Fe-Mn ferro-carbonatites are likely to have been influenced by high-temperature hydrothermal fluids, whereas the low-Fe-Mn ferro-carbonatites only appear to have been affected by low-temperature alteration.

As reported by Bühn and Rankin (1999), Th concentrations of the Kalkfeld carbonatites are very high. Although most trace element abundances in the high-Fe-Mn carbonatites appear to have been diluted by secondary processes, their Th concentrations (481-1215 ppm) and their $^{232}Th/^{204}Pb$ ratios (263-898) extend to much higher values than in the low-Fe-Mn carbonatites (21-820 ppm; 45-299 ppm, respectively) (Figure 3-6). The high-Fe-Mn carbonatites also have very high and variable initial $^{208}Pb/^{204}Pb$ isotope ratios (39.8-43.3) compared to the low and restricted range found in the low-Fe-Mn Kalkfeld carbonatites (38.6-38.8).

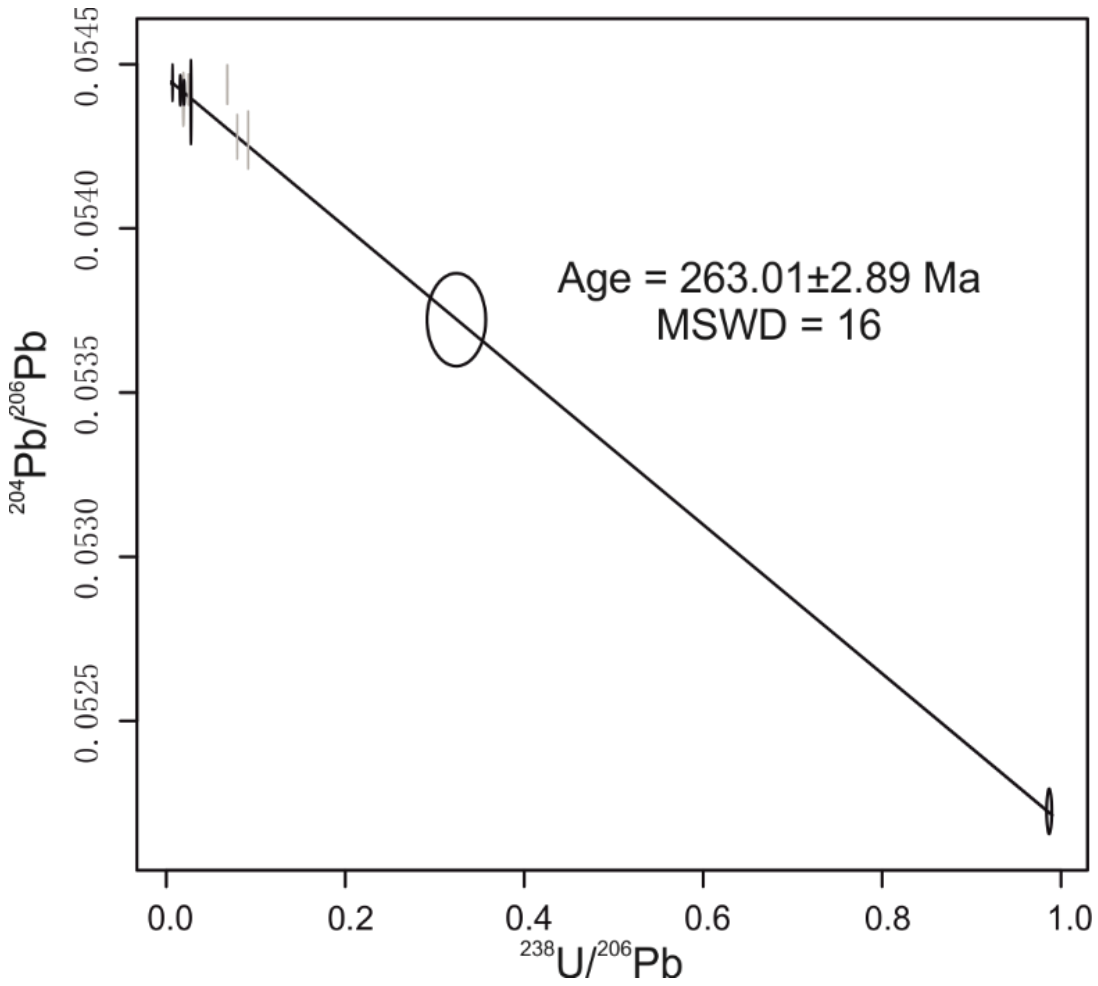

Figure 3-7: U/Pb isochron dating for Kalkfeld carbonatites with linear regression calculated by the maximum likelihood model of IsoplotR ((Vermeesch, 2018)).The iron-rich carbonatites (grey color) are not used for isochron calculation but still fit with the linear trend. The sizes of symbols correspond to their 2σ (external) analytical uncertainties. The error on the age is given as 2σ.

The high $^{232}Th/^{204}Pb$ ratios result in very rapid ingrowth of the thorogenic ^{208}Pb isotope. Considering the uniformity of $^{87}Sr/^{86}Sr$, $^{143}Nd/^{144}Nd$, $^{206}Pb/^{204}Pb$ and $^{207}Pb/^{204}Pb$ isotope ratios, it would be expected that the correction for radiogenic ingrowth would have generated a similar range in the high-Fe-Mn Kalkfeld carbonatites also. The low-Fe-Mn ferro-carbonatite sample (NM49) with the highest $^{232}Th/^{204}Pb$ ratio of 299, yielded an initial $^{208}Pb/^{204}Pb$ of 38.8, yet the high-Fe-Mn ferro-carbonatite (NM41C) with the lowest $^{232}Th/^{204}Pb$ ratio of 263, yielded a much higher initial $^{208}Pb/^{204}Pb$ of 42.0, reflecting its significantly higher measured $^{208}Pb/^{204}Pb$ (44.9 vs. 42.2). Therefore, we do not believe that the much higher and very variable initial $^{208}Pb/^{204}Pb$ ratios of the high-Fe-Mn ferro-carbonatites reflect imprecise determination of the high parent/daughter ratios.

It is also unlikely that the Fe-Mn-enrichment happened significantly later than the emplacement of the Kalkfeld ferro-carbonatites. Had this been the case and we use the older emplacement age of 242 Ma for the age correction, then we would expect an over-correction of the initial $^{208}Pb/^{204}Pb$ isotope ratio, rather than an under-correction resulting in initial $^{208}Pb/^{204}Pb$ ratios that are too high. It is also unlikely that the Fe-Mn-rich fluids had high $^{208}Pb/^{204}Pb$, but similar $^{87}Sr/^{86}Sr$, $^{143}Nd/^{144}Nd$, $^{206}Pb/^{204}Pb$ and $^{207}Pb/^{204}Pb$ to the low-Fe-Mn ferro-carbonatites or that there is a component (such as carbonate sediments) with very high $^{208}Pb/^{204}Pb$ but almost no Sr, Nd, ^{206}Pb and ^{207}Pb that could have contaminated the carbonatites. Apatite, which is a common mineral in carbonatites, can have very high Th (520 ppm) and $^{232}Th/^{204}Pb$ (>6000 ppm) but more modest $^{238}U/^{204}Pb$ (33) as demonstrated for fluorapatite (OK8-3) from Okorusu ((Bühn et al., 2003)). Nevertheless, despite the very large $^{232}Th/^{204}Pb$ and measured $^{208}Pb/^{204}Pb$ (75), the initial $^{208}Pb/^{204}Pb$ for the fluorapatite ($^{206}Pb/^{204}Pb$=18.60, $^{207}Pb/^{204}Pb$=15.61, $^{208}Pb/^{204}Pb$=37.3) is not as high as Kalkfeld high-Fe-Mn carbonatites.

In conclusion, the easiest explanation for the under-correction of the initial $^{208}Pb/^{204}Pb$ isotope ratios in the high-Fe-Mn Kalkfeld carbonatites is that there was a recent loss of Th from these samples, possibly due to low-temperature alteration related to unroofing of the ferro-carbonatite intrusives. Why this recent alteration only appears to have affected the high-Fe-Mn Kalkfeld carbonatites is enigmatic, although the overall higher Th and Th/Pb would make these carbonatites more susceptible to an improper age-correction for $^{208}Pb/^{204}Pb$ ratios. Since the history of secondary processes at Kalkfeld are only poorly known, in particular the timing of different secondary events and their effects on the Th/Pb ratios, we will not consider the isotope ratios of the high Fe-Mn carbonatites for the discussion of potential mantle source and magma genesis.

Hydrothermal fluid circulation also appears to have taken place at Okorusu, forming primarily fluorite (but also Mn oxide, quartz and calcite) rather than iron ore. The Group 2 carbonatites and silicate rocks from Okorusu contain much higher abundances of trace elements, such as Sr, Ba and LREE and to a lesser extent Pb and Th (Figure 3-4), but lower contents of Zr and Hf, which is opposite to the depleted composition of normal sedimentary carbonate and secondary carbonatite ((Frimmel and Lane, 2005)). Bühn et al. (2003) studied the partition coefficients of fluorite and hydrothermal fluids and suggested that Ba, Sr and the LREE are more incompatible than HREE in fluorite

leading to the enriched Ba, Sr and steep REE patterns of carbonatites coexisting with fluorites. After correction for radiogenic ingrowth to 132 Ma, the four fluorite-free samples yield a very restricted range in Pb isotopes ($^{206}Pb/^{204}Pb$=18.504-18.553; $^{207}Pb/^{204}Pb$= 15.612-15.614; $^{208}Pb/^{204}Pb$=38.560-38.661). Three fluorite-bearing samples with mantle-like C isotopes, however, have large error of U/Pb ratios and elevated initial $^{206}Pb/^{204}Pb$. Hence, we do not plot them in the Pb isotope diagrams.

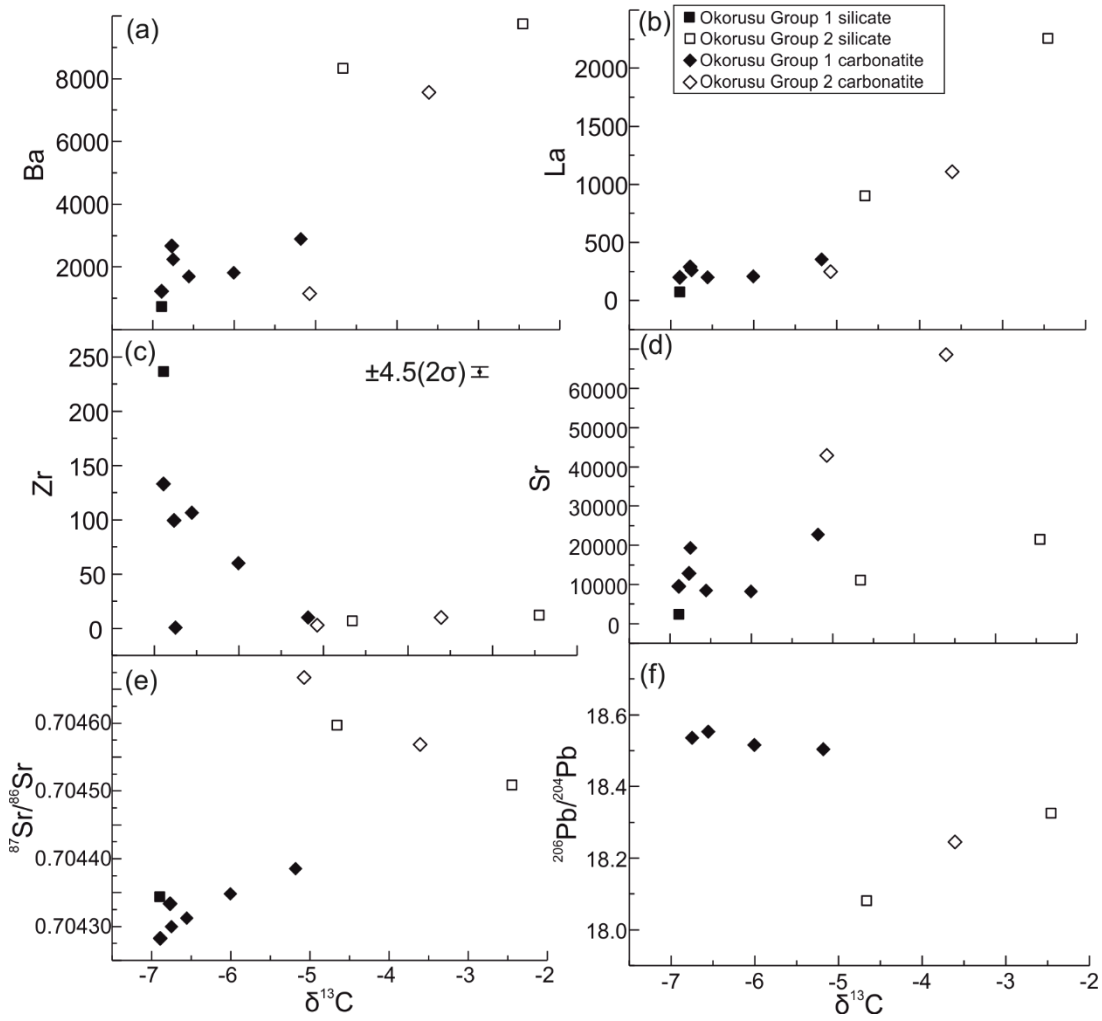

Figure 3-8: $\delta^{13}C$ vs (a) Ba, (b) La, (c) Zr, (d) Sr (e) initial $^{87}Sr/^{86}Sr$ and (f) initial $^{206}Pb/^{204}Pb$ of samples from Okorusu. All trace element concentrations are reported by ppm. The 2 standard deviation (2σ) of most samples are smaller than the symbols, except when marked by error bars.

Fluorite-bearing Okorusu samples with elevated $\delta^{18}O_{SMOW}$ and/or $\delta^{13}C_{PDB}$ (Okorusu Group 2 samples) have highly variable Sr, Ba and LREE, extending to very high concentrations. High Sr concentration is a characteristic of carbonatites and distinguishes them from sedimentary carbonates, which have low abundances for Sr and the REE elements. The Sr ranges from 8,200 to 21,400 ppm in the primary Group

1 Okorusu samples, but gets as high as 68,500 ppm in the Group 2 carbonatite samples. Clearly, samples with such high Sr concentration are difficult to contaminate whether by magmatic (e.g. crustal assimilation) or secondary processes. Pb concentrations vary widely but can get up to 60 ppm. The initial isotope ratios of the two Group 2 silicate samples almost completely overlap the Group 2 carbonatite sample. Whereas Nd isotope ratios of Group 2 rocks (0.51243–0.51251) overlap with the Group 1 Okorusu rocks (0.51247–0.51250), the Pb isotope ratios are lower (18.03–18.32 vs 18.50–18.55) and the Sr isotope ratio is higher (0.70428–0.70439 vs 0.70444–0.70467) in the Group 2 rocks. Due to trace element abundances similar to primary mantle carbonatites, we believe that the stable and radiogenic isotopic composition of the Group 2 carbonatites and silicate rocks reflects those of their mantle source.

3.6.2. Magma origin of carbonatites and silica-unsaturated rocks

The origin of carbonatitic and closely related silica-undersaturated magmas of Namibia is still debated. Their trace element and isotopic composition can be used to draw constraints on their magma source. For some of the silica-unsaturated intrusive complexes (such as Okenyenya), a derivation from lithospheric mantle has been suggested ((Bell and Simonetti, 1996; Le Roex and Lanyon, 1998)). Lamprophyres from Okenyenya in central Damaraland (Figure 3-1) share the same isotopic composition as entrained lower crustal xenoliths. It is difficult to distinguish whether the respective carbonatites were generated by small-degree melting of lithosphere that was metasomatized immediately before by early plume-derived alkaline and carbonatitic melts, or if the heat of the arriving plume caused melting of much earlier metasomatized, fertile lithosphere ((Bell et al., 1998; le Roex and Class, 2014)). In addition, the mantle xenoliths (lherzolite) found in Damara belt ((Class and le Roex, 2006; le Roex and Class, 2014)) have distinct composition from Kalkfeld and Okorusu carbonatites (Figure 10) Therefore, the SCLM should not be the sole origin of Damara alkaline and carbonatitic magmas.

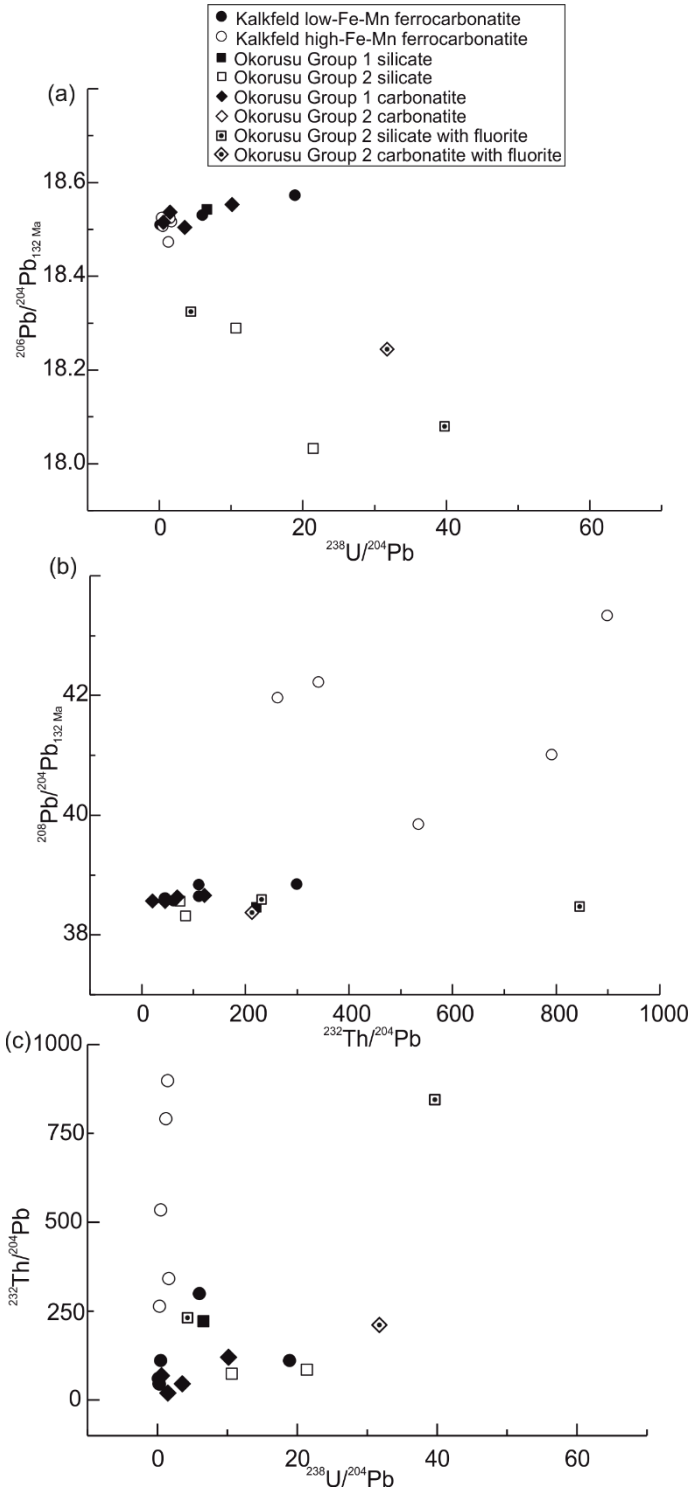

Figure 3-9: (a) $^{238}U/^{204}Pb$ vs $^{206}Pb/^{204}Pb_{132Ma}$ (b) $^{232}Th/^{204}Pb$ vs $^{208}Pb/^{204}Pb_{132Ma}$ and (c) $^{238}U/^{204}Pb$ vs $^{232}Th/^{204}Pb$. High-Fe-Mn Kalkfeld and Group 2 Okorusu show wider range of $^{238}U/^{204}Pb$ and $^{232}Th/^{204}Pb$ ratios, as well as $^{206}Pb/^{204}Pb_{132Ma}$ and $^{206}Pb/^{204}Pb_{132Ma}$ (isotope ratios at 132 Ma, see section 3.4.2 for explanation).

We note that the Okenyenya carbonatites have lower $^{208}Pb/^{204}Pb$ but higher $^{207}Pb/^{204}Pb$ and $^{143}Nd/^{144}Nd$, which is typical of low-Ti Etendeka Doros/Tafelkop-type Etendeka

lavas derived from the Tristan-Gough plume head ((Trumbull, 2003; Zhou et al., 2020)). Even if the Okenyenya rocks are derived from metasomatized SCLM, their isotopic composition is dominated by the Doros/Tafelkop isotopic signature and thus must have been ultimately derived from the Tristan-Gough plume head (Le Roex and Lanyon, 1998). Therefore, regardless if the carbonatites are derived directly from a mantle plume or by plume-metasomatized SCLM, the isotopic composition of the carbonatites most likely reflects the composition of the underlying plume material. In the investigated area of the Damara belt, most carbonatites and silica-undersaturated rocks show the Gough-type isotopic EM1 composition, e.g. Okorusu, Paresis, Etaneno and Osongombo (Figure 3-10). Contemporaneous and isotopically slightly distinct magmas (the low-Ti Doros/Tafelkop-type, characterized by less radiogenic $^{208}Pb/^{204}Pb$ and more radiogenic $^{143}Nd/^{144}Nd$ at a given $^{206}Pb/^{204}Pb$; Figure 3-11) include the Doros basaltic intrusions ((Owen-Smith et al., 2017)), Tafelkop basalts ((Ewart et al., 1998a; Gibson et al., 2000)), Okenyenya lamprophyres ((Le Roex and Lanyon, 1998)) and Messum basanites and basalts ((Zhou et al., 2020) and this study). Below we will discuss a possible model to explain the origin of the two isotopic distinct lava types.

3.6.3. Association of the Okorusu and Kalkfeld magmatism with the Etendeka-Tristan/Gough plume event

As outlined above, major and trace element concentrations of carbonatites can be significantly modified by hydrothermal fluids. Therefore, we exclude the high-Fe-Mn Kalkfeld samples, which have been significantly affected by secondary processes, from further discussion and evaluate the origin of the remaining carbonatite and silicate rocks from Kalkfeld and Okorusu, which show restricted Sr, Nd and Pb isotope ratios (Figure 3-10 and 11).

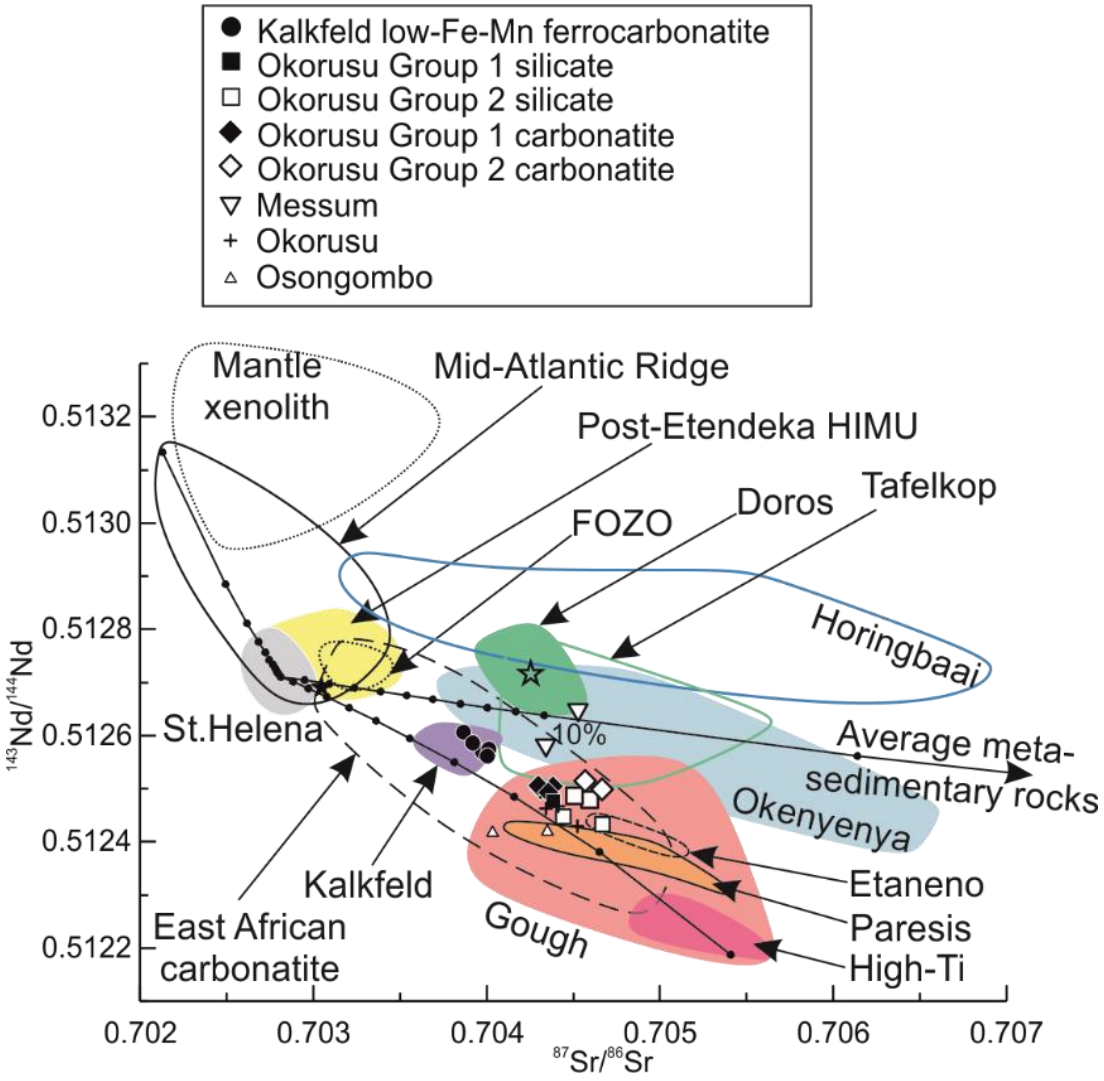

Figure 3-10: Initial $^{87}Sr/^{86}Sr$ vs $^{143}Nd/^{144}Nd$ ratios (at 132 Ma, see section 3.4.2 for explanation) of the investigated rocks with calculations of possible mixing trends. Bulk mixing lines are calculated for end-member compositions of Gough-type sample NAM21 from northern Etendeka high-Ti flood basalt ((Zhou et al., 2020)), the most depleted sample from the Mid-Atlantic-Ridge representing upper mantle (CHRRI88-016-101; Class and Lehnert, 2012), the average value of St.Helena HIMU ((Chaffey et al., 1989; Salters and White, 1998; Thirlwall, 2000; Willbold and Stracke, 2006, 2010)), and an upper continental crustal component (average composition of the Nosib and Swakop metasedimentary group samples; (McDermott and Hawkesworth, 1990)). Reference field sources: Gough ((Hoernle et al., 2015; Homrighausen et al., 2019; Rohde et al., 2013)), Doros ((Owen-Smith et al., 2017; Stroncik et al., 2017)), High-Ti Etendeka ((Zhou et al., 2020)) Mid-Atlantic-Ridge (Class and Lehnert, 2012), post-Etendeka HIMU volcanism ((Homrighausen et al., 2018a; Homrighausen et al., 2018b)), Okenyenya, Kalkfeld, Okorusu, Osongombo ((Le Roex and Lanyon, 1998)), East African carbonatite ((Bell and Tilton, 2001; Kalt et al., 1997)), Etaneno ((Bühn and Trumbull, 2003)), Paresis ((Mingram et al., 2000; Trumbull, 2004)), Tafelkop ((Ewart et al., 1998a; Gibson et al., 2000)), Horingbaai ((Thompson et al., 2001)), mantle xenolith ((Class and le Roex, 2006; le Roex and Class, 2014)), FOZO is represented by the basalts from Rurutu (young volcanics), Atiu and Mauke island ((Chauvel et al., 1997; Nakamura and Tatsumoto, 1988; Stracke et al., 2005)). The green star represents sample 412 ((Stroncik et al., 2017)). Its sampling location is shown in Figure 3-1.

Group 1 and 2 rocks from Okorusu overlap with the Gough-type EM1 composition in all isotope diagrams. The primitive mantle-like $\delta^{18}O_{SMOW}$ and $\delta^{13}C_{PDB}$ values of the Okorusu Group 1 carbonatites (Figure 3-5) indicate that the primary Okorusu magmas were not significantly affected by crustal contamination, consistent with their very high Sr, Nd and Pb concentrations. The 127 Ma age of the Okorusu ((Milner et al., 1995)) fall within the Etendeka flood basalt event. Therefore, it is likely that the Okorusu magmatism shares a common (plume) source with Gough-type Etendeka flood basalts. Group 2 rocks from Okorusu plot in the Gough-type EM1 field also, but have more radiogenic Sr and less radiogenic Pb isotope ratios than the Group 1 carbonatites, pointing towards an even more extreme EMI type composition than for the Group 1 carbonatites. Although the elevated $\delta^{18}O_{SMOW}$ and $\delta^{13}C_{PDB}$ values could reflect lower crustal assimilation in these rocks, their very high Sr (1900–68600 ppm), Nd (80–980 ppm) concentrations, higher than in Group 1 Okorusu carbonatites, require a contaminant with extremely high concentrations of these elements or very low degree melts from such material. Also, this contaminant would dominate the Sr, Nd and Pb isotopic composition of the contaminated carbonatite. The higher C and O isotope ratios, as well as more radiogenic Sr and less radiogenic Pb, could also reflect the presence of ancient subducted carbonate either in the lithospheric mantle or the Tristan-Gough plume head, whereas the extremely enriched trace elements could have been concentrated by the low degree of melting. We note that the Group 2 rocks contain purple fluorites. This phenomenon accord with the result of Bühn et al. (2003), suggesting that the purple fluorite was more influenced by crustal components, leading to the elevated O and C isotope ratios. Therefore, Group 2 Okorusu rocks could be derived ultimately from the same source as the Group 1 Okorusu rocks but reflect the addition of a crustal component, most likely in the lithospheric mantle or plume.

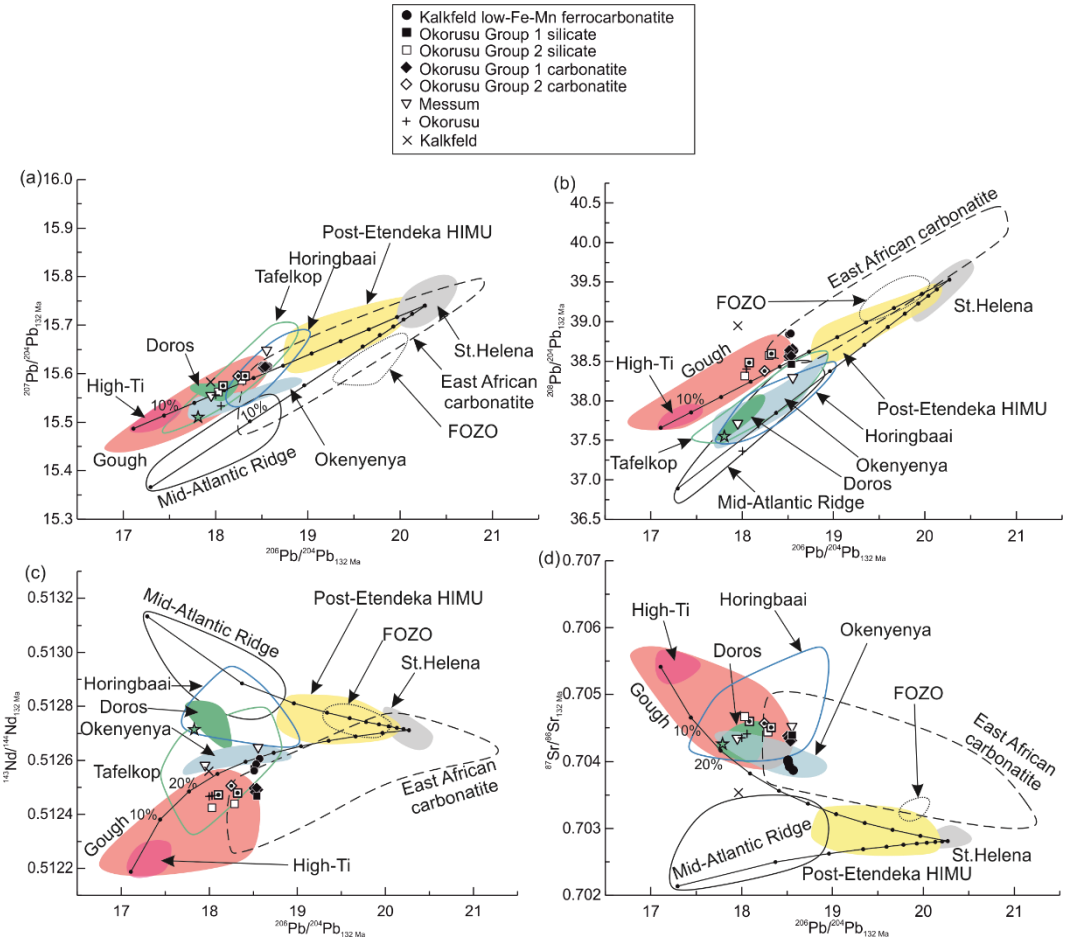

Figure 3-11: Initial (a) $^{206}Pb/^{204}Pb$ vs $^{207}Pb/^{204}Pb$, (b) $^{206}Pb/^{204}Pb$ vs $^{208}Pb/^{204}Pb$, (c) $^{206}Pb/^{204}Pb$ vs $^{143}Nd/^{144}Nd$ and (d) $^{206}Pb/^{204}Pb$ vs $^{87}Sr/^{86}Sr$ at 132 Ma (see section 3.4.2 for explanation). Symbols, data sources are the same as in Figure 3-10. Bulk mixing lines are calculated for end-member compositions of Gough-type sample NAM21 from northern Etendeka high-Ti flood basalt ((Zhou et al., 2020)), the most depleted sample from the Mid-Atlantic-Ridge representing upper mantle (CHRRI88-016-101; Class and Lehnert, 2012) and the average value of St.Helena HIMU ((Chaffey et al., 1989; Salters and White, 1998; Thirlwall, 2000; Willbold and Stracke, 2006, 2010)). The projection of reference field to 132 Ma is explained in section 3.4.2.

In contrast, the Kalkfeld low-Fe-Mn carbonatites are Triassic in age (c. 263 Ma) and have higher $^{143}Nd/^{144}Nd$ than high-Ti (Gough-type) Etendeka lavas and $^{208}Pb/^{204}Pb$ ratios higher than the low-Ti (Doros) type Etendeka lavas (Figure 3-10 and 11). Therefore they cannot be related to the younger Etendeka-Tristan-Gough plume event. A direct derivation of the Kalkfeld carbonatites from crustal sources or depleted upper mantle (N-MORB source) can also be rejected because of their unradiogenic $^{87}Sr/^{86}Sr$ and radiogenic Pb isotopes, respectively. Instead, their moderately isotopically enriched composition overlaps with the mixing trend between EM1 and an endmember with

radiogenic Pb isotopes (e.g. HIMU or FOZO) similar to carbonatite composition from the East African Rift ((Bell and Tilton, 2001)).

In conclusion, the two carbonatite complexes were derived from distinct magma sources. The Okorusu (Group 1) rocks have compositions similar to the high-Ti (Gough-type) Etendeka magmatism, while Kalkfeld has a distinct composition from both the low- and high-Ti Etendeka lavas.

3.6.4. Do isotopic variations of Etendeka igneous rocks reflect a spatial zonation within the Etendeka-Tristan-Gough plume head?

Lateral spatial zonation of the Etendeka-Tristan-Gough plume head was already proposed to explain the division of Etendeka flood basalts into Gough-type (high-Ti basalts) in northern Etendeka and Doros/Tafelkop-type (low-Ti basalts) in southern Etendeka ((Marsh et al., 2001; Zhou et al., 2020)). As shown in this study, the same signatures can also be distinguished in Damara carbonatites. Syn-Etendeka Gough-type carbonatites are only found in the northeastern part and Doros/Tafelkop-type carbonatites exclusively in the southwestern part of the Damara belt (see Figure 3-1). Combining our new data from the Damara carbonatites with the previously published data from other magmatic rocks of the Etendeka event, we can advance the previous model of a spatially zoned plume head.

Gough-type magmatism lasted from ~137-127 Ma throughout the Paraná-Etendeka flood basalt province (Figure 3-1). As noted before, Gough-type magma dominates the entire history of the Etendeka-Tristan/Gough plume. During the plume head stage, Gough-type magmatism took place across a large area from northwestern Namibia (Khumib/high-Ti flood Etendeka flood basalts) to the Central Namibian Damara carbonatites (Okorusu at 127 Ma). The production of Doros/Tafelkop-type magmas started slightly later in western Central Namibia and shows a narrower spatial distribution. The Doros/Tafelkop -type magma erupted from ~133-123 Ma (most low-Ti basalts were erupted in a burst between 133-131 Ma, but the Messum intrusives at 127 Ma and Okenyenya rocks between 129-123 Ma) supporting the previous conclusion that these two domains erupted contemporaneously during the plume head stage. Looking at the geographic distribution of the two different magma types (Figure 3-1), it appears that Gough-type rocks could form a horseshoe-shaped zone that

encircles the Doros/Tafelkop-type rocks. The recognition of this distribution is significantly hampered by the erosion of many of the eruption products, although feeder dikes remain in western Central Namibia, e.g. Henties Bay-Outjo dike swarm (Figure 3-1). In any case, the new data from this study combined with published data (Le Roex and Lanyon, 1998) indicate that the simple lateral zonation between these magma domains between Möwe and Terrance Bay ((Marsh et al., 2001; Zhou et al., 2020)) needs to be refined.

Campbell and Griffiths (1990) have described a concentrically zoned plume head forming a bullseye (if looking from above) with depleted ambient mantle in the middle surrounded by more enriched mantle. Such a structure can form when hotter, more buoyant plume material ascends more rapidly, so that any surrounding plume material spreads radially outwards and wraps into a spherical vortex leading to a concentrically zoned plume head. This zonation would then roughly be reflected by plume head melts that are eventually emplaced within/on the overlying lithosphere above the respective compositional zones. At Etendeka, the isotpically more depleted Doros-type (in comparison with the Gough-Type), except in 207Pb/204Pb, is apparently not derived from the upper mantle, due to high $^{3}He/^{4}He$ ratios ((Stroncik et al., 2017)) and high potential temperatures ((Jennings et al., 2019)) attributed to rocks of Doros composition. Also, the Doros/Tafelkop composition does not plot on a mixing line between the enriched Gough composition and depleted upper mantle on the Pb isotope diagrams. On the uranogenic Pb isotope diagram, the Doros/Tafelkop lavas fall within and extend to more radiogenic Pb isotope ratios having higher 207Pb/204Pb than Mid-Atlantic MORB, whereas on the thorogenic diagram they overlap the Atlantic MORB field nearly completely having lower $^{208}Pb/^{204}Pb$ than the Gough field (Figure 3-11), as noted by Zhou et al (2020). Since both Gough and Doros domains are apparently intrinsic to the plume, we prefer a concentrically zoned plume head. Such a structure could reflect compositional heterogeneity in the plume source region and might persist from the bottom to the top of the plume stem provided ascent by laminar flow (e.g. (Farnetani and Samuel, 2005; Hoernle et al., 2000; Huang et al., 2011; Weis et al., 2011)). The Gough component has been interpreted to be derived from the Large Low-Velocity Shear Province (LLSVP) at the base of the lower mantle (Rohde et al., 2013; Hoernle et al., 2015; Homrighausen et al., 2019). It is not clear if the Doros/Tafelkop material

is derived from the LLSVP (or layer on it) or from the ambient mantle (Zhou et al., 2020).

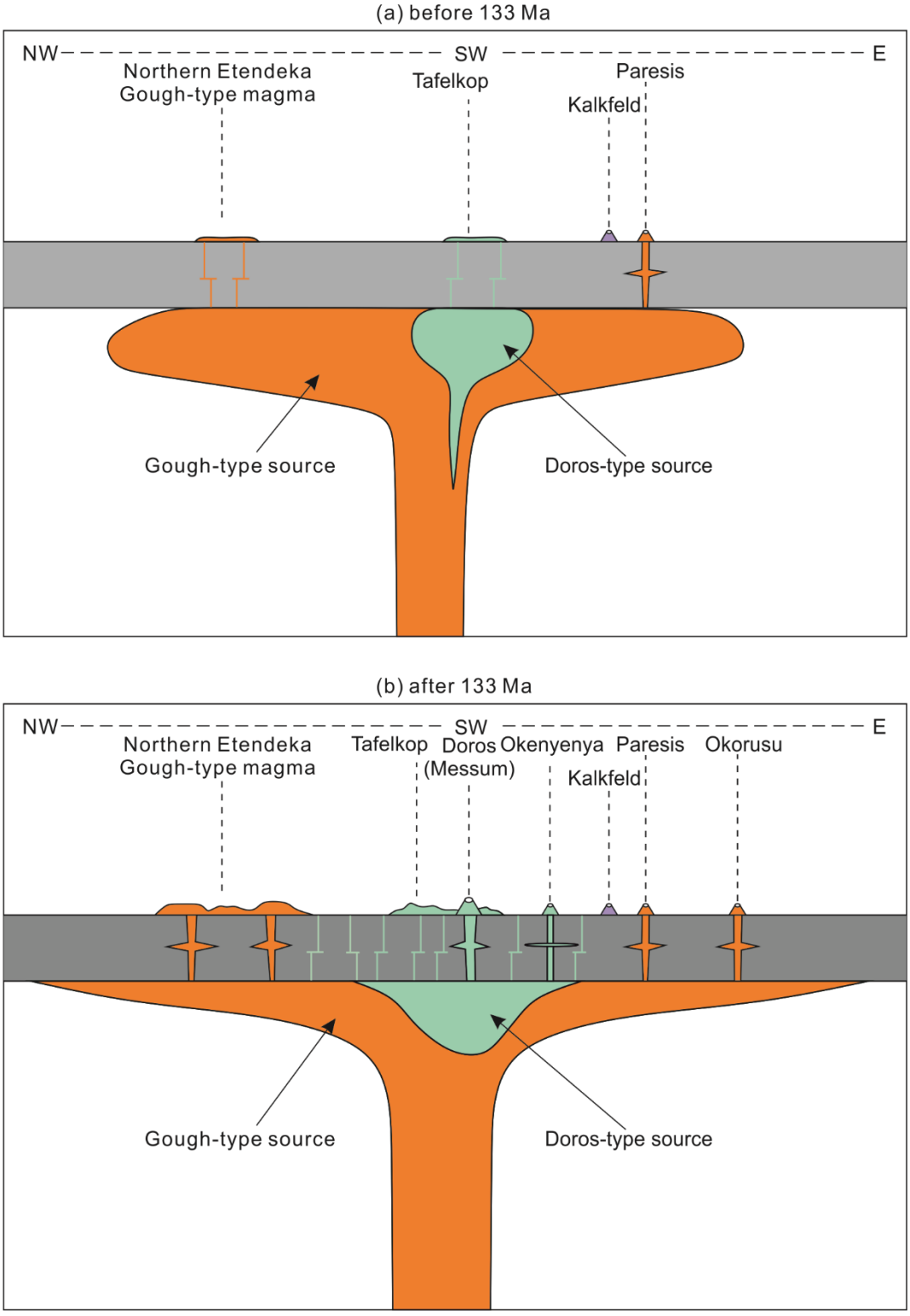

Figure 3-12: Cartoon of Etendeka-Tristan-Gough plume-related magmatism, including the occurrence of plateau basalts, silica-undersaturated rocks and carbonatites. Location of cross section of lithosphere and uppermost mantle is shown in Figure 3-1 (black line).(a) ≥133 Ma:

the concentrically zoned plume head arrived at the base of African continental lithosphere, generating first Gough-type volcanism in northern Etendeka and Paresis and the Doros rocks). (b) <133 Ma: melting within the plume head produces large volumes of flood basalts in northern Etendeka, Tafelkop and subsequent intrusions such as Okenyenya and Okorusu. The intrinsic concentric compositional zonation of the plume head is reflected by the geochemical variation of its eruption products, with an outer semi-circle of Gough-type material (orange) encircling rocks of Doros/Tafelkopf composition (green). The Triassic Kalkfeld carbonatites predate the arrival of the plume and are not associated with the Cretaceous volcanism and thus are shown in a different color.

Interestingly, the Doros-type composition was not found in igneous rocks that are associated with the subsequent plume tail stage ((Zhou et al., 2020)), pointing to a transient supply of Doros material in the plume source or to different plume dynamics. Recently, Jones et al. (2019) have discussed the ascent of plume components with different densities. The less dense component is more buoyant allowing continuous advection. If this buoyant component has a large volume (as in the plume head), it can entrain and carry the denser material in the center of the upwelling plume. The less-voluminous upwelling during the subsequent plume tail stage, however, does not provide enough buoyancy to carry such dense material upwards eventually resulting in the cessation of magma production from this respective composition. Accordingly, the Doros/Tafelkop magmas could originate from denser plume lithologies, entrained and carried within a plume head consisting predominately of Gough-type mantle. Such a model is supported by the exclusive occurrence of Doros/Tafelkop-type magmatism in western Central Namibia, in a more central portion of the plume head. Magmatism with Gough-type composition will then be arranged in an outer ring reflected by the horseshoe-shaped pattern of occurrence in northern and Central Namibia (Figure 3-1 and 12). Although this model is somewhat speculative, it would nicely explain the complex but transitional zonation of magmatism associated with the Etendeka-Gough/Tristan plume head stage and the subsequent dominance of lavas with Gough-type composition along the Walvis Ridge, proposed to have formed by melts from the low-volume plume tail.

The Kalkfeld carbonatites have a very similar Sr and Pb isotopic composition to the Gough-like Okorusu carbonatites, except that they have higher Nd isotope ratios, similar to Doros/Tafelkop lavas. Thus, they appear to represent a similar, yet different compositional flavor than either Gough or Doros/Tafelkop. Although a lithospheric origin for the Kalkfeld carbonatites cannot be discounted, their similarity in

composition to the younger carbonatites suggests they may have been derived from a similar source and thus may ultimately have been derived from an earlier upwelling beneath the Damara Belt from another part of the LLSVP.

3.7. Conclusions

The Kalkfeld carbonatite intrusive complex (263 ± 3 Ma) predates the Etendeka flood basalt event and the other carbonatite/silica-undersaturated silicate complexes in the Damara belt. The low-Fe-Mn carbonatites have higher CaO, but lower $\delta^{13}C$ ratios and trace element contents. Whereas, the high-Fe-Mn carbonatites show higher Fe_2O_3+MnO contents and significantly elevated $^{232}Th/^{204}Pb$ and initial $^{208}Pb/^{204}Pb$ ratios. All Kalkfeld carbonatites have a similar, yet distinct isotopic composition from Etendeka high- and low-Ti plume head lavas. It has intermediate Sr, Nd, Pb isotopes between EM1 and FOZO/HIMU endmember in all isotope diagrams.

The Okorusu carbonatites, which are located east of the Etendeka area. Group 1 Okorusu rocks have mantle-like O and C isotopes, yielding lower trace elements, initial $^{87}Sr/^{86}Sr$ ratios but higher initial $^{206}Pb/^{204}Pb$ ratios. Both Group 1 and 2 have Gough-type isotopic composition similar to the adjacent Paresis and Etaneno silica-undersaturated intrusions as well as high-Ti Gough type basalts in northern Etendeka, Walvis Ridge and the Gough subtrack of the Guyot Province of the Tristan-Gough hotspot track in the south Atlantic. Gabbro and basanite dike from the Messum intrusive complex show a Doros/Tafelkop-type composition, which is the dominate mantle flavor in southwestern Etendeka (western Central Namibia), characterized by unradiogenic $^{208}Pb/^{204}Pb$ and radiogenic $^{143}Nd/^{144}Nd$ at a given $^{206}Pb/^{204}Pb$.

Combining the ages, locations and geochemistry of carbonatite/silica-undersaturated silicate complexes in the Damara Belt (this study and the literature), the distribution of Gough and Doros/Tafelkop-type compositions in southern Etendeka has been constrained. The Doros/Tafelkop volcanic/plutonic complexes occur along the western Central Namibian coast and are surrounded by Gough-type high-Ti Etendeka basalts to the northwest and the Okorusu, Paresis, Etaneno and Ondurakorume carbonatite complexes in Central Namibia, forming half of a possible bullseye pattern. The Doros/Tafelkop-type magma with high $^{3}He/^{4}He$ isotope ratios was derived from the lower mantle and entrained in the center of a large buoyant Gough-type plume head.

Thereafter, the lower-volume plume tail (Gough-type) did not have enough excess buoyancy to entrain significant Doros/Tafelkop-type material.

References

Bell, K., 2001. Carbonatites: relationships to mantle-plume activity. Special Papers-Geological Society of America, 267-290.

Bell, K., Kjarsgaard, B., Simonetti, A., 1998. Carbonatites—into the twenty-first century. J. Petrol. 39, 1839-1845.

Bell, K., Simonetti, A., 1996. Carbonatite magmatism and plume activity: implications from the Nd, Pb and Sr isotope systematics of Oldoinyo Lengai. J. Petrol. 37, 1321-1339.

Bell, K., Tilton, G., 2001. Nd, Pb and Sr isotopic compositions of East African carbonatites: evidence for mantle mixing and plume inhomogeneity. J. Petrol. 42, 1927-1945.

Braunger, S., Marks, M.A.W., Wenzel, T., Chmyz, L., Guitarrari Azzone, R., Markl, G., 2020. Do carbonatites and alkaline rocks reflect variable redox conditions in their upper mantle source? Earth Planet. Sci. Lett. 533, 116041.

Bühn, B., Rankin, A., 1999. Composition of natural, volatile-rich Na–Ca–REE− Sr carbonatitic fluids trapped in fluid inclusions. Geochim. Cosmochim. Acta 63, 3781-3797.

Bühn, B., Schneider, J., Dulski, P., Rankin, A.H., 2003. Fluid–rock interaction during progressive migration of carbonatitic fluids, derived from small-scale trace element and Sr, Pb isotope distribution in hydrothermal fluorite. Geochim. Cosmochim. Acta 67, 4577-4595.

Bühn, B., Trumbull, R., 2003. Comparison of petrogenetic signatures between mantle-derived alkali silicate intrusives with and without associated carbonatite, Namibia. Lithos 66, 201-221.

Burke, K., Ashwal, L.D., Webb, S.J., 2003. New way to map old sutures using deformed alkaline rocks and carbonatites. Geology 31, 391-394.

Campbell, I.H., Griffiths, R.W., 1990. Implications of mantle plume structure for the evolution of flood basalts. Earth Planet. Sci. Lett. 99, 79-93.

Cangelosi, D., Broom-Fendley, S., Banks, D., Morgan, D., Yardley, B., 2019. LREE redistribution during hydrothermal alteration at the Okorusu carbonatite complex, Namibia. Mineral. Mag., 1-54.

Chaffey, D., Cliff, R., Wilson, B., 1989. Characterization of the St Helena magma source. Geological Society, London, Special Publications 42, 257-276.

Chauvel, C., McDonough, W., Guille, G., Maury, R., Duncan, R., 1997. Contrasting old and young volcanism in Rurutu Island, Austral chain. Chem. Geol. 139, 125-143.

Cimen, O., Kuebler, C., Simonetti, S.S., Corcoran, L., Mitchell, R., Simonetti, A., 2019. Combined boron, radiogenic (Nd, Pb, Sr), stable (C, O) isotopic and geochemical investigations of carbonatites from the Blue River Region, British Columbia (Canada): Implications for mantle sources and recycling of crustal carbon. Chem. Geol. 529, 119240.

Class, C., le Roex, A.P., 2006. Continental material in the shallow oceanic mantle—How does it get there? Geology 34, 129.

Class, C., Lehnert, K., 2012. PetDB Expert MORB (Mid-Ocean Ridge Basalt) Compilation, Version1.0. Interdisciplinary Earth Data Alliance (IEDA). https://doi .org /10 .1594 /IEDA /100060.

Clemson, J., Cartwright, J., Booth, J., 1997. Structural segmentation and the influence of basement structure on the Namibian passive margin. Journal of the Geological Society 154, 477-482.

Deines, P., 1989. Stable isotope variations in carbonatites, in: Bell, K. (Ed.), Carbonatites: Genesis and Evolution. Unwin Hyman, london, pp. 301-359.

Erlank, A., Marsh, J., Duncan, A., Miller, R.M., Hawkesworth, C., Betton, P., Rex, D., 1984. Geochemistry and petrogenesis of the Etendeka volcanic rocks from SWA/Namibia. Special Publication of Geological Society of South Africa 13, 195-245.

Ernst, R.E., Bell, K., 2010. Large igneous provinces (LIPs) and carbonatites. Mineral. Petrol. 98, 55-76.

Ewart, A., Milner, S., Armstrong, R., Duncan, A., 1998a. Etendeka volcanism of the Goboboseb Mountains and Messum Igneous Complex, Namibia. Part II: Voluminous quartz latite volcanism of the Awahab magma system. J. Petrol. 39, 227-253.

Ewart, A., Milner, S., Armstrong, R., Dungan, A., 1998b. Etendeka volcanism of the Goboboseb mountains and Messum Igneous Complex, Namibia. Part I: geochemical evidence of early cretaceous Tristan plume melts and the role of crustal contamination in the Paraná–Etendeka CFB. J. Petrol. 39, 191-225.

Farnetani, C., Samuel, H., 2005. Beyond the thermal plume paradigm. Geophys. Res. Lett. 32.

Frimmel, H.E., Lane, K., 2005. Geochemistry of carbonate beds in the Neoproterozoic Rosh Pinah Formation, Namibia: Implications on depositional setting and hydrothermal ore formation. South African Journal of Geology 108, 5-18.

Garbe-Schönberg, C.D., 1993. Simultaneous determination of thirty-seven trace elements in twenty-eight international rock standards by ICP-MS. Geostandards and Geoanalytical Research 17, 81-97.

Garbe-Schönberg, D., Müller, S., 2014. Nano-particulate pressed powder tablets for LA-ICP-MS. J. Anal. At. Spectrom. 29, 990-1000.

Gibson, S., Thompson, R., Dickin, A., 2000. Ferropicrites: geochemical evidence for Fe-rich streaks in upwelling mantle plumes. Earth Planet. Sci. Lett. 174, 355-374.

Goscombe, B., Hand, M., Gray, D., Mawby, J., 2003. The metamorphic architecture of a transpressional orogen: the Kaoko Belt, Namibia. J. Petrol. 44, 679-711.

Govindaraju, K., 1994. 1994 compilation of working values and sample description for 383 geostandards. Geostandards and Geoanalytical Research 18, 1-158.

Green, D.H., Wallace, M.E., 1988. Mantle metasomatism by ephemeral carbonatite melts. Nature 336, 459-462.

Hagni, R.D., 2007. Petrologic controls for fluorspar deposits at Okorusu, Namibia: Hydrothermal replacement of carbonatite, marble and fenite, Proceedings of the 40th Forum on the Geology of Industrial Minerals, Indiana Geological Survey, Occasional Paper, pp. 51-63.

Hagni, R.D., 2012. The replacement of carbonatite and marble by fluorspar ores and its relationship to beneficiation problems at Okorusu, Namibia, Proceedings of the 10th International Congress for Applied Mineralogy (ICAM). Springer, pp. 297-305.

Hammouda, T., Keshav, S., 2015. Melting in the mantle in the presence of carbon: Review of experiments and discussion on the origin of carbonatites. Chem. Geol. 418, 171-188.

Harrison, L.N., Weis, D., Garcia, M.O., 2017. The link between Hawaiian mantle plume composition, magmatic flux, and deep mantle geodynamics. Earth Planet. Sci. Lett. 463, 298-309.

Hegenberger, W., 1988. Karoo sediments of the Erongo Mountains, their environmental setting and correlation. Communications of the Geological Survey of South West Africa/Namibia 4, 51-57.

Hoernle, K., Abt, D.L., Fischer, K.M., Nichols, H., Hauff, F., Abers, G.A., Van Den Bogaard, P., Heydolph, K., Alvarado, G., Protti, M., 2008. Arc-parallel flow in the mantle wedge beneath Costa Rica and Nicaragua. Nature 451, 1094.

Hoernle, K., Hauff, F., Kokfelt, T.F., Haase, K., Garbe-Schönberg, D., Werner, R., 2011. On- and off-axis chemical heterogeneities along the South Atlantic Mid-Ocean-Ridge (5–11°S): Shallow or deep recycling of ocean crust and/or intraplate volcanism? Earth Planet. Sci. Lett. 306, 86-97.

Hoernle, K., Rohde, J., Hauff, F., Garbe-Schonberg, D., Homrighausen, S., Werner, R., Morgan, J.P., 2015. How and when plume zonation appeared during the 132 Myr evolution of the Tristan Hotspot. Nat. Commun. 6, 7799.

Hoernle, K., Tilton, G., 1991. Sr-Nd-Pb isotope data for Fuerteventura (Canary Islands) basal complex and subaerial volcanics: applications to magma genesis and evolution. Schweizerische Mineralogische und Petrographische Mitteilungen 71, 5-21.

Hoernle, K., Tilton, G., Le Bas, M.J., Duggen, S., Garbe-Schönberg, D., 2002. Geochemistry of oceanic carbonatites compared with continental carbonatites: mantle recycling of oceanic crustal carbonate. Contrib. Mineral. Petrol. 142, 520-542.

Hoernle, K., Werner, R., Morgan, J.P., Garbe-Schönberg, D., Bryce, J., Mrazek, J., 2000. Existence of complex spatial zonation in the Galápagos plume. Geology 28, 435-438.

Hofmann, A.W., 1988. Chemical differentiation of the Earth: the relationship between mantle, continental crust, and oceanic crust. Earth Planet. Sci. Lett. 90, 297-314.

Homrighausen, S., Hoernle, K., Geldmacher, J., Wartho, J.-A., Hauff, F., Portnyagin, M., Werner, R., van den Bogaard, P., Garbe-Schönberg, D., 2018a. Unexpected HIMU-type late-stage volcanism on the Walvis Ridge. Earth Planet. Sci. Lett. 492, 251-263.

Homrighausen, S., Hoernle, K., Hauff, F., Geldmacher, J., Wartho, J.-A., van den Bogaard, P., Garbe-Schönberg, D., 2018b. Global distribution of the HIMU end member: Formation through Archean plume-lid tectonics. Earth-Science Reviews 182, 85-101.

Homrighausen, S., Hoernle, K., Hauff, F., Wartho, J.-A., van den Bogaard, P., Garbe-Schönberg, D., 2019. New age and geochemical data from the Walvis Ridge: The temporal and spatial diversity of South Atlantic intraplate volcanism and its possible origin. Geochim. Cosmochim. Acta 245, 16-34.

Homrighausen, S., Hoernle, K., Zhou, H., Geldmacher, J., Wartho, J.-A., Hauff, F., Werner, R., Jung, S., Morgan, J.P., 2020. Paired EMI-HIMU hotspots in the South Atlantic—Starting plume heads trigger compositionally distinct secondary plumes? Science Advances 6, eaba0282.

Hou, Z., Liu, Y., Tian, S., Yang, Z., Xie, Y., 2015. Formation of carbonatite-related giant rare-earth-element deposits by the recycling of marine sediments. Scientific reports 5, 10231.

Huang, S., Hall, P.S., Jackson, M.G., 2011. Geochemical zoning of volcanic chains associated with Pacific hotspots. Nature Geoscience 4, 874-878.

Jacques, G., Hauff, F., Hoernle, K., Werner, R., Uenzelmann-Neben, G., Garbe-Schönberg, D., Fischer, M., 2019. Nature and origin of the Mozambique Ridge, SW Indian Ocean. Chem. Geol. 507, 9-22.

Jennings, E.S., Gibson, S.A., Maclennan, J., 2019. Hot primary melts and mantle source for the Paraná-Etendeka flood basalt province: New constraints from Al-in-olivine thermometry. Chem. Geol. 529, 119287.

Jerram, D., Mountney, N., Holzförster, F., Stollhofen, H., 1999. Internal stratigraphic relationships in the Etendeka Group in the Huab Basin, NW Namibia: understanding the onset of flood volcanism. Journal of Geodynamics 28, 393-418.

Jochum, K.P., Garbe-Schönberg, D., Veter, M., Stoll, B., Weis, U., Weber, M., Lugli, F., Jentzen, A., Schiebel, R., Wassenburg, J.A., 2019. Nano-powdered calcium carbonate reference materials: Significant progress for microanalysis? Geostandards and Geoanalytical Research 43, 595-609.

Jones, T.D., Davies, D.R., Sossi, P.A., 2019. Tungsten isotopes in mantle plumes: Heads it's positive, tails it's negative. Earth Planet. Sci. Lett. 506, 255-267.

Kalt, A., Hegner, E., Satir, M., 1997. Nd, Sr, and Pb isotopic evidence for diverse lithospheric mantle sources of East African Rift carbonatites. Tectonophysics 278, 31-45.

Kasch, K., 1983. Continental collision, suture progradation and thermal relaxation: a plate tectonic model for the Damara orogen in central Namibia.

Keller, J., Hoefs, J., 1995. Stable Isotope Characteristics of Recent Natrocarbonatites from Oldoinyo Lengai, in: Bell, K., Keller, J. (Eds.), Carbonatite Volcanism: Oldoinyo Lengai and the Petrogenesis of Natrocarbonatites. Springer Berlin Heidelberg, Berlin, Heidelberg, pp. 113-123.

Kogarko, L.N., Veselovskiy, R.V., 2019. Geodynamic origin of carbonatites from the absolute paleotectonic reconstructions. Journal of Geodynamics 125, 13-21.

Kramm, U., Körner, T., Kittel, M., Baier, H., Sindern, S., 2017. Triassic emplacement age of the Kalkfeld complex, NW Namibia: implications for carbonatite magmatism and its relationship to the Tristan Plume. International Journal of Earth Sciences 106, 2797-2813.

Le Maitre, R., Bateman, P., Dudek, A., Keller, J., Lameyre, J., Le Bas, M., Sabine, P., Schmid, R., Sorensen, H., Streckeisen, A., 1989. A classification of igneous rocks and glossary of terms. Recommendations of the IUGS Subcommission on the Systematics of Igneous rocks. London: Blackwell Scientific Publications.

Le Maitre, R.W., Streckeisen, A., Zanettin, B., Le Bas, M., Bonin, B., Bateman, P., 2005. Igneous rocks: a classification and glossary of terms: recommendations of the International Union of Geological Sciences Subcommission on the Systematics of Igneous Rocks. Cambridge University Press.

le Roex, A., Class, C., 2014. Metasomatism of the Pan-African lithospheric mantle beneath the Damara Belt, Namibia, by the Tristan mantle plume: geochemical evidence from mantle xenoliths. Contrib. Mineral. Petrol. 168.

Le Roex, A.P., Lanyon, R., 1998. Isotope and Trace Element Geochemistry of Cretaceous Damaraland Lamprophyres and Carbonatites, Northwestern Namibia: Evidence for Plume—Lithosphere Interactions. J. Petrol. 39, 1117-1146.

Marsh, J., Ewart, A., Milner, S., Duncan, A., Miller, R.M., 2001. The Etendeka Igneous Province: magma types and their stratigraphic distribution with implications for the evolution of the Paraná-Etendeka flood basalt province. Bulletin of Volcanology 62, 464-486.

McDermott, F., Hawkesworth, C., 1990. Intracrustal recycling and upper-crustal evolution: a case study from the Pan-African Damara mobile belt, central Namibia. Chem. Geol. 83, 263-280.

Miller, R.M., 1983. The Pan-African Damara Orogen of South West Africa/Namibia, Evolution of the Damara Orogen of South West Africa/Namibia.

Miller, R.M., 2008. The geology of Namibia. Ministry of Mines and Energy, Geological Survey.

Milner, S., Le Roex, A., O'CONNOR, J., 1995. Age of Mesozoic igneous rocks in northwestern Namibia, and their relationship to continental breakup. Journal of the Geological Society 152, 97-104.

Milner, S.C., Le Roex, A.P., Watkins, R.T., 1993. Rb-Sr age determinations of rocks from the Okenyenya igneous complex, northwestern Namibia. Geological Magazine 130, 335-343.

Mingram, B., Trumbull, R., Littman, S., Gerstenberger, H., 2000. A petrogenetic study of anorogenic felsic magmatism in the Cretaceous Paresis ring complex, Namibia: evidence for mixing of crust and mantle-derived components. Lithos 54, 1-22.

Müller, B., 1996. Ring complexes of the Damaraland Alkaline Province, Namibia in the light of geochemistry and Rb-Sr, U-Pb, Pb-Pb isotopes. ETH Zurich.

Nakamura, Y., Tatsumoto, M., 1988. Pb, Nd, and Sr isotopic evidence for a multicomponent source for rocks of Cook-Austral Islands and heterogeneities of mantle plumes. Geochim. Cosmochim. Acta 52, 2909-2924.

O'Connor, J.M., Duncan, R.A., 1990. Evolution of the Walvis Ridge-Rio Grande Rise Hot Spot System: Implications for African and South American Plate motions over plumes. J. Geophys. Res. 95, 17475.

Owen-Smith, T., Ashwal, L., Sudo, M., Trumbull, R., 2017. Age and petrogenesis of the Doros Complex, Namibia, and implications for early plume-derived melts in the Paraná–Etendeka LIP. J. Petrol. 58, 423-442.

Peate, D.W., 1997. The Paraná-Etendeka Province. Large igneous provinces: Continental, oceanic, and planetary flood volcanism, 217-245.

Pirajno, F., Phillips, D., Armstrong, R.A., 2000. Volcanology and eruptive histories of the Erongo volcanic complex and the Paresis igneous complex, Namibia: implications for mineral deposit styles. Commun Geol Surv Namibia 12, 301-312.

Raab, M.J., Brown, R.W., Gallagher, K., Carter, A., Weber, K., 2002. Late Cretaceous reactivation of major crustal shear zones in northern Namibia: constraints from apatite fission track analysis. Tectonophysics 349, 75-92.

Ray, J.S., Pande, K., Bhutani, R., Shukla, A.D., Rai, V.K., Kumar, A., Awasthi, N., Smitha, R., Panda, D.K., 2013. Age and geochemistry of the Newania dolomite carbonatites, India: implications for the source of primary carbonatite magma. Contrib. Mineral. Petrol. 166, 1613-1632.

Renne, P.R., Glen, J.M., Milner, S.C., Duncan, A.R., 1996. Age of Etendeka flood volcanism and associated intrusions in southwestern Africa. Geology 24, 659-662.

Rohde, J., Hoernle, K., Hauff, F., Werner, R., O'Connor, J., Class, C., Garbe-Schonberg, D., Jokat, W., 2013. 70 Ma chemical zonation of the Tristan-Gough hotspot track. Geology 41, 335-338.
Salters, V.J., White, W.M., 1998. Hf isotope constraints on mantle evolution. Chem. Geol. 145, 447-460.
Sibley, D., 1978. Dolomite textures, Sedimentology. Springer Berlin Heidelberg, Berlin, Heidelberg, pp. 370-375.
Song, W., Xu, C., Smith, M.P., Kynicky, J., Huang, K., Wei, C., Zhou, L., Shu, Q., 2016. Origin of unusual HREE-Mo-rich carbonatites in the Qinling orogen, China. Sci Rep 6, 37377.
Stracke, A., Bizimis, M., Salters, V.J., 2003. Recycling oceanic crust: Quantitative constraints. Geochem. Geophys. Geosyst. 4.
Stracke, A., Hofmann, A.W., Hart, S.R., 2005. FOZO, HIMU, and the rest of the mantle zoo. Geochem. Geophys. Geosyst. 6, n/a-n/a.
Stroncik, N.A., Trumbull, R.B., Krienitz, M.-S., Niedermann, S., Romer, R.L., Harris, C., Day, J., 2017. Helium isotope evidence for a deep-seated mantle plume involved in South Atlantic breakup. Geology 45, 827-830.
Thirlwall, M., 2000. Inter-laboratory and other errors in Pb isotope analyses investigated using a 207Pb–204Pb double spike. Chem. Geol. 163, 299-322.
Thompson, R., Gibson, S., Dickin, A., Smith, P., 2001. Early Cretaceous basalt and picrite dykes of the southern Etendeka region, NW Namibia: windows into the role of the Tristan mantle plume in Paraná–Etendeka magmatism. J. Petrol. 42, 2049-2081.
Trumbull, R., 2004. Oxygen and neodymium isotope evidence for source diversity in Cretaceous anorogenic granites from Namibia and implications for A-type granite genesis. Lithos 73, 21-40.
Trumbull, R., Emmermann, R., Bühn, B., Gerstenberger, H., Mingram, B., Schmitt, A., Volker, F., 2000. Insights on the genesis of the Cretaceous Damaraland igneous complexes in Namibia from a Nd-and Sr-isotopic perspective. Communications of the Geological Survey of Namibia 12, 313-324.
Trumbull, R.B., 2003. The Petrology of Basanite-Tephrite Intrusions in the Erongo Complex and Implications for a Plume Origin of Cretaceous Alkaline Complexes in Namibia. J. Petrol. 44, 93-112.
Trumbull, R.B., Reid, D.L., de Beer, C., van Acken, D., Romer, R.L., 2007. Magmatism and continental breakup at the west margin of southern Africa: A geochemical comparison of dolerite dikes from northwestern Namibia and the Western Cape. South African Journal of Geology 110, 477-502.
Trumbull, R.B., Vietor, T., Hahne, K., Wackerle, R., Ledru, P., 2004. Aeromagnetic mapping and reconnaissance geochemistry of the Early Cretaceous Henties Bay-Outjo dike swarm, Etendeka Igneous Province, Namibia. Journal of African Earth Sciences 40, 17-29.
Valley, J.W., Taylor, H.P., O'Neil, J.R., 2018. Stable isotopes in high temperature geological processes. Walter de Gruyter GmbH & Co KG.
van Wyk de Vries, B., Merle, O., 1996. The effect of volcanic constructs on rift fault patterns. Geology 24, 643-646.
Van Zijl, P.J., 1962. The Geology, Structure and Petrology of the Alkaline Intrusions of Kalkfeld and Okorusu and the Invaded Damara Rocks. Pro Ecclesia.
Vermeesch, P., 2018. IsoplotR: A free and open toolbox for geochronology. Geoscience Frontiers 9, 1479-1493.

Weis, D., Garcia, M.O., Rhodes, J.M., Jellinek, M., Scoates, J.S., 2011. Role of the deep mantle in generating the compositional asymmetry of the Hawaiian mantle plume. Nature Geoscience 4, 831-838.

Willbold, M., Stracke, A., 2006. Trace element composition of mantle end-members: Implications for recycling of oceanic and upper and lower continental crust. Geochem. Geophys. Geosyst. 7.

Willbold, M., Stracke, A., 2010. Formation of enriched mantle components by recycling of upper and lower continental crust. Chem. Geol. 276, 188-197.

Workman, R.K., Hart, S.R., 2005. Major and trace element composition of the depleted MORB mantle (DMM). Earth Planet. Sci. Lett. 231, 53-72.

Zhou, H., Hoernle, K., Geldmacher, J., Hauff, F., Homrighausen, S., Garbe-Schönberg, D., Jung, S., 2020. Geochemistry of Etendeka magmatism: Spatial heterogeneity in the Tristan-Gough plume head. Earth Planet. Sci. Lett. 535, 116123.

Ziegler, U.R.F., 1992. Preliminary results of geochemistry, Sm-Nd and Rb-Sr studies of post-Karoo carbonatite complexes in Southern Africa. Schweizerische Mineralogische und Petrographische Mitteilungen 72, 135-142.

Chapter 4.

A HIMU volcanic belt along the SW African coast (83–49 Ma): New geochemical clues to deep mantle dynamics from carbonatite and silica-undersaturated complexes in Namibia

This chapter has been submitted to GCA for peers review in December 2020.

Authors: **H.Zhou**[a*], K.Hoernle[a, b], J.Geldmacher[a], F.Hauff[a], S.Homrighausen[a], D.Garbe-Schönberg[b], S. Jung[c], I. Bindemann[d]

[a]GEOMAR Helmholtz Centre for Ocean Research Kiel, Wischhofstr. 1-3, 24148 Kiel, Germany

[b]Institute of Geosciences, Kiel University, Ludewig-Meyn-Str. 10, 24118 Kiel, Germany

[c]Institute of Mineralogy and Petrography, Universität Hamburg, Grindelallee 48, 20146 Hamburg, Germany

[d]Department of Earth Sciences, University of Oregon, Eugene, OR, USA.

4.1. Abstract

The origin of carbonatitic and highly silica-undersaturated volcanism, common along the SW coast of Africa extending from Angola through Namibia to the tip of South Africa, is still poorly understood. Here we present new geochemical data (major and trace element and Sr-Nd-Pb-Hf-O-C isotopes) from the Agate Mountain calcio- to magnesio-carbonatites, Dicker Willem calcio-carbonatites (49 Ma) and Swakopmund basanitic plugs (76–75 Ma) along the coast of Namibia that were emplaced after the Etendeka flood basalt event. The trace element and isotopic composition of these carbonatites and basanites indicate a HIMU-type (high time-integrated $^{238}U/^{204}Pb$ with radiogenic Pb isotope ratios) magma source, similar to the global HIMU mantle end member composition of St. Helena, South Atlantic. The similar isotopic composition of dated phonolites near Agate Mountain with the carbonatites points to a common derivation at a similar or older age (≥82 Ma) and thus an association with late-stage Walvis Ridge HIMU seamounts sitting on the EM1-type (enriched mantle one, characterized by radiogenic $^{87}Sr/^{86}Sr$, $^{207}Pb/^{204}Pb$ and $^{208}Pb/^{204}Pb$ but unradiogenic $^{206}Pb/^{204}Pb$ and $^{143}Nd/^{144}Nd$ isotope ratios) Walvis Ridge basement. The HIMU carbonatitic and silica-undersaturated rocks form age-progressive volcanic tracks extending: 1) Along the Walvis Ridge, through NW Namibia, to central Angola, 2) from the Vema seamount to Dicker Willem carbonatite to Gibeon kimberlites and carbonatites, 3) from the Warmbad to Bushmanland to Namaqualand clusters, and 4) along the Shona volcanic track extending into South Africa. Geochemical and seismic tomographic data reveal that the EMI and HIMU mantle plumes are generated from different geochemical domains in the deep mantle: the Tristan-Gough, Discovery and Shona EM1 volcanic tracks are derived from a common low-velocity anomaly (super-plume) ascending from the outer margin of the LLSVP and more irregular HIMU upwellings rise from an internal step ~900–1200 km east from the outer margin.

4.2. Introduction

Although carbonatites contribute only a tiny fraction of Earth's crustal rocks, their unusual composition, debated origin and significance as metallic resource deposits makes them particularly interesting for geochemical investigations. Carbonatites and associated alkaline rocks are the most important source of economically exploitable REE and Nb, with >98% of mine production of Nb being from carbonatite (U.S.

Geological Survey). While REEs, Nb and Ta are essential for the advanced digital and green high technology applications, the composition and origin of carbonatites need to be elucidated in order to better understand where carbonatites can be found and what kinds of carbonatites contain the highest abundances of economically important metals.

Carbonatite melts are believed to form by very low degrees of melting (Gudfinnsson and Presnall, 2005) of carbonated peridotite (Dasgupta and Hirschmann, 2006) or eclogite/pyroxenite (Dasgupta et al., 2007; Litasov and Ohtani, 2010). Depending on source composition (e.g., H_2O content), temperature and pressure, both calcio- and magnesio-carbonatites can form through melting of mantle rocks (Doroshkevich et al., 2010; Gittins et al., 2005; Harmer and Gittins, 1997; Weidendorfer et al., 2020). With increasing degree of melting, a series of carbonatite to silica-undersaturated rocks (carbonatites, kimberlites, melilitites, nephelines basanites and alkali basalts) can be generated from the same mantle source (Dasgupta et al., 2007; Gudfinnsson and Presnall, 2005). In addition, experimental studies show that CO_2 plays an important role in the melting of mantle rocks to generate highly silica-undersaturated compositions (Dasgupta and Hirschmann, 2006; Gudfinnsson and Presnall, 2005).

Carbonatites that are found on ocean islands point towards derivation from mantle plumes (Hoernle et al., 2002; Hoernle et al., 1991). Continental carbonatitic and silica-undersaturated (alkalic) volcanism in East Africa and the Kola Peninsula are also believed to be linked to plume activity (Bell, 2001; Bell and Tilton, 2001; Kogarko and Veselovskiy, 2019). Carbonatites are also commonly associated with continental large igneous provinces believed to form at the initial (plume head) stage of hotspot (plume) volcanism, for example, at Afar (Bell and Tilton, 2001), Deccan (Simonetti et al., 1998), Etendeka-Paraná-Angola (Kramm et al., 2017; Toyoda et al., 1994) and the Siberian flood basalts (Egorov, 1970; Vladykin, 2009).

In oceanic settings, carbonatites are extremely rare and only known to occur at the Kerguelen, Cape Verde and Canary hotspots (Woolley and Church, 2005). Oceanic carbonatites are always associated with silica-undersaturated volcanism with HIMU (high time-integrated $\mu = {}^{238}U/{}^{204}Pb$) type isotopic signatures (Hoernle et al., 2002; Hoernle et al., 1991; Ray et al., 1999). HIMU magmas are characterized by radiogenic Pb and intermediate Nd and Sr isotope ratios (Zindler and Hart, 1986). For the HIMU-like Canary and Cape Verde oceanic carbonatites, it has been argued that carbonate

(veins and vugs) within the subducting basaltic oceanic crust is the ultimate source of the carbonatites (Doucelance et al., 2003; Hoernle et al., 2002). In order to explain the apparent decoupling of U/Pb and Rb/Sr in the HIMU source necessary to generate radiogenic Pb but unradiogenic Sr, Castillo (2015) proposed that HIMU magmas including carbonatites are derived from recycled Archaean marine carbonates and a depleted peridotite source, such as oceanic lithospheric mantle(necessary to explain the radiogenic Nd isotopic composition). More recent studies have proposed that the end member HIMU composition could be generated by addition of (metasomatism by) 1–5% carbonatitic melts from subducting oceanic crust to the overlying depleted peridotitic sub-continental lithosphere mantle (SCLM) during the Archean, followed by recycling through the lower mantle via delamination and eventual ascent back to the surface via mantle plumes (Homrighausen et al., 2018b; Weiss et al., 2016).

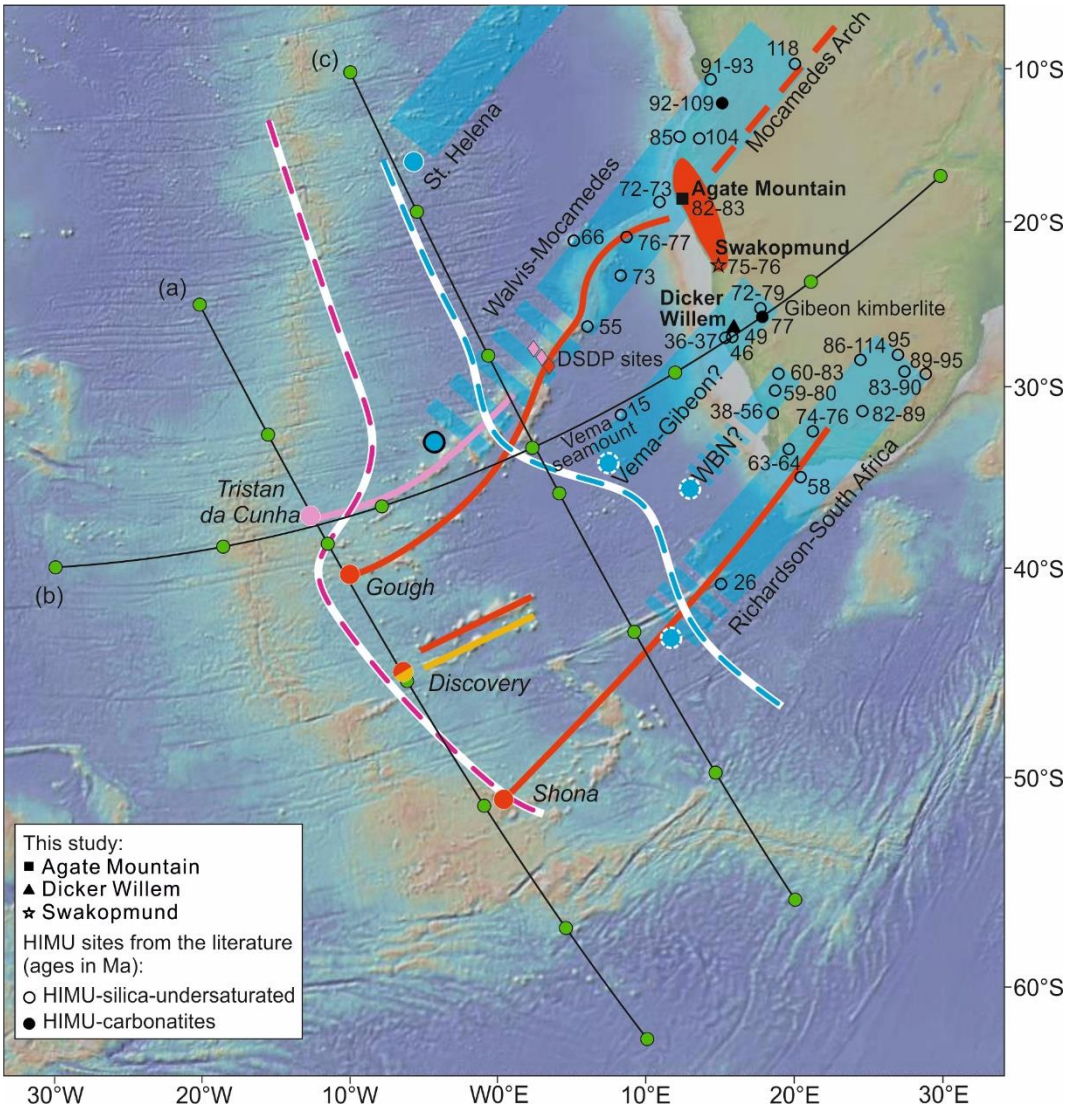

Figure 4-1: Map of the South Atlantic and southwest Africa, showing all previously known sample locations with HIMU signature in this area (circles) and their respective published ages (numbers in Ma) (Collerson et al., 2010; Griffin et al., 2014; Homrighausen et al., 2020; Janney et al., 2002; Janney and Bell, 2017; Marsh et al., 2018; Marzoli et al., 1999; Moore, 1979; O'Connor and le Roex, 1992; Reid et al., 1990; Robles-Cruz et al., 2012; Rohde et al., 2013b; Silva and Pereira, 1973). Filled symbols indicate carbonatites and open symbols denote silica-undersaturated rocks. Red field adjacent to the intersection of Walvis Ridge with the African continent denotes the location of Etendeka flood basalt volcanism (Marsh et al., 2001). Hotspot locations in the Atlantic Ocean and associated postulated tracks are colored according to the isotopic composition of their lavas (EM 1: red = Gough type, pink = Tristan type, orange = southern Discovery; HIMU: thick blue belts). The blue circle with black outline marks the location of a recent earthquake (Haxel and Dziak, 2005), which may indicate the present position of the Walvis–Mocamedes hotspot. Thick red and blue stippled lines mark the postulated boundaries of the respective EMI and HIMU compositional domains in/on the large low-shear velocity province (LLSVP) at the base of the lower mantle (projected to the surface) – see section 4.6. Black lines (a, b, c) with green circles denote the seismic tomography profile locations of Figure 4-9a, b and c. WBN represents the Warmbad, Bushmanland and Namaqualand volcanic clusters. Map generated by GeoMapApp (http://www.geomapapp.org).

Offshore SW Africa, the submarine Tristan-Gough-Walvis Ridge and the Shona linear volcanic tracks are believed to be formed by deep-seated mantle plumes starting from the margin of the African large low-shear-velocity province (LLSVP) (Burke et al., 2008; Torsvik et al., 2006) (Figure 4-1). Lavas forming these hotspot tracks have enriched mantle 1 (EM1) geochemical compositions, characterized by radiogenic $^{87}Sr/^{86}Sr$ and $^{208}Pb/^{204}Pb$ but relatively unradiogenic $^{143}Nd/^{144}Nd$ and $^{206}Pb/^{204}Pb$ (e.g., Zindler and Hart, 1986). Recently, secondary age-progressive volcanic tracks with St. Helena type HIMU composition were discovered superimposed on and adjacent to the EM1 Walvis Ridge and Shona volcanic tracks (Homrighausen et al., 2018a; Homrighausen et al., 2020). It was proposed that these low-volume HIMU lavas erupted ~30 Ma after the EMI-type volcanism at any given site and were derived from secondary plumes that upwelled 900–1200 km northeastwards (in the direction of plate motion) of the main Tristan-Gough and Shona plumes, thus sampling an internal part of or an upper layer on the African LLSVP which has HIMU composition (Homrighausen et al., 2020). The small-scale HIMU secondary plumes were presumably triggered by the removal of large amounts of EMI material from the LLSVP margin by the starting plume heads of the Tristan-Gough and Shona hotspots that generated the Etendeka/Parana and the Karoo flood basalts. Seismic tomography shows a steep internal slope/step ~900–1200 km northeastwards of the outer LLSVP margin, which has been interpreted as the generation zone for the secondary HIMU plumes (Homrighausen et al., 2020). If this model is correct, additional HIMU volcanism, post-dating the flood basalt events, could also have erupted (and be preserved) on Namibia and South Africa at the time when they were located above this steep step.

In order to test this hypothesis and to gain a better understanding of the post-Etendeka HIMU-type volcanism, as expressed by carbonatitic and silica-undersaturated volcanism in Namibia, we present major and trace element and Sr-Nd-Pb-Hf-O-C isotope data from the following complexes along the western coast of Namibia (going from north to south): Agate Mountain carbonatite complex, Swakopmund basanite plugs and Dicker Willem carbonatite complex. In addition, we combine our results with published data from Vema Seamount, Gibeon Kimberlite province, Walvis Ridge, Mocamedes Arch, Shona track, Warmbad, Bushmanland and Namaqualand clusters. We postulate a broad HIMU compositional volcanic belt along the coast of southwest

Africa tapping a distinct HIMU reservoir located on the inner part of the African LLSVP.

4.3. Geological background and previous research

4.3.1. General background

On the African plate, several age-progressive hotspot tracks, including Tristan-Gough, Discovery and Shona track, are proposed to be generated from mantle plumes detaching from/along the SW margin of the African LLSVP (Homrighausen et al., 2019; O'Connor et al., 2012). The Tristan-Gough and Shona volcanism initiated with the Etendeka/Parana and Karoo flood basalt events, respectively, supporting the classic plume head – plume tail model (Richards et al., 1989). The arrival of the Tristan-Gough plume head trigged widespread flood basalt volcanism between ~135 and 130 Ma in Namibia (Etendeka) and the conjugate South America margin (Parana). It was contemporaneous with breakup between Africa and South America (Milner et al., 1995; Renne et al., 1996), whereas the arrival of the Shona plume head most likely formed the Karoo flood basalt province at ~180 Ma (Homrighausen et al., 2020; Jourdan et al., 2007; Storey et al., 2001).

The Tristan-Gough-Walvis hotspot track is considered a type locality for the global geochemical mantle EM1 end member in the Atlantic Ocean. Recently it was documented that this hotspot track is isotopically zoned over the last ≥70 Ma, comprising a Gough composition (southern portion of SW end of the Walvis Ridge, including DSDP Site 525A, and southern part of the Guyot Province that extends towards Gough Island = Gough sub-track) and a Tristan composition (northern part of the SW Walvis Ridge, including DSDP Sites 527 and 528, and the part of the seamount chain that leads to Tristan Island) (Figure 4-1; Hoernle et al., 2015; Rohde et al., 2013). Both compositions have an overall EM1 signature, but the Gough component possesses higher $^{207}Pb/^{204}Pb$ but similar $^{208}Pb/^{204}Pb$, Sr, Nd, Hf isotope ratios at a given $^{206}Pb/^{204}Pb$ ratio (Hoernle et al., 2015; Homrighausen et al., 2019; Rohde et al., 2013). The Walvis Ridge northeast of DSDP sites 525A, 527 and 528 (see Figure 4-1) does not show any zonation and primarily has a Gough-type composition. Another geochemical zonation has also been identified in the Etendeka flood basalts between high-Ti tholeiitic basalts with Gough-type isotopic composition, which occur in

northwestern Namibia, and low-Ti tholeiitic basalts with a more depleted composition, which is distinct from Atlantic MORB due to its higher $^{207}Pb/^{204}Pb$ (but similar $^{208}Pb/^{204}Pb$) at a given $^{206}Pb/^{204}Pb$ isotope ratio and which occurs in central western Namibia (Zhou et al., 2020). To the south of Gough Island, the Discovery track is also geochemically zoned into a northern Discovery Gough-type subtrack and a southern Discovery subtrack with more enriched composition (more radiogenic Sr and $^{207}Pb/^{204}Pb$ but less radiogenic Nd and Hf isotopic composition than the Gough-type; Schwindrofska et al., 2016). Still further south, the Shona track consists almost exclusively of Gough-type composition (Hoernle et al., 2016). Therefore, although all three hotspot tracks consist of EM1 (or extreme DUPAL, Class and le Roex, 2011) type material, there are four distinct flavors. The dominant flavor, found at the three aforementioned South Atlantic hotspots (Tristan-Gough, Discovery and Shona) and the Etendeka flood basalts, is the Gough-type flavor. Associated geochemical anomalies at the South Atlantic mid-ocean ridge reveal that the northern Discovery and Shona domains have high $^{3}He/^{4}He$ and primitive Ne isotopic compositions, consistent with a lower mantle origin for the Gough-type composition (Sarda et al., 2000). High $^{3}He/^{4}He$ ratios were also detected in the low-Ti basalts from Etendeka (Stroncik et al., 2017).

The recent discovery of the low-volume, late-stage seamount volcanism with HIMU composition that was found superimposed on and adjacent to the main EM1 basement of the Walvis Ridge and which apparently extends to the Mocamedes Arch in Angola (Homrighausen et al., 2018a) and as a second track running from Richardson Seamount to South Africa (Homrighausen et al., 2018b) was unexpected. Since similar low-volume, young (relative to Etendeka) alkalic-carbonatitic igneous centers can be also found on the west coast of Namibia (e.g., Comin-Chiaramonti et al., 2011; Marsh, 1987; Verwoerd, 1993) their relationship to this HIMU volcanism is investigated in this study. These centers include Agate Mountain, the alkaline plugs near Swakopmund, Dicker Willem and Gibeon kimberlite-carbonatite complexes.

4.3.2. Agate Mountain Carbonatite Complex

The Agate Mountain carbonatite complex is located in northwestern Namibia near the continental extension of the Walvis Ridge (Figure 4-1). It was geologically mapped by Miller (2000) (Figure 4-2a). The complex is intruded into the surrounding Proterozoic Kaoko Belt (Goscombe et al., 2003), the Cretaceous Khumib formation tholeiitic lavas

and the Skeleton Coast quartz latite sub-group of the Etendeka flood basalt event (Marsh et al., 2001). Therefore, the carbonatite complex must be younger than the ~130 Ma plateau volcanism. Based on seismic data, Agate Mountain could be a satellite plug of a much larger (now largely offshore) volcanic complex (Phoenix Volcano; Miller, 2008). Agate Mountain is composed of two domains, separated by ring faults: 1) main body of the carbonatite complex, filling the center of the ring structure and 2) predominantly fenite and fenitized quartz latite from the intrusive carbonatite forms the outer ring structure, preserved west of the mountain's summit (Miller, 2008). The carbonatites and alkaline rocks investigated in this study were sampled from dikes and scattered plugs in the center of the complex and adjacent to the Khumib basaltic lavas (Figure 4-2a). There is no age or geochemical data published thus far (to our knowledge) of the Agate Mountain carbonatites. The only age and geochemical data come from two nearby phonolitic dikes dated at 83–82 Ma, which have a HIMU isotopic composition (Homrighausen et al., 2020) (Figure 4-2a).

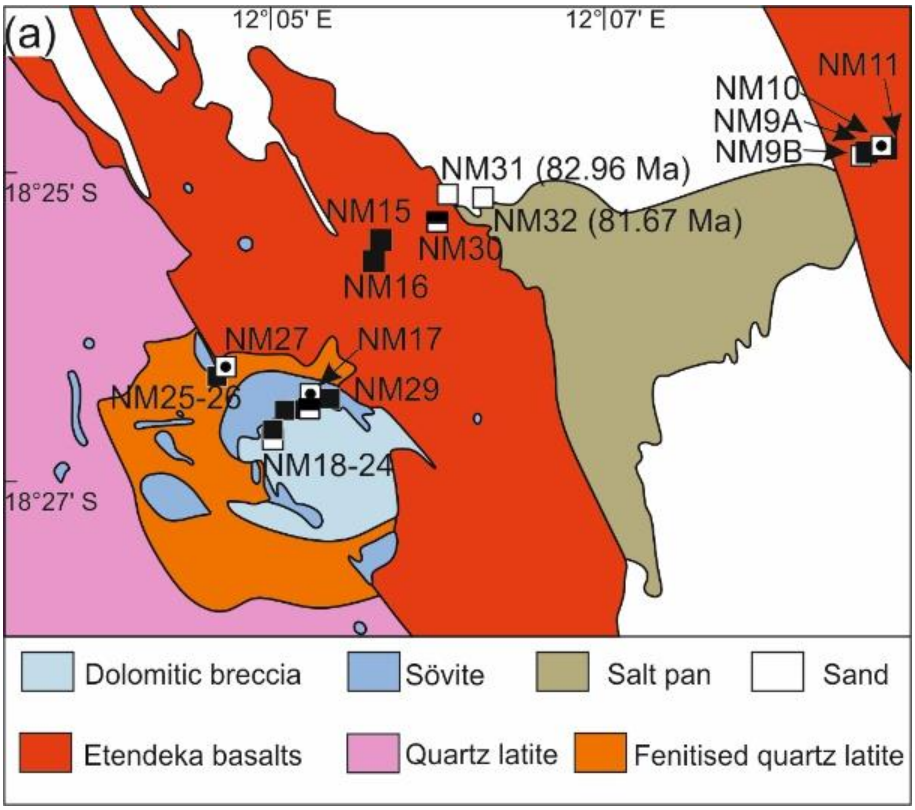

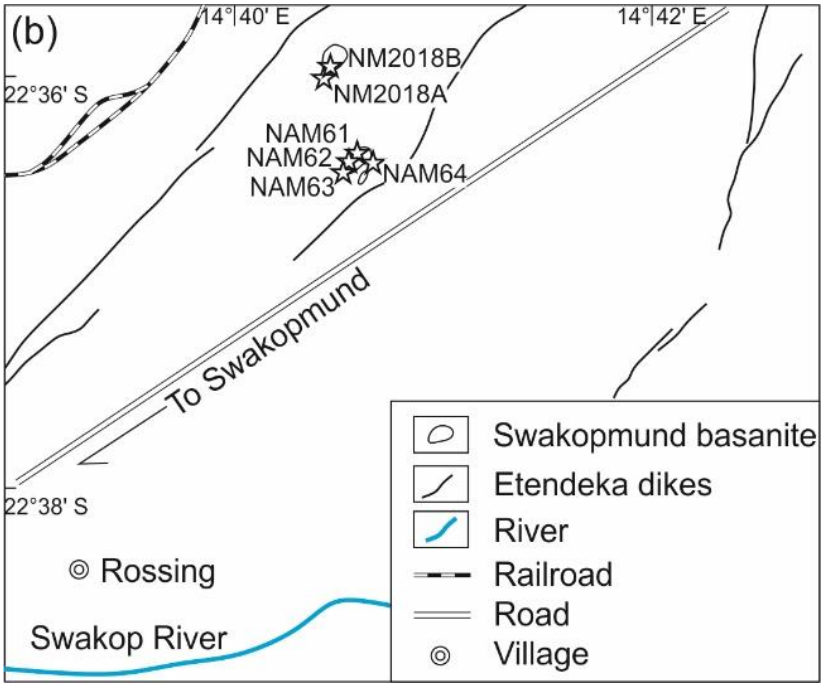

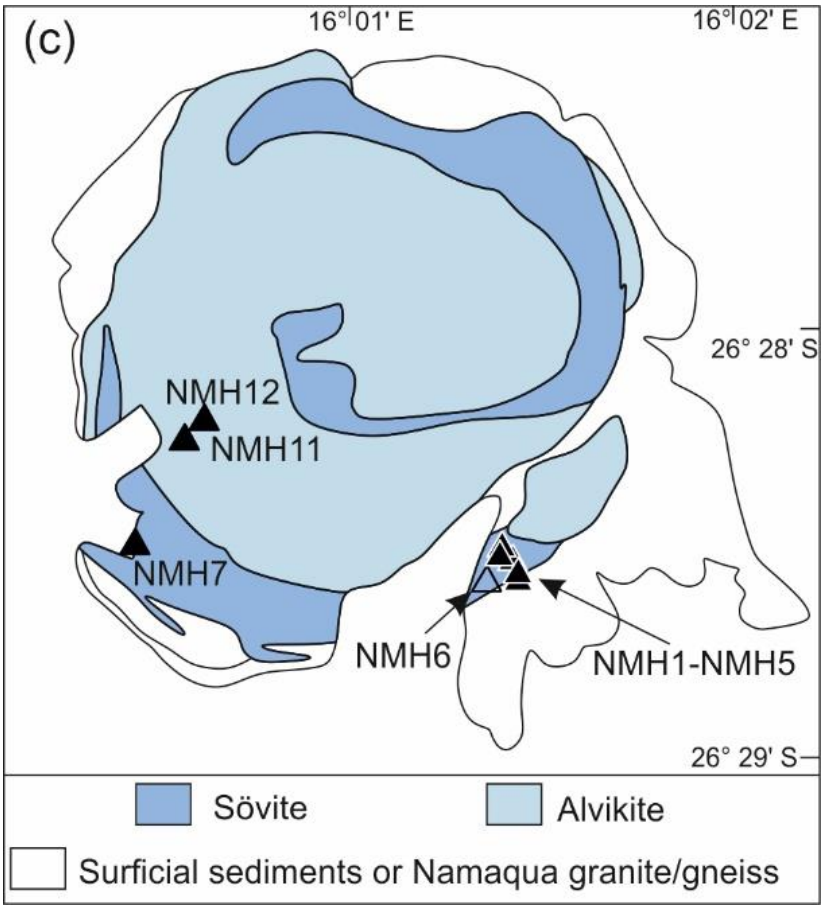

Figure 4-2: Simplified geological/topographic maps of (a) Agate Mountain after Miller (2000), (b) Swakopmund basanite outcrops, and (c) Dicker Willem complex after Cooper (1988), respectively. Filled/open sample symbols denote carbonatites/silica-undersaturated rocks,

respectively. The open symbols with a dot in the center denote secondary silicate and carbonate veins.

4.3.3. Alkaline plugs near Swakopmund

A cluster of intrusive alkaline plugs, about 17km east of Swakopmund in western central Namibia (Figure 4-2b), was first described by Whitehead et al. (2002). The exposed plugs on both sides of the road from Swakopmund to Usakos form up to 25m high hills in the eroded Proterozoic Damara Belt rocks. Previously, major and trace element data were published for two basanites (see Figure 4-3b; termed nephelinites in Whitehead et al., 2002) and for a phonolitic sample from these plugs. Two Ar-Ar whole-rock ages (76.08 ± 0.86; 74.86 ± 0.92 Ma) from basanite samples were reported in Whitehead et al. (2002), but no further details of the age measurements were published. A slightly younger pseudo plateau age of 72.50±0.47 Ma from sample NAM61 collected north of the Swakop River, for which we provide geochemical data in this study, has also been published (Homrighausen et al., 2020). No isotope data were published from these plugs thus far. Samples for this study are taken from the two plugs north of the Swakop river and the road from Usakos to Swakopmund (Figure 4-2b).

Although the overall volume of the plugs is small, their abundant lherzolite xenoliths have been used to constrain the composition of the subcontinental lithosphere mantle (SCLM) beneath the Damara Belt (Whitehead et al., 2002). Accordingly, Swakopmund lherzolite xenoliths show very low $^{87}Sr/^{86}Sr_{70Ma}$ (0.70237–0.70250) and high $^{143}Nd/^{144}Nd_{70Ma}$ (0.51318–0.51320) ratios, and thus show no signs of HIMU influence but rather indicate a depleted (DM) subcontinental lithospheric mantle (SCLM) beneath the Swakopmund intrusions (Class and le Roex, 2006). A cluster of intrusive alkaline plugs, about 17km east of Swakopmund in western central Namibia (Figure 4-2b), was first described by Whitehead et al. (2002). The exposed plugs on both sides of the road from Swakopmund to Usakos form up to 25m high hills in the eroded Proterozoic Damara Belt rocks. Previously, major and trace element data were published for two basanites (see Figure 4-3b; termed nephelinites in Whitehead et al., 2002) and for a phonolitic sample from these plugs. Two Ar-Ar whole-rock ages (76.08 ± 0.86; 74.86 ± 0.92 Ma) from basanite samples were reported in Whitehead et al. (2002), but no further details of the age measurements were published. A slightly younger pseudo plateau age of 72.50±0.47 Ma from sample NAM61 collected north of the Swakop

River, for which we provide geochemical data in this study, has also been published (Homrighausen et al., 2020). No isotope data were published from these plugs thus far. Samples for this study are taken from the two plugs north of the Swakop river and the road from Usakos to Swakopmund (Figure 4-3b).

Although the overall volume of the plugs is small, their abundant lherzolite xenoliths have been used to constrain the composition of the subcontinental lithosphere mantle (SCLM) beneath the Damara Belt (Whitehead et al., 2002). Accordingly, Swakopmund lherzolite xenoliths show very low $^{87}Sr/^{86}Sr_{70Ma}$ (0.70237–0.70250) and high $^{143}Nd/^{144}Nd_{70Ma}$ (0.51318–0.51320) ratios, and thus show no signs of HIMU influence but rather indicate a depleted (DM) subcontinental lithospheric mantle (SCLM) beneath the Swakopmund intrusions (Class and le Roex, 2006).

4.3.4. Dicker Willem

Dicker Willem stands out as an inselberg in SW Namibia (Figure 4-2c). It consists mainly of carbonatitic magma intruded into the surrounding 1.0–1.3 Ga old Namaqua Metamorphic Complex (Miller, 2012). With an age of 49±1 Ma constrained by K-Ar and Rb-Sr dating (Reid et al., 1990), Dicker Willem is significantly younger than the Etendeka flood basalt episode and the initiation of the Walvis Ridge hotspot track. Cooper (1988) classified the carbonatites of Dicker Willem as sövites, alvikites, beforsites, ferro-alvikites and also described dikes of carbonatite, microbreccia and tuffisite. The major and trace element variation of the carbonatitic rock types is attributed to the continuous fractionation of a common parental magma (Cooper and Reid, 1998). Sövites form the outer margin as an intermittent concentric ring and can be coherently traced along the northeastern and southern flanks of Dicker Willem. Ijolite-syenite xenoliths occur within the sövites and are likely to be related to the carbonatites (Cooper, 1988). The center of the Dicker Willem complex is formed by alvikites. Sövite dikes and veins are the latest intrusions at Dicker Willem, occurring both within and outside of the complex. The carbonatites for this study are taken from the sövite ring on the southern slope and the alvikitic center (Figure 4-2c). One phonolite was taken from the trachyte breccia at the southeastern flank, which is also described in Cooper (1988). Published Sr-Nd-Pb isotope data from Dicker Willem

show a wide range between a HIMU endmember and the local upper crust Namaqua gneiss composition (Cooper and Reid, 2000).

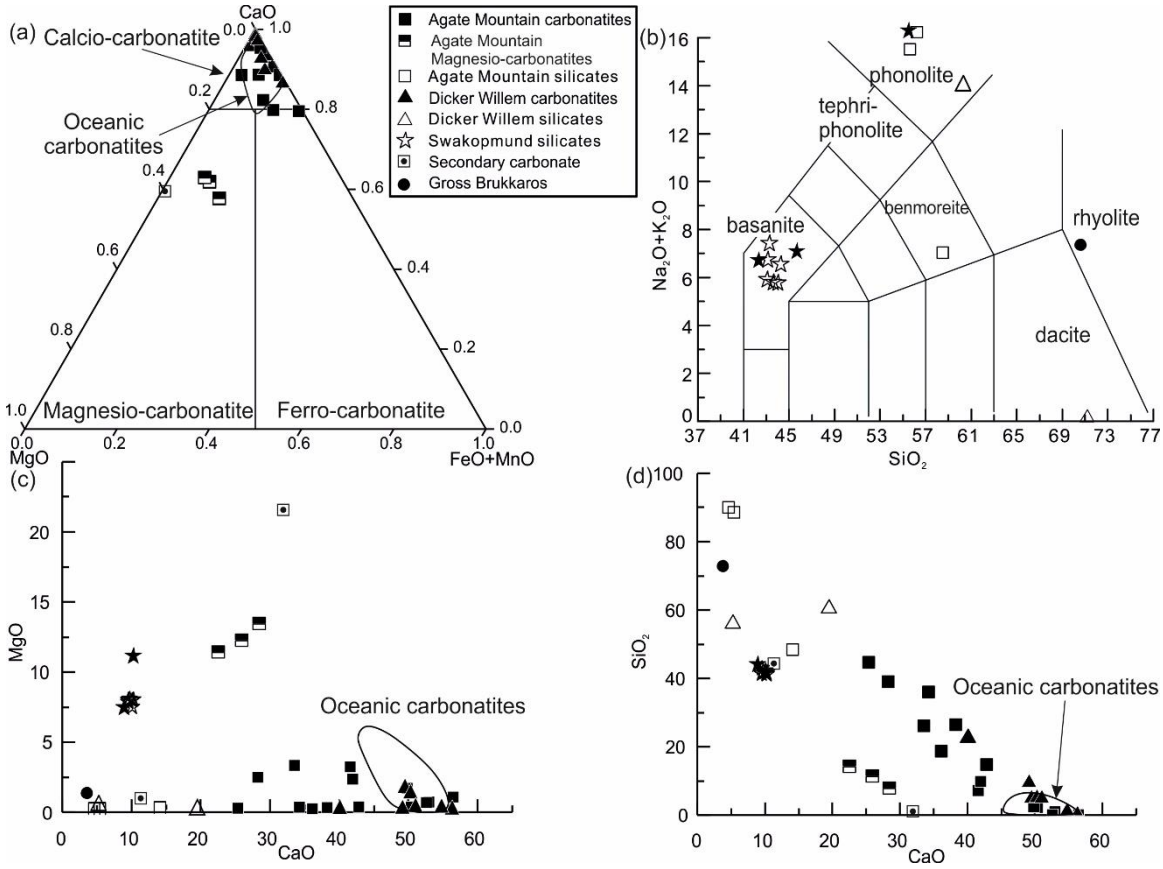

Figure 4-3: (a) Carbonatite classification diagram after Le Maitre et al. (1989). Most samples from Agate Mountain and Dicker Willem are calcio-carbonatites. Four samples from Agate Mountain are magnesio-carbonatites. (b) Sampled silicates of Agate Mountain (with two phonolites included from Homrighausen et al., 2020), Dicker Willem and the Swakopmund plugs (solid black stars denote samples published in Whitehead et al., 2002) plotted (as weight percentages recalculated to 100% on a volatile-free basis) on the total alkali vs. silica diagram (TAS) of Le Bas et al. (1986). (c) CaO vs MgO and (d) CaO vs SiO_2 (in wt.%). Oceanic carbonatite field shown for comparison (Hoernle et al., 2002).

4.4. Samples, petrography and analytical methods

Our carbonatite samples from Agate mountain are divided into sövites and alvikites by their grain size (Le Maitre et al., 2005). The sövite dike rocks contain up to 30% quartz, radiating clusters of opaque minerals and skeletal crystals of dolomite (0.2–0.4 mm). Similar petrographic features were also described by Miller (2000). Alvikites are fine grained and contain Fe oxides and quartz. Some carbonatite dike samples contain more

accessory minerals, such as nepheline, fluorite, melilite, clusters of aegirine, phlogopite and opaque ore.

Dicker Willem samples comprise sövite, alvikite and silicate rocks. The sampled sövite rocks mainly contain up to 4 mm large anhedral calcite and accessory minerals such as biotite (0.05–0.4 mm), apatite (~0.2 mm), aegirine (~2 mm) and magnetite (~5 mm). Alvikites have a typical calcitic groundmass and varying contents of opaque Fe-oxide minerals. The phonolite contains alkali feldspar, nepheline, aegirine and alkali amphibole. The matrix consists largely of calcite, which is similar to trachyte breccia with strong alteration described in Cooper (1988).

The basanite plug rocks sampled near Swakopmund are aphyric to sparsely porphyric with 10–20% olivine and augite phenocrysts (~0.5mm). The matrix consists of feldspathoid and Fe-Ti oxide microphenocrysts (0.03–0.05 mm). The rocks contain abundant lherzolite xenoliths as previously reported by Whitehead et al. (2002). The xenoliths have a holocrystalline texture with anhedral olivine, clinopyroxene and rare spinel (0.4–2 mm).

The sample material was crushed in a jaw crusher, cleaned in an ultrasonic bath with deionized water, sieved and carefully hand-picked under a binocular microscope to avoid secondary fillings of cavities/ fractures and xenolithic material. Selected whole-rock chips (~10g) of each sample were milled to fine powders and dried at 105°C overnight.

Major elements of most samples (see Table 4-1) were measured at the Institute of Mineralogy and Petrography at the University of Hamburg on a Magix Pro PW 2540 X-ray fluorescence spectrometer (XRF). International rock standards JGB-1, JB-3, JB-2, JA-3, JG-3, JG-2 were analyzed together with the samples. The difference between measured and accepted literature values (Govindaraju, 1994) of major elements is less than 7%, except for elements that are lower than 1 wt%. Since eight carbonatites possess high concentrations of Sr and Ba (higher concentrations than covered by the calibration curve and therefore yielding high analytical errors when measured by XRF), the major element composition of these samples was determined by inductively coupled plasma optical emission spectrometry (ICP-OES) on a SPECTRO CIROS SOP at the Institute of Geosciences at Kiel University. The reference standards MACS-3 (Jochum et al.,

2019) and COQ-1 (Ray et al., 2013) were measured together with samples. The difference between measured and literature values are less than 6%, except for elements that are lower than 1 wt%. The precision of ICP-OES measurements based on duplicate measurements is better than 5%.

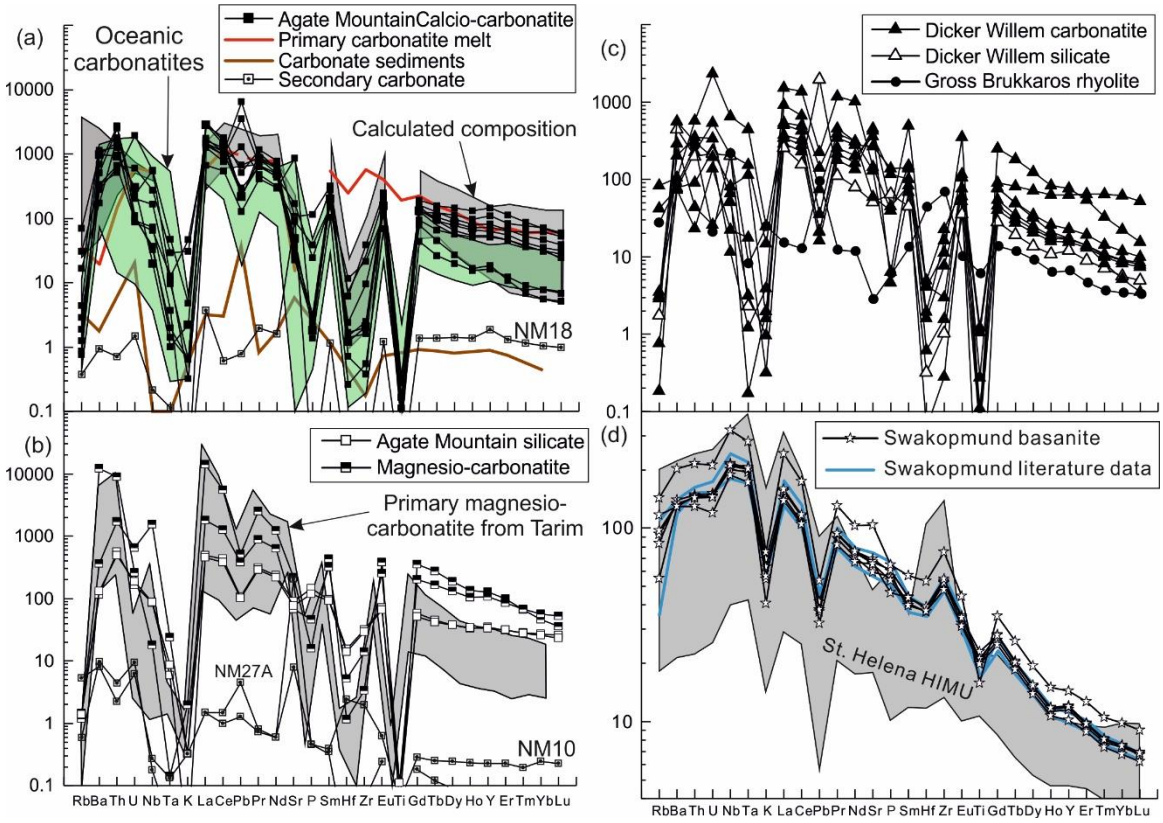

Figure 4-4: Multi-element diagrams normalized to primitive mantle (Sun and McDonough, 1989): (a) Calcio-carbonatites from Agate Mountain compared with estimated primary carbonatite melts (see section 4.6.2 and Table 4-4; Walter et al., 2008), calculated composition of carbonatite melts (grey field, see in section 4.6.2 and Table 4-4 for details of calculation), oceanic carbonatite from the Cape Verde islands (green field; Hoernle et al., 2002) and the average composition of carbonate sediments (Frimmel and Lane, 2005). (b) Magnesio-carbonatite and silicate-undersaturated rocks from Agate Mountain compared with the primary magnesio-carbonatites from the Tarim LIP (Cheng et al., 2017). (c) Carbonatite and silicate rocks from Dicker Willem and Gross Brukkaros. (d) Basanites from Swakopmund plugs (including two published Swakopmund basanites from Whitehead et al., 2002) compared with basanites from St. Helena with HIMU composition (Chaffey et al., 1989; Kawabata et al., 2011; Willbold and Stracke, 2006).

Trace elements were determined with an AGILENT 7500cs inductively coupled plasma mass spectrometer (ICP-MS) at the Institute of Geosciences at Kiel University. Carbonatites were decarbonized by diluted hydrochloic acid. Then rock powders (~100 mg) were treated with HF-$HClO_4$-aqua regia following the standard decomposition procedure of Garbe-Schönberg (1993). The carbonatitic powders, however, could not

be fully dissolved by this method. Therefore, these samples were milled to nano-particulate powders and measured by laser ablation inductively coupled plasma mass spectrometer (LA-ICP-MS). About 2g powder for each sample was milled with 8 ml deionized water for 3 min in a planetary mill at 700–800 rpm. All samples were then carefully rinsed into polycarbonate beakers and freeze-dried. After 5 minutes of re-homogenization, about 300 mg powder were pressed into tablets under 0.74×10^6 kPa (Garbe-Schönberg and Müller, 2014). The tablets were measured by Agilent 7900 ICP-MS coupled with a GeoLas HD (Coherent) 193 nm ArF excimer laser ablation system at Kiel University. Every tablet was measured three times and the average value is reported. The uncertainty combines both the uncertainty from the measurement (including slightly higher variability of aerosol generation during laser ablation of nano-powder) and the uncertainty from any remaining heterogeneity of the tablet. Most RSD% (relative standard deviation) of replicates are lower than 5%, except for elements with lower than 1 μg/g concentrations. A carbonatite standard, MACS-3 NP, was measured together with the nano-powder tablets. The difference between measured and literature data (Jochum et al., 2019) is less than 8%, except for Mn, Fe, Rb, Zr, Sr.

Carbon and oxygen isotopes were measured at the University of Oregon using a Gasbench continuous flow line coupled with Thermo-Finnigan MAT253 gas isotope ratio mass spectrometer. The freshest carbonate minerals (0.4 mg) were ground and put into 10 ml vials, which were flushed with He, then acidified with phosphoric acid inside of a thermal block held at 70°C. After equilibration for 2 h, the samples were run sequentially, and an analysis run included NBS19 standard and in house carbonatite standard MCA. Carbon isotope values are reported relative to the PDB standard. The NBS19 standard yielded $\delta^{13}C$ =2.09±0.032‰ PDB (2SE). Oxygen isotope values are reported relative to the international Vienna Standard Mean Ocean Water (VSMOW) standard. The measured $\delta^{18}O$ values of NBS19 are 28.03±0.057 (2SE). The analytical values were adjusted by the difference between our measured and recommended values of standard (0.14 for $\delta^{13}C$ and -0.61 for $\delta^{18}O$).

The Sr-Nd-Pb isotope ratios were measured at the GEOMAR Helmholtz Centre for Ocean Research Kiel by thermal ionization mass spectrometry (TIMS) using a Thermo-Scientific TRITON *Plus*. About 20–30 mg powders were dissolved by Hf-HNO_3. Ion chromatography followed standard procedures described in Hoernle et al. (2008). The

Sr and Nd isotopic ratios were normalized within-run to $^{86}Sr/^{88}Sr$ = 0.1194 and $^{146}Nd/^{144}Nd$ = 0.7219 and fractionation-corrected to NBS987 and La Jolla standards that were measured along with the samples. Since installation of the instrument in 2014, NBS987 yield $^{87}Sr/^{86}Sr$ = 0.710268 ± 0.000029 (n=743; 2 standard deviation (SD)) and La Jolla averages $^{143}Nd/^{144}Nd$ = 0.511846 ± 0.000012 (n=505; 2SD). Sample data are adjusted to $^{87}Sr/^{86}Sr$ = 0.710250 for NBS987 and $^{143}Nd/^{144}Nd$ = 0.511850 for La Jolla. Pb isotopes were measured using the double-spike (Pb-DS) technique (Hoernle et al., 2011). The DS corrected NBS981 values since 2014 are $^{206}Pb/^{204}Pb$ = 16.9408 ± 0.0018, $^{207}Pb/^{204}Pb$ = 15.4975 ± 0.0018, $^{208}Pb/^{204}Pb$ = 36.7207 ± 0.0047 (n=178; 2SD). Unleached powders (200–300 mg) were prepared for Hf isotope measurements following the method of Blichert-Toft et al. (1997). Hf isotope ratios were also measured at GEOMAR on a NU MC-ICP-MS and sample data were fractionation-corrected by the standard bracketing method. The in-house standard SPEX Hf ICP solution (lot#9) yielded $^{176}Hf/^{177}Hf$ = 0.282170 ± 0.000005 (n=13; 2SD) corresponding to a JMC457 value = 0.282163 (Blichert-Toft et al., 1997). Procedural blanks were <30pg for Pb and <100pg for Sr-Nd-Hf.

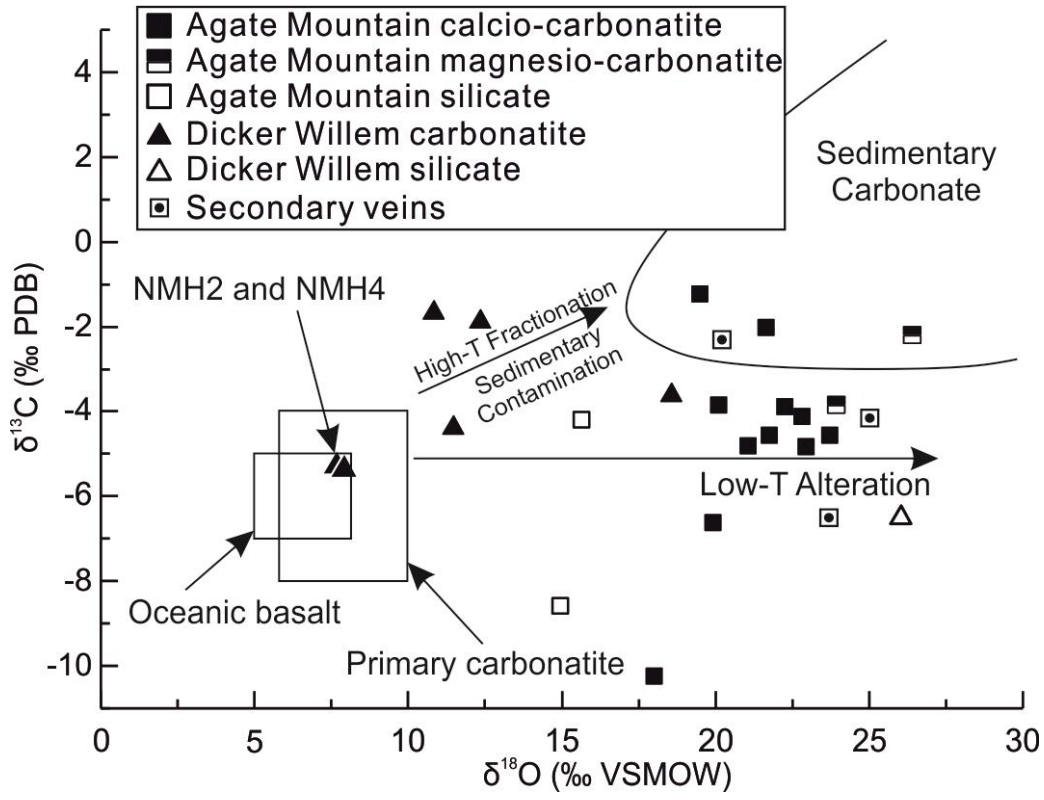

Figure 4-5: Oxygen and carbon isotopes of the investigated rocks from Agate Mountain and Dicker Willem. The composition of primary carbonatite and oceanic basalts are from Keller

and Hoefs (1995). Most samples have higher $\delta^{18}O$ than primary carbonatite but similar $\delta^{13}C$, suggesting low temperature alteration (Bell, 1989).

4.5. Results

4.5.1. Major and trace element data

All major and trace element data are given in Table 4-1. The carbonatites show large variations in CaO (22.5–56.4 wt%), MgO (0–13.4 wt%), Fe_2O_3 (0–8.3 wt%) and SiO_2 (0–43.8 wt.%). All carbonatites show extremely low TiO_2 concentrations (0–0.22 wt%). Such TiO_2 depletion has been reported for carbonatites world-wide (Cooper and Reid, 1991; Cooper and Reid, 1998; Hoernle et al., 2002; Ionov and Harmer, 2002). Following the classification of Le Maitre et al. (1989), carbonatites can be divided into three groups based on their Ca, Mg and Fe + Mn contents (Figure 4-3a). Accordingly, most of the sampled carbonatites are classified as calcio-carbonatite (> 80% CaO) but four samples from Agate Mountain are magnesio-carbonatites and two samples plot on the calcio-/ferro-carbonatite boundary. In comparison to oceanic carbonatites from ocean islands, the Namibian carbonatites have less sövitic compositions and trend towards lower CaO concentrations but higher SiO_2 (Figure 4-3 c and d). CaO content is generally negatively correlated with SiO_2.

As characteristic for carbonatitic rocks, most samples show highly enriched Ba, Sr, Th, Pb and rare earth element (REE) concentrations, highly variable Nb, and depletion in high field strength elements (HFSE) (Ta, Hf, Zr, Ti), U (in most samples) and Rb resulting in highly spiked patterns on standard multi-element diagrams (Figure 4-4a–c). Regarding trace elements, no principal difference between calcio- and magnesio-carbonatites is observed in our sample set (compare Figure 4-4a and b). Three vein samples (NM10, NM18, NM27A, indicated in Figure 4-4) yield significantely more depleted trace element patterns than typical magmatic carbonatites, similar to secondary carbonate (Frimmel and Lane, 2005) and are therefore considered as secondary carbonate veins in the following (and indicated by a separate symbol in the figures). Another well-known feature is that element pairs with similar partition coefficients in silicate melts, such as Nb-Ta and Zr-Hf (and therefore generally similar normalized concentrations), are decoupled in carbonatitic rocks (Chakhmouradian and Williams, 2004). Thus, the ratios of Nb/Ta of the investigated carbonatites (13–6735) are much

higher than the (silicate) chondrite value (19.9±0.6; Münker et al., 2003). Zr/Hf also varies considerably (19 to 303; chondritic value: 34.3±0.3; Münker et al., 2003).

Compared to carbonatites from Bayan Obo (Inner Mongolia), the largest REE mine of the world (Yang et al., 2011; Zhongxin et al., 1992), Agate Mountain carbonatites have slightly higher average Nb (173 µg/g compared to 160 µg/g in Bayan Obo) and significantly higher HREE contents (total HREE concentration from Tb to Lu is 129 µg/g compared to 72 µg/g). In contrast, the total LREE concentrations at Agate Mountain carbonatites (6456 µg/g) and Dicker Willem (1893 µg/g) are much lower than in Bayan Obo (28900 µg/g).

The sampled silicate rocks range from basanite to phonolite to benmoreite in the total alkali vs. silica diagram (Figure 4-3b). All samples from the Swakopmund plugs have basanitic compositions in accordance with two previously published samples from these outcrops (Whitehead et al., 2002). In contrast, the sampled silicates from Agate Mountain and Dicker Willem are more differentiated and range from benmoreite to phonolitic compositions.

In multi-element diagrams, Swakopmund basanites show uniform patterns with enrichment of more incompatible over less incompatible elements, enrichment in Nb, Ta, and depletion in K, Pb, Ti and steep negative HREE patterns (Figure 4-4d). These patterns resemble typical HIMU-type OIB trace element patterns as shown by basanites from the St. Helena Island type locality in the South Atlantic (Chaffey et al., 1989).

4.5.2. Isotope data

The results of the isotope measurements are also presented in Table 4-2 and Table 4-3. Oxygen and carbon isotope ratios are plotted in Figure 4-5. All radiogenic isotope ratios were corrected for radiogenic ingrowth to 70 Ma, which is the average age of Agate Mountain, Dicker Willem and Swakopmund plugs (Figure 4-6 and Figure 4-7; see figure caption for details).

The investigated carbonatites show a large range in $\delta^{18}O$, with most samples having higher $\delta^{18}O$ (>10‰) but $\delta^{13}C$ similar to primary (mantle-derived) carbonatites (Figure 4-5). Five carbonatites show slightly higher $\delta^{13}C$ (>-3‰). Two samples from Dicker Willem (NMH2 and NMH4) fall within the commonly accepted range of primary

mantle-derived $\delta^{13}C$ and $\delta^{18}O$ values of -7 to -5‰ and 5 to 8‰, respectively (Keller and Hoefs, 1995). Neither $\delta^{18}O$ or $\delta^{13}C$ correlate with radiogenic isotope ratios.

The analyzed carbonatites show a large range in initial Sr isotope ratios (0.7032 to 0.7066) but fairly restricted initial Nd isotope ratios (0.51262 to 0.51276) largely overlapping the St. Helena HIMU composition (Figure 4-6a). The Swakopmund basanites show a much smaller spread of their Sr isotope ratios, largely overlapping with the Walvis Ridge HIMU silicates except for sample NM2018A, which yields $^{86}Sr/^{86}Sr_{in}$ of 0.7041. Initial Pb isotope compositions of carbonatites from the Agate Mountain complex range from moderately radiogenic ratios ($^{206}Pb/^{204}Pb_{in}$=19.14, $^{207}Pb/^{204}Pb_{in}$=15.69, $^{208}Pb/^{204}Pb_{in}$=39.08, sample NM26B) to very radiogenic signatures ($^{206}Pb/^{204}Pb_{in}$=20.66, $^{207}Pb/^{204}Pb_{in}$=15.83, $^{208}Pb/^{204}Pb_{in}$=40.13, sample NM24), which are similar to St. Helena lavas ($^{206}Pb/^{204}Pb_{in}$=19.47–20.84, $^{207}Pb/^{204}Pb_{in}$=15.64–15.95, $^{208}Pb/^{204}Pb_{in}$=39.01–40.35; Chaffey et al., 1989) (Figure 4-7). Sample NM10, a secondary silicate vein with depleted trace element composition (Figure 4-4b), yields distinctly less radiogenic Pb isotopes ($^{206}Pb/^{204}Pb_{in}$=17.61, $^{207}Pb/^{204}Pb_{in}$=15.55, $^{208}Pb/^{204}Pb_{in}$=38.55), plotting in/near the field for high-Ti Etendeka basalts (also in the Sr vs Nd isotope diagram of Figure 4-6). This sample comes from a vein cutting the Etendeka basalts (high-Ti Khumib formation) east of Agate Mountain and has obviously picked up the isotopic composition of its host rock, which is very distinct from the Agate Mountain carbonatites (see Figure 4-2a and Section 4.3.2).

Our Dicker Willem carbonatite samples have a very restricted range in $^{206}Pb/^{204}Pb_{in}$ (20.50–21.66), $^{207}Pb/^{204}Pb_{in}$ (15.80–15.88), $^{208}Pb/^{204}Pb_{in}$ (39.78–40.09), $^{87}Sr/^{86}Sr_{in}$ (0.7032–0.7034) and $^{143}Nd/^{144}Nd_{in}$ (0.51266–0.51269), except for one sample (NMH1) with slightly more enriched $^{87}Sr/^{86}Sr_{in}$ (0.70383) and $^{143}Nd/^{144}Nd_{in}$ (0.51262). Its $^{206}Pb/^{204}Pb_{in}$ (20.27) isotope ratio is lower, but $^{207}Pb/^{204}Pb_{in}$ and $^{208}Pb/^{204}Pb_{in}$ are similar to the other samples. The Nd isotope ratios of Dicker Willem carbonatites are slightly lower than the Agate Mountain and Swakopmund samples at a given Sr isotope ratio (Figure 4-6a). Previously published isotope data from Dicker Willem ($^{87}Sr/^{86}Sr_{in}$ = 0.70324–0.77104; $^{143}Nd/^{144}Nd_{in}$ = 0.51178–0.51269; $^{206}Pb/^{204}Pb_{in}$ = 18.59–20.97) (Cooper and Reid, 2000; Cooper and Reid, 1998) extend to more radiogenic Sr and unradiogenic Nd isotopic composition, likely reflecting greater amounts of bulk crustal

assimilation than in the samples that we collected for this study (see Section 4.6.1 below).

The Swakopmund basanite plug lavas also have radiogenic Pb isotope ratios ($^{206}Pb/^{204}Pb_{in}$ = 19.70–20.16; $^{207}Pb/^{204}Pb_{in}$ = 15.70–15.72, $^{208}Pb/^{204}Pb_{in}$ = 39.39–39.76) and have systematically lower $^{207}Pb/^{204}Pb$ for a given $^{206}Pb/^{204}Pb$ than the carbonatite samples. When considering their combined Sr, Nd and Hf isotope ratios, the basanites largely overlap the composition of the late-stage HIMU seamounts on Walvis Ridge (Figure 4-6–Figure 4-7).

Overall, the Pb isotope ratios of the Agate Mountain carbonatites and silica-undersaturated volcanic rocks largely overlap with the Walvis Ridge HIMU and St. Helena HIMU compositions, and form good linear trends ($^{206}Pb/^{204}Pb$ vs. $^{207}Pb/^{204}Pb$, r^2=0.99; and vs. $^{208}Pb/^{204}Pb$, r^2=0.85) between the St. Helena HIMU endmember and the high-Ti Etendeka silicate rocks (Figure 4-7a, b). The two Dicker Willem carbonatites with mantle-like O and C isotopes, however, have higher $^{206}Pb/^{204}Pb_{in}$ and lower $^{143}Nd/^{144}Nd_{in}$ than St. Helena basanite lavas or Agate Mountain carbonatites.

Table 4-1: Major and trace element data from HIMU-like intrusions

Sample name	NAM61	NAM62	NAM63	NAM64	NM2018A	NM2018B	NM9A	NM9B	NM10	NM11	NM15	NM16	NM17	NM18
Location	Swakopmund	Swakopmund	Swakopmund	Swakopmund	Swakopmund	Swakopmund	Agate Mountain	Agate Mountain	Agate Mountain	Agate Mountain	Agate Mountain	Agate Mountain	Agate Mountain	Agate Mountain
Lithology	basanite	basanite	basanite	basanite	basanite	basanite	Calcio-carbonatite	Benmoreite with carbonate	Secondary silicate+carbonate vein	Calcio-carbonatite	Calcio-carbonatite	Calcio-carbonatite	Calcio-carbonatite	Secondary calcium carbonate vein
SiO_2	41.72	42.84	42.17	41.07	42.01	41.29	2.06	48.31	44.33	2.32	7.16	14.77	0.83	b.d.l.
Al_2O_3	12.39	12.57	13.31	12.24	12.24	11.94	0.04	10.52	16.10	b.d.l.	0.06	1.18	0.09	b.d.l.
Fe_2O_3	14.28	13.98	14.14	14.29	13.9	13.80	b.d.l.	2.88	0.21	0.13	6.42	3.61	2.67	b.d.l.
MgO	7.95	7.82	7.5	8.03	8.05	7.96	0.16	0.06	0.98	1.67	3.24	0.29	0.70	1.04
MnO	0.22	0.21	0.18	0.22	0.2	0.27	0.02	0.04	0.06	0.29	1.55	0.88	0.58	b.d.l.
CaO	10.13	9.62	10.16	10.3	9.73	9.57	50.43	14.16	11.35	49.89	41.64	42.87	52.97	56.52
Na_2O	4.46	4.44	4.37	4.02	3.77	4.75	b.d.l.	5.77	9.13	b.d.l.	0.26	0.19	b.d.l.	b.d.l.
K_2O	2.07	1.9	1.23	1.62	1.75	2.33	b.d.l.	0.04	0.01	b.d.l.	0.01	0.96	0.15	b.d.l.
TiO_2	3.64	3.56	4	3.64	3.6	2.86	0.01	0.80	0.01	0.01	0.06	0.05	0.03	b.d.l.
P_2O_5	1.26	1.18	0.98	1.26	1.17	1.41	0.01	0.16	0.01	b.d.l.	2.53	0.53	0.05	b.d.l.
SO_3	0.02	0.03	0.03	0.04	0.12	0.09	0.11	0.03	0.04	0.02	0.26	2.37	0.16	0.05
SrO														
BaO														
Sum	99.28	99.15	99.56	99.39	99.21	98.79	95.18	98.09	98.51	96.84	98.11	98.52	99.03	100.94
L.O.I	1.16	1.03	1.52	2.7	2.79	2.61	42.45	15.35	16.32	42.53	35.18	33.19	40.96	43.38
Li	13.1	15.5	8.36	8.41	8.28	15.6			1.18		12.3	9.44	114	0.120
Sc	18.4	20.4	18.3	20.6	17.4	12.0			5.62		2.23	5.07	9.58	0.337
V	215	234	216	241	214	157			40.2		70.0	117	107	0.0424
Cr	199	198	196	220	191	223			3.05		4.82	73.3	14.5	3.60
Co	41.4	45.2	41.4	46.0	41.8	36.1			0.878		7.29	7.22	3.18	0.0782
Ni	141	153	150	165	129	188			2.14		23.7	32.9	6.98	0.752
Cu	35.7	38.3	35.6	37.6	37.2	27.4			29.3		4.89	5.54	4.84	0.172
Zn	151	165	184	169	153	193			3.86		542	263	165	16.0
Ga	25.9	27.0	25.9	27.4	25.2	29.3			43.8		36.1	27.5	19.3	0.0791
Rb	44.5	29.4	49.9	51.9	62.3	76.7			2.81		1.54	16.5	8.93	0.203
Sr	1261	1077	1200	1217	1191	1892			146		1945	3042	411	1710

Y	47.4	45.7	46.5	47.2	40.0	56.5	0.897	571	73.4	201	7.30
Zr	514	504	507	530	467	729	19.1	378	211	19.7	0.190
Nb	133	125	130	131	116	199	0.166	332	168	342	0.132
Cs	1.20	1.57	1.66	1.65	1.17	2.17	28.9	0.02	0.129	0.164	
Ba	847	783	800	812	782	1227	49.4	2014	2045	1048	5.70
La	95.7	89.0	94.9	97.2	85.3	148	0.905	1697	1065	901	2.30
Ce	186	173	183	187	167	279	1.58	2897	1694	1514	0.978
Pr	22.7	21.3	22.4	22.7	19.8	31.6	0.176	285	161	153	0.476
Nd	89.9	84.5	88.9	90.3	79.7	123	0.711	929	515	520	1.89
Sm	17.0	15.9	16.8	16.9	15.3	22.1	0.150	125	62.2	72.8	0.447
Eu	5.09	4.70	5.04	5.04	4.53	6.48	0.0909	35.7	16.2	19.3	0.175
Gd	14.4	13.5	14.3	14.3	12.8	18.0	0.146	97.9	40.1	47.9	0.706
Tb	1.93	1.82	1.90	1.91	1.75	2.44	0.0237	14.5	4.17	6.20	0.128
Dy	9.76	9.30	9.69	9.81	8.86	12.3	0.155	92.7	17.1	35.7	0.899
Ho	1.69	1.60	1.66	1.67	1.52	2.14	0.0331	18.6	2.40	7.19	0.194
Er	4.08	3.89	4.02	4.04	3.70	5.28	0.0934	47.2	4.53	19.4	0.538
Tm	0.524	0.505	0.514	0.519	0.474	0.678	0.0126	5.63	0.439	2.43	0.0744
Yb	3.13	3.04	3.09	3.11	2.80	4.08	0.100	28.7	2.29	12.7	0.431
Lu	0.441	0.429	0.427	0.439	0.395	0.574	0.0144	3.62	0.326	1.54	0.0635
Hf	10.4	9.90	10.3	10.5	9.95	14.2	0.642	1.64	3.08	0.451	
Ta	7.26	6.80	7.05	7.14	6.04	9.86	0.0046	0.399	1.01	1.66	
Pb	6.65	7.28	6.48	6.61	5.62	9.39	0.221	90.3	41.1	51.8	0.138
Th	12.1	11.8	11.8	11.7	10.5	17.5	0.183	41.9	54.0	144	0.0571

Table 4-1: (continued)

Sample name	NM19A	NM20A	NM20B	NM21	NM22A	NM22B	NM23	NM24	NM25	NM26A	NM26B	NM27A	NM29	NM30
Location	Agate Mountain	Agate Mountain	Agate Mountain	Agate Mountain	Agate Mountain	Agate Mountain	Agate Mountain	Agate Mountain	Agate Mountain	Agate Mountain	Agate Mountain	Agate Mountain	Agate Mountain	Agate Mountain
Lithology	Calcio-carbonatite	Magnesio-carbonatite	Magnesio-carbonatite	Calcio-carbonatite	silicious dike related to carbonatite intrusion	silicious dike related to carbonatite intrusion	Calcio-carbonatite	Calcio-carbonatite with quartz	Calcio-carbonatite	Calcio-carbonatite	Calcio-carbonatite	Secondary magnesite vein	Calcio-carbonatite	Magnesio-carbonatite
SiO_2	35.91	9.80	13.23	18.20	89.88	88.46	26.37	43.79	38.88	9.14	25.18	0.50	b.d.l.	7.90
Al_2O_3	0.02	0.10	0.12	0.10	0.02	0.03	b.d.l.	0.12	0.02	1.30	0.10	b.d.l.	b.d.l.	0.07
Fe_2O_3	2.12	2.53	2.69	1.85	0.51	0.59	0.72	5.03	2.71	4.15	2.91	b.d.l.	b.d.l.	8.25
MgO	0.11	12.21	11.36	0.15	0.03	0.04	0.22	0.17	2.47	2.36	3.30	21.56	0.67	13.41
MnO	0.29	1.94	3.31	2.63	0.30	0.28	0.20	1.85	1.21	1.14	1.06	b.d.l.	b.d.l.	1.55
CaO	34.29	25.93	22.53	36.19	4.65	5.44	38.28	25.41	28.32	41.96	33.56	31.97	52.65	28.44
Na_2O	b.d.l.	b.d.l.	0.05	b.d.l.	0.23	0.19	b.d.l.	b.d.l.	0.04	b.d.l.	b.d.l.	0.02	b.d.l.	0.22
K_2O	b.d.l.	0.06	0.09	0.07	b.d.l.	0.01	b.d.l.	0.07	0.02	1.43	0.07	b.d.l.	b.d.l.	0.01
TiO_2	0.01	0.01	0.01	0.01	0.01	0.02	0.01	0.01	0.02	0.05	0.01	b.d.l.	b.d.l.	0.02
P_2O_5	0.05	0.34	1.53	0.76	3.18	2.56	0.03	0.06	0.07	0.05	0.07	0.01	b.d.l.	1.00
SO_3	0.17	10.08	16.31	0.16	0.08	0.06	2.99	0.16	0.15	0.55	0.21	0.07	0.08	0.20
SrO		0.47	0.44	0.19				0.11		0.06	0.08			
BaO		8.27	12.31	0.76				0.66		0.68	0.46			
Sum	99.99	100.00	100.00	100.00	99.98	100.05	96.60	100.00	99.07	100.00	100.00	100.87	96.50	98.97
L.O.I	27.19	36.61	31.15	38.61	1.17	2.43	30.77	21.98	25.31	37.15	32.43	46.81	43.21	38.10
Li		8.56	9.40	8.90	11.0	15.8	9.63	1.89	2.50	1.33	1.50	6.49		5.77
Sc		1.58	2.57	3.43	6.49	4.92	2.46	2.17	6.83	5.88	3.62	0.173		11.0
V		130	152		24.1	25.1	5.86		100.0	115		0.224		131
Cr		7.80	4.13		0.958	0.805	2.61		5.81	7.62		3.15		19.4
Co		1.10	0.841		0.623	0.495	0.242		4.02	3.80		0.0860		46.9
Ni		3.32	3.26		3.61	3.11	0.428		3.43	3.64		0.764		196

Cu	0.334	0.528	1.20	2.67	2.27	1.18	2.47	0.983	5.00	1.20	1.66	16.2
Zn	492	667	176	116	114	73.9	590	575	1090	1832	4.67	462
Ga	120	128		11.6	10.3	12.9		26.3	23.9		0.215	27.0
Rb	0.634	0.714	2.37	0.716	0.744	0.470	0.412	0.997	37.3	0.659	0.316	0.765
Sr	3979	3751	1619	1620	1398	15647	891	574	483	670	3658	1242
Y	502	347	435	136	132	63.2	283	243	214	320	0.331	416
Zr	32.4	136	91.8	307	282	5.33	20.2	15.7	24.2	3.66	0.558	135
Nb	11.2	24.9	22.9	52.4	53.8	45.2	12.1	101	39.1	20.1	0.109	962
Cs	0.0861	0.0088	1.76	0.0830	0.0936	0.191	0.224	0.125	0.529	0.192	0.0130	0.107
Ba	74071	110249	6826	698	800	1716	5943	3010	6076	4143	58.6	2195
La	8698	7542	773	298	278	410	1723	991	836	895	0.911	1112
Ce	8889	9543	1207	686	608	873	2247	1948	1529	1742	2.35	2021
Pr	606	707	116	75.7	69.1	99.9	203	211	161	201	0.193	214
Nd	1449	1675	368	276	261	347	590	762	587	702	0.700	755
Sm	165	114	58.4	37.1	35.6	40.1	77.4	105	104	107	0.125	123
Eu	54.9	27.2	20.0	10.4	9.59	10.1	22.6	27.0	30.2	29.8	0.0352	36.9
Gd	179	76.6	63.9	29.6	26.4	22.5	66.6	68.6	77.9	82.8	0.0924	104
Tb	25.6	9.56	11.5	4.22	3.90	2.49	9.89	8.58	8.51	11.6	0.0112	15.2
Dy	120	53.7	71.4	24.2	24.0	12.5	54.4	48.6	41.4	61.5	0.0579	84.3
Ho	19.0	10.9	13.8	4.74	4.79	2.20	10.1	9.40	7.69	11.6	0.0109	14.8
Er	41.5	32.3	34.2	12.8	13.1	5.11	26.2	22.9	19.3	27.1	0.0275	35.2
Tm	4.24	4.32	4.97	1.82	1.80	0.584	3.95	2.71	2.32	3.39		4.29
Yb	18.9	23.3	29.5	11.1	10.7	3.18	25.1	14.4	13.1	19.0	0.0211	23.6
Lu	2.27	3.03	3.79	1.61	1.47	0.435	3.30	1.99	1.75	2.46		3.31
Hf	0.305	0.952	0.650	4.10	3.76	0.0704	0.323	0.375	0.400	0.189		1.38
Ta	0.0050	0.0071	0.0495	0.204	0.302	0.129	0.0356	0.331	0.446	0.0683		0.839
Pb	90.0	101	228	18.8	17.9	22.2	38.5	118	612	1108	0.767	65.7
Th	719	159	101	45.6	39.5	49.8	75.8	202	124	219	0.361	140

Table 4-1: (continued)

Sample name	NMH1	NMH2	NMH3	NMH4	NMH5	NMH6	NMH7	NMH11	NMH12	NMK2
Location	Dicker Willem	Dicker Willem	Dicker Willem	Dicker Willem	Dicker Willem	Dicker Willem	Dicker Willem	Dicker Willem	Dicker Willem	Gross Brukkaros
Lithology	Calcio-carbonatite	Calcio-carbonatite	Calcio-carbonatite	Calcio-carbonatite	Calcio-carbonatite	phonolite	Calcio-carbonatite with quartz	Calcio-carbonatite	Calcio-carbonatite	rhyolite
SiO_2	22.54	0.13	4.80	1.12	4.99	55.91	60.34	3.21	7.23	66.32
Al_2O_3	b.d.l.	b.d.l.	1.09	0.04	0.70	13.21	b.d.l.	0.09	0.07	7.49
Fe_2O_3	3.45	0.21	4.11	0.63	2.76	4.31	2.36	0.41	0.80	7.02
MgO	0.15	0.09	1.72	0.33	1.34	0.49	0.11	0.34	0.22	1.61
MnO	2.88	0.13	0.28	0.15	0.18	0.19	1.14	0.20	0.38	0.07
CaO	40.15	56.36	49.53	54.76	50.34	5.24	19.50	51.06	49.15	4.03
Na_2O	0.09	b.d.l.	0.35	0.14	0.34	1.87	b.d.l.	< 0.005	< 0.005	6.15
K_2O	0.03	0.01	0.77	0.05	0.46	11.22	b.d.l.	0.12	0.06	0.75
TiO_2	0.05	b.d.l.	0.22	0.02	0.19	0.27	0.01	0.01	0.01	1.09
P_2O_5	0.14	0.10	3.02	0.97	2.54	0.38	1.41	0.86	0.87	0.13
SO_3	0.05	0.13	b.d.l.	0.01	0.02	b.d.l.	b.d.l.	0.32	0.40	0.06
SrO								0.31	0.13	
BaO								0.38	0.19	
Sum	100.87	100.34	101.55	99.38	99.71	97.14	99.49	100.00	100.00	98.66
L.O.I	31.39	43.31	35.66	41.17	35.87	4.05	14.62	41.41	38.74	4.00
Li	4.56	0.227	9.91	1.35	4.97		0.417	33.6	0.423	36.8
Sc	2.29	0.214	0.810	0.525	1.06		6.05	5.44	2.66	26.3
V	83.0	0.872	54.4	20.8	54.5		74.2		17.8	317
Cr	5.92	3.69	2.43	3.96	3.74		1.91		1.05	256
Co	0.493	0.108	4.75	0.277	2.47		0.183		0.127	14.0
Ni	1.16	0.303	0.590	0.271	0.565		0.298		0.106	32.2
Cu	0.652	0.149	1.59	0.324	0.741		0.360	0.296	0.0735	22.3

Zn	998	2.46	116	11.3	72.1	596	23.9	18.0	43.3
Ga	13.9	5.43	21.3	7.14	14.1	3.49		9.89	9.30
Rb	1.56	0.409	44.7	1.90	22.6	0.944	1.67	0.0981	14.6
Sr	2334	7802	4819	8313	6461	923	2650	1073	50.5
Y	248	61.9	88.8	67.0	68.4	47.6	303	67.6	25.7
Zr	28.6	2.77	158	75.5	220	10.0	109	15.3	655
Nb	31.8	13.6	397	50.5	126	124	7.21	40.8	131
Cs	0.0179	0.0067	0.448	0.0379	0.280	0.0197	0.0984		0.381
Ba	1232	445	630	474	456	2699	3389	1745	504
La	564	180	308	211	230	156	934	329	9.07
Ce	1051	371	678	445	512	253	2161	782	20.2
Pr	109	42.7	83.6	51.6	62.3	27.2	286	93.7	2.89
Nd	370	162	330	196	241	95.2	1197	365	13.9
Sm	52.9	26.5	54.9	32.0	38.8	17.2	188	58.6	5.09
Eu	15.7	7.54	15.2	8.84	11.1	5.21	50.9	16.9	1.46
Gd	46.5	20.9	39.5	23.7	28.0	14.6	129	39.8	6.82
Tb	7.70	2.58	4.68	2.90	3.30	1.81	17.0	4.54	1.09
Dy	45.5	13.1	22.1	14.6	15.7	8.76	79.0	20.4	5.68
Ho	8.91	2.27	3.65	2.47	2.60	1.54	11.8	2.96	0.887
Er	26.7	5.43	8.02	5.85	5.88	3.74	22.6	5.77	1.88
Tm	4.17	0.636	0.911	0.698	0.670	0.454	2.12	0.525	0.230
Yb	25.8	3.43	4.85	3.81	3.71	2.34	9.33	2.14	1.40
Lu	3.33	0.473	0.635	0.532	0.501	0.316	1.000	0.224	0.205
Hf	1.15	0.0166	0.522	0.429	1.33	0.0864	1.10	0.164	11.4
Ta	0.111	0.619	15.6	3.98	5.39	0.0815	0.0432	0.0061	0.283
Pb	24.5	2.85	6.19	3.75	3.64	341	39.1	13.0	16.2
Th	28.5	1.91	46.1	7.38	18.4	16.0	24.7	3.61	21.2

b.d.l. below the detection limit

Table 4-2: C-O-Sr-Nd- Hf isotope data from the HIMU-like intrusions

Sample name	$^{143}Nd/^{144}Nd$	$^{143}Nd/^{144}Ndi$	$^{87}Sr/^{86}Sr$	$^{87}Sr/^{86}Sri$	$^{176}Hf/^{177}Hf$	$^{176}Hf/^{177}Hf_i$	$\delta^{18}O$	$\delta^{13}C$
NAM61	0.512873	0.512777	0.703257	0.703066	0.282901	0.282894		
NAM62	0.512860	0.512809	0.703520	0.703440				
NAM63	0.512867	0.512772	0.703478	0.703253	0.282899	0.282892		
NAM64	0.512867	0.512816	0.703676	0.703550				
NM2018A	0.512862	0.512810	0.704218	0.704064	0.282873	0.282866		
NM2018B	0.512868	0.512820	0.703352	0.703233	0.282869	0.282862		
NM10	0.512340	0.512289	0.705738	0.705677			20.22	-2.32
NM15	0.512752	0.512726	0.703584	0.703585			21.65	-2.03
NM16	0.512777	0.512755	0.706151	0.706136			19.50	-1.23
NM17	0.512781	0.512753	0.706627	0.706557			22.28	-3.90
NM18	0.512775	0.512716	0.706438	0.706441			23.70	-6.51
NM20A	0.512764	0.512744	0.704184	0.704187			23.94	-3.88
NM21	0.512782	0.512748	0.704639	0.704638			22.96	-4.83
NM22A	0.512778	0.512751	0.703319	0.703321			15.66	-4.20
NM23	0.512765	0.512745	0.703935	0.703938			21.77	-4.57
NM24	0.512783	0.512758	0.704235	0.704237			21.08	-4.81
NM25	0.512773	0.512745	0.705118	0.705115			22.82	-4.13
NM26A	0.512750	0.512710	0.706064	0.705807			23.72	-4.57
NM26B	0.512793	0.512761	0.704923	0.704923			20.10	-3.86
NM27A	0.512744	0.512703	0.705977	0.705980			25.03	-4.17
NM30	0.512792	0.512756	0.704514	0.704515			26.42	-2.18

NMH1	0.512679	0.512622	0.703832	0.703825	18.58	-3.63
NMH2	0.512729	0.512668	0.703338	0.703332	7.88	-5.25
NMH3	0.512718	0.512657	0.703448	0.703423	11.48	-4.39
NMH4	0.512726	0.512665	0.703293	0.703286	7.92	-5.25
NMH7	0.512742	0.512678	0.703433	0.703425	26.04	-6.51
NMH11	0.512754	0.512694	0.703176	0.703169	12.35	-1.90
NMH12	0.512743	0.512683	0.703178	0.703171	10.84	-1.68
NMK2	0.512236	0.512135	0.722306	0.721453		

Table 4-3: Pb isotope data from the HIMU-like intrusions

Sample name	$^{206}Pb/^{204}Pb$	$^{207}Pb/^{204}Pb$	$^{208}Pb/^{204}Pb$	$^{238}U/^{204}Pb$	$^{235}U/^{204}Pb$	$^{232}Th/^{204}Pb$	$^{206}Pb/^{204}Pb_i$	$^{207}Pb/^{204}Pb_i$	$^{208}Pb/^{204}Pb_i$
NAM61	20.4940	15.7304	40.1969	30.7048	0.2227	125.5436	20.155	15.714	39.755
NAM62	20.0024	15.7206	39.7757	27.0318	0.1961	110.9093	19.705	15.707	39.386
NAM63	20.0826	15.7191	39.8537	30.3309	0.2200	124.5591	19.748	15.703	39.416
NAM64	20.2945	15.7268	40.0719	29.6011	0.2147	121.5141	19.968	15.711	39.645
NM2018A	20.1248	15.7300	40.0489	28.8497	0.2092	128.7930	19.807	15.715	39.596
NM2018B	20.4953	15.7316	40.0937	30.6170	0.2221	128.4973	20.158	15.716	39.642
NM10	18.0327	15.5657	38.7345	35.7510	0.2593	54.1373	17.611	15.546	38.551
NM15	20.6971	15.8203	39.9084	29.2414	0.2121	32.0645	20.360	15.804	39.817
NM16	20.9884	15.8368	40.5011	19.9232	0.1445	91.9116	20.771	15.826	40.167
NM17	20.6966	15.8265	40.8896	6.1795	0.0448	195.0028	20.655	15.824	40.136
NM18	19.6240	15.7391	39.3485	14.4527	0.1048	27.9845	19.476	15.732	39.273
NM20A	20.6518	15.8223	43.1422	4.1236	0.0299	575.0159	20.637	15.822	40.844
NM21	20.6767	15.8280	40.1432	0.5850	0.0042	30.6860	20.707	15.829	40.058
NM22A	20.8777	15.8386	40.6711	11.9859	0.0869	169.4035	20.762	15.833	40.022
NM23	20.7610	15.8304	40.8080	5.6204	0.0408	156.6378	20.727	15.829	40.211
NM24	20.7635	15.8304	40.6489	10.7043	0.0776	137.7545	20.664	15.826	40.128
NM25	19.7014	15.7441	39.9363	2.3075	0.0167	117.0092	19.709	15.744	39.499
NM26A	19.1251	15.6925	39.1182	0.1887	0.0014	13.5098	19.159	15.694	39.101
NM26B	19.1004	15.6906	39.0996	0.1286	0.0009	13.2040	19.135	15.692	39.084
NM27A	19.3886	15.7060	39.2240	16.4074	0.1190	31.6664	19.215	15.698	39.133
NM30	20.8940	15.8369	40.6055	13.6789	0.0992	149.4289	20.757	15.830	40.037
NMH1	20.4742	15.8151	40.1954	18.6600	0.1353	80.5300	20.266	15.805	39.931
NMH2	21.6782	15.8674	40.1355	67.4456	0.4892	47.1575	21.097	15.840	39.952
NMH4	22.4027	15.9107	40.4956	88.0826	0.6388	140.2193	21.663	15.876	40.085

NMH7	20.8430	15.8330	40.0167	0.8566	0.0062	3.2508	20.770	15.830	39.940
NMH11	20.7021	15.8133	40.0055	6.7682	0.0491	43.7375	20.584	15.808	39.831
NMH12	20.5915	15.7997	39.8910	2.6992	0.0196	19.1108	20.505	15.796	39.776
NMK2	20.0814	15.7807	40.2292	1.7181	0.0125	89.9342	20.068	15.780	39.915

Table 4-4: Calculation of melts that coexist with perovskite and majorite and final carbonatite magma composition after the separation of silicate and carbonatite melts.

	Perovskite[1] (μg/g)	Primary carbonatitem elt (presence of perovskite)[2] (μg/g)	D_1 carbonatitic/ phonolitic melt[3]	Separated carbonatite magma (perovskite)[4] (μg/g)	Primitive mantle normalized[7]	Majorite[1] (μg/g)	D_2 majorite/ melt[5]	Primary carbonatite melt (presense of majorite) [6] (μg/g)	Separated carbonatite magma (majorite)[4] (μg/g)	Primitive mantle normalized[7]
Rb	1.7	18.7	0.70	13.1	24.4	15	0.0055	2727.2	1908.7	3565.6
Ba	7.0	117	2.37	277.6	45.9	0.6	0.0001	6000	14234.7	2353.2
U	63.9	12.7	1.14	14.4	711.2	0.2	0.023	8.7	9.89	487.0
Nb	353.2	315	0.72	226.3	366.4	2.8	0.007	400	287.3	465.3
La	1628.8	369	2.49	920.0	1498.6	0.2	0.003	66.7	166.2	270.8
Ce	9670.4	1866	2.47	4604.9	2876.1	6.0	0.016	375	925.4	578.0
Nd	5769.3	940	2.44	2293.6	1928.7	20.9	0.061	342.6	836.0	703.0
Sr	351.3	281	2.48	696.5	38.2	5.0	0.0031	1612.9	3997.9	219.5
Sm	1281.8	212	2.40	509.6	1318.4	6.7	0.22	30.5	73.2	189.4
Hf	32.8	65.7	0.09	6.13	22.9	2.5	0.91	2.75	0.256	1.0
Zr	2765.6	5531	0.19	1027.2	105.7	69.1	0.75	92.1	17.1	1.8
Eu	330.8	57.6	2.39	137.6	944.9	1.9	0.36	5.28	12.6	86.6
Gd	606.5	114	2.37	270.5	527.6	5.5	0.54	10.2	24.2	47.1
Tb	69.4	14.5	2.36	34.2	364.1	0.9	0.46	1.96	4.62	49.1
Dy	328.7	78.2	2.31	180.7	283.4	4.6	0.64	7.19	16.6	26.0
Er	92.4	29.3	2.25	65.9	158.2	3.0	2.4	1.25	2.81	6.75
Yb	59.5	25.3	2.15	54.3	131.0	3.7	3.6	1.03	2.21	5.32
Lu	8.0	3.9	2.15	8.38	131.5	0.6	4.3	0.14	0.300	4.70

1. Trace elements concentrations of perovskite and majorite, respectively, from Walter et al. (2008).

2. Calculated melt composition which coexists with perovskite (Walter et al., 2008), assumed to reflect primary carbonatite melt.

3. Partition coefficients between carbonatite melt and silicate (phonolitic) melt based on the experimental study of Martin et al. (2013).

4. Carbonatite magma composition, after the separation of silicate and carbonatite melts, calculated by the relation $C_{\text{separated carbonatite melt}} = C_{\text{primary carbonatite melt}} \times D_1$.

5. $D_{\text{Majorite/melt}}$ from the experimental study of Dalou et al. (2009).

6. Calculated primary melt composition which coexists with majorite, are calculated by the relation $C_{\text{melt}} = C_{\text{majorite}}/D_2$.

7. Resulting carbonatite melt compositions normalized to Primitive Mantle, respectively (Hofmann, 1988) forming lower and upper bounds of grey field in Figure 4-4a.

4.6. Discussion

4.6.1. Alteration and Crustal contamination

A potential problem with carbonatites is alteration and recrystallization. The Agate Mountain carbonatite complex is heavily eroded and it is located in a remote desert region without any fresh outcrops. Although most of the samples have C isotopic compositions consistent with a mantle composition, the elevated $\delta^{18}O$ clearly shows that the carbonatites have undergone low-temperature alteration. Unforunately none of the samples have mantle-like O isotope ratios. On the other hand, two samples from the Dicker Willem carbonatite complex have mantle-like O and C isotope ratios, plotting within the field for oceanic basalts and primary carbonatites from Keller and Hoefs (1995). Several samples have maintained their mantle C isotope compositions, but two samples have slightly elevated $\delta^{18}O$ and $\delta^{13}C$, which could reflect high-temperature alteration or sediment assimilation. These two samples however have the lowest initial Sr isotope ratios, thus show no clear evidence of crustal assimilation. The two samples with the highest initial Sr isotope ratios also have high $\delta^{18}O$, suggesting that low-T alteration may have resulted in some exchange of Sr in the carbonatites with crustal Sr. The Swakopmund basanite samples have very similar concentrations of incompatible trace elements with the exception of sample NM2018B, which has higher concentrations of all incompatible elements than the other samples except for TiO_2. Alteration appears to have had little affect on these samples.

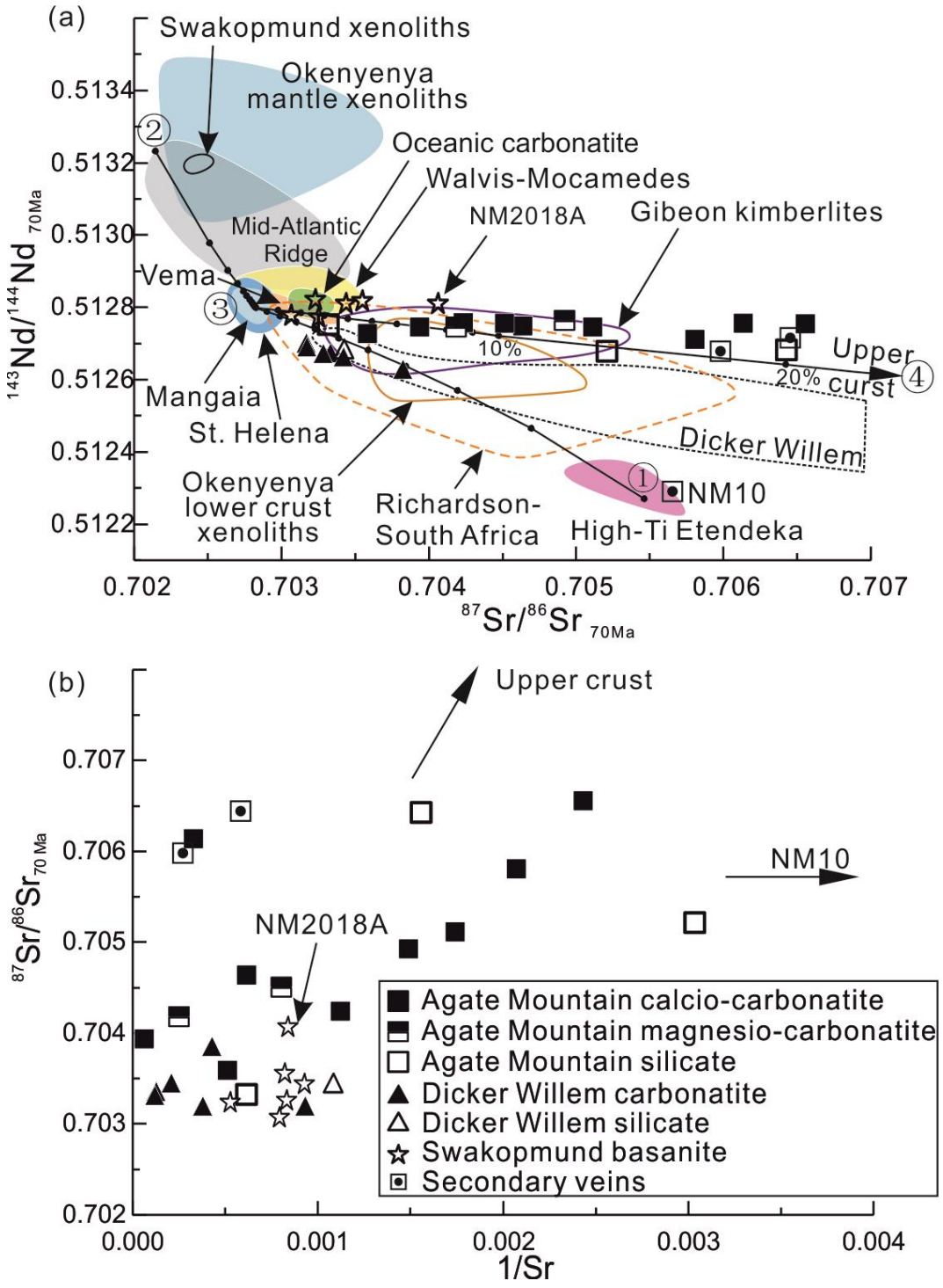

Figure 4-6: (a) Initial $^{87}Sr/^{86}Sr$ vs $^{143}Nd/^{144}Nd$ ratios (age corrected to 70 Ma) of the investigated rocks showing possible mixing trends. The trend in the Agate Mountain samples towards extremely high $^{87}Sr/^{86}Sr$ isotope ratios is consistent with crustal assimilation (see Section 4.6.1 for detailed discussion). Bulk mixing lines are calculated for endmember compositions of ① Gough-type sample NAM21 from northern Etendeka high-Ti flood basalt (Zhou et al., 2020),② the most depleted sample from the Mid-Atlantic Ridge representing upper mantle (CHRRI88-016-101; Class and Lehnert, 2012), ③ the average value of St. Helena HIMU (Chaffey et al., 1989; Salters et al., 2011), and ④ an upper continental crustal component (average composition of the Nosib and Swakop metasedimentary group samples; McDermott and Hawkesworth,

1990). Black dots on the mixing lines mark 10% increments except when marked. Samples that constitute the following reference fields were extrapolated to 70 Ma using the following parent-daughter ratios for their potential source composition: Gough EM1 composition: U/Pb = 0.1367, Th/Pb = 0.6758, Rb/Sr = 0.0204, Sm/Nd = 0.3378; HIMU-St. Helena: U/Pb = 0.3043, Th/Pb = 0.9565, Rb/Sr = 0.0071, Sm/Nd = 0.3590 (Stracke et al., 2003; Willbold and Stracke, 2006); Mid-Atlantic Ridge basalts: U/Pb = 0.1667, Th/Pb = 0.4444, Rb/Sr = 0.0065, Sm/Nd = 0.4114 (Workman and Hart, 2005). Reference sources: High-Ti basalts from Northern Etendeka (representing the Gough-type EM1 plume source in the study area) (Zhou et al., 2020); Mid-Atlantic Ridge (Class and Lehnert, 2012); Walvis–Mocamedes (HIMU-composition) hotspots (Homrighausen et al., 2018a; Homrighausen et al., 2018b); St. Helena HIMU (Chaffey et al., 1989; Salters and White, 1998; Thirlwall, 2000; Willbold and Stracke, 2006, 2010); Vema seamount (Class and le Roex, 2011); additional Dicker Willem samples (Cooper and Reid, 2000; Cooper and Reid, 1998); Gibeon kimberlites (Davies et al., 2001); Okenyenya mantle and lower crust xenoliths (Class and le Roex, 2006; le Roex and Class, 2014); Swakopmund xenoliths (Class and le Roex, 2006); Richardson-South Africa (Becker and Roex, 2006; Collerson et al., 2010; Erlank et al., 1987; Homrighausen et al., 2018b; Janney et al., 2002; Nowell, 2004; Rogers et al., 1992); Mangaia HIMU from Austral volcanic chain (Nakamura and Tatsumoto, 1988; Palacz and Saunder, 1986; Woodhead, 1996). Oceanic carbonatite field represents the calcio-carbonatites from the Canary and Cape Verde hotspot islands (Hoernle et al., 2002). (b) 1/Sr vs initial $^{87}Sr/^{86}Sr$. Arrows point in the direction of upper crust contamination (Nosib and Swakop metasediments; McDermott and Hawkesworth, 1990) and towards sample NM10 composition, a secondary silicate vein with very low Sr concentration and with the same $^{87}Sr/^{86}Sr$ and $^{143}Nd/^{144}Nd$ as its hosting Etendeka (Gough-type) flood basalts.

Unlike magmas erupted in ocean basins such as the late-stage Walvis Ridge HIMU seamounts, magmas forming Agate Mountain, Dicker Willem and the Swakopmund plugs had to pass through 40 km thick Proterozoic continental crust (Yuan et al., 2017) with extreme trace element and isotopic composition. In particular, continental crust is characterized by high abundances of highly incompatible elements (such as the Large Ion Lithophile Elements and Pb) and low relative abundances of Nb and Ta (Hofmann, 1988). The high composition of incompatible elements in carbonatites and silica undersaturated rocks, however, makes any recognition of crustal contamination based solely on trace elements very difficult (Ionov and Harmer, 2002). To comprehensively evaluate any crustal influence on silicate and carbonatitic rocks, we thus also need to evaluate their isotopic signatures.

Sr isotope ratios are widely used in evaluating the crustal contamination of basaltic rocks, due to the extreme differences in $^{87}Sr/^{86}Sr$ between the mantle, such as 0.7025–0.7035 for upper mantle MORB source and as high as ~0.706 for intraplate ocean island basalts (OIBs) (Figure 4-6a), and the regional (upper) continental crust ($^{87}Sr/^{86}Sr_{70\ Ma}$ = 0.71–0.88, for Nama group and Kuiseb, Khan, Etusis formation metasedimentary rocks; McDermott and Hawkesworth, 1990). The Sr isotope ratios of calcio-carbonatites are

usually resistant to significant crustal contamination, because of their high Sr concentration (average of 5662 μg/g; Hoernle et al., 2002). Excluding the secondary silicate and carbonate veins (NM10, NM18 and NM27A) with overall low incompatible element abundances, the Sr concentrations in the carbonatite and basanite samples range from 410–8,313 μg/g (average = 2,364 μg/g) except NM23 from Agate Mountain with 15,647 μg/g of Sr. Considering the extreme Sr isotope ratios of upper crustal material, the Sr isotope ratios of the carbonatite and basanite samples, however, are still sensitive to crustal contamination, especially in the silicious carbonatites with low Sr concentration. As shown in Figure 4-6b, calcio-carbonatites from Agate mountain show a good positive correlation of 1/Sr versus $^{87}Sr/^{86}Sr$ ratio, consistent with greater upper crustal contamination in samples with lower Sr concentration. If we assume that St. Helena lavas, erupted on oceanic lithosphere, represent the primary source composition, the trend towards radiogenic Sr isotope compositions of the Agate Mountain carbonatites can be modelled by St. Helena HIMU magmas assimilating up to 20% regional upper crust (applying a simple bulk mixing calculation, Figure 4-6a). In contrast, the two samples from Swakopmund (NM2018A) and Dicker Willem (NMH1) with slightly elevated $^{87}Sr/^{86}Sr$ ratios require less than 8% crustal assimilation.

In contrast to Sr, the Nd (79.7–1,675 μg/g) and Pb (2.85–1,108 μg/g) contents of the investigated samples (excluding secondary silicate rocks/carbonates and a Gross Brukkaros rhyolite) are generally higher than in the regional upper crust i.e. the Nama group and Kuiseb, Khan, Etusis formations metasedimentary rocks (average concentration of Nd is 37.0 and Pb is 18.0 μg/g; McDermott and Hawkesworth, 1990). Thus, these elements, and therefore their respective isotope ratios, are less susceptible to crustal contamination. Accordingly, our samples show very little variation in Nd isotopes (Figure 4-6a): Agate Mountain carbonatites range from 0.51271–0.51276 and silicate rocks from 0.512678–0.512778 (including NM31 and NM32 from Homrighausen et al. (2020)); Dicker Willem from 0.51262–0.51269 and Swakopmund basanites from 0.51277–0.51282. As noted above, however, all of the Dicker Willem samples have slightly less radiogenic Nd isotope ratios than St. Helena (with a range of 0.51273–0.51287). The Dicker Willem sample NMH1 with a Nd isotope ratio of 0.51262 can be derived from the remaining samples (0.51266–0.51269) by less than 10% crustal assimilation (Figure 4-7C). The remaining Dicker Willem samples also have

slighltly more radiogenic Sr and less radiogenic Nd isotope ratios and extend to more radiogenic Pb isotopic composition than the oceanic St. Helena basanites. Although the high-Ti Etendeka basalts (Gough-type EM1) have more radiogenic Sr and less radiogenic Nd than the Dicker Willem samples, they also have less radiogenic Pb isotope ratios and thus the Dicker Willem samples cannot be derived by mixing of St. Helena and high-Ti Etendeka type sources. We also note that no high-Ti basalts have been found in the Dicker Willem area to date. Finally, the two samples with most radiogenic Pb of 21.10 (NMH2) and 21.66 (NMH4) have O and C isotopic composition within the range of oceanic basalts and primary carbonatites, suggesting that the Dicker Willem HIMU source has more radiogenic Sr and Pb but less radiogenic Nd isotope ratios than St. Helena (Figure 4-6a, Figure 4-7).

4.6.2. Generation of the carbonatite magmas

There are two main theories about the ultimate magmatic origin of carbonatites: (1) the metasomatized SCLM model (Green and Wallace, 1988; Hou et al., 2015; Le Roex and Lanyon, 1998; Song et al., 2016), or (2) deep-seated mantle plumes (Ernst and Bell, 2010; Hoernle et al., 2002; Hoernle et al., 1991; Kogarko and Veselovskiy, 2019).

Low degree melts of metasomatized SCLM can explain the EM1-like composition of Cretaceous carbonatites in the Damara Belt that have ages of 130–120 Ma (Le Roex and Lanyon, 1998), but are not likely to have generated the significantly younger (~80–40 Ma) HIMU-like carbonatites and alkaline rocks. If the SCLM was metasomatized by the Tristan-Gough plume, and played an important role in generating the Agate Mountain, Swakopmund and Dicker Willem magmas, we would expect them to have a similar isotopic composition to the Etendeka flood basalts, rather than end member HIMU type compositions. Furthermore, the mantle xenoliths (lherzolite) found in the Swakopmund plug magmas and at other locations in Namibia (e.g., at Okenyenya, 200 km NE of Swakopmund, an alkaline intrusive complex that formed ~129–123 Ma ago, shortly after the Etendeka event; Milner et al., 1993) do not have HIMU-like composition (Figure 4-6) arguing against a widespread dispersion of HIMU material in the regional subcontinental lithosphere (Class and le Roex, 2006). In addition, xenoliths from the lower crust (also found at Okenyenya) that are proposed to reflect the effect of metasomatism by the Tristan-Gough plume show only intermediate Sr-Nd isotopes ratios (Figure 4-6), rather than a HIMU composition (le Roex and Class, 2014). Instead,

the Okenyenya lamprophyre lavas, for which Pb isotopes are available (yielding high $^{207}Pb/^{204}Pb$ and low $^{208}Pb/^{204}Pb$ for a given $^{206}Pb/^{204}Pb$; Figure 4-7) and which are believed to be derived from metasomatized lithospheric mantle (Geldmacher et al., 2008; Le Roex and Lanyon, 1998), confirm that the metasomatizing agent has an EM1-like (Etendeka type) composition, albeit resembling the specific southern Etendeka peculiarity (Doros component) as recently refined by Zhou et al. (2020). It is, however, possible that the arrival of the postulated (small-scale) HIMU plume(s) (see Section 4.6.3. below) lead to a (minor) secondary refertilization of the regional lithosphere with HIMU-type material such as proposed for the lithosphere beneath the Kaapvaal craton (Kobussen et al., 2008; Weiss and Goldstein, 2018). In any case, the postulated trace element enrichment in the lithosphere by this metasomatism (if directly related to the Etendeka flood basalt event as generally believed, e.g., Le Roex and Lanyon, 1998) occurred just 40–80 Ma before the emplacement of the post-Etendeka carbonatites investigated here. The time interval is not long enough to generate HIMU compositions in the magma source by radiogenic ingrowth (1.0–3.2 Ga; Homrighausen et al., 2018b).

Ruling out a lithospheric source, the carbonatites could be primary melts from an upwelling deep-seated mantle plume of HIMU composition, such as proposed for the Canary, Cape Verde and the Eocene Tamazert alkaline complex in the High Atlas mountains (e.g., Bouabdellah et al., 2010; Doucelance et al., 2003; Hoernle et al., 2002; Hoernle et al., 1991). The spiked multi-element patterns with strong enrichments of most incompatible elements including the REEs (Figure 4-4), as widely observed in carbonatites (e.g. Doroshkevich et al., 2017; Hoernle et al., 2002), can be explained by very low degree of melting and high partition coefficients for REEs in carbonatitic melts (Dasgupta and Hirschmann, 2006; Martin et al., 2013). The significantly depleted HFSE concentrations, however, primarily reflect the low partition coefficients for these elements in carbonatitic liquids and/or fractionation of phases rich in HFSEs (see below).

The postulated “primary carbonatite melts” are proposed to be generated by low degree melts of deeply subducted, altered (containing some carbonate) oceanic crust (Dasgupta et al., 2007; Hammouda and Keshav, 2015; Hoernle et al., 2002). Walter et al. (2008) calculated the compositions of such primary melts at the temperature and pressure conditions of the mid-mantle transition zone, based on Ca-rich inclusions in diamonds

(red line in Figure 4-4a). Their compositions, however, do not show significant depletion in Hf and Zr. HFSEs are estimated to reside in certain minerals such as perovskite (Chakhmouradian, 2006) and rutile in eclogite (Zack et al., 2002). Adding this fractionation effect by calculating respective "differentiated carbonatite melts" coexisting with perovskite and majorite garnet, a certain Zr and Hf depletion is achieved (Walter et al., 2008), but not sufficient enough to explain the extreme depletion seen in natural carbonatites such as in our samples (Figure 4-4a, b, c).

The immiscibility of silicate and carbonate melts could serve as another process to generate more pronounced negative Hf and Zr anomalies. At 1–3 GPa, the carbonatite/silicate melt partition coefficients (D) of HFSE for an H_2O-rich system are lower than 1 and D^{REEs} are higher than 1 (Martin et al., 2013). It was shown that the pressure does not have a major influence on element partitioning, but that the presence of H_2O (2–4 wt%) is crucial for increasing the partition coefficients of the REEs, which explains some previous contrary results suggesting that D^{REE} is lower than 1 in dehydrated systems (Veksler et al., 1998). At such conditions (1–3 GPa, 1150–1200°C, 2–4 wt% of water), the partition coefficients between carbonatite and silicate melts can enhance the depletion of HFSEs and the enrichment of REEs.

If we accept that carbonatite magmas formed by low-degree melts of subducted, carbonated oceanic crust (returned by mantle plumes) coexisting with perovskite and majorite garnet in the deep upper mantle (Walter et al., 2008), and subsequently undergoing an immiscible process at shallower depth, their composition can be calculated based on the partition coefficients between silicate and carbonate melts at 1–3 GPa (Martin et al., 2013). Our respective calculations are shown in Figure 4-4a (grey-shaded field). The upper and lower boundary of this field is defined by carbonatite melt fractionation either in the presence of perovskite or majorite garnet, respectively (see details of modelling in Table 1 caption). The calculated carbonatite compositions largely overlap with the Agate Mountain and Dicker Willem patterns including their distinctive Zr and Hf depletion. Our results are therefore consistent with the hypothesis that carbonatites are created by low-degree melts of recycled, carbonated ocean crust (Dasgupta et al., 2007; Hammouda and Keshav, 2015; Hoernle et al., 2002) with carbonatitic melts getting subsequently separated from silicate melts by immiscibility.

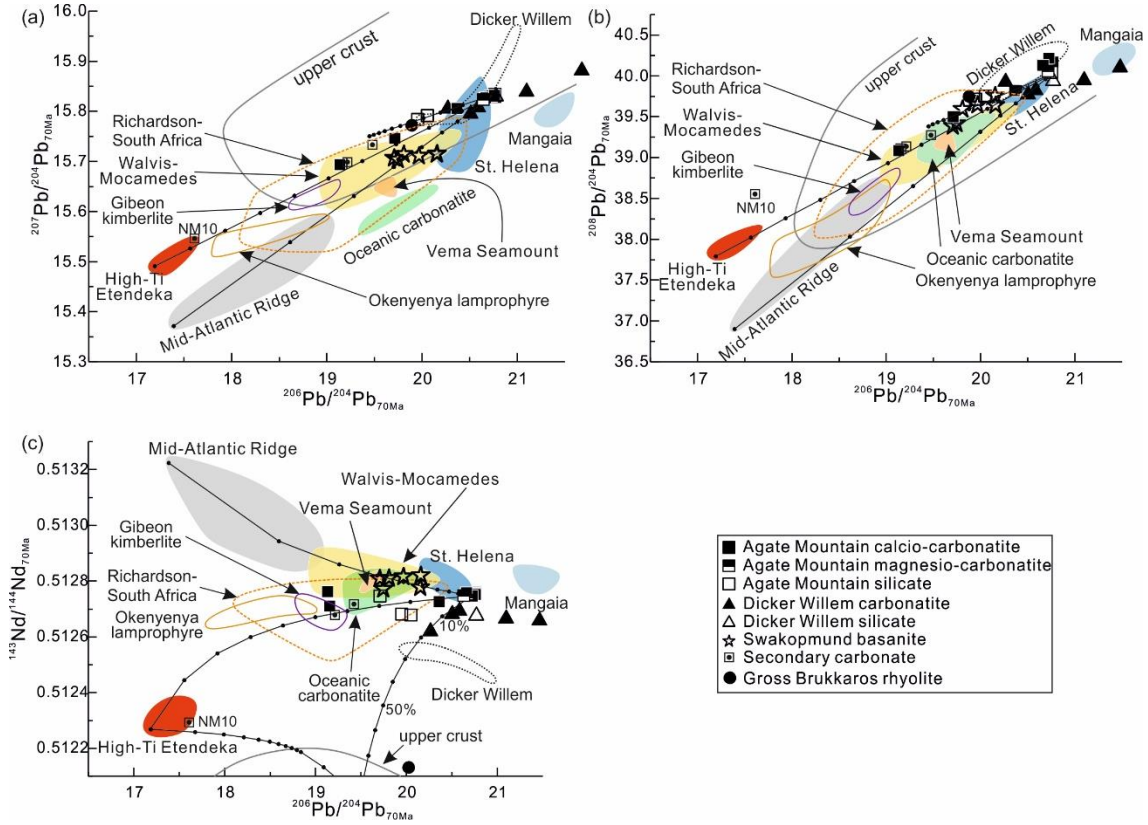

Figure 4-7: Initial (a) $^{206}Pb/^{204}Pb$ vs. $^{207}Pb/^{204}Pb$, (b) $^{206}Pb/^{204}Pb$ vs. $^{208}Pb/^{204}Pb$ and (c) $^{206}Pb/^{204}Pb$ vs. $^{143}Nd/^{144}Nd$ isotope diagrams (projected to 70 Ma ago). Data sources and endmember compositions used for calculation of mixing lines and projection of reference field to 70 Ma are the same as in Figure 4-6, except for the replacement of the average St. Helena value by Agate Mountain carbonatite sample NM22A (this study) for the HIMU mixing line endmember. Reference sources: Okenyenya lamprophyre (Le Roex and Lanyon, 1998).

A problem with this model is that subducted oceanic crust (and most mantle components, such as EM1, HIMU, depleted mantle (DM)), are generally considered to be dehydrated during the subduction process and thus the water concentration is only a few hundreds of μg/g at most (Dixon et al., 2002), which is lower than the assumed water concentration required for the immiscibility process. The potential source of the extra water could be: (1) hydration of the upper mantle below Namibia by subduction processes. Although the most recent subduction ceased at ~460 Ma ago (Miller, 1983), the flat-subducted Late Proterozoic oceanic lithosphere (Jung et al., 2020) could have added water to the shallow lithospheric mantle. It is, however, not clear whether the water content in the lithospheric mantle can influence immiscibility of the plume-derived carbonatite magma. (2) trapped water in the mantle transition zone or deep-subducted components. The transition zone has a high water-storage capacity (Bercovici and Karato, 2003) and its minerals have unusually high water solubilities

(Williams and Hemley, 2001). Various approaches were used to infer the water solubility or the actual water content of the transition zone. Ringwoodite inclusions in diamonds contain about 1 wt% H_2O (Pearson et al., 2014), and magmatic water concentrations of clinopyroxene phenocrysts in Bermuda lavas range from 1.9 to 5.7 wt%, which is attributed to a wet transition zone (Mazza et al., 2019). Water distribution models based on experimental and geophysical approaches also give a mean 1 wt% H_2O content in the transition zone (Bercovici and Karato, 2003; Karato, 2011). Alternatively, high pressure experiments indicate that water can be delivered to the core-mantle boundary by deep-subducted slabs (Nishi et al., 2014). Hence, the lower mantle (and mantle plumes rising from it) could carry excess water enabling the separation of carbonatite magmas.

4.6.3. Isotopic Composition of post-Etendeka HIMU volcanism

As mentioned above, the post-Etendeka HIMU volcanism along the coast of Namibia (Agate Mountain, Dicker Willem and basanite plugs near Swakopmund) are significantly younger than the EM1 dominated Etendeka flood basalt event. The temporal relationship and isotopic composition of these carbonatitic and silica-undersaturated igneous rocks are very similar to the late-stage HIMU volcanism on the Walvis Ridge and Shona tracks, which succeeded the formation of the age-progressive volcanism of the EM1-dominated Tristan-Gough-Walvis and Shona hotspot tracks by ~30 Ma at a given location (Homrighausen et al., 2018a; Homrighausen et al., 2020). It is likely that the carbonatitic complexes and basanitic plugs were derived from the same source as the late-stage HIMU volcanism on the Walvis Ridge and may also form one or several age-progressive hotspot track(s) extending into Angola (Homrighausen et al., 2020) and South Africa, respectively. Therefore, we will compare the composition of the carbonatite-silica-undersaturated rocks with the late-stage Walvis Ridge seamounts and St. Helena (the proposed radiogenic mixing endmember for all regional HIMU magmas) in more detail below.

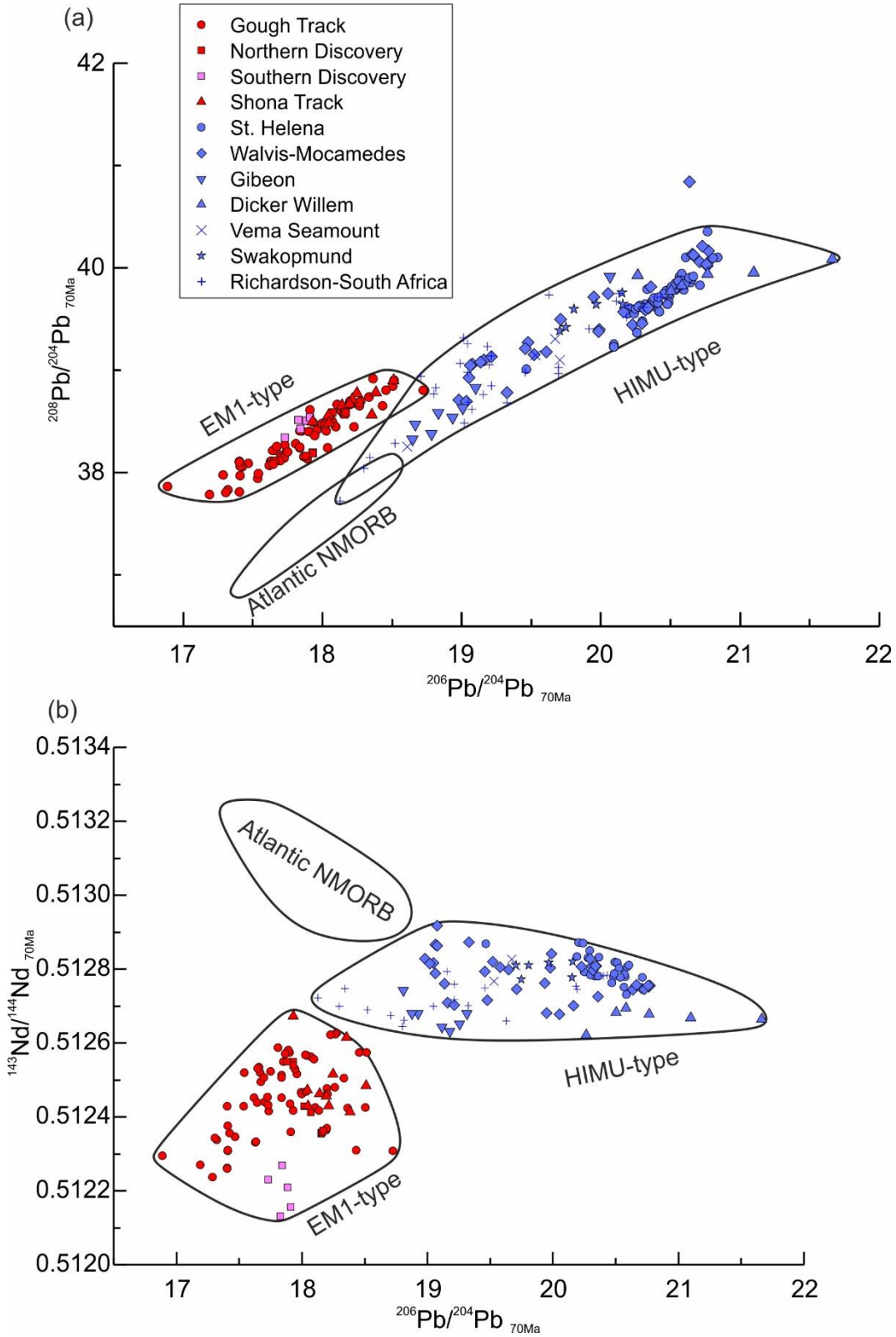

Figure 4-8: Initial (a) $^{206}Pb/^{204}Pb$ vs. $^{208}Pb/^{204}Pb$ and (b) $^{206}Pb/^{204}Pb$ vs. $^{143}Nd/^{144}Nd$ isotope diagrams (projected to 70 Ma ago), showing distinct compositions for South Atlantic depleted upper mantle, South Atlantic (EMI-type) mantle plumes and African margin (HIMU-type) mantle upwellings. South Atlantic depleted upper mantle is based on the composition of Mid-Atlantic Ridge (Atlantic NMORB) samples (Class and Lehnert, 2012), excluding samples

located adjacent to Azores (35°N–43°N), Sierra Leone (1.5°S–6°N), Ascension (~9°S) and Jan Mayen (~71°N) plumes. The EM1-type field comprises samples from the Gough track (Hoernle et al., 2015; Homrighausen et al., 2019; Rohde et al., 2013a), Northern and Southern Discovery (Schwindrofska et al., 2016), and Shona track (Hoernle et al., 2016). The HIMU-type field contains samples from St. Helena (Chaffey et al., 1989; Salters and White, 1998; Thirlwall, 2000; Willbold and Stracke, 2006, 2010), Walvis–Mocamedes (including Agate Mountain; Homrighausen et al., 2018a; Homrighausen et al., 2018b; this study), Gibeon (Davies et al., 2001), Dicker Willem (this study), Vema seamount (Class and le Roex, 2011), Swakopmund (this study) and Richardson–South Africa track (Becker and Roex, 2006; Collerson et al., 2010; Erlank et al., 1987; Homrighausen et al., 2018b; Janney et al., 2002; Nowell, 2004; Rogers et al., 1992). Two samples from the continental part of the Richardson–South Africa track show $^{208}Pb/^{204}Pb$ and $^{143}Nd/^{144}Nd$ ratios distinct from the HIMU-type field, indicating contamination by continental crust and thus were not plotted.

Except for their Sr isotope ratios (Figure 4-6), which extend to much higher ratios than St. Helena HIMU and which are most likely caused by the susceptibility of Sr to crustal contamination of these relatively Sr-poor carbonatite magmas (see Section 4.6.1), all other isotope ratios of the carbonatites analyzed in this study (Figure 4-6, Figure 4-7) are relatively similar to the HIMU-type late-stage seamounts. These include the late-stage seamounts on and next to the Walvis Ridge and Shona volcanic track (Walvis-Mocamedes and Richardson-South Africa; Homrighausen et al., 2020), whose composition was proposed to be generated by mixing of a HIMU endmember with a low-μ component (a mixture of Gough-type plume and normal upper mantle; Homrighausen et al., 2018a). Likewise, the lavas investigated here converge towards a common, extreme HIMU endmember, regardless if the depleted end of possible mixing trajectories point to upper mantle, High-Ti Etendeka (Gough plume), or crustal composition (Figure 4-6, Figure 4-7).

Compared to the (silicate) HIMU-like late-stage volcanism on Walvis Ridge (yellow field in Figure 4-7), the carbonatites of this study show slightly more radiogenic Pb and less radiogenic Nd isotope ratios. The two Dicker Willem samples (NMH2 and NMH4) with mantle-type O and C isotopic composition also have the most radiogenic Pb and the least radiogenic Nd (excluding sample NMH1 which shows evidence of crustal contamination). NMH2 and NMH4 also have slightly higher initial $^{206}Pb/^{204}Pb$ than the (age-corrected) field of the classic St. Helena HIMU endmember. A similar deviation has also been observed in previously published data from East African carbonatites (Bell and Tilton, 2001). Therefore, the extreme (most enriched) HIMU signal may be most pronounced in very low-degree carbonatitic melts (in comparison to the basanitic melts exposed on St. Helena island). We note that the Pacific HIMU endmember

localities on Mangaia Island of the Austral volcanic chain (Nakamura and Tatsumoto, 1988; Palacz and Saunder, 1986; Woodhead, 1996) also have more radiogenic $^{206}Pb/^{204}Pb$ than St. Helena lavas (Chaffey et al., 1989), whereas the Mangaia composition is slightly different (lower $^{207}Pb/^{204}Pb$ and higher $^{143}Nd/^{144}Nd$ ratios) than Dicker Willem NMH2 and NMH4 samples. Therefore, the Dicker Willem carbonatities appear to represent one of the most extreme HIMU-type magmas found on Earth thus far.

In conclusion, carbonatites and silica-undersaturated rocks from Agate Mountain, Swakopmund, Dicker Willem, the Walvis–Mocammedes and Richardson–South Africa tracks as well as the other regional HIMU lavas in southern Angola (Mocamedes) and South Africa seem to be derived from a common St. Helena type HIMU mantle source.

4.6.4. Belt of HIMU volcanism along the SW coast of Africa

The Dicker Willem carbonatites also appear to be aligned in an age-progressive succession of adjacent HIMU volcanism extending in the direction of plate motion. This track comprises (from NE to SW) Gibeon Kimberlites (79–72 Ma; Reid et al., 1990) and Gross Brukkaros (77±2 Ma; Reid et al., 1990), Dicker Willem carbonatites (49±1 Ma; Reid et al., 1990), Klinghardt phonolites (46 Ma; Marsh et al., 2018), Swartkop phonolite (37 Ma; Kröner, 1973) and the Schwarzeberg nephelinite (36 Ma; Kröner, 1973) emplaced on continental crust, extending to Vema seamount (15 Ma; O'Connor and le Roex, 1992). The Gibeon Kimberlites have similar isotope ratios to Walvis–Mocamedes and Richardson–South Africa lavas (Figure 4-6, Figure 4-7), further supporting the idea of a common deep HIMU source (Section 4.6.3) feeding separate hotspot tracks on the surface. A rhyolite from Gross Brukkaros also shows HIMU-like Pb isotope ratios (and is therefore included in Figure 4-7a, b), although its elevated Pb concentration (Figure 4-4c), radiogenic $^{87}Sr/^{86}Sr$ and unradiogenic $^{143}Nd/^{144}Nd$ indicate significant crustal contamination. Schwarzeberg nephelinites also have HIMU-like Sr-Nd-Pb isotopic composition (Janney, 2007).

The problem with assuming several separate hotspot tracks is that the age-progression of the potential Vema hotspot track (corresponding to 20.2 mm/year) does not conform with that of the nearby late-stage Walvis–Mocamedes track, which indicates an average plate velocity of about 36 mm/year (Homrighausen et al., 2020). In addition, the

Swakopmund basanites cannot be associated with any nearby age-progressive volcanism, yet they show the same isotopic composition as other HIMU-like post Etendeka carbonatites and silica-undersaturated volcanism. They almost completely overlap with the late-stage Walvis Ridge seamounts (likewise basanites and alkali basalts) in all isotopic systems, suggesting that they are derived from a similar source. There is also a group of low-volume, silica-undersaturated volcanic rocks and carbonatites of HIMU composition located near the southwest African coast between the potential Vema and Shona tracks, consisting of the Warmbad, Bushmanland and Namaqualand volcanic clusters (abbreviated as WBN in Figure 4-1). These volcanic complexes, located 500 km north of the axis of the Shona hotspot track, show a plausible age progression (83–38 Ma) similar to the Shona track (Figure 4-1).

All of the younger age-progressive hotspot tracks (St. Helena, Walvis–Mocamedes, Gibeon–Vema, Richardson–South Africa) have HIMU-type isotopic composition, which is distinct from the older EM1-type hotspot tracks (Tristan-Gough, Discovery and Shona) and the ambient depleted upper mantle (DMM) (Figure 4-8). We thus propose that there is a belt of HIMU rocks that extends from St. Helena Island in the Central South Atlantic to Angola and then along the southwestern margin of Africa to Namibia and to South Africa. Many of these HIMU volcanic groups belong to age-progressive volcanic tracks that become younger towards the southwest but not at exactly the same rates. This HIMU volcanic belt extends sub-parallel to the southwestern African LLSVP margin but is located 900–1200 km within the LLSVP (blue stippled line in Figure 4-1).

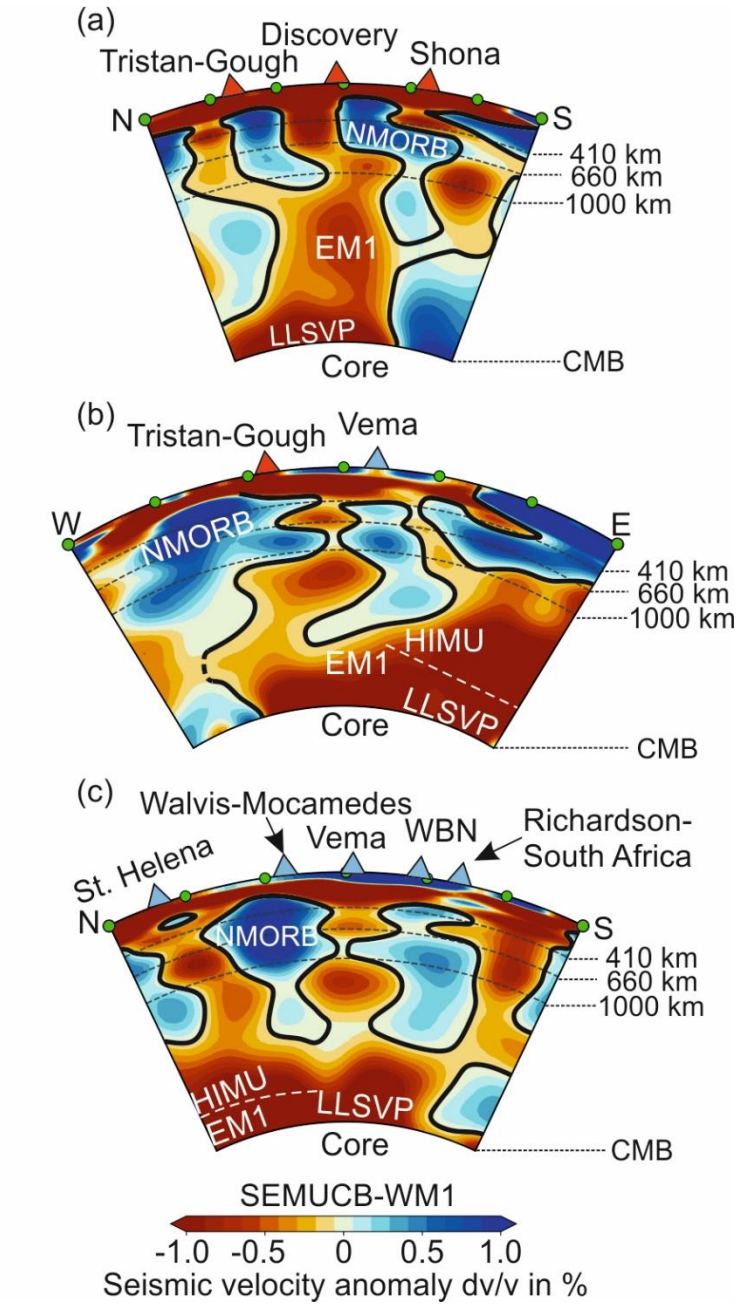

Figure 4-9: Seismic tomographic profiles using velocity model SEMUCB-WM1 (French and Romanowicz, 2014) through today's mantle: (a) N-S profile through the mantle beneath Tristan-Gough, Discovery and Shona (EM1-type) hotspots, (b) E-W profile through Tristan-Gough (EMI-type) and VEMA–Gibbeon (HIMU-type) hotspots, and (c) N-S profile through St. Helena, Walvis–Mocamedes, Vema–Gibbeon, WBN and Richardson–South Africa (HIMU-type) hotspots. Profile (a) shows a large low-velocity anomaly rising from the LLSVP at the lower mantle with three branches (arms) emanating from it that can be traced to three EM1-type hotspots. Profile (b) shows near continuous low-velocity anomalies ascending from the LLSVP to the lithosphere beneath Tristan-Gough and Vema. The low-velocity anomalies are interpreted as mantle plumes derived from the outer margin (EMI-type) and from an inner (~900–1200km east) step (HIMU-type) of the LLSVP. Profile (c) shows a continuous low-velocity anomaly extending from the LLSVP to the lithospheric base of the St. Helena and the Richardson–South Africa HIMU volcanic tracks and a near continuous low-velocity anomaly ascending beneath the Walvis–Mocamedes, Swakopmund, Vema–Dicker Willem–Gibeon and

the WBN HIMU volcanic tracks. Figures produced with the SubMachine software (Hosseini et al., 2018). The locations of cross-sections are shown in Figure 4-1. Abbreviations: NMORB = normal mid-Atlantic ridge basalt; WBN = Warmbad, Bushmanland and Namaqualand volcanism; CMB = Core mantle boundary.

A N-S profile from seismic tomography model SEMUCB-WM1 (French and Romanowicz, 2014) through the EM1-type Tristan-Gough, Discovery and Shona hotspots shows a large low-velocity anomaly (~1600–1800 km width in the N-S direction) ascending from the southwestern (outer) margin of the African LLSVP to a depth of ~1100 km (Figure 4-9a). Between depths of ~2000–1000 km, three arms/branches emanate from this large (trunk-like) anomaly that ascend beneath Tristan-Gough, Discovery and Shona hotspots. Therefore, the three hotspots with a common Gough-type EMI composition appear to be derived from a single superplume upwelling from the southwest boundary of the African LLSVP. The superplume structure looks like a tree in N-S cross-section, but the trunk and three arms/branches are largely located in a two-dimensional plane ascending from the outer LLSVP margin and thus resemble more a planar candelabra with three candles. This type of a branching superplume was first recognized by Fukao et al. (1994) and has been described in more detail recently by Tsekhmistrenko (2019) and Liu and Leng (2020). The outer margin of the LLSVP is assumed to be the generation zone for (large) primary mantle plumes (e.g., Burke et al., 2008; Torsvik et al., 2006), resulting from the flow of mantle pushed by subducting slabs along the core-mantle boundary until it is deflected upwards at the margin of a denser/more viscous LLSVP. Since the current location of the EM1 hotspots in the South Atlantic (Tristan-Gough, Discovery and Shona) and the reconstructed locations of their corresponding flood basalt (plume head) stages (Etendeka and Karoo) lie above this boundary, it is likely that the EM1 source resides in this part (or in the proposed “primordial” layer) of the LLSVP. The flow of hot, ambient lower mantle against the edge of the LLSVP could heat LLSVP material, reducing its density and viscosity, thus triggering its upwelling. Alternatively, the EM1 type material could be located outside of the LLSVP and then be deflected upwards when it flows against the steep outer margin of the LLSVP.

Seismic tomographic models show a steep inner step/slope on the surface of the African LLSVP about 900–1200 km eastward from its southwest margin (e.g., French and Romanowicz, 2014; Ritsema et al., 2011) (Figure 4-9b). As shown in Figure 4-1 by the

blue stippled line, the strike of this step, if projected to the surface, would roughly match the extension of the HIMU hotspot tracks (formed between ~120–15 Ma) to the present (blue circles). Various geophysical observations, such as viscosity variations, numerical and tomographic modelling support the idea of a compositionally layered LSSVP (Ballmer et al., 2016; Garnero et al., 2016; Mulyukova et al., 2015), with a lower "primordial" layer and an upper "ancient basaltic" layer (Ballmer et al., 2016). It has also been proposed that primary plumes ascend at the outer margin of the LLSVPs and secondary plumes ascend from the margin of the internal basaltic layer. The upper basaltic layer could be derived from ancient (Archean to Early Protrerozoic) subducted oceanic crust, which has evolved to a HIMU-type composition by radiogenic ingrowth (e.g., Hofmann and White, 1982; White and Hofmann, 1982). This model is consistent with derivation of the Namibian carbonatite magmas from a carbonated subducted crustal protolith, as has been proposed for the origin of oceanic carbonatites on the Cape Verdes (Hoernle et al., 2002). Alternatively, the HIMU composition of carbonatites and silica-undersaturated volcanic rocks in Namibia could reflect recycling of subcontinental lithospheric mantle (SCLM), metasomatized by carbonate melts from subducting plates in the Archean/Early Proterozoic (Homrighausen et al., 2018b; Weiss et al., 2016), subsequently delaminated and then stored on the LLSVP. Instabilities caused by the detachment of the Karoo and Etendeka-Parana starting plume heads and the subsequent steady drainage of plume stem material by the Tristan/Gough and Shona hotspots from the (EM 1) edge of the LLSVP might have triggered secondary plume detachment from this inner step formed by a compositionally distinct upper layer (Homrighausen et al., 2020), as can be seen by the low-velocity anomalies ascending from this step (the outer boundary of the inner and upper layer) beneath the HIMU hotspot volcanism (St. Helena, Walvis–Mocamdes, Vema–Gibean, WBN and Richardson–South Africa) (Figure 4-9b and c). This hypothesis can explain the formation of the secondary hotspot tracks, which partially overlie the primary (EMI-type) hotspot tracks with similar time-progressive eruption ages (because they formed on the same moving plate).

Because of their similar HIMU-type isotopic composition and age-progression, the on-shore post-Etendeka HIMU carbonatite and silica-undersaturated volcanism (<120 Ma) could therefore represent earlier parts of the now submarine HIMU hotspot tracks,

consisting of silica-undersaturated volcanism (basanites and alkali basalts). The progressively younger ages of the volcanism towards the SW within this HIMU belt can be attributed to the NW-directed African plate motion. Some of the irregularities in the age progressions of volcanism on Africa no doubt reflect greater difficulties of these low-volume melts to pass through thick, low-density continental crust, thus more spreading out along the base of the lithosphere until they find easy pathways to the surface along tectonic structures and mobile belts. The Swakopmund plugs, for example, are aligned along the crustal-scale fracture of the Omaruru Lineament (Miller, 2008) and the Dicker Willem complex is located within the Kuckaus Mylonite Zone (Rennie et al., 2013). The irregular-spaced intraplate volcanism and poor age progressions could also reflect magmatism from pulsating secondary plumes or strings of discretely and discontinuously upwelling blobs (Figure 4-9c; Heyn et al., 2020; Long et al., 2020). Beneath the thick continental lithosphere (compared to the thinner oceanic lithosphere), the melting column will be shorter and melting of upwelling mantle will only be able to produce low-degree carbonatite, kimberlite and other low-degree silica-undersaturated melts (Braunger et al., 2020; Hammouda and Keshav, 2015; Homrighausen et al., 2018a). In contrast, upwelling beneath the thinner oceanic lithosphere allows upwelling of plume material to shallower depths and thus greater degrees of decompression melting resulted in the formation of alkali basalts and basanites from the same HIMU plume source (Homrighausen et al., 2018a).

Over time, the radius of the entrainment region sampled by the plume roots will increase, preventing further detachment of independent blobs in their vicinity (sucking effect; Campbell, 1998; Jones et al., 2016). This mechanism might explain the apparent weakening of some HIMU volcanic tracks during the last 40–50 Ma (e.g., Walvis–Mocamedes, Warmbad–Bushmanland–Namaqualand, short-lived Swakopmund). The overall HIMU-like volcanism in the south Atlantic, however, has been generally weakened in the last 40 Ma, including the Gibeon–Vema track and Richardson–South Africa track (only St. Helena has been active within the past 10 Ma). This might not be simply caused by the sucking effect, because it doesn't seem realistic to coalesce all these HIMU plumes/blobs into the St. Helena plume between ~1500–3500 km to the north. To the contrary, it is likely that the step was more pronounced and unstable in the past and has slowly been leveling out and stabilized due to removal of material since

then, which has resulted in cessation of the secondary upwellings (plumes/blobs) except at St. Helena. It is also possible that younger HIMU volcanism exists at the ends of these chains but simply has not been detected yet.

In summary, voluminous (plume head) and continuous (plume tail) drainage along the outer margins of LLSVPs might cause destabilization of potentially upper LLSVP layers, such that the internal contacts (boundaries between compositional layers) could become secondary plume generation zones. These secondary zones could tap different geochemical reservoirs on or within the LLSVPs, generating the spatial geochemical contrast in the upwellings as described in this study. With time these secondary plume generation zones (steps in the surface of the LLSVPs) could dissipate, shutting down the secondary upwellings.

4.7. Conclusions

The Agate Mountain carbonatites display HIMU-like isotopic composition, similar to the late-stage Walvis HIMU seamounts and adjacent phonolites, which yield ages of 82-83 Ma. Therefore, we conclude that the Agate Mountain carbonatite complex also formed at 82-83 Ma and forms part of a Walvis-Mocamedes HIMU volcanic hotspot track.

The Swakopmund basanites and Dicker Willem carbonatites, along the coast of southwestern Namibia, also have HIMU-like isotopic composition. Even though the Swakopmund basanites are not part of an age-progressive track and the Gibeon-Dicker Willem-Vema track show a compressed age-progressive track, they appear to be derived from the same HIMU source, as proposed for St. Helena, Walvis-Mocamedes and Shona-Africa age-progressive volcanic tracks, and could represent week pulsating plumes or strings of ascending blobs.

Together with other clusters of HIMU volcanism, such as WBN, along the central SW coast of South Africa, the HIMU volcanism forms a well-defined belt sub-parallel to the outer LLSVP margin. Whereas EMI-type plumes (Tristan-Gough, Discovery and Shona) are believed to ascend from the outer margin of the LLSVP, the HIMU volcanism appears to be related to a topographic step on the surface of the LLSVP, which is about 1000-1500 km within (east of the outer margin of) the LLSVP. Multiple upwellings along this step might have caused the widespread belt of HIMU volcanism

extending from St. Helena along the southwest coast of Africa to the southern tip of Africa. Except for St. Helena, it appears that all of these secondary HIMU hotspot tracks have shut down, since there is no volcanism presently where the hotspots should be located based on extrapolation of their age progressions. Cessation of these secondary hotspots may reflect a leveling out of a formerly larger step on the surface of the LLSVP formed directly after removal of the Tristan-Gough and Shona starting plume heads that formed the Karoo and Etendeka/Parana flood basalts.

References

Ballmer, M.D., Schumacher, L., Lekic, V., Thomas, C., Ito, G., 2016. Compositional layering within the large low shear-wave velocity provinces in the lower mantle. Geochemistry, Geophysics, Geosystems 17, 5056-5077.

Becker, M., Roex, A.P.L., 2006. Geochemistry of South African on-and off-craton, Group I and Group II kimberlites: petrogenesis and source region evolution. Journal of Petrology 47, 673-703.

Bell, K., 1989. Stable isotope variations in carbonatites. Unwin-Hyman, London.

Bell, K., 2001. Carbonatites: relationships to mantle-plume activity. Special Papers-Geological Society of America, 267-290.

Bell, K., Tilton, G., 2001. Nd, Pb and Sr isotopic compositions of East African carbonatites: evidence for mantle mixing and plume inhomogeneity. Journal of Petrology 42, 1927-1945.

Bercovici, D., Karato, S.-i., 2003. Whole-mantle convection and the transition-zone water filter. Nature 425, 39.

Blichert-Toft, J., Chauvel, C., Albarède, F., 1997. Separation of Hf and Lu for high-precision isotope analysis of rock samples by magnetic sector-multiple collector ICP-MS. Contributions to Mineralogy and Petrology 127, 248-260.

Bouabdellah, M., Hoernle, K., Kchit, A., Duggen, S., Hauff, F., Klügel, A., Lowry, D., Beaudoin, G., 2010. Petrogenesis of the Eocene Tamazert continental carbonatites (Central High Atlas, Morocco): implications for a common source for the Tamazert and Canary and Cape Verde Island carbonatites. Journal of Petrology 51, 1655-1686.

Braunger, S., Marks, M.A.W., Wenzel, T., Chmyz, L., Guitarrari Azzone, R., Markl, G., 2020. Do carbonatites and alkaline rocks reflect variable redox conditions in their upper mantle source? Earth and Planetary Science Letters 533, 116041.

Burke, K., Steinberger, B., Torsvik, T.H., Smethurst, M.A., 2008. Plume Generation Zones at the margins of Large Low Shear Velocity Provinces on the core–mantle boundary. Earth and Planetary Science Letters 265, 49-60.

Campbell, I., 1998. The mantle's chemical structure: insights from the melting products of mantle plumes. The Earth's mantle: composition, structure and evolution, 259-310.

Campeny, M., Kamenetsky, V.S., Melgarejo, J.C., Mangas, J., Manuel, J., Alfonso, P., Kamenetsky, M.B., Bambi, A.C.J.M., Gonçalves, A.O., 2015. Carbonatitic lavas in Catanda (Kwanza Sul, Angola): Mineralogical and geochemical constraints on the parental melt. Lithos 232, 1-11.

Castillo, P.R., 2015. The recycling of marine carbonates and sources of HIMU and FOZO ocean island basalts. Lithos 216-217, 254-263.

Chaffey, D., Cliff, R., Wilson, B., 1989. Characterization of the St Helena magma source. Geological Society, London, Special Publications 42, 257-276.

Chakhmouradian, A., Williams, C., 2004. Mineralogy of high-field-strength elements (Ti, Nb, Zr, Ta, Hf) in phoscoritic and carbonatitic rocks of the Kola Peninsula, Russia. Phoscorites and carbonatites from mantle to mine: the key example of the Kola Alkaline Province 10, 293-340.

Chakhmouradian, A.R., 2006. High-field-strength elements in carbonatitic rocks: Geochemistry, crystal chemistry and significance for constraining the sources of carbonatites. Chemical Geology 235, 138-160.

Cheng, Z., Zhang, Z., Hou, T., Santosh, M., Chen, L., Ke, S., Xu, L., 2017. Decoupling of Mg–C and Sr–Nd–O isotopes traces the role of recycled carbon in magnesiocarbonatites from the Tarim Large Igneous Province. Geochimica et Cosmochimica Acta 202, 159-178.

Class, C., le Roex, A., 2011. South Atlantic DUPAL anomaly — Dynamic and compositional evidence against a recent shallow origin. Earth and Planetary Science Letters 305, 92-102.

Class, C., le Roex, A.P., 2006. Continental material in the shallow oceanic mantle—How does it get there? Geology 34, 129.

Class, C., Lehnert, K., 2012. PetDB Expert MORB (Mid-Ocean Ridge Basalt) Compilation, Version1.0. Interdisciplinary Earth Data Alliance (IEDA). https://doi .org /10 .1594 /IEDA /100060.

Collerson, K.D., Williams, Q., Ewart, A.E., Murphy, D.T., 2010. Origin of HIMU and EM-1 domains sampled by ocean island basalts, kimberlites and carbonatites: The role of CO2-fluxed lower mantle melting in thermochemical upwellings. Physics of the Earth and Planetary Interiors 181, 112-131.

Comin-Chiaramonti, P., De Min, A., Girardi, V.A.V., Ruberti, E., 2011. Post-Paleozoic magmatism in Angola and Namibia: A review. Volcanism and Evolution of the African Lithosphere. Geological Society of America, Special Paper 478, 223-247.

Cooper, A., 1988. Geology of Dicker Willem, a subvolcanic carbonatite complex in south-west Africa. Comm. GeoI. Surv. SW Afr./Namibia 4, 3-12.

Cooper, A., Reid, D., 1991. Textural evidence for calcite carbonatite magmas, Dicker Willem, southwest Namibia. Geology 19, 1193-1196.

Cooper, A., Reid, D., 2000. The association of potassic trachytes and carbonatites at the Dicker Willem Complex, southwest Namibia: coexisting, immiscible, but not cogenetic magmas. Contributions to Mineralogy and Petrology 139, 570-583.

Cooper, A.F., Reid, D.L., 1998. Nepheline sövites as parental magmas in carbonatite complexes: evidence from Dicker Willem, southwest Namibia. Journal of Petrology 39, 2123-2136.

Dasgupta, R., Hirschmann, M.M., 2006. Melting in the Earth's deep upper mantle caused by carbon dioxide. Nature 440, 659-662.

Dasgupta, R., Hirschmann, M.M., Smith, N.D., 2007. Partial Melting Experiments of Peridotite + CO2 at 3 GPa and Genesis of Alkalic Ocean Island Basalts. Journal of Petrology 48, 2093-2124.

Davies, G., Spriggs, A., Nixon, P., 2001. A non-cognate origin for the Gibeon kimberlite megacryst suite, Namibia: implications for the origin of Namibian kimberlites. Journal of Petrology 42, 159-172.

Dixon, J.E., Leist, L., Langmuir, C., Schilling, J.-G., 2002. Recycled dehydrated lithosphere observed in plume-influenced mid-ocean-ridge basalt. Nature 420, 385-389.

Doroshkevich, A.G., Veksler, I.V., Klemd, R., Khromova, E.A., Izbrodin, I.A., 2017. Trace-element composition of minerals and rocks in the Belaya Zima carbonatite complex (Russia): Implications for the mechanisms of magma evolution and carbonatite formation. Lithos 284, 91-108.

Doroshkevich, A.G.e., Ripp, G., Viladkar, S., 2010. Newania carbonatites, Western India: example of mantle derived magnesium carbonatites. Mineralogy and Petrology 98, 283-295.

Doucelance, R., Escrig, S., Moreira, M., Gariépy, C., Kurz, M.D., 2003. Pb-Sr-He isotope and trace element geochemistry of the Cape Verde Archipelago. Geochimica et Cosmochimica Acta 67, 3717-3733.

Egorov, L.S., 1970. Carbonatites and ultrabasic-alkaline rocks of the Maimecha-Kotui region, N. Siberia. Lithos 3, 341-359.

Erlank, A., Waters, F., Hawkesworth, C., Haggerty, S., Allsopp, H., Rickard, R., Menzies, M., 1987. Mantle metasomatism.

Ernst, R.E., Bell, K., 2010. Large igneous provinces (LIPs) and carbonatites. Mineralogy and Petrology 98, 55-76.

French, S., Romanowicz, B., 2014. Whole-mantle radially anisotropic shear velocity structure from spectral-element waveform tomography. Geophysical Journal International 199, 1303-1327.

Frimmel, H.E., Lane, K., 2005. Geochemistry of carbonate beds in the Neoproterozoic Rosh Pinah Formation, Namibia: Implications on depositional setting and hydrothermal ore formation. South African Journal of Geology 108, 5-18.

Garbe-Schönberg, C.D., 1993. Simultaneous determination of thirty-seven trace elements in twenty-eight international rock standards by ICP-MS. Geostandards and Geoanalytical Research 17, 81-97.

Garbe-Schönberg, D., Müller, S., 2014. Nano-particulate pressed powder tablets for LA-ICP-MS. Journal of Analytical Atomic Spectrometry 29, 990-1000.

Garnero, E.J., McNamara, A.K., Shim, S.-H., 2016. Continent-sized anomalous zones with low seismic velocity at the base of Earth's mantle. Nature Geoscience 9, 481-489.

Geldmacher, J., Hoernle, K., Kluegel, A., van den Bogaard, P., Bindeman, I., 2008. Geochemistry of a new enriched mantle type locality in the northern hemisphere: Implications for the origin of the EM-I source. Earth and Planetary Science Letters 265, 167-182.

Gittins, J., Harmer, R., Barker, D., 2005. The bimodal composition of carbonatites: Reality or misconception? Lithos 85, 129-139.

Goscombe, B., Hand, M., Gray, D., Mawby, J., 2003. The metamorphic architecture of a transpressional orogen: the Kaoko Belt, Namibia. Journal of Petrology 44, 679-711.

Govindaraju, K., 1994. 1994 compilation of working values and sample description for 383 geostandards. Geostandards and Geoanalytical Research 18, 1-158.

Green, D.H., Wallace, M.E., 1988. Mantle metasomatism by ephemeral carbonatite melts. Nature 336, 459-462.

Griffin, W., Batumike, J., Greau, Y., Pearson, N., Shee, S., O'Reilly, S.Y., 2014. Emplacement ages and sources of kimberlites and related rocks in southern Africa: U–Pb ages and Sr–Nd isotopes of groundmass perovskite. Contributions to Mineralogy and Petrology 168, 1032.

Gudfinnsson, G.H., Presnall, D.C., 2005. Continuous Gradations among Primary Carbonatitic, Kimberlitic, Melilititic, Basaltic, Picritic, and Komatiitic Melts in Equilibrium with Garnet Lherzolite at 3–8 GPa. Journal of Petrology 46, 1645-1659.

Hammouda, T., Keshav, S., 2015. Melting in the mantle in the presence of carbon: Review of experiments and discussion on the origin of carbonatites. Chemical Geology 418, 171-188.

Harmer, R.E., Gittins, J., 1997. The origin of dolomitic carbonatites: field and experimental constraints. Journal of African Earth Sciences 25, 5-28.

Haxel, J., Dziak, R., 2005. Evidence of explosive seafloor volcanic activity from the Walvis Ridge, South Atlantic Ocean. Geophysical research letters 32.
Heyn, B.H., Conrad, C.P., Trønnes, R.G., 2020. Core-mantle boundary topography and its relation to the viscosity structure of the lowermost mantle. Earth and Planetary Science Letters 543, 116358.
Hoernle, K., Abt, D.L., Fischer, K.M., Nichols, H., Hauff, F., Abers, G.A., Van Den Bogaard, P., Heydolph, K., Alvarado, G., Protti, M., 2008. Arc-parallel flow in the mantle wedge beneath Costa Rica and Nicaragua. Nature 451, 1094.
Hoernle, K., Hauff, F., Kokfelt, T.F., Haase, K., Garbe-Schönberg, D., Werner, R., 2011. On- and off-axis chemical heterogeneities along the South Atlantic Mid-Ocean-Ridge (5–11°S): Shallow or deep recycling of ocean crust and/or intraplate volcanism? Earth and Planetary Science Letters 306, 86-97.
Hoernle, K., Rohde, J., Hauff, F., Garbe-Schonberg, D., Homrighausen, S., Werner, R., Morgan, J.P., 2015. How and when plume zonation appeared during the 132 Myr evolution of the Tristan Hotspot. Nature Communications 6, 7799.
Hoernle, K., Schwindrofska, A., Werner, R., van den Bogaard, P., Hauff, F., Uenzelmann-Neben, G., Garbe-Schönberg, D., 2016. Tectonic dissection and displacement of parts of Shona hotspot volcano 3500 km along the Agulhas-Falkland Fracture Zone. Geology 44, 263-266.
Hoernle, K., Tilton, G., Le Bas, M.J., Duggen, S., Garbe-Schönberg, D., 2002. Geochemistry of oceanic carbonatites compared with continental carbonatites: mantle recycling of oceanic crustal carbonate. Contributions to Mineralogy and Petrology 142, 520-542.
Hoernle, K., Tilton, G., Schmincke, H.-U., 1991. SrNdPb isotopic evolution of Gran Canaria: Evidence for shallow enriched mantle beneath the Canary Islands. Earth and Planetary Science Letters 106, 44-63.
Hofmann, A.W., 1988. Chemical differentiation of the Earth: the relationship between mantle, continental crust, and oceanic crust. Earth and Planetary Science Letters 90, 297-314.
Hofmann, A.W., White, W.M., 1982. Mantle plumes from ancient oceanic crust. Earth and Planetary Science Letters 57, 421-436.
Homrighausen, S., Hoernle, K., Geldmacher, J., Wartho, J.-A., Hauff, F., Portnyagin, M., Werner, R., van den Bogaard, P., Garbe-Schönberg, D., 2018a. Unexpected HIMU-type late-stage volcanism on the Walvis Ridge. Earth and Planetary Science Letters 492, 251-263.
Homrighausen, S., Hoernle, K., Hauff, F., Geldmacher, J., Wartho, J.-A., van den Bogaard, P., Garbe-Schönberg, D., 2018b. Global distribution of the HIMU end member: Formation through Archean plume-lid tectonics. Earth-Science Reviews 182, 85-101.
Homrighausen, S., Hoernle, K., Hauff, F., Wartho, J.-A., van den Bogaard, P., Garbe-Schönberg, D., 2019. New age and geochemical data from the Walvis Ridge: The temporal and spatial diversity of South Atlantic intraplate volcanism and its possible origin. Geochimica et Cosmochimica Acta 245, 16-34.
Homrighausen, S., Hoernle, K., Zhou, H., Geldmacher, J., Wartho, J.-A., Hauff, F., Werner, R., Jung, S., Morgan, J.P., 2020. Paired EMI-HIMU hotspots in the South Atlantic—Starting plume heads trigger compositionally distinct secondary plumes? Science Advances 6, eaba0282.
Hosseini, K., Matthews, K.J., Sigloch, K., Shephard, G.E., Domeier, M., Tsekhmistrenko, M., 2018. SubMachine: Web-based tools for exploring seismic

tomography and other models of Earth's deep interior. Geochemistry, Geophysics, Geosystems 19, 1464-1483.
Hou, Z., Liu, Y., Tian, S., Yang, Z., Xie, Y., 2015. Formation of carbonatite-related giant rare-earth-element deposits by the recycling of marine sediments. Scientific reports 5, 10231.
Ionov, D., Harmer, R.E., 2002. Trace element distribution in calcite–dolomite carbonatites from Spitskop: inferences for differentiation of carbonatite magmas and the origin of carbonates in mantle xenoliths. Earth and Planetary Science Letters 198, 495-510.
Janney, P., 2007. Sr-Nd-Pb-Hf isotope geochemistry of mafic alkaline igneous rocks from the Gibeon Dicker Willem lineament, southern Namibia. AGUFM 2007, V13D-1590.
Janney, P., Le Roex, A., Carlson, R., Viljoen, K., 2002. A chemical and multi-isotope study of the Western Cape olivine melilitite province, South Africa: implications for the sources of kimberlites and the origin of the HIMU signature in Africa. Journal of Petrology 43, 2339-2370.
Janney, P.E., Bell, D.R., 2017. Hidden reservoirs in the continental lithosphere? Evidence from Hf-Sr-Nd-Pb isotopes in southern African kimberlite megacrysts, International Kimberlite Conference: Extended Abstracts.
Jochum, K.P., Garbe-Schönberg, D., Veter, M., Stoll, B., Weis, U., Weber, M., Lugli, F., Jentzen, A., Schiebel, R., Wassenburg, J.A., 2019. Nano-powdered calcium carbonate reference materials: Significant progress for microanalysis? Geostandards and Geoanalytical Research 43, 595-609.
Jones, T., Davies, D., Campbell, I., Wilson, C., Kramer, S., 2016. Do mantle plumes preserve the heterogeneous structure of their deep-mantle source? Earth and Planetary Science Letters 434, 10-17.
Jourdan, F., Bertrand, H., Schärer, U., Blichert-Toft, J., Féraud, G., Kampunzu, A.B., 2007. Major and Trace Element and Sr, Nd, Hf, and Pb Isotope Compositions of the Karoo Large Igneous Province, Botswana–Zimbabwe: Lithosphere vs Mantle Plume Contribution. Journal of Petrology 48, 1043-1077.
Jung, S., Hauff, F., Berndt, J., 2020. Generation of a potassic to ultrapotassic alkaline complex in a syn-collisional setting through flat subduction: Constraints on magma sources and processes (Otjimbingwe alkaline complex, Damara orogen, Namibia). Gondwana Research 82, 267-287.
Karato, S.-i., 2011. Water distribution across the mantle transition zone and its implications for global material circulation. Earth and Planetary Science Letters 301, 413-423.
Kawabata, H., Hanyu, T., Chang, Q., Kimura, J.-I., Nichols, A.R., Tatsumi, Y., 2011. The petrology and geochemistry of St. Helena alkali basalts: evaluation of the oceanic crust-recycling model for HIMU OIB. Journal of Petrology 52, 791-838.
Keller, J., Hoefs, J., 1995. Stable Isotope Characteristics of Recent Natrocarbonatites from Oldoinyo Lengai, in: Bell, K., Keller, J. (Eds.), Carbonatite Volcanism: Oldoinyo Lengai and the Petrogenesis of Natrocarbonatites. Springer Berlin Heidelberg, Berlin, Heidelberg, pp. 113-123.
Kobussen, A.F., Griffin, W.L., O'Reilly, S.Y., Shee, S.R., 2008. Ghosts of lithospheres past: Imaging an evolving lithospheric mantle in southern Africa. Geology 36, 515-518.
Kogarko, L.N., Veselovskiy, R.V., 2019. Geodynamic origin of carbonatites from the absolute paleotectonic reconstructions. Journal of Geodynamics 125, 13-21.

Kramm, U., Körner, T., Kittel, M., Baier, H., Sindern, S., 2017. Triassic emplacement age of the Kalkfeld complex, NW Namibia: implications for carbonatite magmatism and its relationship to the Tristan Plume. International Journal of Earth Sciences 106, 2797-2813.

Kröner, A., 1973. Comments on "Is the African plate stationary?". Nature 243, 29-30.

Le Bas, M.J., Le Maitre, R., Streckeisen, A., Zanettin, B., 1986. A chemical classification of volcanic rocks based on the total alkali-silica diagram. Journal of petrology 27, 745-750.

Le Maitre, R., Bateman, P., Dudek, A., Keller, J., Lameyre, J., Le Bas, M., Sabine, P., Schmid, R., Sorensen, H., Streckeisen, A., 1989. A classification of igneous rocks and glossary of terms. Recommendations of the IUGS Subcommission on the Systematics of Igneous rocks. London: Blackwell Scientific Publications.

Le Maitre, R.W., Streckeisen, A., Zanettin, B., Le Bas, M., Bonin, B., Bateman, P., 2005. Igneous rocks: a classification and glossary of terms: recommendations of the International Union of Geological Sciences Subcommission on the Systematics of Igneous Rocks. Cambridge University Press.

le Roex, A., Class, C., 2014. Metasomatism of the Pan-African lithospheric mantle beneath the Damara Belt, Namibia, by the Tristan mantle plume: geochemical evidence from mantle xenoliths. Contributions to Mineralogy and Petrology 168.

Le Roex, A.P., Lanyon, R., 1998. Isotope and Trace Element Geochemistry of Cretaceous Damaraland Lamprophyres and Carbonatites, Northwestern Namibia: Evidence for Plume—Lithosphere Interactions. Journal of Petrology 39, 1117-1146.

Litasov, K., Ohtani, E., 2010. The solidus of carbonated eclogite in the system CaO–Al2O3–MgO–SiO2–Na2O–CO2 to 32GPa and carbonatite liquid in the deep mantle. Earth and Planetary Science Letters 295, 115-126.

Long, X., van der Zwan, F., Geldmacher, J., Hoernle, K., Hauff, F., Garbe-Schönberg, D., Augustin, N., 2020. Insights into the petrogenesis of an intraplate volcanic province: Sr-Nd-Pb-Hf isotope geochemistry of the Bathymetrists Seamount Province, eastern equatorial Atlantic. Chemical Geology, 119599.

Marsh, J., Ewart, A., Milner, S., Duncan, A., Miller, R.M., 2001. The Etendeka Igneous Province: magma types and their stratigraphic distribution with implications for the evolution of the Paraná-Etendeka flood basalt province. Bulletin of Volcanology 62, 464-486.

Marsh, J., Phillips, D., Lock, B., 2018. 40Ar/39Ar dating of the Klinghardt and Stalhart Phonolites, Namibia, and Comments on the Evolution of the Klinghardt Volcanic Field. Communications of the Geological Survey of Namibia 20, 1-8.

Marsh, J.S., 1987. Evolution of a strongly differentiated suite of phonolites from the Klinghardt Mountains, Namibia. Lithos 20, 41-58.

Martin, L.H., Schmidt, M.W., Mattsson, H.B., Guenther, D., 2013. Element partitioning between immiscible carbonatite and silicate melts for dry and H2O-bearing systems at 1–3 GPa. Journal of Petrology 54, 2301-2338.

Marzoli, A., Melluso, L., Morra, V., Renne, P.R., Sgrosso, I., D'antonio, M., Morais, L.D., Morais, E., Ricci, G., 1999. Geochronology and petrology of Cretaceous basaltic magmatism in the Kwanza basin (western Angola), and relationships with the Paraná-Etendeka continental flood basalt province. Journal of Geodynamics 28, 341-356.

Mazza, S.E., Gazel, E., Bizimis, M., Moucha, R., Beguelin, P., Johnson, E.A., McAleer, R.J., Sobolev, A.V., 2019. Sampling the volatile-rich transition zone beneath Bermuda. Nature 569, 398-403.

McDermott, F., Hawkesworth, C., 1990. Intracrustal recycling and upper-crustal evolution: a case study from the Pan-African Damara mobile belt, central Namibia. Chemical Geology 83, 263-280.

Miller, R.M., 1983. The Pan-African Damara Orogen of South West Africa/Namibia, Evolution of the Damara Orogen of South West Africa/Namibia.

Miller, R.M., 2000. The Agate Mountain Carbonatite Complex, Cape Fria, NW Namibia. communs geol. Surv. Namibia 12, 369-382.

Miller, R.M., 2008. The geology of Namibia. Ministry of Mines and Energy, Geological Survey.

Miller, R.M., 2012. Review of Mesoproterozoic magmatism, sedimentation and terrane amalgamation in southwestern Africa. South African Journal of Geology 115, 417-448.

Milner, S., Le Roex, A., O'CONNOR, J., 1995. Age of Mesozoic igneous rocks in northwestern Namibia, and their relationship to continental breakup. Journal of the Geological Society 152, 97-104.

Milner, S.C., Le Roex, A.P., Watkins, R.T., 1993. Rb-Sr age determinations of rocks from the Okenyenya igneous complex, northwestern Namibia. Geological Magazine 130, 335-343.

Moore, A., Blenkinsop, T., Cotterill, F., 2008. Controls on post-Gondwana alkaline volcanism in Southern Africa. Earth and Planetary Science Letters 268, 151-164.

Moore, A.E., 1979. The geochemistry of the Olivine Melilitetes and related rocks of Namaqualand Bushmanland, South Africa. University of Cape Town.

Mulyukova, E., Steinberger, B., Dabrowski, M., Sobolev, S.V., 2015. Survival of LLSVPs for billions of years in a vigorously convecting mantle: replenishment and destruction of chemical anomaly. Journal of Geophysical Research: Solid Earth 120, 3824-3847.

Münker, C., Pfänder, J.A., Weyer, S., Büchl, A., Kleine, T., Mezger, K., 2003. Evolution of planetary cores and the Earth-Moon system from Nb/Ta systematics. Science 301, 84-87.

Nakamura, Y., Tatsumoto, M., 1988. Pb, Nd, and Sr isotopic evidence for a multicomponent source for rocks of Cook-Austral Islands and heterogeneities of mantle plumes. Geochimica et Cosmochimica Acta 52, 2909-2924.

Nishi, M., Irifune, T., Tsuchiya, J., Tange, Y., Nishihara, Y., Fujino, K., Higo, Y., 2014. Stability of hydrous silicate at high pressures and water transport to the deep lower mantle. Nature Geoscience 7, 224-227.

Nowell, G.M., 2004. Hf Isotope Systematics of Kimberlites and their Megacrysts: New Constraints on their Source Regions. Journal of Petrology 45, 1583-1612.

O'Connor, J.M., Jokat, W., Le Roex, A.P., Class, C., Wijbrans, J.R., Keßling, S., Kuiper, K.F., Nebel, O., 2012. Hotspot trails in the South Atlantic controlled by plume and plate tectonic processes. Nature Geoscience 5, 735.

O'Connor, J.M., le Roex, A.P., 1992. South Atlantic hot spot-plume systems: 1. Distribution of volcanism in time and space. Earth and Planetary Science Letters 113, 343-364.

O'Connor, J.M., Jokat, W., 2015. Tracking the Tristan-Gough mantle plume using discrete chains of intraplate volcanic centers buried in the Walvis Ridge. Geology 43, 715-718.

Palacz, Z.A., Saunder, A.D., 1986. Coupled trace element and isotope enrichment in the Cook-Austral-Samoa islands, southwest Pacific. Earth and Planetary Science Letters 79, 270-280.

Pearson, D.G., Brenker, F.E., Nestola, F., McNeill, J., Nasdala, L., Hutchison, M.T., Matveev, S., Mather, K., Silversmit, G., Schmitz, S., Vekemans, B., Vincze, L., 2014. Hydrous mantle transition zone indicated by ringwoodite included within diamond. Nature 507, 221-224.

Ray, J.S., Pande, K., Bhutani, R., Shukla, A.D., Rai, V.K., Kumar, A., Awasthi, N., Smitha, R., Panda, D.K., 2013. Age and geochemistry of the Newania dolomite carbonatites, India: implications for the source of primary carbonatite magma. Contributions to Mineralogy and Petrology 166, 1613-1632.

Ray, J.S., Ramesh, R., Pande, K., 1999. Carbon isotopes in Kerguelen plume-derived carbonatites: evidence for recycled inorganic carbon. Earth and Planetary Science Letters 170, 205-214.

Reid, D., Cooper, A., Rex, D., Harmer, R., 1990. Timing of post–Karoo alkaline volcanism in southern Namibia. Geological Magazine 127, 427-433.

Renne, P.R., Glen, J.M., Milner, S.C., Duncan, A.R., 1996. Age of Etendeka flood volcanism and associated intrusions in southwestern Africa. Geology 24, 659-662.

Rennie, S., Fagereng, Å., Diener, J., 2013. Strain distribution within a km-scale, mid-crustal shear zone: the Kuckaus Mylonite Zone, Namibia. Journal of Structural Geology 56, 57-69.

Richards, M.A., Duncan, R.A., Courtillot, V.E., 1989. Flood basalts and hot-spot tracks: plume heads and tails. Science 246, 103-107.

Ritsema, J., Deuss, A., van Heijst, H.J., Woodhouse, J.H., 2011. S40RTS: a degree-40 shear-velocity model for the mantle from new Rayleigh wave dispersion, teleseismic traveltime and normal-mode splitting function measurements. Geophysical Journal International 184, 1223-1236.

Robles-Cruz, S.E., Escayola, M., Jackson, S., Galí, S., Pervov, V., Watangua, M., Gonçalves, A., Melgarejo, J.C., 2012. U–Pb SHRIMP geochronology of zircon from the Catoca kimberlite, Angola: Implications for diamond exploration. Chemical Geology 310-311, 137-147.

Rogers, N., Hawkesworth, C., Palacz, Z., 1992. Phlogopite in the generation of olivine-melilitites from Namaqualand, South Africa and implications for element fractionation processes in the upper mantle. Lithos 28, 347-365.

Rohde, J., Hoernle, K., Hauff, F., Werner, R., O'Connor, J., Class, C., Garbe-Schonberg, D., Jokat, W., 2013a. 70 Ma chemical zonation of the Tristan-Gough hotspot track. Geology 41, 335-338.

Rohde, J.K., van den Bogaard, P., Hoernle, K., Hauff, F., Werner, R., 2013b. Evidence for an age progression along the Tristan-Gough volcanic track from new 40Ar/39Ar ages on phenocryst phases. Tectonophysics 604, 60-71.

Salters, V.J., Mallick, S., Hart, S.R., Langmuir, C.E., Stracke, A., 2011. Domains of depleted mantle: New evidence from hafnium and neodymium isotopes. Geochemistry, Geophysics, Geosystems 12.

Salters, V.J., White, W.M., 1998. Hf isotope constraints on mantle evolution. Chemical Geology 145, 447-460.

Sarda, P., Moreira, M., Staudacher, T., Schilling, J.G., Allègre, C.J., 2000. Rare gas systematics on the southernmost Mid-Atlantic Ridge: Constraints on the lower mantle and the Dupal source. Journal of Geophysical Research: Solid Earth 105, 5973-5996.

Schwindrofska, A., Hoernle, K., Hauff, F., van den Bogaard, P., Werner, R., Garbe-Schönberg, D., 2016. Origin of enriched components in the South Atlantic: Evidence from 40 Ma geochemical zonation of the Discovery Seamounts. Earth and Planetary Science Letters 441, 167-177.

Silva, M., Pereira, E., 1973. Estrutura vulcanico-carbonatitica da Catanda (Angola). Boletim dos Servicos de geologia e Minas de Angola 24, 5-14.

Simonetti, A., Goldstein, S., Schmidberger, S., Viladkar, S., 1998. Geochemical and Nd, Pb, and Sr isotope data from Deccan alkaline complexes—inferences for mantle sources and plume–lithosphere interaction. Journal of Petrology 39, 1847-1864.

Song, W., Xu, C., Smith, M.P., Kynicky, J., Huang, K., Wei, C., Zhou, L., Shu, Q., 2016. Origin of unusual HREE-Mo-rich carbonatites in the Qinling orogen, China. Sci Rep 6, 37377.

Storey, B.C., Leat, P.T., Ferris, J.K., 2001. The location of mantle-plume centers during the initial stages of Gondwana breakup. SPECIAL PAPERS-GEOLOGICAL SOCIETY OF AMERICA, 71-80.

Stracke, A., Bizimis, M., Salters, V.J., 2003. Recycling oceanic crust: Quantitative constraints. Geochemistry, Geophysics, Geosystems 4.

Strganac, C., Salminen, J., Jacobs, L.L., Polcyn, M.J., Ferguson, K.M., Mateus, O., Schulp, A.S., Morais, M.L., da Silva Tavares, T., Gonçalves, A.O., 2014. Carbon isotope stratigraphy, magnetostratigraphy, and 40Ar/39Ar age of the Cretaceous South Atlantic coast, Namibe Basin, Angola. Journal of African Earth Sciences 99, 452-462.

Stroncik, N.A., Trumbull, R.B., Krienitz, M.-S., Niedermann, S., Romer, R.L., Harris, C., Day, J., 2017. Helium isotope evidence for a deep-seated mantle plume involved in South Atlantic breakup. Geology 45, 827-830.

Sun, S.-S., McDonough, W.F., 1989. Chemical and isotopic systematics of oceanic basalts: implications for mantle composition and processes. Geological Society, London, Special Publications 42, 313-345.

Thirlwall, M., 2000. Inter-laboratory and other errors in Pb isotope analyses investigated using a 207Pb–204Pb double spike. Chemical Geology 163, 299-322.

Torsvik, T.H., Smethurst, M.A., Burke, K., Steinberger, B., 2006. Large igneous provinces generated from the margins of the large low-velocity provinces in the deep mantle. Geophysical Journal International 167, 1447-1460.

Toyoda, K., Horiuchi, H., Tokonami, M., 1994. Dupal anomaly of Brazilian carbonatites: geochemical correlations with hotspots in the South Atlantic and implications for the mantle source. Earth and Planetary Science Letters 126, 315-331.

U.S. Geological Survey, 2020, Mineral commodity summaries 2020: U.S. Geological Survey, 200 p., https://doi.org/10.3133/mcs2020.

Veksler, I.V., Petibon, C., Jenner, G.A., Dorfman, A.M., Dingwell, D.B., 1998. Trace Element Partitioning in Immiscible Silicate–Carbonate Liquid Systems: an Initial Experimental Study Using a Centrifuge Autoclave. Journal of Petrology 39, 2095-2104.

Verwoerd, W., 1993. Update on carbonatites of South Africa and Namibia. South African Journal of Geology 96, 75-95.
Vladykin, N., 2009. Potassium alkaline lamproite-carbonatite complexes: petrology, genesis, and ore reserves. Russian Geology and Geophysics 50, 1119-1128.
Walter, M.J., Bulanova, G.P., Armstrong, L.S., Keshav, S., Blundy, J.D., Gudfinnsson, G., Lord, O.T., Lennie, A.R., Clark, S.M., Smith, C.B., Gobbo, L., 2008. Primary carbonatite melt from deeply subducted oceanic crust. Nature 454, 622-625.
Weidendorfer, D., Manning, C.E., Schmidt, M.W., 2020. Carbonate melts in the hydrous upper mantle. Contributions to Mineralogy and Petrology 175, 1-17.
Weiss, Y., Class, C., Goldstein, S.L., Hanyu, T., 2016. Key new pieces of the HIMU puzzle from olivines and diamond inclusions. Nature 537, 666-670.
Weiss, Y., Goldstein, S.L., 2018. The involvement of diamond-forming fluids in the metasomatic 'cocktail'of kimberlite sources. Mineralogy and Petrology 112, 149-167.
White, W.M., Hofmann, A.W., 1982. Sr and Nd isotope geochemistry of oceanic basalts and mantle evolution. Nature 296, 821-825.
Whitehead, K., Le Roex, A., Class, C., Bell, D., 2002. Composition and Cretaceous thermal structure of the upper mantle beneath the Damara Mobile Belt: evidence from nephelinite-hosted peridotite xenoliths, Swakopmund, Namibia. Journal of the Geological Society 159, 307-321.
Willbold, M., Stracke, A., 2006. Trace element composition of mantle end-members: Implications for recycling of oceanic and upper and lower continental crust. Geochemistry, Geophysics, Geosystems 7.
Willbold, M., Stracke, A., 2010. Formation of enriched mantle components by recycling of upper and lower continental crust. Chemical Geology 276, 188-197.
Williams, Q., Hemley, R.J., 2001. Hydrogen in the deep Earth. Annual Review of Earth and Planetary Sciences 29, 365-418.
Woodhead, J.D., 1996. Extreme HIMU in an oceanic setting: The geochemistry of Mangaia Island (Polynesia), and temporal evolution of the Cook—Austral hotspot. Journal of Volcanology and Geothermal Research 72, 1-19.
Woolley, A., Church, A., 2005. Extrusive carbonatites: a brief review. Lithos 85, 1-14.
Workman, R.K., Hart, S.R., 2005. Major and trace element composition of the depleted MORB mantle (DMM). Earth and Planetary Science Letters 231, 53-72.
Yang, K.-F., Fan, H.-R., Santosh, M., Hu, F.-F., Wang, K.-Y., 2011. Mesoproterozoic carbonatitic magmatism in the Bayan Obo deposit, Inner Mongolia, North China: Constraints for the mechanism of super accumulation of rare earth elements. Ore Geology Reviews 40, 122-131.
Yuan, X., Heit, B., Brune, S., Steinberger, B., Geissler, W.H., Jokat, W., Weber, M., 2017. Seismic structure of the lithosphere beneath NWNamibia: Impact of the Tristan da Cunha mantle plume. Geochemistry, Geophysics, Geosystems 18, 125-141.
Zack, T., Kronz, A., Foley, S.F., Rivers, T., 2002. Trace element abundances in rutiles from eclogites and associated garnet mica schists. Chemical Geology 184, 97-122.
Zhongxin, Y., Ge, B., Chenyu, W., Zhongqin, Z., Xianjiang, Y., 1992. Geological features and genesis of the Bayan Obo REE ore deposit, Inner Mongolia, China. Applied Geochemistry 7, 429-442.

Zhou, H., Hoernle, K., Geldmacher, J., Hauff, F., Homrighausen, S., Garbe-Schönberg, D., Jung, S., 2020. Geochemistry of Etendeka magmatism: Spatial heterogeneity in the Tristan-Gough plume head. Earth and Planetary Science Letters 535, 116123.

Zindler, A., Hart, S., 1986. Chemical geodynamics. Annual review of earth and planetary sciences 14, 493-571.

Chapter 5.

Conclusions and Outlook

The objective of my PhD thesis is to study the composition and origin of the Etendeka flood basalts and related alkaline and carbonatite intrusive complexes. Based on our new samples and geochemical data, I could address all my objectives (Chapter 1).

Are the Etendeka flood basalts formed by the plume head stage of the Tristan-Gough plume?

The high-Ti basalts were only discovered in Northern Etendeka. They show restricted trace element and isotope composition without significantly crustal contamination, representing their magma source composition. All high-Ti basalts in Etendeka show the same isotopic composition as Gough hotspot track and the EM1 basement lavas of Walvis Ridge. Their locations and constrained ages are also consistent with an age-progression from Angola to the volcanic active Gough Island, suggesting that the high-Ti basalts were indeed derived from the Tristan-Gough plume. Combined with previous research (Hoernle et al., 2015), my new findings support the view that the Gough-type magma source dominates the Tristan-Gough mantle plume at all times whereas the transiently occurring Tristan-type magma source could not be detected in the plume head stage.

What caused the distinct composition of high-Ti and low-Ti lavas: shallow lithospheric contamination or a heterogeneous plume source? What is their distribution in SW Africa?

The spatial chemical zonation of Etendeka flood basalt was originally defined by their different Ti content. Our new samples accord with this classification and confirm that all high-Ti basalts located in Northern Etendeka and low-Ti basalts dominate in Southern Etendeka. As outlined above, the high-Ti basalts can be associated with a source intrinsic to the Tristan-Gough plume. The low-Ti basalts, on the other hand, were strongly contaminated by the local upper crust complicating any assignment to a particular source. The least contaminated low-Ti basalts, however, show specifically unradiogenic $^{208}Pb/^{204}Pb$ and radiogenic $^{143}Nd/^{144}Nd$ compositions that are distinct from the Gough-type. Such composition is characteristic for rocks from the Doros intrusion

and Horingbaai dikes and accordingly, I assign this composition to a distinct component (Doros).

The high $^{3}He/^{4}He$ measured for Doros-type rocks (Stroncik et al., 2017) reject a lithospheric origin. Additionally, rocks with similar Doros composition were also found in the oceanic Mozambique Ridge (Jacques et al., 2019) in the Indian Ocean, which plume source is believed to be derived from the southern margin of the African LLSVP. Combining these observations, I believe that the low-Ti magma also originated from the deep mantle sources at the edge of African LLSVP. Therefore, the distinct composition of high- and low-Ti magma (Gough-Doros zonation) could reflect geochemical heterogeneity in the lower mantle subsequently leading to a heterogeneous plume, rather than assigning this heterogeneity to contrasting continental lithosphere assimilation.

Carbonatites and silica-undersaturated rocks in the Damara belt are less influenced by crustal contamination. The geochemical composition of the investigated rocks from the Damara carbonatitic and silica-undersaturated intrusions indicate that not all magmatism in southern Etendeka was derived from the Doros-domain of the plume. Whereas the southeastern Etendeka province shows Gough-type isotopic composition, rocks with Doros-type composition are constrained to southwestern Etendeka. This study is the first that reports rocks with Gough-type composition in southern Etendeka. The Gough-type magmatism in northern and southeastern Etendeka appears to form a horseshoe-shaped zone that surrounds the Doros-type magmatism in southwestern Etendeka.

Is there any late-stage HIMU-like volcanism in the Etendeka area? Do the late-stage silica-undersaturated rocks and carbonatites fit into the late-stage hotspot track model?

Our new isotope data from Agate Mountain, Swakopmund basanite plugs and Dicker Willem clearly show that they have a similar composition as the late-stage HIMU-like seamounts on the Walvis Ridge. In addition, the eruption ages of Agate Mountain and Dicker Willem could fit into several (parallel) age-progressive hotspot tracks of HIMU composition, such as Mecamedes – Walvis track and Gibeon – Vema track, respectively. Although the Swakopmund plugs do not belong to any known age-progressive volcanic chain, their ages coincide with the HIMU signature belt if we project their location

orthogonally to the adjacent hotspot tracks. Hence, silica-undersaturated rocks and carbonatites from Agate Mountain, Dicker Willem and Swakopmund plugs seem to have originated from the same magma source as the late-stage seamounts of HIMU composition that were found on the Walvis Ridgebasement. Combining all HIMU-like volcanisms in SW Africa and the SE Atlantic, they appear to form a belt of HIMU signature rocks about 1000-1500 km within (east of the outer margin of) the LLSVP. The ages and locations of these age-progressive HIMU-like hotspots, such as St.Helena, Walvis – Agate Mountain – Mocamedes, Gibeon – Dicker Willem – Vema, and Shona – Arrica, allow us to trace their plume source back to a steep step inside the LLSVP in the lower mantle, which is visible in multiple seismic tomographic models.

What are the geochemical fingerprints of Damara alkaline and carbonatitic intrusive complexes?

Besides the significantly older Kalkfeld carbonatites, all investigated Cretaceous carbonatites show EM1 isotopic composition. They have the most radiogenic $^{206}Pb/^{204}Pb$ ratios and the most depleted Sr, Nd isotopes within the Gough compositional field. Some small but not neglectable differences, such as slightly more unradiogenic $^{208}Pb/^{204}Pb$ and radiogenic $^{143}Nd/^{144}Nd$ ratios, are discussed in Chapter 3. I propose that the different isotopic compositions of EM1 carbonatites are inherited from the mantle plume.

The Kalkfeld carbonatites show $^{87}Sr/^{86}Sr$, $^{143}Nd/^{144}Nd$ isotopic ratios which are clearly distinct from the Tristan-Gough plume source. Moreover, their Triassic age is significantly older than the plume head stage of the Tristan-Gough plume, clearly ruling out any genetic relationship with the Tristan-Gough plume.

Does the geochemical composition of the carbonatites in Namibia provide further insights into their origin?

The origin of Triassic and lower Cretaceous carbonatitic rocks in Namibia are controversially discussed. In Chapter 4, I test the hypothesis that carbonatite magmas formed by low-degree melts of subducted, carbonated oceanic crust (returned by mantle plumes) coexisting with perovskite and majorite garnet in the deep upper mantle, subsequently undergoing an immiscible process upon further ascend at a shallower depth. The measured trace element concentrations of carbonatites are consistent with this model, supporting an origin by recycled carbonated oceanic crust. Their HIMU-

like compositions and the close relationship with the LLSVP indicate a lower mantle origin. The new geochemical data that I present in Chapter 3 and Chapter 4 of my thesis indicate that the Namibian carbonatites are plotted within the “carbonatite box” between the EM1 and HIMU-like endmembers (Bell and Tilton, 2001). There is no evidence that this composition is affected by the continental lithospheric mantle. Therefore, the compositions of Cretaceous carbonatites are proposed to reflect their respective mantle plume source.

References

Bell, K., Tilton, G., 2001. Nd, Pb and Sr isotopic compositions of East African carbonatites: evidence for mantle mixing and plume inhomogeneity. Journal of Petrology 42, 1927-1945.

Jacques, G., Hauff, F., Hoernle, K., Werner, R., Uenzelmann-Neben, G., Garbe-Schönberg, D., Fischer, M., 2019. Nature and origin of the Mozambique Ridge, SW Indian Ocean. Chemical Geology 507, 9-22.

Stroncik, N.A., Trumbull, R.B., Krienitz, M.-S., Niedermann, S., Romer, R.L., Harris, C., Day, J., 2017. Helium isotope evidence for a deep-seated mantle plume involved in South Atlantic breakup. Geology 45, 827-830.

Appendix

Appendix A

Table A1: Ages of Etendeka volcanisms

Area		Lithology	Age (Ma, ±2σ)	Method	author
Doros	intrusion	gabbros	130±1	Ar-Ar	(Owen-Smith et al., 2017)
Tafelkop	lavas	Sample ET94-18	132.9±0.6	Ar-Ar	(Jerram et al., 1999)
Horingbaai	dikes	dolerite	131-132	Dikes intersection	(Thompson et al., 2001)
			125&130	Ar-Ar	(Erlank et al., 1984)
Tafelberg	lavas	plagioclase	132.3±0.7	Ar-Ar	(Renne et al., 1996)
Brandberg	intrusion	Biotite	133.0±0.8	Ar-Ar	(Schmitt et al., 2000)
		Biotite	132.6±1.8	Ar-Ar	
Erongo	intrusion	Zircon	135.3±6.4	U-Pb zircon	(Pirajno et al., 2000)
		Granite, rhyolite, basic alkaline plug	130.3-132.6	Ar-Ar, U-Pb zircon	(Wigand et al., 2004)
Messum	intrusion	Gabbro, Quartz-Diorite	132±0.7	Ar-Ar	(Renne et al., 1996)
		Nepheline-syenite	129±0.7	Ar-Ar	
Cape Cross	intrusion	Nepheline-syenite	135±0.7	Ar-Ar	(Milner et al., 1995)
Huab sills	dikes	Plagioclase	132±0.7	Ar-Ar	(Renne et al., 1996)

Table A2: Major element data of rock standards

Element	JGB-1	JGB-1*	diff.(%)	JB-3	JB-3*	diff.(%)	JB-2	JB-2*	diff.(%)
SiO_2	43.33	43.44	0.25	50.39	51.04	1.27	52.76	53.2	0.83
Al_2O_3	17.78	17.66	0.68	17.46	16.89	3.37	14.83	14.67	1.09
Fe_2O_3	15.22	15.16	0.40	11.97	11.88	0.76	14.36	14.34	0.14
MnO	0.18	0.17	5.88	0.17	0.16	6.25	0.21	0.2	5.00
MgO	7.81	7.83	0.26	5.14	5.2	1.15	4.61	4.66	1.07
CaO	12.12	11.98	1.17	10.01	9.86	1.52	10.02	9.89	1.31
Na_2O	1.23	1.23	0.00	2.78	2.82	1.42	2.05	2.03	0.99
K_2O	0.22	0.24	8.33	0.75	0.78	3.85	0.4	0.42	4.76
TiO_2	1.61	1.62	0.62	1.44	1.45	0.69	1.18	1.19	0.84
P_2O_5	0.05	0.05	0.00	0.3	0.29	3.45	0.1	0.1	0.00
Element	JA-3	JA-3*	diff.(%)	JG-3	JG-3*	diff.(%)	JG-2	JG-2*	diff.(%)
SiO_2	61.2	62.26	1.70	66.12	67.1	1.46	76.04	76.95	1.18
Al_2O_3	15.75	15.57	1.16	15.47	15.52	0.32	12.43	12.41	0.16
Fe_2O_3	6.58	6.59	0.15	3.67	3.73	1.61	0.9	0.92	2.17
MnO	0.1	0.106	5.66	0.07	0.072	2.78	0.02	0.015	33.33
MgO	3.71	3.65	1.64	1.79	1.79	0.00	0.05	0.04	25.00
CaO	6.45	6.28	2.71	3.82	3.76	1.60	0.72	0.8	10.00
Na_2O	3.25	3.17	2.52	4.09	4.03	1.49	3.85	3.55	8.45
K_2O	1.37	1.41	2.84	2.56	2.63	2.66	4.6	4.72	2.54
TiO_2	0.69	0.68	1.47	0.47	0.48	2.08	0.04	0.04	0.00
P_2O_5	0.11	0.11	0.00	0.13	0.12	8.33	0.01	0.002	400.00

* Working values are from Govindaraju (1994).

Table A3: Trace element concentration of reference material BIR-1

Sample:	#1	#2	#3	#4	Mean	Std. dev. (±1σ abs)	Std. dev. (±1σ %)	GEOREM	diff. (%)
Li (ppm)	3.34	3.39	3.45	3.39	3.39	0.05	1.41	3.2	6.0
Sc (ppm)	44.5	44.0	43.3	42.9	43.66	0.70	1.60	43	1.5
V (ppm)	317	316	313	307	313.12	4.40	1.40	319	1.8
Cr (ppm)	378	373	382	374	376.71	4.24	1.13	391	3.7
Co (ppm)	51.8	51.4	50.6	51.4	51.31	0.52	1.01	52	1.3
Ni (ppm)	174	172	162	164	167.95	6.01	3.58	166	1.2
Cu (ppm)	120	121	110	112	115.70	5.48	4.73	119	2.8
Zn (ppm)	67.7	67.2	70.9	70.1	68.99	1.81	2.62	72	4.2
Ga (ppm)	16.3	16.1	15.9	15.8	16.03	0.23	1.43	15.3	4.8
Rb (ppm)	0.22	0.22	0.22	0.21	0.22	0.00	1.29	0.2	8.9
Sr (ppm)	111	111	110	110	110.45	0.78	0.70	109	1.3
Y (ppm)	16.3	16.3	16.0	15.9	16.10	0.22	1.36	15.6	3.2
Zr (ppm)	15.6	15.6	15.6	15.3	15.52	0.16	1.01	14	10.9
Nb (ppm)	0.55	0.56	0.56	0.55	0.56	0.00	0.89	0.55	1.0
Cs (ppm)	0.01	0.01	0.01	0.01	0.01	0.00	8.09	0.007	4.1
Ba (ppm)	7.06	6.75	6.48	6.94	6.81	0.25	3.71	7.14	4.7
La (ppm)	0.63	0.62	0.62	0.61	0.62	0.01	0.85	0.615	0.8
Ce (ppm)	1.93	1.93	1.93	1.91	1.93	0.01	0.67	1.92	0.3
Pr (ppm)	0.38	0.38	0.38	0.37	0.38	0.00	1.11	0.37	2.2
Nd (ppm)	2.47	2.48	2.48	2.43	2.46	0.03	1.02	2.38	3.5
Sm (ppm)	1.14	1.15	1.13	1.12	1.14	0.02	1.32	1.12	1.4
Eu (ppm)	0.54	0.55	0.54	0.53	0.54	0.01	1.13	0.53	2.0
Gd (ppm)	1.84	1.85	1.84	1.81	1.83	0.02	0.91	1.87	2.0
Tb (ppm)	0.36	0.37	0.37	0.36	0.36	0.00	0.94	0.36	1.2
Dy (ppm)	2.64	2.65	2.64	2.60	2.63	0.02	0.89	2.51	4.9
Ho (ppm)	0.58	0.58	0.58	0.57	0.58	0.01	1.15	0.56	3.3
Er (ppm)	1.67	1.67	1.66	1.64	1.66	0.02	0.96	1.66	0.1
Tm (ppm)	0.25	0.25	0.25	0.25	0.25	0.00	0.52	0.25	0.6
Yb (ppm)	1.67	1.68	1.67	1.64	1.66	0.02	1.08	1.65	0.9
Lu (ppm)	0.26	0.26	0.26	0.26	0.26	0.00	0.92	0.25	3.4
Hf (ppm)	0.58	0.58	0.59	0.58	0.58	0.00	0.00	0.582	0.1
Ta (ppm)	0.04	0.04	0.04	0.04	0.04	0.00	0.00	0.036	16.1
Pb (ppm)	3.24	3.19	3.00	3.13	3.14	0.10	0.08	3.1	1.2
Th (ppm)	0.03	0.03	0.03	0.03	0.03	0.00	0.00	0.032	1.2
U (ppm)	0.01	0.01	0.01	0.01	0.01	0.00	4.49	0.01	31.1

References Appendix A

Erlank, A., Marsh, J., Duncan, A., Miller, R.M., Hawkesworth, C., Betton, P., Rex, D., 1984. Geochemistry and petrogenesis of the Etendeka volcanic rocks from SWA/Namibia. Special Publication of Geological Society of South Africa 13, 195-245.

Govindaraju, K., 1994, Compilation of Working Values and Sample Description for 383 Geostandards: Geostandards Newsletter, v. 18, no. 2, p. 331-331.

Jerram, D., Mountney, N., Holzförster, F., Stollhofen, H., 1999. Internal stratigraphic relationships in the Etendeka Group in the Huab Basin, NW Namibia: understanding the onset of flood volcanism. Journal of Geodynamics 28, 393-418.

Milner, S., Le Roex, A., O'CONNOR, J., 1995. Age of Mesozoic igneous rocks in northwesternNamibia, and their relationship to continental breakup. Journal of the Geological Society 152, 97-104.

Owen-Smith, T., Ashwal, L., Sudo, M., Trumbull, R., 2017. Age and petrogenesis of the Doros Complex, Namibia, and implications for early plume-derived melts in the Paraná–Etendeka LIP. Journal of Petrology 58, 423-442.

Pirajno, F., Phillips, D., Armstrong, R.A., 2000. Volcanology and eruptive histories of the Erongo volcanic complex and the Paresis igneous complex, Namibia: implications for mineral deposit styles. Commun Geol Surv Namibia 12, 301-312.

Renne, P.R., Glen, J.M., Milner, S.C., Duncan, A.R., 1996. Age of Etendeka flood volcanism and associated intrusions in southwestern Africa. Geology 24, 659-662.

Schmitt, A., Emmermann, R., Trumbull, R., Bühn, B., Henjes-Kunst, F., 2000. Petrogenesis and 40Ar/39Ar geochronology of the Brandberg Complex, Namibia: evidence for a major mantle contribution in metaluminous and peralkaline granites. Journal of Petrology 41, 1207-1239.

Thompson, R., Gibson, S., Dickin, A., Smith, P., 2001. Early Cretaceous basalt and picrite dykes of the southern Etendeka region, NW Namibia: windows into the role of the Tristan mantle plume in Paraná–Etendeka magmatism. Journal of Petrology 42, 2049-2081.

Wigand, M., Schmitt, A.K., Trumbull, R.B., Villa, I.M., Emmermann, R., 2004. Short-lived magmatic activity in an anorogenic subvolcanic complex: 40Ar/39Ar and ion microprobe U–Pb zircon dating of the Erongo, Damaraland, Namibia. Journal of Volcanology and Geothermal Research 130, 285-305.

Appendix B

Table B1: Major element data of rock standards

	SiO2 (wt%)	Al2O3 (wt%)	Fe2O3 (wt%)	MgO (wt%)	MnO (wt%)	CaO (wt%)	Na2O (wt%)	K2O (wt%)	TiO2 (wt%)	P2O5 (wt%)	SO3 (wt%)	Sum Of Conc.
JB-3	50.81	17.31	11.93	5.11	0.17	9.93	2.63	0.74	1.43	0.29	0.07	100.33
JB-3*	51.04	16.89	11.88	5.2	0.16	9.86	2.82	0.78	1.45	0.29		
diff%	0.45	2.49	0.42	1.73	6.25	0.71	6.74	5.13	1.38	0.00		
JB-2	53.06	14.71	14.32	4.56	0.21	9.96	1.95	0.4	1.18	0.1	0.06	100.4
JB-2*	53.2	14.67	14.34	4.66	0.2	9.89	2.03	0.42	1.19	0.1		
diff%	0.26	0.27	0.14	2.15	5.00	0.71	3.94	4.76	0.84	0.00		
JA-3	61.71	15.62	6.57	3.69	0.1	6.41	3.09	1.36	0.69	0.11	0.1	99.91
JA-3*	62.26	15.57	6.59	3.65	0.106	6.28	3.17	1.41	0.68	0.11		
diff%	0.88	0.32	0.30	1.10	5.66	2.07	2.52	3.55	1.47	0.00		
JG-3	66.35	15.36	3.66	1.78	0.07	3.76	3.9	2.53	0.48	0.13	0.08	99.16
JG-3*	67.1	15.52	3.73	1.79	0.072	3.76	4.03	2.63	0.48	0.12		
diff%	1.12	1.03	1.88	0.56	2.78	0.00	3.23	3.80	0.00	8.33		
JG-2	76.56	12.4	0.91	0.05	0.02	0.72	3.65	4.58	0.04	0.01	0.21	99.78
JG-2*	76.95	12.41	0.92	0.04	0.015	0.8	3.55	4.72	0.04	0.002		
diff%	0.51	0.08	1.09	25.00	33.33	10.00	2.82	2.97	0.00	400.00		
JGB-1	43.43	17.52	15.16	7.74	0.18	11.95	1.16	0.22	1.6	0.05	0.31	100.32
JGB-1*	43.44	17.66	15.16	7.83	0.17	11.98	1.23	0.24	1.62	0.05		
diff%	0.02	0.79	0.00	1.15	5.88	0.25	5.69	8.33	1.23	0.00		

* Working values are from Govindaraju (1994).

Table B2: Trace element concentration of reference material (MACS-3 NP 20140925-A-01) by LA-ICP-MS

	#1	#2	#3	#4	#5	#6	Average	RSD%	Reference value*	diff%
Li	65.8	66.4	67.2	67.3	66.3	66.8	66.63	0.8	63	5.8
Sc	23.8	23.9	23.4	22.7	23.3	22.8	23.30	2.1		
V	45.1	47.0	46.7	46.7	47.5	45.9	46.47	1.8	46.7	0.5
Cr	117	118	120	120	120	116	118.45	1.4	114	3.9
Mn	544	556	553	542	555	531	546.81	1.8	505	8.3
Fe	10919	10968	10797	10980	11046	10889	10933.21	0.8	11900	8.1
Co	57.2	56.1	58.0	57.0	58.2	56.9	57.23	1.4	56.2	1.8
Ni	58.5	58.5	60.4	59.1	59.2	60.7	59.41	1.6	58.7	1.2
Cu	122	124	126	122	124	123	123.34	1.2	118	4.5
Zn	144	148	151	149	154	147	148.90	2.1	145	2.7
Ga	15.2	15.2	15.4	14.9	15.4	15.2	15.20	1.1		
Rb	0.0	0.0	0.0	0.0	0.1	0.0	0.05	3.4	0.044	9.5
Sr	6868	6969	6987	6869	7063	6955	6951.95	1.1	6970	0.3
Y	24.6	24.5	23.9	23.4	24.2	23.4	23.99	2.2	23	4.3
Zr	9.25	9.27	9.07	8.73	9.09	8.79	9.03	2.5	8.08	11.8
Nb	51.2	52.2	51.6	50.6	52.5	51.2	51.57	1.4		
Cs	0.0	0.0	0.0	0.0	0.0	0.0	0.01	3.9	0.01	10.0
Ba	57.3	59.9	59.6	58.0	60.1	61.0	59.30	2.3	59.7	0.7
La	10.8	11.4	11.2	10.9	11.3	11.3	11.16	2.2	11.1	0.5
Ce	11.2	11.4	11.4	11.4	11.6	11.7	11.45	1.5	11.4	0.4
Pr	11.5	12.0	11.9	11.6	12.0	12.0	11.84	1.9	11.9	0.5
Nd	10.8	11.1	11.1	10.8	11.1	11.1	10.98	1.5	11.2	2.0
Sm	10.6	10.9	10.8	10.4	10.8	10.8	10.72	1.7	11	2.5
Eu	11.1	11.6	11.4	11.1	11.5	11.8	11.39	2.5	11.6	1.8
Gd	10.3	10.7	10.7	10.1	10.3	10.6	10.44	2.4	10.6	1.5
Tb	10.4	10.7	10.7	10.2	10.6	10.7	10.52	1.9	10.5	0.2
Dy	10.5	10.8	10.7	10.1	10.6	10.8	10.60	2.5	11	3.6
Ho	11.1	11.4	11.2	10.7	11.1	11.2	11.12	2.0	11.1	0.2
Er	11.1	11.3	11.2	10.6	11.1	11.2	11.09	2.2	11.3	1.9
Tm	11.4	11.7	11.5	11.0	11.5	11.6	11.44	2.0	11.6	1.4
Yb	10.7	11.0	10.8	10.4	10.9	11.1	10.80	2.3	11.6	6.9
Lu	10.7	10.9	10.9	10.4	10.7	11.0	10.76	2.2	11.1	3.0
Hf	4.66	4.76	4.73	4.51	4.67	4.82	4.69	2.3	4.94	5.0
Ta	19.6	19.8	19.7	19.0	19.9	20.4	19.73	2.3		
W	1.88	1.99	2.03	1.94	2.07	2.12	2.00	4.4		
Pb	55.7	57.2	58.1	56.1	57.7	60.3	57.52	2.8	60	4.1
Th	50.3	52.7	53.0	50.9	53.1	54.8	52.45	3.1	54	2.9
U	1.30	1.37	1.40	1.36	1.42	1.47	1.39	4.3	1.5	7.6

* Working values are from Jochum (2019)

Table B3: Trace element concentration of reference material by ICP-MS

	BIR-1	BIR-1	Mean	Std. dev. (±1σ abs)	Std. dev. (±1σ %)	GEOREM	diff. (%)	BHVO-2	BHVO-2	Mean	Std. dev. (±1σ abs)	Std. dev. (±1σ %)	GEOREM	diff. (%)
Li	3.28	3.29	3.28	0.01	0.22	**3.4**	3.5	4.48	4.51	4.50	0.02	0.45	**4.6**	2.3
Sc	40.7	41.2	40.97	0.34	0.84	**44**	6.9	30.7	31.4	31.08	0.48	1.56	**31.8**	2.3
Cu	107	107	106.61	0.11	0.11	**126**	15.4	127	128	127.71	0.86	0.67	**127**	0.6
Zn	68.7	67.9	68.31	0.56	0.81	**71**	3.8	135	105	120.17	21.66	18.02	**103**	16.7
Rb	0.210	0.207	0.21	0.00	0.96	**0.212**	1.8	9.16	9.25	9.21	0.06	0.66	**9.2**	0.1
Sr	103	104	103.93	0.68	0.65	**104**	0.1	385	388	386.44	1.90	0.49	**395**	2.2
Y	14.9	15.0	14.99	0.07	0.49	**16**	6.3	25.3	25.5	25.40	0.11	0.42	**25.5**	0.4
Zr	14.6	14.6	14.61	0.02	0.11	**14**	4.4	164	164	163.96	0.40	0.24	**174**	5.8
Cs	0.006	0.006	0.01	0.00	0.00	**0.005**	30.0	0.109	0.108	0.11	0.00	0.74	**0.11**	1.7
Ba	6.49	6.58	6.53	0.07	1.01	**5.83**	12.1	128	128	127.87	0.34	0.27	**130**	1.6
La	0.593	0.592	0.59	0.00	0.06	**0.62**	4.5	15.0	15.1	15.07	0.05	0.35	**15.2**	0.8
Ce	1.82	1.83	1.83	0.01	0.59	**1.95**	6.4	36.9	36.8	36.88	0.08	0.22	**38**	3.0
Pr	0.364	0.365	0.36	0.00	0.12	**0.38**	4.1	5.28	5.28	5.28	0.00	0.05	**5.3**	0.4
Nd	2.37	2.39	2.38	0.01	0.58	**2.5**	4.8	24.7	24.8	24.74	0.07	0.26	**25**	1.0
Sm	1.09	1.11	1.10	0.01	1.19	**1.1**	0.3	6.14	6.13	6.14	0.01	0.19	**6.2**	1.0
Eu	0.515	0.521	0.52	0.00	0.82	**0.54**	4.1	2.06	2.09	2.07	0.02	0.81	**2.06**	0.7
Gd	1.75	1.75	1.75	0.00	0.04	**1.85**	5.3	6.08	6.10	6.09	0.01	0.21	**6.3**	3.4
Tb	0.353	0.354	0.35	0.00	0.17	**0.36**	1.9	0.942	0.940	0.94	0.00	0.18	**0.93**	1.2
Dy	2.54	2.54	2.54	0.00	0.05	**2.5**	1.8	5.31	5.31	5.31	0.00	0.04	**5.25**	1.1
Ho	0.561	0.564	0.56	0.00	0.36	**0.57**	1.3	0.971	0.977	0.97	0.00	0.37	**0.99**	1.6
Er	1.61	1.62	1.62	0.01	0.38	**1.7**	4.9	2.44	2.43	2.44	0.01	0.36	**2.5**	2.5
Tm	0.244	0.243	0.24	0.00	0.37	**0.26**	6.5	0.325	0.326	0.33	0.00	0.08	**0.34**	4.2
Yb	1.63	1.62	1.62	0.00	0.09	**1.65**	1.5	1.98	2.00	1.99	0.01	0.66	**2.00**	0.5
Lu	0.249	0.251	0.25	0.00	0.54	**0.26**	3.8	0.284	0.284	0.28	0.00	0.05	**0.28**	1.4
Hf	0.587	0.583	0.58	0.00	0.37	**0.581**	0.7	4.49	4.46	4.47	0.02	0.48	**4.074**	9.8
Tl	0.004	0.004	0.00	0.00	4.93	**0.01**	56.8	0.026	0.025	0.03	0.00	2.38	**-**	
Pb	3.10	2.96	3.03	0.10	3.40	**3.08**	1.6	1.78	1.55	1.67	0.16	9.43	**1.7**	2.0
Th	0.030	0.031	0.03	0.00	2.99	**0.03**	1.7	1.17	1.19	1.18	0.01	1.14	**1.21**	2.7
U	0.011	0.011	0.01	0.00	1.09	**0.01**	10.7	0.391	0.396	0.39	0.00	0.86	**0.41**	4.1

References Appendix B

Jochum K.P., 2019, Nano-powdered calcium carbonate reference materials: Significant progress for microanalysis?. Geostandards and Geoanalytical Research, 43 (4), 595-609

Acknowledgements

First, I would like to express my deeply gratitude to my supervisors: Prof. Dr. Kaj Hoernle and PD. Dr. Jörg Geldmacher for their powerful encouraging and supervising. After 4 years close cooperation with them, I have learned a lot from their rigorous scientific spirit. Their professional instructions help me to overcome all the difficulties of my PhD researches. Additionally, they also help me to realize the German customs, leading me into pleased and courageous life in Germany.

Second, I would like to thank all co-authors, such as Folkmar Hauff, Stephan Homrighausen, Dieter Garbe-Schönberg, Stefan Jung, Ilya Bindeman, Jo-Anne Wartho, for their essential help for the research and publications.

I also would like to express my appreciation to Folkmar Hauff, Silke Hauff, Karin Junge, Jo-Anne Wartho, Ulrike Westernströer, Maxim Portnyagin and Thor Hansteen for their great help about the sample analysis and data interpretation. I also thank the Geological Survey of Namibia for the help and permission to carry out field studies in Namibia and sending samples outside of Namibia for geochemical analyses.

Many thanks also to colleges and friends (Hongbo Liu, Christina Bonanati, Susanne Grahl, Malte Eggersglüß, Yueyang Xia and Bo Ma) for their kindness and constant support of daily routine affairs.

I am also grateful for the China scholarship Council (CSC), GEOMAR Helmholtz Center for Ocean Research Kiel, German Ministry of Education and Research, the International Center of Kiel University for for their financial fundings during my PhD research.

I am glad that Prof. Dr. Kaj Hoernle and PD. Dr. Thor Hansteen become the reviewer and examiners of my thesis.

At last, the final thanks belong to my family: my girlfriend Yiqiong Zhang and my parents. They always emotionally support me for my daily work and chasing the good life.